Secondary Uranium Phases of Spent Nuclear Fuel – Coffinite, $USiO_4$, and Studtite, $UO_4 \cdot 4H_2O$ – Synthesis, Characterization, and Investigations Regarding Phase Stability

Sabrina Labs

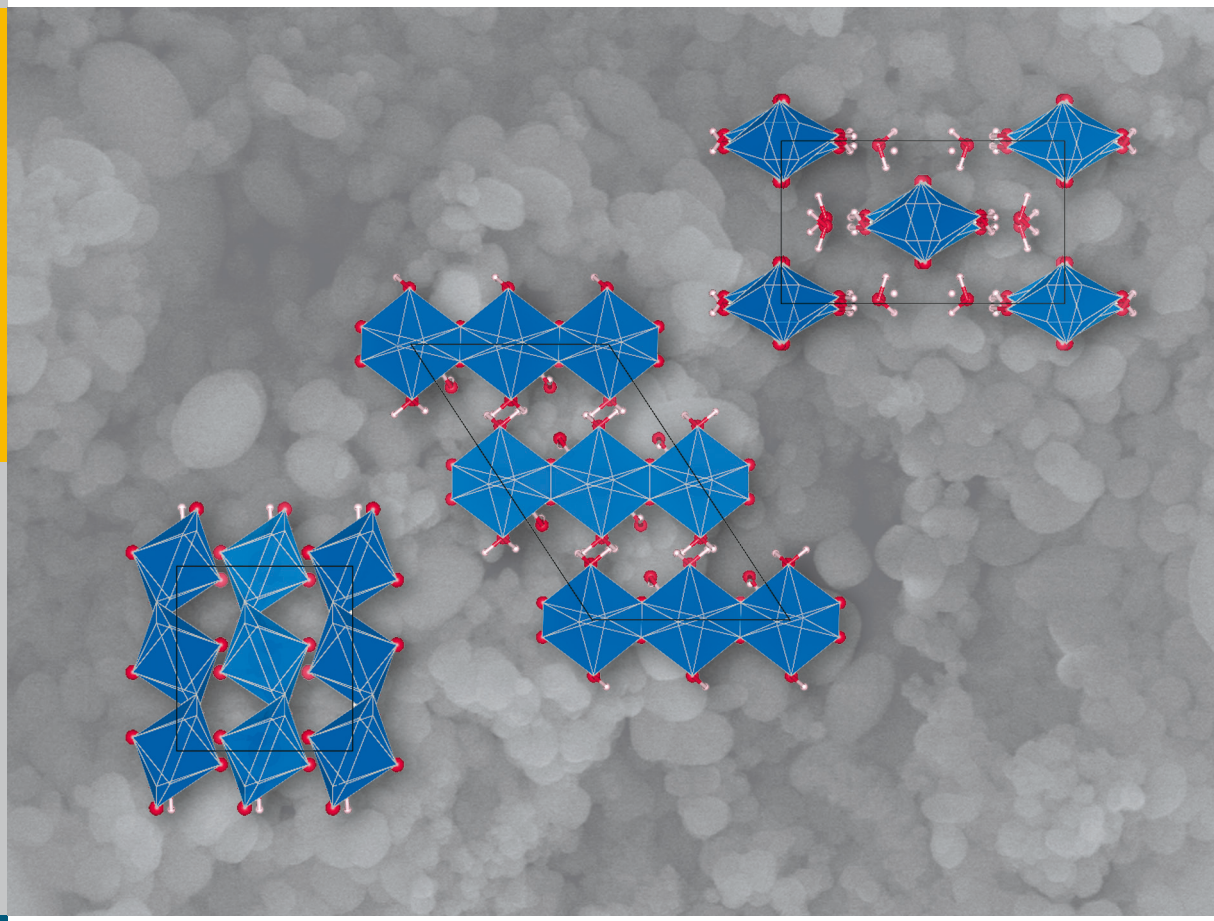

Energie & Umwelt / Energy & Environment
Band / Volume 267
ISBN 978-3-95806-063-0

JÜLICH
FORSCHUNGSZENTRUM

Schriften des Forschungszentrums Jülich
Reihe Energie & Umwelt / Energy & Environment Band / Volume 267

Forschungszentrum Jülich GmbH
Institut für Energie- und Klimaforschung
Nukleare Entsorgung und Reaktorsicherheit (IEK-6)

Secondary Uranium Phases of Spent Nuclear Fuel – Coffinite, $USiO_4$, and Studtite, $UO_4 \cdot 4H_2O$ – Synthesis, Characterization, and Investigations Regarding Phase Stability

Sabrina Labs

Schriften des Forschungszentrums Jülich
Reihe Energie & Umwelt / Energy & Environment Band / Volume 267

ISSN 1866-1793 ISBN 978-3-95806-063-0

Bibliographic information published by the Deutsche Nationalbibliothek.
The Deutsche Nationalbibliothek lists this publication in the Deutsche Nationalbibliografie; detailed bibliographic data are available in the Internet at http://dnb.d-nb.de.

Publisher and Distributor: Forschungszentrum Jülich GmbH
Zentralbibliothek
52425 Jülich
Tel: +49 2461 61-5368
Fax: +49 2461 61-6103
Email: zb-publikation@fz-juelich.de
www.fz-juelich.de/zb

Cover Design: Grafische Medien, Forschungszentrum Jülich GmbH

Printer: Grafische Medien, Forschungszentrum Jülich GmbH

Schriften des Forschungszentrums Jülich
Reihe Energie & Umwelt / Energy & Environment, Band / Volume 267

D 82 (Diss. RWTH Aachen University, 2014)

ISSN 1866-1793
ISBN 978-3-95806-063-0

The complete volume is freely available on the Internet on the Jülicher Open Access Server (JuSER) at www.fz-juelich.de/zb/openaccess.

Zusammenfassung

In dieser Arbeit wurde das Verhalten des $USiO_4$ – $ThSiO_4$ Mischkristallsystems untersucht. Die Endlgieder und zehn der $U_xTh_{(1-x)}SiO_4$ Mischkristalle mit x = 0.12 – 0.92 konnten erfolgreich und ohne Anwesenheit weiterer Uranphasen hergestellt werden. Die erhaltenen Proben wurden umfangreich untersucht. Aus den erhaltenen XRD Daten wurden die Gitterparameter sowie das Elementarzellvolumen ermittelt. Diese folgen der Vegard'schen Regel und suggerieren eine vollständige Mischkristallbildung. Die lokale Struktur wurde weiter mittels EXAFS untersucht. Hier werden kleine Unterschiede in der Nahordnung bedingt durch die unterschiedlichen Atomradien von U(IV) und Th(IV) sichtbar. Die vollständige Mischbarkeit von $USiO_4$ – $ThSiO_4$ wird bestätigt. Die Struktur der Endglieder wird im Detail mittels XRD analysiert und die Position der Sauerstoffatome in der Struktur diskutiert. Speziell die Länge der Si-O Bindung wird genauer betrachtet. $USiO_4$ wurde frei von UO_2 synthetisiert und die Gitterparameter c = 6.2606(3) Å und a = 6.9841(3) Å aus der Rietveldverfeinerung erhalten. Für die Si-O Bindunge in $USiO_4$ wird ein Wert von 1.64 Å erhalten, welcher sinnvoller ist als bisher berichtete Werte.
Synchrotron Pulverdiffraktion und Raman Experimente an synthetischem Coffinit, $USiO_4$, wurden für Drücke bis 35 GPa bzw. 18 GPa durchgeführt. Aus den Änderungen in den Pulverdiffraktogrammen wird ersichtlich, dass $USiO_4$ eine druckinduzierte strukturelle Phasenumwandlung erster Ordnung durchläuft. Bei ca. 15 GPa wandelt sich bei Normaltemperatur die Struktur der Elementarzelle von Zirkon- (Raumgruppe *I* $4_1/amd$) zu Scheelitstruktur (Raumgruppe *I* $4_1/a$) um. Im Gegensatz zur bisherigen Berichten in der Literatur zeigen die erhaltenen Daten, dass die Phasenumwandlung für $USiO_4$ komplett reversibel ist. Die Druckabhängigkeit der Ramanmoden von $USiO_4$ im Zirkontyp sind größer als die Literaturwerte von Hafnon, $HfSiO_4$, oder Zirkon, $ZrSiO_4$. Demnach ist Coffinit, $USiO_4$ stärker komprimierbar als diese Orthosilikate. Aus den gemessenen *p-V* werden die Kompressionsmodule der LP-Zirkon- und der HP-Scheelitphase von $USiO_4$ ermittelt, diskutiert und mit Literaturwerten für $MSiO_4$ (M = U, Hf, Zr) verglichen. Für $USiO_4$ wird ein Kompressionsmodul von 180(7) GPa erhalten. Dieses ist kleiner als das Kompressionsmodul von $ZrSiO_4$ (205 GPa [1]), was aufgrund der größeren Elementarzelle von $USiO_4$ zu erwarten ist. Bis 18 GPa werden keine neuen Peaks im Ramanspektrum von $USiO_4$ beobachtet. Ebenso sind keine abrupten Änderungen in den Druckabhängigkeiten der einzelnen Ramanmoden ersichtlich. Des Weiteren konnte gezeigt werden, dass B_{1g}- und A_{1g}-Moden des SiO_4^{4-} Tetraeders im Ramanspektrum sehr nahe beieinander liegen und unter Normalbedingungen überlappen.

Strukturelle Untersuchungen mittels Synchrotron- und Neutronenpulverdiffraktion ermöglichten eine genauere Bestimmung der Wasserstoffpositionen in der Struktur von Studtit. Die U–O Abstände der ersten Koordinationssphäre und der U–U Abstand von Studtit und Metastudtit

wurden durch EXAFS Experimente erhalten und mit denen aus den Diffraktionsexperimenten ermittelten sowie den in der Literatur vorhandenen Werten verglichen und diskutiert. Während die so erhaltenen atomaren Abstände die bekannte Struktur von Studtit bestätigen und in sehr guter Übereinstimmung zu den Diffraktionsdaten sind, zeigen die von der Metastudtit-Probe erhaltenen Messungen eine Auffälligkeit im U–U Abstand. Das von Weck et al.[2] anhand von DFT-Rechnungen vorgeschlagene Modell wird generell durch die Diffraktionsdaten bestätigt. Allerdings zeigen die aus der Neutronenpulverdiffraktion erhaltenen Ergebnisse eine Änderung der Struktur, sodass eines der Uranyl–Sauerstoffatome auf einer neuen Gitterposition zuliegen kommt. Das neue Strukturmodell ist plausibel und bietet eine Grundlage für weitere Diskussionen. Aus der Lage der ν(O-O_{peroxo})^{sym} Streckschwingung in den Ramanspektren wird ersichtlich, dass der O–O Abstand in Studtit und Metastudtit gleich sind. Die korrespondierenden IR Spektren wiederum zeigen, dass Wasser in Metastudtit stark gebunden sein muss. Das Signal für die ν(U=O)^{asym} Schwingung ist in Metastudtit aufgespalten, was ein Anzeichen für zwei unterschiedliche U=O–Abstände ist. In Studtit kann das Vorliegen von „freiem“ Kristallwasser einerseits durch eine starke Bande der ν(OH) Mode im IR Spektrum bestätigt werden. Andrerseits sind nur im IINS Spektrum von Studtit die Librationen von Wasser zu beobachen. Im IINS Spektrum von Metastudtit fehlen diese komplett, dafür sind die Signale der δ(HOH) Schwingungen sehr stark ausgeprägt. Dies weist auf stark gebundenes Wasser bzw. OH-Gruppen in Metastudtit mit deutlicher O$\cdots$H Vernetzung hin.

Die Morphologie der Studtit und Metastudtitproben wurden mittels REM und TEM untersucht. Beide bilden schmale elongierte Plättchen, welche ihrerseits aus zahlreichen 5 – 10 nm großen Kristalliten bestehen. In DSC-TG Messungen zeigt sich, dass die Phasentransformation von Studtit zu Metastudtit bei 80 °C stattfindet. Bei ca. 215 °C folgt die weitere Zersetzung zum amorphen Dehydratationsprodukt. Durch in-situ XRD Messungen wurde ermittelt, dass die Studtit $\longrightarrow$ Metastudtit Phasentransformation bereits bei 39 °C einsetzt und bei 56 °C vollendet ist. Die vollständige Amorphisation wird bei 212 °C beobachtet. Die thermische Ausdehnung der Gitterparameter von Studtit und Metastudtit wurden untersucht. Dabei zeigt sich, dass jene Achsen, entlang derer die [UO_8]-Polyederketten verlaufen, am wenigsten durch eine Temperaturerhöhung beeinflusst werden. Aus den Hochdruck-Ramanspektren wurde die Lage der zu ν(U=O)^{sym} und ν(O-O_{peroxo})^{sym} Streckschwingung gehörenden Peaks ermittelt. Hieraus wurde die Druckabhängigkeit dieser Moden bestimmt. Durch Auftauchen der ν(U-O-U-O) Schwingung kann auf eine beginnende Zersetzung zu UO_3 geschlossen werden. Diese findet in Metastudtit bei 14 GPa statt. Studtit ist weniger stabil und beginnt bereits ab 1.6 GPa sich zu zersetzen. Eine druckinduzierte Phasentransformation von Studtit zu Metastudtit konnte hingegen nicht beobachtet werden.

Abstract

The miscibility behavior of the $USiO_4$ – $ThSiO_4$ system was investigated. The end members and ten solid solutions $U_xTh_{(1-x)}SiO_4$ with x = 0.12 – 0.92 were successfully synthesized, without formation of other secondary uranium or thorium phases. Lattice parameters of the solid solutions evidently follow Vegard's Law. Investigation of the local structure with EXAFS reveals small differences between U and Th environment attributed to different atomic radii of the metal atoms but no implications for a miscibility gap. The data provided confirms complete miscibility for the system $USiO_4$ – $ThSiO_4$. The structure of the end members was studied in detail with XRD and discussed with special regard to the oxygen positions and the often neglected Si-O bond length. $USiO_4$ could be obtained without UO_2 impurities and the lattice parameters derived from Rietveld refinement as c = 6.2606(3) Å and a = 6.9841(3) Å. The Si-O distance in $USiO_4$ appears to be 1.64 Å, which is more reasonable than earlier reported values.

Synchrotron X-ray powder diffraction pattern and Raman spectra of synthetic coffinite, $USiO_4$, were obtained for pressures up to 35 GPa and 18 GPa, respectively. From the changes in the diffraction pattern it can be concluded that $USiO_4$ undergoes a first order phase transition from zircon-type (space group *I* $4_1/amd$) to scheelite-type structure (space group *I* $4_1/a$) at $\approx$ 15 GPa and room-temperature. Contrary to earlier reports, the data indicates that this transition is completely reversible upon pressure release. Pressure dependencies of the Raman modes for the zircon structured phase are larger than those reported for hafnon, $HfSiO_4$, and zircon, $ZrSiO_4$, indicating that coffinite, $USiO_4$, is more compressible than these orthosilicates. Bulk moduli fitted from the *p-V* data for the zircon-type and scheelite-type $USiO_4$ phase are compared to those known to literature for other $MSiO_4$ (M = U, Hf, Zr) compounds. The bulk modulus for zircon-type $USiO_4$ is 180(7) GPa and hence lower than those of $ZrSiO_4$ (205 GPa[1]) as expected from the larger unit cell. The pressure dependence of the Raman modes of $USiO_4$ was studied up to 18 GPa, yet no abrupt changes of peaks or in the peak shifts appear. Furthermore it could be established, that the B_{1g}- and the A_{1g}-modes of the SiO_4^{4-}-tetrahedron in the Raman spectrum are very close and overlap at ambient conditions.

Structural investigations employing synchrotron X-ray and neutron powder diffraction allowed for a better determination of hydrogen positions in the studtite structure. Through EXAFS measurements the U–O distances of the first coordination sphere and the U–U distance were determined for studtite and metastudtite and compared to those reported in literature and derived from powder diffraction data. While the derived atomic distances reassured the studtite structure and were in good accordance with diffraction data, the spectrum of metastudtite showed an interesting feature in the range of the U–U distance. The structure model from Weck et al.[2] for metastudtite is generally supported by the diffraction data. Through the results derived from

NPDF it was possible to amend the model, which ended up in a different atomic position for one uranyl O atom. However, the derived new model seems plausible and encourages further discussion on the topic. Furthermore, this is the first comprehensive synchrotron and neutron powder diffraction study reported on studtite and metastudtite so far. The Raman spectra show no differences in the ν(O-O$_{peroxo}$)^{sym} stretching mode, implying that this distance is the same in studtite as in metastudtite. From IR spectra it can be observed, that the modes associated to water are strictly confined in metastudtite. The ν(U=O)^{asym} is split in metastudtite, a sign for two different U=O–distances. For studtite the presence of crystal water is observed in the strong ν(OH) mode in the IR spectrum, and confirmed by the observance of the librational modes of water in the IINS spectra. The IINS spectrum of metastudtite completely lacks any features of the librations of water, instead, the δ(HOH) vibrations give a strong signal. Suggesting, that metastudtite only contains directly bound water with strong O$\cdots$H coordination.
The morphology of studtite and metastudtite was investigated with SEM and TEM. Both materials appeared as small elongated platelets and consist of numerous nano-scaled grains, with 5 – 10 nm in dimension. DSC-TG measurements showed that the dehydration of studtite to metastudtite takes place at 80 °C and that the amorphization happens at $\sim$ 215 °C. During the in-situ X-ray diffraction study, the onset of the studtite $\longrightarrow$ metastudtite transition was observed at 39 °C and the reaction was completed at 56 °C. Further amorphization was observed at 212 °C. The thermal expansion of the lattice parameters of studtite and metastudtite were investigated, showing that the axes perpendicular to the [UO$_8$]-polyhedra are least influenced by temperature. The pressure dependence of the ν(U=O)^{sym} and ν(O-O$_{peroxo}$)^{sym} stretching vibrations were derived in a high pressure Raman study. Judging from the appearance of the ν(U-O-U-O) long range mode, metastudtite undergoes amorphization to UO$_3$ at 14 GPa. Studtite is less stable and already decomposes at 1.6 GPa. A pressure induced transformation from studtite to metastudtite could not be observed.

Nunca te rindas. Cuando tu corazón se canse,
camina soló con tus piernas – pero sigue adelante.

(Paulo Coelho)

Declaration of Authenticity

I certify hereby that except where due acknowledgement has been made, the work is that of the author alone; the work has not been submitted previously, in whole or in part, to qualify for any other academic award; the content of the thesis is a result of work which has been carried out since the official commencement date of the approved research program; and, any editorial work, paid or unpaid, carried out by a third party is acknowledged.

Rheinbach, June 12, 2015 Sabrina Labs

To my parents and my family.
You gave me firm ground to stand on and wings to fly.

Acknowledgments

I would like to thank my thesis adviser Prof. Dirk Bosbach for the interesting topic, his extensive support and sharing his expertise with me. Also I would like to thank Prof. Georg Roth for taking the task of the second reviewer.

Dearest appreciation goes to Hilde Curtius, who is a supervisor second to none. Thank you and all of the team, especially Zaina, Gaby, and Emil, for the constant support, guidance, and making me a better scientist; the funny "coffee-brake" discussions, the good time, and always having a warm word. I would like to thank Christoph Hennig from ROBL for the great support during the EXAFS measurements and the help with fitting the EXAFS spectra. The interesting discussions concerning the $U_xTh_{1-x}SiO_4$ solid solutions and a lot of advice on $USiO_4$ have encouraged me many times. Very special acknowledgement has to be given to Stephan Weiß from HZDR, for many hours of help and assistance with synthesis work at the glovebox. For enabling the wonderful time at the Lujan Center, I wish to thank Monika Hartl and Luke Daemen. In these four months I have learned so much on a professional as well as personal basis. I also want to thank Sven Vogel for the support with the HiPPO measurements and his patience when answering my numerous questions involving neutron diffraction. Big thanks also go to thank Andreas Neumann for many fruitful discussions on X-ray diffraction, its challenges and limitations. Also I am very grateful for his help with the in-situ X-ray diffraction study of studtite and many many hours of discussion on plausible structures of metastudtite; the pitfalls of structure refinement and the main differences of XRD refinement software. Sincere thanks Johannes Bauer from Prof. Winkler's group (Uni Frankfurt a. M.) for collaborative work on the high-pressure topics, plenty of hours filled with interesting discussions; beamtimes full of chaos, laughter, and nearly disaster; and last but not least a very subtle kind of humor.
To all my friends and those, who have supported and believed in me during this exciting and sometimes stressful time, through all the ups and downs - Thank you!

This work was made possible by a financial support through a sponsorship of the Freunde und Förderer des Forschungszentrum Jülich in connection with a research fellowship of the Gesellschaft für Nuklearservice (GNS).
Beamtime for the EXAFS measurements was granted under ACTINET-i3, proposal no: AC4-JRP04.

Synchrotron diffraction data were collected on beamlines P02.1 and P02.2 of the PETRA III facility at the Deutsches Elektronen Synchrotron (DESY) in Hamburg, Germany.

This work has benefited from the use of FDS, NPDF, and HiPPO at the Lujan Center at Los Alamos Neutron Science Center, funded by DOE Office of Basic Energy Sciences. Los Alamos National Laboratory is operated by Los Alamos National Security LLC under DOE Contract DE-AC52-06NA25396.

Contents

Chapter 1

Introduction

1.1 The Safe Disposal of Nuclear Waste

Countries employing nuclear energy will at some point have to face the effort of disposal of the incidental nuclear waste. The radiotoxicity of the nuclear waste, i.e. the contained radionuclids therein, constitutes a severe threat to the environment and health. Due to the long half-live of some of the inventory, the contained radiation limits will reach the natural background level not before 10^5 – 10^6 yrs.[3] The nuclear waste hence needs to be disposed of in a way, that none of the hazardous inventory can disseminate into the biosphere before the natural radiation level has been reached. Even after that, the impact of chemotoxicity of the now contained heavy metals should not be neglected. Creation of such a safe and secure final repository for the created nuclear waste cannot by common agreement be imparted on future generations.[4] The world-wide used classification scheme of the International Atomic Energy Agency (IAEA) also divides radioactive waste into groups according to the heat generated from radioactive decay. For the final disposal in a deep geological repository low-level waste (LLW), intermediate-level waste (ILW) and high-level waste (HLW) are designated. LLW only has limited amounts of long-lived radionuclides, and no measurable amount of heat produced through the radioactive decay. It requires robust containment, but no extensive shielding during handling and storage. Contaminated material with a measurable content of long-lived radionuclides and heat generation, e.g. from reactor decommissioning, is regarded as ILW. By definition the heat generation must not exceed 200 W/m^2 and the temperature increase must not exceed 3 K on the emplacement walls. This type of waste requires adequate shielding during handling and storage and poses a higher risk than LLW. Waste with activity levels high enough to produce significant amounts of heat due to radioactive decay and waste which contains large quantities of long-lived radionuclides is defined as HLW. These HLW contain the fission products and minor actinides generated during radioactive burn-up. Due to the high radioactivity and heat dissemination ($>$ 3 K on the emplacement walls), this type of waste not only requires extensive shielding, but also cooling.

Spent nuclear fuel (SNF) comprises the biggest part of the HLW inventory in Germany (see table 1.1). Handling, transport and storage of this waste type needs to be conducted with major safety precautions. The final disposal, especially of the HLW poses a massive challenge on scientific research in geology, chemistry, physics, and engineering.

The long-term radiotoxicity is dominated by Pu and the minor actinides as can be seen in the

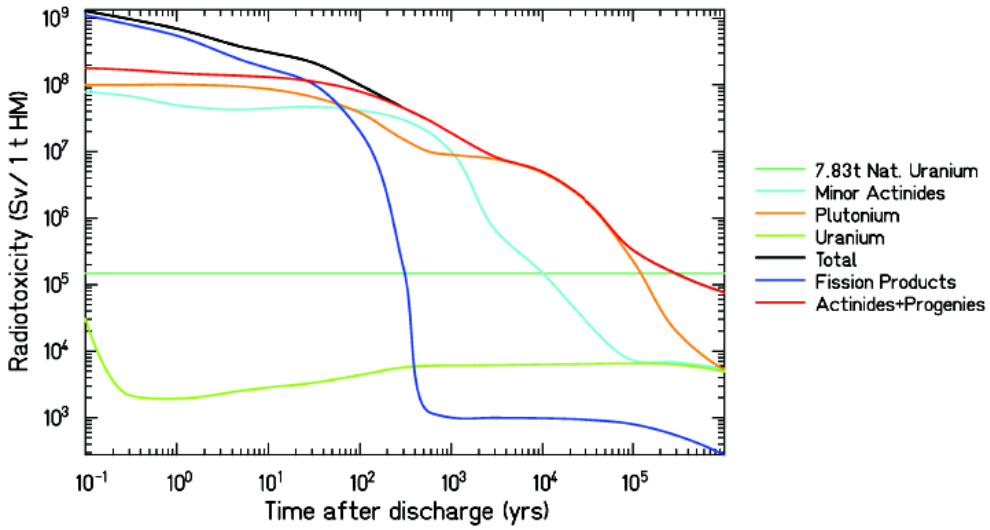

Figure 1.1: Illustration of the radiotoxicity of spent nuclear fuel, minor actinides, and Pu over time with comparison to natural U and background. Reference level : Ingestion radiotoxicity of the natural uranium required to produce 1 ton of enriched U-nuclear fuel (4.2 % ^{235}U, 7.83 t nat. U) in equilibrium with its decay products = $1.47 \cdot 10^5$ Sv.[webKORIGEN SIMULATION 55 MWd/kg 4.5 % UOX PWR FUEL][5]

illustration from figure 1.1. The minor actinides are contained as fission products in the SNF and pose a special hazard. Germany currently has decided on the direct disposal of spent nuclear fuel (SNF). Final repositories in deep geological formations are favored for this matter in the EU and particularly in Germany. Salt, granite rock and opalinous clay are the three potential host rock formations for such a final repository. Germany does not host suitable granite rock formations, therefore clay or salt formations will have to be employed for this purpose. The final repository comprises different types of barriers towards leakage into the biosphere. So if one barrier fails, a succeeding containment is still intact to retend the radionuclids. The first barrier is, in fact, the original and undisturbed cladding of the fuel pellets and total fuel rods. These again are contained in an iron container (depending on the scenario copper or other alloys might also be used), approved for final disposal. The container is put into the repository, and depending on the repository scenario the void filled with bentonite clay (the application of additional backfill material is also discussed). The last barrier is then the host rock itself. Since Germany has decided to phase out nuclear energy, the discussion arose, what to do with the U stockpile and its

potential fate is to be disposed of as waste. The projection for 2040 for the amount of non heat-generating low- and intermediate-level radioactive waste (LLW and ILW) is 303 000 m^3, whereas the heat-generating high-level (HLW) and intermediate-level waste amounts to only 29 000 m^3. While the volume fraction of the HLW is only $\sim$ 7.8 % it comprises 99 % of the radioactivity (and hence the radiotoxicity). The total amount of heat-generating nuclear waste in Germany

Table 1.1: Composition of the waste inventory nuclear waste in Germany, projection for 2040[6].

non heat-generating LLW & ILW (303 000 m^3)		heat-generating HLW & ILW(29 000 m^3)	
nuclear power plant shutdown	61.9 %	nuclear fuel rods	83.7 %
research	23.6 %	reprocessing	11.7 %
nuclear industry	3.7 %	vitrified waste	3.6 %
other	3.8 %	other	1.0 %
Total volume:	92.2 %		7.8 %
Radioactivity:	1 %		99 %

appears rather small compared to other wastes produced, e.g. during the U enrichment process per 1 t enriched U (3.6 % ^{235}U) 5.6 t depleted U (0.3 %^{235}U)[7] are produced.
Nevertheless, the final repository needs to be put at the best possible location, where safety and security can be sufficiently ensured. For the non heat-generating LLW and ILW final repositories in Morsleben and Konrad have been decided on. The final repository Konrad will start with the process not before 2021[8]. However, no site for a licensed final repository for HLW has been decided on in Germany, yet. Within the EU only Finland has decided on a licensed final repository in Olkiluoto and is planned to start encapsulation of HLW in 2020.[4]

1.2 Motivation

For the long term safety assessment the release of radionuclides into the near field and ultimately into the environment is of great importance. This process is dictated mainly by the dissolution of the fuel matrix and the formation of secondary phases (schematically drawn in 1.2). Steel canisters used as containment will eventually corrode and actinides could leach into the near-field. While U(IV) species are generally insoluble, the U(VI) compounds can have appreciable solubility in water, and the speciation can be complex.[9;10] Interactions of radioactive ions with mineral surfaces can act as a mechanism to lower the mobility of the specific radionuclid and retard it, even redox chemistry is possible.

The long-term safety of a final repository must be demonstrated by modeling the geochemical processes in the particular natural system over geological timescales. This safety analysis employs model calculations where the thermodynamic data is combined for these processes in the so-called source term. The approach of using "conservative" assumptions has some shortcomings and recent developments strive for "realistic" models instead.[11;12;13] To achieve this, fundamental knowledge of the properties of the relevant secondary phases is necessary, and $USiO_4$

the synthetic equivalent to coffinite[14] is to be a major secondary phase. Furthermore, in some European countries there is the issue of legacy waste, which needs to be taken care of. A reliable statement as to what corrosion products are to be expected and how stable they are, will certainly support decisions on following actions.

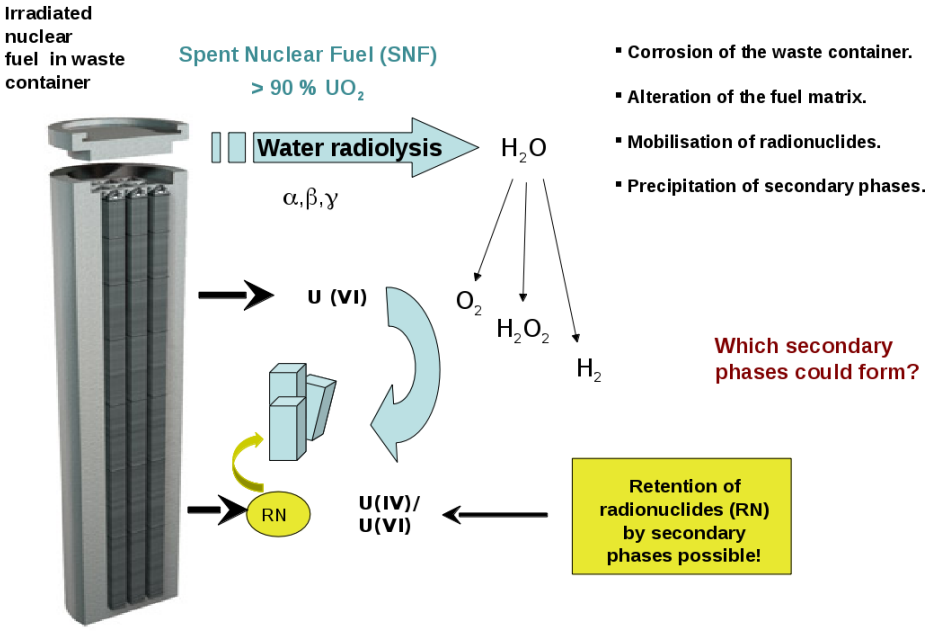

Figure 1.2: Scheme of the corrosion of spent nuclear fuel and the formation of secondary phases.

On the other hand, $USiO_4$ is also one of the most important uranium bearing ores. It has been found in numerous ore deposits, e.g. New Mexico[15], China[16], as well as the Oklo natural nuclear rector site in Gabon.[17;18] If for instance nuclear power generation by nuclear fission will be included in national energy policies then the demand for uranium could also increase. Reliable knowledge of the thermodynamic parameters can improve the leaching and refining processes of uranium. Significant amounts of $USiO_4$ are also present on the mining dumps and mine tailings, where the washout of uranium from $USiO_4$ is often neglected but can have major influence on the environment. A thorough understanding of the mechanism, e.g. colloid formation, adsorption, precipitation, can enhance the success of the remediation efforts undertaken to decontaminate polluted soil.[15] SNF consists to > 90 % of UO_2[3] hence alteration products of UO_2 are expected to appear eventually in the final repository. The replacement of uraninite under reducing conditions in the presence of silicates has been postulated under certain circumstances by Langmuir[19] in 1978 and is reported from Janeczek[20] as the process of 'coffinization'. Propinquity

of particularly uranium bearing natural minerals to secondary phases, proposed in a final repository in deep geological formation, has been established by different authors.[3;21;22;23;24] To ascertain the appearance of $USiO_4$, however, validated thermodynamic data is required. The synthesis of coffinite has recently been reported, but samples often contained nanocrystalline UO_2[25] or amorphous uranium containing phases.[26] The available thermodynamic data is hence estimated from natural samples.[27] From dissolution studies[28] of the solid solutions of $Th_{(1-x)}U_xSiO_4$ (x = 0 – 0.6) the solubility product of pure $USiO_4$ was derived. The most recent investigation therefore imply that $USiO_4$ is metastable with respect to UO_2 + SiO_2 by + 16 $^{kJ}/_{mol}$, which is a very small difference though.

Another important corrosion product of SNF, yet under oxidizing conditions, is uranium peroxide, $UO_2(O_2)(H_2O)_2{\cdot}2H_2O$. Its natural counterpart is the mineral studtite. Studtite and its dehydration product metastudtite, $UO_2(O_2)(H_2O)_2$, can also be contained in the so called "yellow cake". After the nuclear reactor accident of the Fukushima-Daiichi power plant, polyuranylate-clusters (which are closely structurally related to studtite) were postulated as U(VI) species the marine seawater of the Japanese coast.[29] Adsorption and incorporation of Np into studtite has recently been studied.[30] Because of the high specific activities of the transuranic elements, particularly the shorter lived actinides, such as Np, Pu, Am and Cm (e.g. ^{239}Pu has a halflive of $2.4 \cdot 10^5$ yrs.), long-term storage and subsequent final disposal represent a significant technical challenge. How radionuclides with long half-lives can interact with these phase changed uranyl compounds is important as retardation or redox reactions could occur which further influence the near-field impact of SNF.[31]

This work focuses primarily on the development of a reproducible synthesis route for coffinite, $USiO_4$, as a thorough thermodynamic characterization will greatly benefit the safety assessment of a final repository for spent nuclear fuel. However, even if overall reducing conditions will exist in the repository, through α-radiation in contact with the pore water, the local conditions might become oxidizing. In this type of environment studtite, $UO_2(O_2)(H_2O)_2{\cdot}2H_2O$, or even metastudtite $UO_2(O_2)(H_2O)_2$ could precipitate. The other aspect which this work therefore covers is the characterization of studtite and metastudtite and a comprehensive investigation of the phase relationship of the two phases.

Chapter 2

Materials and methods

2.1 Hydrothermal Synthesis

The term "hydrothermal" refers to conditions of an aqueous solution above the boiling point of water, i.e. 100 °C, with a pressure $>$ 1 bar.[32] Hydrothermal synthesis routes have first been applied in the synthesis of synthetic minerals and the extraction of elements from ore. Nowadays, these techniques have widely been applied in the syntheses of conventional and advanced materials, and mimicking geothermal processes. Hydrothermal process routes are employed in many commercial productions, like the refining of metals, e.g. the Bayer process, and synthesis of pigments and colors. Single crystals of pristine quality are often grown under hydrothermal conditions. Variations of this syntheses types include *solvothermal syntheses* where other media, like HF, NH_3 (*ammonothermal*), SO_2 or CH_2Cl_2 are employed.[33] Many compounds or materials with special structures and properties, which cannot be prepared from solid state synthesis, may be obtained by hydrothermal procedures. Meta stable compounds, hard to attain oxidation states, e.g. Cr(IV), or so called low temperature phases such as γ–CuI are accessible by hydrothermal preparation methods. Physical and chemical properties of the medium water are very well known. Under elevated pressures, the liquid phase reaches temperatures $>$ 100 °C, enhancing the solubility of hardly soluble reagents. Moreover, mineralizers can be added to the mixture to further enhance solubility. The dielectric constant of water increases with dependence to increasing temperature and increasing pressure. Conditions become similar to those in molten salts. With increasing pressure also the viscosity of the medium decreases. Dissolved ions hence become more volatile, promoting transport processes. The group of hydrothermal syntheses can therefore also be regarded as a special case of transport reaction. Growth of single crystals is often undertaken by placing a seed crystal at one end and the feed stock at the other. The kinetics of transport are completely controlled by the thermal convection. Special transport reactions are conducted in a horizontal setup, employing a temperature gradient. In nature, wonderful large grown crystals often are retrieved from geods (also called crystal druses) which pose as a natural

reactor vessel. The laboratory setup is adapted from this template. Usually an autoclave with PTFE, Teflon or metal inlet is used for syntheses. Depending on the temperature and pressure range different types and designs have been developed.[32;33] Also a simple ampule, depending on the reaction conditions made from SiO_2, Pt-metal or other corrosion resistant alloys, can serve as a reaction vessel. Especially, when protective atmospheres need to be applied, this setup has been shown to be useful. To withstand the bursting through the immanent pressure build-up the ampule is placed into an autoclave and a counter pressure is applied. The synthesis setup used in this work is specified later on.

2.2 High-pressure Experiments

The synthesis and investigation of materials under elevated pressures is of great interest for the scientific field of physics, solid state chemistry, geology and mineralogy but also in engineering sciences. It is postulated, that over 90 % of the universe's matter is present at pressures over 9 GPa.[34] The Earth's core has an estimated pressure of 330 – 360 GPa and it is proposed, that pressures on Jupiter are high enough that metallic hydrogen exists in its core.[35] In fact, the 'normal temperature and pressure', i.e. 293 K and 1 bar, scientists generally refer to are in this context rather exotic conditions.

High pressure experiments are particularly interesting for scientists of all fields because this way the atomic distances and hence electron states of materials can effectively be changed. Electrical conductivity, optical absorption, and magnetic properties of the solid can establish new and unique values under elevated pressures.[36] This allows fundamental science to validate and improve postulated models[37] and even offers access to new materials with special properties.

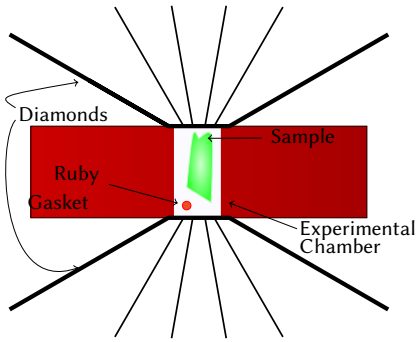

Figure 2.1: Schematic drawing of the experimental setup in a diamond-anvil-cell, DAC.[38]

Producing high pressures under laboratory conditions is not a trivial task. For synthesis se-

tups multi-anvil hydraulic presses or, when a medium is involved, autoclaves might do the job. However, reaching high pressures in a large volume is complicated. Usually a setup involves two components:
1) the anvil – a removable assembly, to load the press and increase the force on the sample;
2) the experimental chamber – a pressure 'resistant' chamber in which the sample accompanied with a pressure-transmitting medium is placed. The pressure transmitting-medium is crucial to attain near hydrostatic conditions. However, there is no such thing as an ideal medium. Pressure media can be liquids, e.g. ethanol/water 4:1 or methanol/ethanol/water 16:3:1 mixtures, or inert noble gases. The pressure medium has significant effect on the conditions in the experimental chamber and can even affect collected data. For instance, the range in which the pressure medium itself freezes, can be regarded as the limit to where hydrostaticity is maintained. Depending on this structural changes might be observed at different pressures, just due to the medium used.[39] Among the available high-pressure apparatuses, diamond-anvil-cells (DACs) are currently the most widely used. The small volume of the DAC allows for very high static pressures in a relatively easy and safe manner like a laboratory environment. Furthermore, it makes experimental measurements to pressure as high as 100 GPa possible. In figure 2.1 the setup of such a diamond-anvil-cell is illustrated. A DAC consists of two brilliant-cut, flat faced diamonds with a metal foil in between. These flat faces of the diamonds are referred to as culets and can have different size, depending on the application. Into the metal foil, which is called gasket, a laser drilled hole is cut to serve as sample chamber. This chamber is less than 500 μm in diameter, and sample sizes are correspondingly even smaller. To monitor the pressure inside such a DAC, a tiny ruby ($Cr:Al_2O_3$) is loaded together with the sample. The position of the ruby R_1 laser fluorescence signal is pressure dependent,[40;41] by evaluating the lifetime of the signal, also the temperature can be measured.

2.3 Powder diffraction

In a certain way, the fundamentals of crystallography were described by Johannes Kepler in 1611 in his work "Strena seu de nive sexangula", concerning the sixfold symmetry of snowflakes.[42] From his observations he concluded, that *there must be reason, why every snowflake under investigation established the six-fold symmetry.* * While Kepler did not explicitly refer to atomic structures, he drew strong parallels to the hexagonal symmetry of close packed spheres. † Solid materials either contain a long-range order, which makes them crystalline solids, or they estab-

*"Es muß einen bestimmten Grund geben, warum bei Einsetzen des Schneefalls die Anfangsformationen unverändert die Form eines sechseckigen Sternchens haben. Sollte es durch Zufall erfolgen, warum fallen sie dann nicht mit fünf oder sieben Ecken."

†Interestingly a nuclear physicist, Ukichiro Nakaya, dedicated his life to the study of snowflakes and categorized 40 systematical pattern, as well as the conditions under which a certain morphology evolves.[43] These relationships are comprised in the Nakaya-diagram.

lish only short-range order, then they can be regarded as amorphous solids.
Powder diffraction is an analytical tool, especially suitable for structural analysis of crystalline solids with spatial resolution down to 1/1000 Å. Figure 2.3 schematically shows how two beams with identical wavelength are scattered off by the lattice planes within a crystalline solid. The intensity of the beams is only registered at the detector, if there is constructive interference of the beams. This is the case if the extra traversed length δ, i.e. the path length which is $d\ sin\ \theta$, is equal to an integer multiple of the wavelength λ of the radiation.

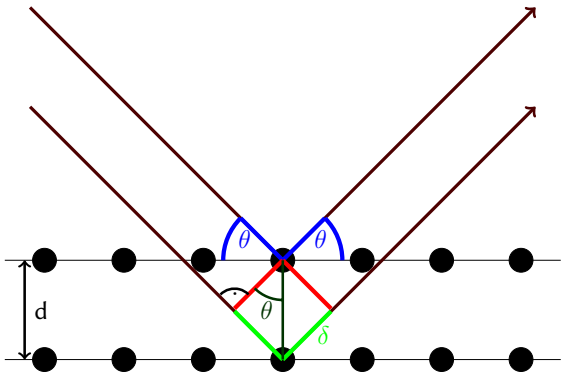

Figure 2.2: Two beams with identical wavelength and phase approach a crystalline solid and are scattered off the lattice planes within it.

$$n{\cdot}\lambda = 2d{\cdot}sin\theta \tag{2.1}$$

Using Bragg's law (see equation 2.1 where λ is the employed wavelength, θ the scattering angle, d the distance of the crystallographic planes, and n an integer determined by the order given) λ is fixed and well known, while θ is being scanned. This way the distances of the lattice planes d can be obtained. From the measurement the intensity of the diffracted beam versus 2θ is collected. Pattern are characteristic for crystal symmetries and by comparison of discrete peak positions and intensities to a pattern database qualitative phase identification is possible.
Reflection positions allow determination of the Bravais-type and lattice parameters. Intensities, more precisely the area of the reflection, contains information on atomic positions and thermal displacement. Texture effects or preferred orientation of the powder sample also influence the reflection intensities. The reflection profiles, i.e. the full-width half-maximum (FWHM) and asymmetry in the peak shape, give additional information on the crystallite size - the dimension of the coherent scattering domains -, internal stress and strain of the structure, as well as hints toward stacking faults and other disorder phenomena. Finally, the background oscillations may contain information on the short range order in the material.

2.3.1 X-ray Diffraction

Powder diffraction assumes a regular powder, in which small crystallites are statistically oriented in such a way, that all lattice planes are equally represented and in Bragg condition. The three-dimensional reciprocal space this way is projected onto a single dimension. The detected intensity is then described by the formula given in equation 2.2. In the diffraction pattern hence not individual point reflections associated with a reflection, e.g. (100), are observed, but reflection intensities of type $\{100\}$. For instance, for a cubic structure all reflections $\{100\}$, associated to the six cubic planes appear at the same 2θ value. This symmetry related correction is taken into account through the *multiplicity factor*, M. Additionally the intensity is influenced by the *Lorentz factor* and the *polarization factor*. The *Lorentz factor* results from the fact that reflections appearing at small diffraction angles cross the Ewald sphere quickly, while those at high diffraction angles are nearly tangential to the Ewald sphere and linger longer. The initial radiation is unpolarized. However the amount of this radiation, which due to the setup is polarized perpendicular to the reflection plane, is deflected and does not contribute to the detected intensity. To correct for this decrease in intensity the *polarization factor* is included in the equation. Often both factors are referred to in combination as LP – correction. Depending on the measurement conditions (Bragg-Brentano-, Debye-Scherrer-geometry) and the sample (flat or cylindrical sample) the absorption of the X-rays or neutrons within the sample is corrected by the absorption correction A. If the crystallites in the sample are not oriented randomly, but exhibit a *preferred orientation* then reflection intensities are not reliable. On a 2D diffraction pattern, texture might be observed directly. For the specific investigation of these texture effects different models are available for interpretation of the texture, T (ODF, spherical harmonics, March-Dollarse), for other purposes (quantitative Rietveld refinement) the appearance of texture can be a disaster. Texture cannot be "known" a priori, a blind correction of this parameter therefore might lead to big mistakes.

$$I = A{\cdot}M{\cdot}LP{\cdot}T{\cdot}|F_{hkl}|^2 \tag{2.2}$$

The intensity of a reflection point is directly related to the squared magnitude of the structure factor, $|F_{hkl}|^2$. In the structure factor the atomic positions and the atomic form factor of an atom of type i are comprised according to equation 2.3.[44;45;33]

$$\begin{aligned} F_{hkl} &= \sum_i f_i \cdot e^{2\pi i(hx_i+ky_i+lz_i)} \\ &= \sum_i f_i \cdot [cos2\pi(hx_i+ky_i+lz_i) + i \cdot sin2\pi(hx_i+ky_i+lz_i)] \end{aligned} \tag{2.3}$$

The atomic form factor f specifies, how strong a certain atom type deflects X-rays. This determines how much these atoms contribute towards the structure factor. For X-rays, f strongly

depends on the number of electrons and the dimension of the electron density, furthermore it strongly decreases with increasing diffraction angle. Neutrons on the other hand are deflected by the atomic core. The scattering cross sections for neutrons differ extremely from that of X-rays and can vary strongly depending on a specific isotope, e.g. H and D. Here the atomic form factors are independent of the diffraction angle. Values for f are listed in the International Tables for Crystallography.[46]

$$\begin{aligned} f' &= f_0 \cdot e^{-B \cdot \frac{sin^2\theta}{\lambda^2}} \\ &= f_0 \cdot e^{-8\pi^2 U \cdot \frac{sin^2\theta}{\lambda^2}} \end{aligned} \tag{2.4}$$

The atomistic scattering factor so far has only described ideal spherical atoms, which are in a fixed position. However, the atoms oscillate around their position due to thermal motion. This roughens the lattice planes and the scattering intensity decays even stronger. The thermal motion is included into the atomistic scattering factor through equation 2.4. It is corrected by an exponential term, including B, the *Debye-Waller factor*, which describes the isotropic displacement of the atom in all three dimensions. While the *Debye-Waller factor* is important in spectroscopy and many fields of physics, crystallography often refers to U, the average square of the oscillation amplitude ($U = \frac{B}{8\pi^2}$).[45]

Rietveld refinement

In a Le Bail[47] or Pawley-fit the intensity of each reflection is treated independently and overlapping reflections are not individually deconvoluted. The Rietveld method[48] not only takes into account the intensities of the individual Bragg reflection but the whole diffraction pattern. More data-points become available for the structure refinement than in a simple Le Bail fit.[47] The measured data-points are hereby approximated through a mathematical fitfunction M, see equation 2.5. The characteristic parameters for M are simultaneously determined and M minimized by a least squares refinement.

$$M = \sum_1 W_i \{\ y_i(obs) - \frac{1}{c} y_i(calc)\ \}^2 \tag{2.5}$$

where W_i is the statistical weight of a certain data point i, $y_i(obs)$ the observed intensity, $y_i(calc)$ the calculated intensity according to the model, and c an overall scale factor. The quality of the Rietveld refinement is determined by the a couple of different factors. On the one hand the plausibility of the solution, e.g. physically sensible bond lengths and angles, non-negative thermal parameters, is important. Standard deviations of refined parameters should not only be as low as possible but in the same region for all refined parameters. If one standard deviation differs significantly from the others, at least a reasonable explanation should be sought. It is of great importance that correlation between simultaneously refined parameters is low, so refinement

is not redundant. This can influence the quality of the single parameters as well as the whole refinement, leading to wrong reliability factors. On the contrary the absolute value of the profile R-factors (cf. equation 2.6) has little significance because their values depend on the quality of the data as well as on the goodness of the structural model. Also the difference plot has to be observed at all times.

$$\chi^2 = (R_{wp})^2/(R_{exp})^2 \tag{2.6}$$

where
weighed profile R_{wp} = weighed profile reliability factor (important),
expected R_{exp} = statistically best R_{wp}, and
reduced χ^2 must be ≥ 1.
The unweighed R_p is also usually reported, though not as important for interpretation.

Data Acquisition

X-ray diffraction pattern are obtained on either a Bruker *AXS* D4 or D8 diffractometer. Both are flat-plate diffractometer with Bragg-Brentano $\theta - \theta$ geometry and equipped with conventional laboratory CuK$_\alpha$ X-ray tube. The Bruker *AXS* D4 diffractometer employs a LynxEye line sensitive detector for signal acquisition and a Ni-foil as K$_\beta$ filter. The Bruker *AXS* D8 can be either equipped with a VÅnTec line sensitive detector or a point detector, which then also uses a Graphite monochromator. In both cases a Ni-foil acts as K$_\beta$ filter. Unless noted otherwise all diffraction pattern were obtained using a fixed divergence slit.

2.3.2 Radiation Sources

Conventional X-ray diffractometer are equipped with a high vacuum X-ray tube. Inside a cathode is heated to emit electrons, which then are accelerated through high voltage onto a metallic anode. On one hand a broad continuum of background *Bremsstrahlung* is produced. On the other hand the primary electron knocks a core electron, usually from the K-shell, out of its orbit into the continuum. A higher energy electron transits into the void; only transitions with $\Delta\pm$ 1 are allowed. The energy difference is emitted as element specific X-ray radiation. Common anode materials are Cu, Mo and Co and the characteristic wavelengths follow *Mosley's Law*.[45] The emitted spectrum comprises the K$_\beta$ as well as K$_{\alpha 1,2}$ lines. While the K$_\beta$ usually can be eliminated through the use of thin metal foils as filters, e.g. Ni, it takes a monochromater, e.g. a Si(111) or Ge(111) crystal, to separate K$_{\alpha 1,2}$.
In a Synchrotron, charged particles are accelerated and forced on a close to circular orbit by magnets. This angular acceleration results in the tangential emission of polarized high energy hard X-rays, so called synchrotron radiation. The radiation is focused by magnetic wigglers and/or undulators before being supplied to the experimental station. Here the initial white radiation can be tuned to a certain wavelength by large monochromators and/or focused by mirrors.

Synchrotron sources offer tunable high intensity, highly monochromatic, polarized X-rays for diffraction, scattering and spectroscopic experiments.
Neutrons can be either generated from a nuclear reactor or by spallation target neutron sources. While deflection intensities from neutrons are not as high as from X-ray due to the low interaction, neutrons offer the advantage of deep penetration into materials. The investigation of densely packed, large scale bulk material or texture analysis of compacted samples this way becomes possible. Also neutrons interact with magnetic structures, a feature, which is hardly possible to investigate with X-rays. Since scattering cross section derive significantly from those for X-rays, the detection of light elements, specifically D, next to heavy elements becomes possible. However, neutrons require special sample preparation, like deuteration, and due to the low interaction large amounts of sample.

2.3.3 Synchrotron Diffraction Experiments

Powder diffraction pattern at elevated pressures were collected on the P02.2 *Extreme Conditions Beamline* at the PETRA III synchrotron radiation facility of the Deutsches Elektronen-Synchrotron (DESY) in Hamburg, Germany. Measurements were carried out at an energy of 42.7 keV (λ = 0.2895 Å) with a beamsize of 1.6 μm x 1.6 μm (FWHM) and in Debye-Scherrer geometry.[49] For collection of the pattern a 2D image plate detector (PerkinElmer XRD 1621) was used. Sample to detector distance was fixed and at 500 mm, the exact distance was refined and calibrated using a CeO_2 scientific standard (NIST 674a). The collected 2D pattern were processed with fit2d.[50;51] Strong single crystal reflections from the diamonds of the DAC as well as the shadow from the beam stop mounting and dead pixels of the detector were masked manually. After integration the large background is subtracted manually with fityk.[52] In order to not oversee weak reflections and accidentally discard them as background, several (at least 5) diffraction pattern of each measurement point (DAC, p, ω) are stacked and the common background determined and subtracted. A schematic overview on the data reduction process is shown in figure 2.3. Due to the small sample size and the highly focused beam, intensities are not evenly distributed in the 2D pattern and cannot be safely determined in the 1D pattern. A Rietveld refinement of the gathered data is hence not feasible. For determination of the lattice parameters in the samples, a Le Bail fit[47] is sufficient.

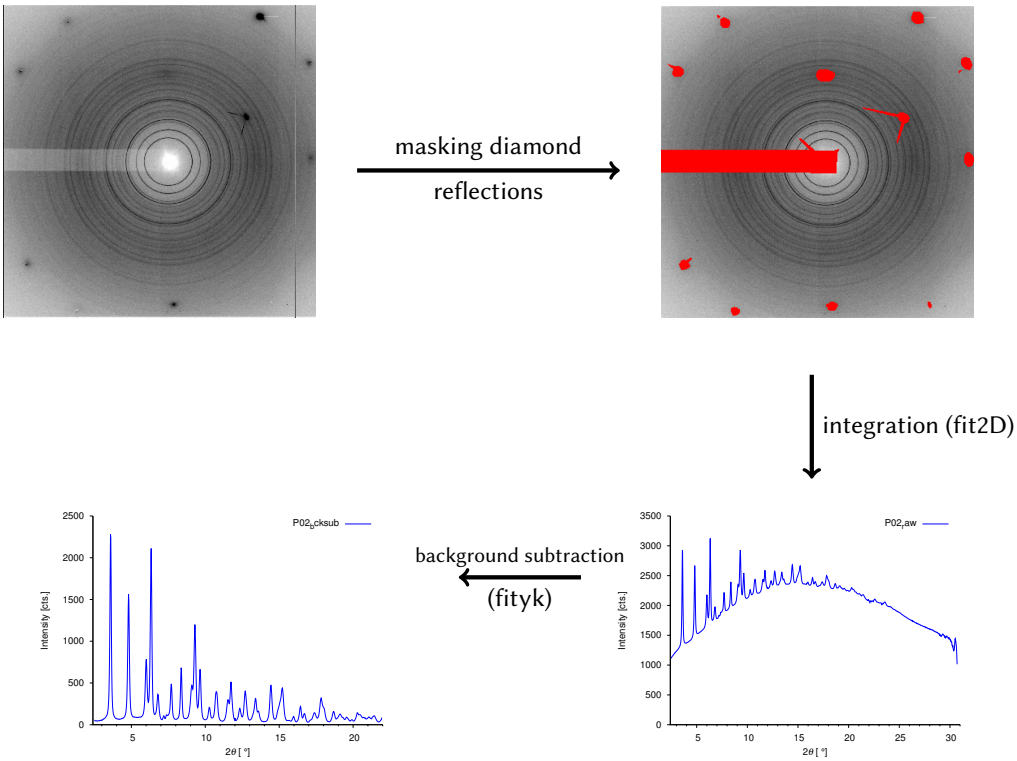

Figure 2.3: Schematic flow chart of the data reduction process.

Powder pattern of studtite and metastudtite were collected at the P02.1 *High Resolution Powder Diffraction* (HRPD) beamline at PETRA III.[53] Measurements were carried out at an energy of 60 keV (λ = 0.2071 Å) and in Debye-Scherrer geometry. For collection of the pattern a 2D image plate detector (PerkinElmer XRD 1621) was used. Sample to detector distance was fixed, the exact distance was refined and calibrated using Si or CeO_2 scientific standards (NIST 640b, NIST 674a). The collected 2D pattern were integrated using fit2d[50;51] and used for structure solution with EXPO2009[54] and Rietveld refinement employing GSAS and EXPGUI.[55;56;57]

2.3.4 Neutron Powder Diffraction

Neutron powder diffraction was performed on deuterated studtite and metastudtite samples on the Neutron Powder Diffractometer of the LANSCE, Manuel Lujan, Jr. user facility in Los Alamos, New Mexico, USA. The setup of the NPDF instrument is illustrated in figure 2.4. Initial neutrons from the spallation target are cooled by a chilled water moderator before hitting the sample located in the center. Four "banks" in 40 °, 90 °, 119 ° and 149 ° position equipped with ^{3}He detector tubes are used for data collection. The backscattering region of the instrument (banks at 119 ° and 149 °) has 20 detector panels with 160 separate position-sensitive detectors in total. These specifications give the instrument a high resolution and a large Q-range. The beam size is fixed to 1 cm × 5 cm. A vanadium can of these dimension is used as sample container and for decent data quality should be at least half filled.

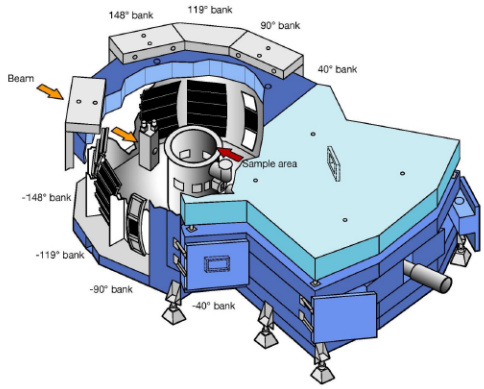

Figure 2.4: Setup of the Neutron Powder Diffractometer (NPDF) of the LANSCE, Lujan Center.[58]

2.3.5 In-situ X-ray Diffraction

Temperature dependent in-situ XRD experiments were conducted on the Bruker *AXS* D8 diffractometer using the HOT HUMIDITY climate chamber by Materials Research Instruments (MRI). This temperature stage is equipped with a Ni plated Cu sample holder and can be operated in the temperature range of 20 – 250 °C with a maximum heating rate of 2 $^{K}/_{min}$ and an accuracy of ± 1 K. The whole chamber can be flushed with standard laboratory gases (N_2, Ar, 5 % H_2/N_2, CO_2). Humidity can be set between 5 – 95 % (max. T = 100 °).

2.4 Electronmicroscopy

Electrons are fundamental particles existing in the atomic shell with a negative charge and and a mass which is a ten-thousandth of a proton or neutron. Through application of an electric or magnetic field, they can be easily manipulated. Electrons cannot only be treated as particles, as they also show the preferences of waves (wave particle dualism). According to the relationship discovered by de Broglie in 1924:

$$\lambda = \frac{h}{m \cdot \nu} = \frac{h}{\sqrt{2 \cdot mE}} \tag{2.7}$$

an electron of a certain energy can be treated as a material wavefunction with wavelength λ. For instance, electrons with an energy of
10 keV equal λ = 12.2 pm
300 keV equal λ = 1.97 pm,
in comparison the visible spectrum of light is in the range of λ = 0.38 – 0.78 μm. In order to show diffraction behavior, the wavelength of the radiation employed needs to be in the magnitude of the atomic distances. It is therefore not possible, to possible to investigate atomic structures with light of the visible spectra. X-rays and particle waves, such as neutron or electrons are suitable for this purpose. The resolution limit follows the Rayleigh equation 2.8:

$$d = 0.61 \frac{\lambda}{n \cdot sin\alpha} \tag{2.8}$$

with wavelength(λ), aperture opening angle (α), and refraction index (n). For visible light, e.g. λ = 500 nm, n = 1, sinα = 1, the maximum theoretical resolution amounts to d = 0.3 μm, an improvement could be either made by bigger n or smaller λ. For electrons with an energy of 300 keV, equal to λ = 0.197 nm a maximum resolution of 0.16 nm is possible. There are, however, problems associated with electron diffraction itself.[59] Electrons require magnetic lenses, these exhibit inadequateness compared to optical lenses, which cannot be overcome by skillful design. Diverging lenses are, for instance, non existent in electron microscopy. Hence, the spherical aberration needs to be corrected by other means, like the newly developed C_S corrective phase plates.

All types of electron microscopes are comprised of three parts: the electron source, the focusing system, and the imaging apparatus. The electron beam is produced in the electron source. It can either be produced through classic thermal emittance, e.g. from a tungsten cathode, or by extraction with a field-emission-gun (FEG), e.g. from LaB_6 crystal. In the focusing system the electron beam is aligned, and focused on the sample; in the transmission electron microscope also the transmitted beam is further handled. Finally, the imaging system can either be an image plate or photographic film, or an imaging detector connected to a monitor or other device.

2.4.1 Scanning Electron Microscopy - SEM

Scanning Electron Microscopy is mostly a technique used to the study surfaces and especially topologies of materials. The SEM focuses an electron beam at a point on the surface of the sample. These electrons are either backscattered (BSE) or encourage the emittance of secondary electrons (SE) from the sample which are then detected. By doing this in a raster pattern across the surface an image is formed, pixel by pixel. The imaging follows the raster process, so that the surface is projected. When the electron beams, i.e. the primary electrons, impact the surface they generate secondary electrons (SE), backscattered electrons (BSE), but also Auger electrons, X-ray photons (usable for qualitative and quantitative sample analysis) and cathodeluminescence (cf. figure 2.5).

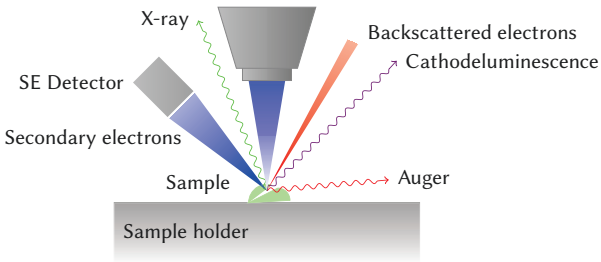

Figure 2.5: Scheme of the beam path in the Scanning Electron Microscope

The picture generated needs to be interpreted carefully. Brightness and contrast observed are not identical to those used to from the light microscope. Heavy elements scatter electrons stronger than light elements. From the signal of a back scattered electron detector (BSED), therefore, the Z contrast is visible in these type of micrographs. Heavy elements appear bright, light elements dark. Homogeneity of the sample, segregation processes in a sample or enrichment of one component in a certain area can be observed this way. Secondary electrons are on the other hand usually generated in the samples surface and give a good impression of the topology of the surface. Yet, the sample itself strongly influences the secondary electrons emitted. The yield of secondary electrons is higher at edges and can also depend on the crystal orientation.

Sample Preparation

SEM investigations were carried out on a FEI Quanta FEG 200G, which can be use in high vacuum mode p = 10^{-5} Pa, as well as low vacuum mode with H_2O as medium. The low vacuum mode has the advantage, that the samples do not need to be coated with a special conductive layer to discharge the build up charge from the primary electrons. This device also can operate in Environmental Scanning Electron Microscopy (ESEM) mode. This makes it possible to heat the sample in a H_2O rich atmosphere, during examination. For preparation, a small amount of substance is placed on a carbon pad, which is glued onto an aluminium sample holder. If not

especially noted otherwise SEM investigations were performed at 30 kV using the low vacuum mode with 70 Pa H_2O.

2.4.2 Transmission Electron Microscopy - TEM

In the Transmission Electron Microscope (TEM) the information is primarily obtained through the transmitted electrons. Certain sample conditions are hence necessary for a TEM. Samples need to be thin enough to be transparent for electrons, i.e. depending on the involved elements, not thicker than $\sim$ 100 nm. The electron beam is highly energetic. This needs to be taken into account, when examining sensitive samples, as they may decompose or suffer significant irradiation damages. TEM technique offers a highly sensitive local analysis and direct imaging of the electron densities of a sample. Yet, one should always bear in mind, that this might not reflect the overall situation in the material. A schematic overview of the beam path in the TEM is shown in figure 2.6. At the top of the TEM the source of the free electrons is located. As a very narrow beam for high resolution is wanted in the TEM, field emission guns are preferred and more common than in SEM for this matter. Directly below the source is the condenser system, some microscopes, e.g. the Zeiss LIBRA series, also have a monochromator system built in. The condenser system itself has been optimized in recent developments. The most modern microscopes even have additional corrections for spherical and chromatic aberration.[60] The condenser system focuses the electron beam onto the sample, interacts (phase and amplitude) and the transmitted electron beam now features the additional information of the sample. Below or nearly in the sample's plane is the objective lens and aperture which collect and convey the electrons to the projector system. The projector system (drawn here as one large lens) usually consists of 2-3 projector lenses and 1-3 apertures. The imaging system in the TEM usually still consists of a Eu doped ZnO phosphor screen, for first examination, which can be drawn back to open the entrance to a CCD or photographic film camera. Additionally, further analysis systems for Electron Energy Loss Spectroscopy (EELS) can be coupled to the TEM.

Transmission electron microscopy can be performed in two different modi: imaging and diffraction. In imaging mode the main techniques are bright field imaging (BF), employing the transmitted primary electrons, and dark field (DF) extracting the image from a diffracted beam. In diffraction mode the enlarged electron diffraction pattern is obtained. In conventional BF imaging at low magnification the contrast results from absorption of the electrons in the sample. Heavy elements appear darker than light elements, thick areas of the sample darker than thin parts. Similar to SEM, this makes segregation or inhomogeneity of the sample visible. To a first approximation the image can be regarded as simple projection and may be modeled via Beer's law, taking into account only the amplitude information. Where no sample is, the image appears bright – hence the name bright field. Further magnification discloses the diffraction contrast in the specimen. This contrast results from the electrons undergoing Bragg scattering at the

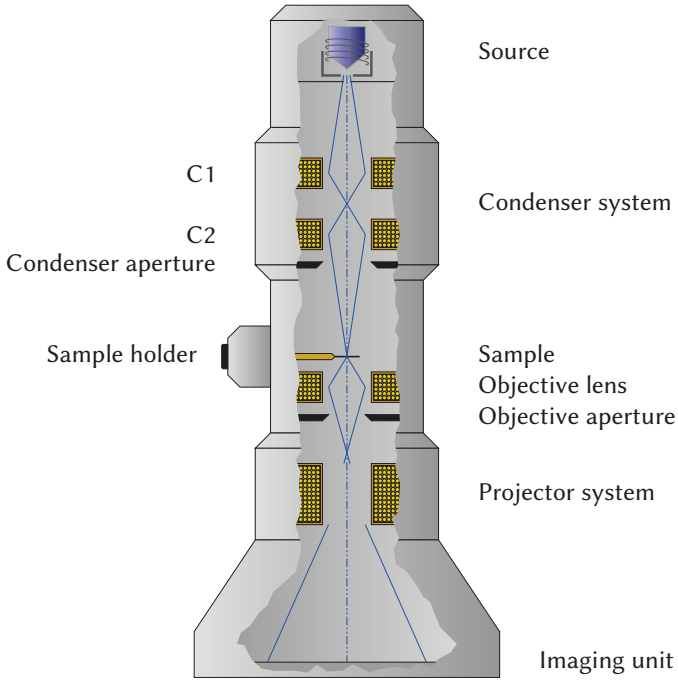

Figure 2.6: Simplified scheme of the beam path in the Transmission Electron Microscope

crystal planes in a crystalline sample. It can also appear as a result of disturbances or faults in the crystal lattice, like from dislocations, stacking faults or if the structure exhibits strong stress and strain. Another type of diffraction contrast, is when the sample thickness increases (wedge contrast).[61] By the placement of apertures in the back focal plane, i.e. the objective aperture, desired Bragg reflections for further investigation can be selected (or excluded). This way only parts of the sample that are causing the electrons to scatter to the selected reflections will end up projected onto the imaging apparatus. Usually the unscattered beam is not selected. A region without a specimen will not contribute to the scattered electrons, therefore will appear dark – leading to the name dark field image.

Electron diffraction can be performed to investigate the local structure of a sample, i.e. at phase boundaries of layered structures, twinning phenomena or inversion domain boundaries. For this purpose apertures to select a certain area are inserted in the beam path. Selected Area Electron Diffraction pattern (SAED) for crystalline samples, provide dot pattern, equivalent to single crystal diffraction patterns. They provide general information on symmetry and space group of the crystal and the position towards the incident beam. Indexation follows the same rules. Thicker samples also exhibit inelastic (diffuse) scattering. When the diffuse scattered electrons afterwards are again diffracted at the lattice planes, this leads to the appearance of the Kikuchi-lines and -patterns. In addition, Convergent Beam Electron Diffraction (CBED) can in some cases be

employed to gather information on the full three dimensional structure of a sample.
High Resolution Transmission Electron Microscopy (HRTEM) is a technique, which allows to image the structure of a specimen with (sub)atomic resolution.[62] The incident electron wave passes through the only few nm thick sample and interacts with the potentials of the structure, i.e. interference of the phase and the amplitude. Contrast in the HRTEM mainly results from the phase contrast, making a direct interpretation of the obtained images very difficult. Lattice planes and angles can usually be derived directly from the image. Yet, high intensity might or might not indicate the presence of an atom column in that precise location. True atomic positions are contained in the *electron exit wave*, which is existent directly after the sample. The *electron exit wave* passes through the imaging system of the microscope. During this it is further influenced by focusing lenses and apertures of the microscope's imaging system. The relationship between the *electron exit wave* and the detected *image wave* is complicated. Hence the detected *image wave* needs to be deconvoluted with the specific *contrast transfer function (CTF)* of the microscope, which comprises the influence lenses, apertures and general setup of the microscope have. In order to reconstruct the *exiting wave function* usually a series of images of the sample spot with different defocus are recorded. (One of the biggest problems to overcome here is the thermal drift.) With knowledge of the *CTF* the real *exiting wave function* can then be calculated and further interpreted, e.g. by comparison with simulations for different structure models.
TEM and HRTEM images were collected on a Philips CM300 FEG UT/STEM equipped with a Thermo Fisher Scientific EDS-system (HPGe detector and Noran System Seven) and a FEI Titan 80-300 with HAADF detector system at 300 kV acceleration voltage.

Sample Preparation

A small amount of substance is finely ground in an agate mortar, then suspended in H_2O demin. After allowing the suspension a few minutes to settle, few drops of the supernatant are dropped onto a PLANO 200 mesh carbon film TEM-sample grid. The grid is allowed to dry under ambient conditions. To confirm adequate sample coverage of the TEM sample grid, the samples are examined with SEM as seen in figure 2.7. This way, it is ensured, that enough sample is present on the grid to perform TEM and that it's evenly distributed. On the other hand it is also confirmed, that the amount on the grid is well below the permitted limit to transport the samples out of a radioactive controlled area. Of course, samples were checked by a radioactive control technician before transport.

2.4.3 Energy Dispersive X-ray Spectroscopy - EDS

Energy Dispersive X-ray Spectroscopy is a technique which allows a non destructive investigation of a samples composition. In the primary process a high energy electron knocks an inner shell electron from it's position. EDS systems are hence often coupled to a SEM or TEM. The

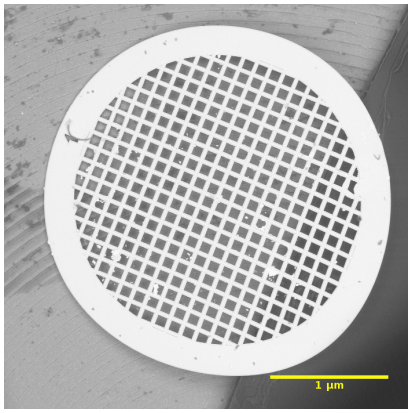

(a) SEM micrograph of the TEM sample grid. The grid is mounted on an aluminum SEM sample holder with a bit of sticky carbon pad (black area to the right).

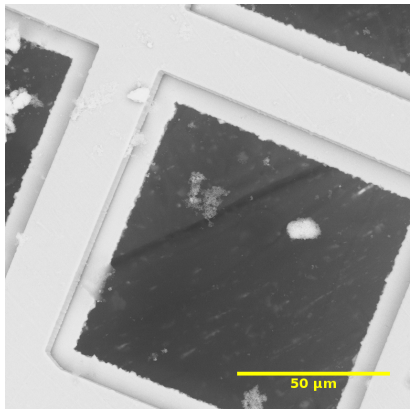

(b) Close-up of one mesh of the TEM grid. The sample can be distinguished as bright "cloudy" spots. As the thin carbon film is electron transparent, the SEM sample holder can be seen in the background.

Figure 2.7: SEM microgaphs of the prepared TEM-sample grid to confirm quality and coverage prior to the TEM experiment.

resulting hole is filled by an electron from a higher energy level. During this secondary process energy in form of electromagnetic radiation is either emitted (X-ray) or transferred onto another electron (Auger process). The energy of the emitted X-ray radiation is characteristic for a specific element, while from the intensity of the signal implications on the amount of this element can be drawn.

Whith EDS a qualitative and quantitative examination of a sample are simultaneously possible. However, EDS analysis is always a relative analysis, no absolute values can be obtained. The aim is to determine the ratio between two or more elements investigated. For the qualitative analysis the main errors are overlapping of peaks, especially if many heavy atoms are present in the sample. Weak peaks of an element could be concealed. The reliability of the quantitative analysis of a spectra depends on many factors such as absorption, fluorescence phenomena and excitation energy. To reduce the effect of absorption, it is useful to investigate a thin part of the sample. As only a limited sample volume is measured each time, the investigation of several sample spots should be done to reduce the risk of overestimating one component (inhomogenous samples) and improve statistics. The composition of a sample can then be determined using the Cliff-Lorimer Equation.[63]

$$\frac{c_A}{c_B} = k_{A,B} \cdot \frac{I_A}{I_B} \tag{2.9}$$

The k factor is usually derived by calibration with a scientific standard. A standard-less method is also possible, but usually not as accurate. For the standard-less analysis, usually the ZAF

correction is applied, using documented values.

$$k_i = Z_i \cdot A_i \cdot F_i \tag{2.10}$$

with Z_i = mass factor for element i
A_i = absorption factor for element i
F_i = fluorescence factor for element i

In any case the counting time needs to be high enough in order to get a reliable result. Spatial resolution is very limited in SEM-EDS due to the deep penetration of the electrons into the sample volume. The emitted X-rays therefore result from a rather large (approximately 1-2 μm in diameter) bulb, see figure 2.8. In TEM-EDS the samples are much thinner and absorption is minimal. The excited sample volume is rather small and spatial resolution is much better. Also as absorption errors can be discarded, the overall error is smaller.

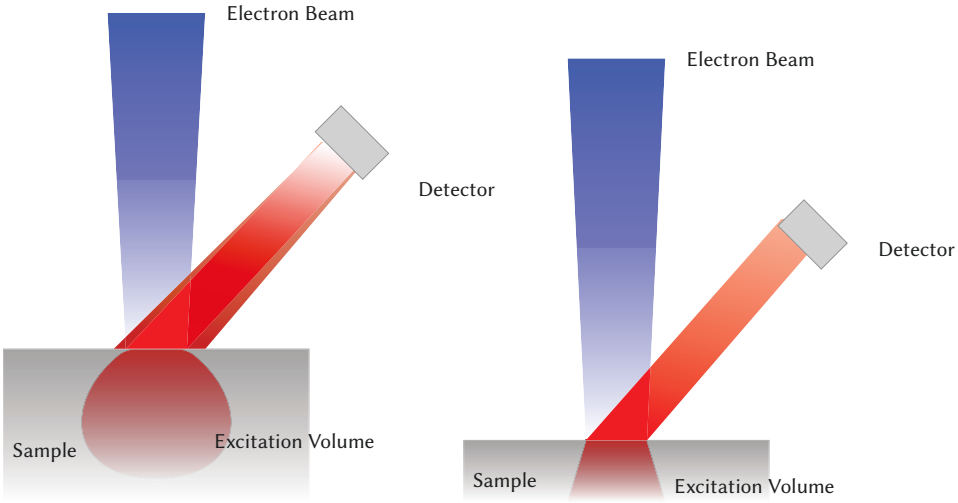

(a) Illustration of the excitation volume and resulting EDS signal in SEM-EDS.

(b) Illustration of the excitation volume TEM-EDS.

Figure 2.8: Comparison of the excitation volume in SEM-EDS and TEM-EDS. Due to the smaller sample thickness in TEM-EDS, the spatial resolution for the EDS signal is higher.

2.5 Spectroscopy Experiments

Spectroscopy techniques exploit the fact that atoms, ions and molecules interact with electromagnetic radiation. Within the large field of spectroscopy different methods exist. Samples can be studied regarding their absorption properties, the resulting spectra are absorption spectra (cf. IR, EELS, EXAFS). If the emission of radiation from a sample after excitation is investigated, the obtained spectra are called emission spectra (so in EDS, Raman). Atomic spectra yield important information on the electronic structure of the atoms, which further builds the basis for discussion of bonding behavior and properties. Understanding of periodic structures and magnetic properties would not be possible without it. Molecular spectra offer a greater complexity but also more information than the pure atomic spectra. Besides the electronic transitions, they contain additional vibrational and rotational transitions of the molecules. These give information on the true shape of the molecule as well as the strength and rigidness of the contained bonds.
In general, vibrational transitions appear at lower energies ϵ, than rotational transitions; electronic transition appear at the highest energy, $\epsilon_{vib} < \epsilon_{rot} < \epsilon_{el}$. Conclusively, at energies ϵ_{rot}, where rotational transitions are active, vibrational transitions are already excited. This allows for mixing of both phenomena, which adds to the complexity of the spectra and makes interpretation sometimes difficult. Whether or not a certain spectroscopic transition can appear, depends on general properties of the molecule and/or specific atom. These so called *selection rules* differ depending on the spectroscopic method and type of transition.
The possible transitions can be derived from the total degrees of freedom of the molecule. For a non-linear molecule with *N* atoms, T_{tot} = 3· *N* degrees of freedom exist. This corresponds to three independent spatial coordinates, *x, y, z*, of each atom. Three degrees of freedom are consumed by the translations along the principal axes, T_x, T_y, T_z, another three by rotation about these axes, R_x, R_y, R_z. The degrees of freedom hence is reduced to 3· *N* - 6, which comprise the so called *normal vibrations* or *normal modes*. By convention the following symbols are used to specify:
ν = stretching vibrations,
δ = bending vibrations,
γ = out-of-plane deformation vibration,
τ = torsional vibration.[64;65] The special Herzberg notation[66] offers a simple way to denote more complex vibrations of polyatomic molecules. For penta-atomic tetrahedral XY_4 molecules, like SiO_4^{4-}, the ν_1 = A_1, total symmetric stretching vibration,
ν_2 = E, double degenerate bending vibration,
ν_3 = F_2, triple degenerate bending vibration,
ν_4 = F_2, triple degenerate stretching vibration.[67;68]

2.5.1 Infrared spectroscopy - IR

Infrared spectroscopy (IR) uses light in the range of 10 – 14000 cm^{-1}. Standard procedures, especially in organic chemistry, usually only employ the mid-infrared region, 400 – 4000 cm^{-1}, for analysis. Through absorption of a photon, $E = h \cdot \nu_{vib}$ a normal mode of the molecule is activated, $\Delta\, v \;=\; \pm\, 1$. Activation of overtones, $\Delta\, v \;>\; \pm\, 1$, by high energies is also possible, but activation probabilities and hence intensities are much lower. In general, stretching modes, ν, where molecular bonds are elongated and pressed, require higher energies than bending modes, δ, which only deform the bond angles. In order for a vibrational mode to be active in the IR, the dipole moment of the molecule or ion must change.[69] For centrosymmetric molecules nearly all symmetric vibrations are hence forbidden. Due to the mutual exclusion rule also those vibrations, which are observed in the IR spectrum cannot be found in the Raman spectrum and vice verse.

For experimental measurements usually Fourier Transform Infrared Spectrometers (FT-IR) equipped with Michelson interferometer are used. A broad band of infrared radiation, covering the wavelengths to be measured, is generated. The emitter can be some sort of black body, Nernst lamps are also still in use. The light shines into the Michelson interferometer, where it is split into two parts. One is led onto a fixed, the other one on a movable mirror. The two beams are then merged so that they interfere with each other and led through the sample. By moving the mobile mirror in the system the complete range of wavelengths can be tuned. The light beam is then detected by a photon sensitive detector. As a result an interferogramm is obtained, which then is Fourier transformed to yield a spectrum.[64] This spectrum can then be interpreted, e.g. through comparison with reference data or assignment of the vibrational modes expected from group theory.[69]

Sample Preparation

Measurements were conducted on a Bruker *Equinox 55* TGA-IR in transmission mode. Samples for investigation are prepared by grinding approximately 1–3 mg substance together with 250 mg potassium bromide. This mass is pressed into a thin platelet using a standard laboratory press and employing a pressure of 10 bar over approximately 15 minutes. The obtained spectra are treated with the commercial OPUS software package, to derive the peak positions. For some samples this is done using the free gnuplot 4.6 software. The collected spectra are first flipped vertically, then the maxima are fitted using Gaussian fit functions to obtain the peak positions.

2.5.2 Raman and High-pressure Raman spectroscopy

When a sample is exposed to monochromatic light, usually from a laser source, most of the light passes though the sample unaffected. However, the remaining light interacts with the sample and is scattered to all directions. A small portion of the light is scattered as Rayleigh scattering; the frequency of this fraction (factor 10^{-4}) remains the same as the initial frequency. An even

smaller part (factor 10^{-8}) is inelastically scattered and the frequency of these photons show a distribution. The frequencies can be larger or smaller than the initial excitation frequency. This distribution results from absorption and emission processes as well as vibrational excitations. The vibrations, which are characteristic for a special molecule or ion, are not denoted in the frequency, but in the difference, the Raman shift, between the excitation frequency and the detected frequency. For Raman lines to appear, it is necessary, that the polarisability changes during the absorption process. Polarisability can be regarded as the ability of the electron cloud of the ion or molecule to deform. Clearly, a large and diffuse electron cloud, like that of I^-, is easier to deform than that of the smaller F^-. One of the biggest problems for Raman spectroscopy is, if fluorescence from the sample or contamination is present. The fluorescence radiation can completely cover the Raman spectrum, making an interpretation merely impossible.
Lasers are the only feasible light sources for Raman spectrometers, providing enough intensity and monochromatic radiation. The light passes through the sample and the Raman scattering is emitted perpendicular to the transmitted radiation. To increase the intensity of the radiation, the transmitted light is often reflected back onto the sample by a mirror. The Raman scattering is focused by a lens and aperture system. A mirror system with integrated grating splits up the beam into its spectral components. Finally, the resulting beam is lead onto a photoelectric detector and recorded as spectrum.

Sample Preparation

Confocal micro-Raman measurements were carried out with a Renishaw Raman System (RM-1000) equipped with a Leica DMLM optical microscope, a grating with 1800 grooves per mm, and a Peltier-cooled charge-coupled device (CCD) detector. For excitement the 532 nm emission line of a Nd:YAG laser was used. We employed a 20 objective lens with a long working distance. The spectra were recorded in the range from 100 to 1200 cm^{-1} with exposure times of 150 s and a laser power of 10 mW to 100 mW. The system was calibrated using the band at 519 cm^{-1} of a Si wafer.[70] All obtained spectra were background corrected and fitted using Pseudovoigt functions employing the fityk[52] software package. For the high-pressure Raman studies samples are loaded into Boehler-Allmax type diamond-anvil-cell (DAC)[38], equipped with a tungsten gasket. The 140 μm in diameter gasket hole was laser drilled into pre-indented (to 40 – 50 μm thickness) tungsten gaskets and served as sample chamber. Several small ruby grains were included in the sample chamber and the pressure was measured using standard ruby fluorescence technique through the position of the ruby R_1 peak.[71] Ne was used as hydrostatic pressure medium. Raman and high-pressure Raman investigations were performed in the group of Prof. Björn Winkler at the University of Frankfurt. Laser drilling of the gaskets and gas-loading of the DAC were done by Dr. Johannes Bauer.

2.5.3 Extended X-ray Absorption Fine Structure - EXAFS

EXAFS is a technique very suitable for the investigation of the short range order in materials. The information extracted by use of this method are element specific and yields first hand information on the electronic structure in the material. This directly yields the oxidation state of the elements in the material but also bond lengths and angles. This makes EXAFS a very powerful local probe for investigation, especially of disordered or even amorphous materials, which do not establish long range order. Hence, structure of such materials is not approachable by diffraction techniques or electron microscopy. For crystalline materials it is the opportunity to verify the obtained data from diffraction and methods which rely on a given long range order.[72]

General Process

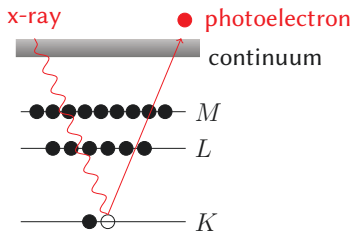

Figure 2.9: Schematic drawing of the photoelectric effect

Basically the spectra collection is a scan of the photon energy, hence making a tunable X-ray beam necessary. Because of this and the better intensity and high brilliance, EXAFS is generally performed at synchrotron radiation sources. Through absorption of X-ray radiation one of the core level electrons is excited into an unoccupied state or the continuum (absorption process of the photoelectron, cf. figure 2.9). The absorption energy needed to elevate the core electron is element specific. Since the absorption rapidly increases at this energy, giving the spectra a sharp edge, this energy, E_{edge}, is also called the absorption edge. Depending on the principal quantum number of the core electron, which is exited the absorption edge is called K-, L- or M-edge. The core level is then refilled by an electron of another level, either leading to emittance of a photoquant of a characteristic frequency (fluorescence) or an Auger electron (emission process). These processes are proportional to the absorbed amount of X-ray radiation. Usually the absorption coefficient $\mu(E)$ an can more easily be measured this way than by measuring the direct transmitted intensity.

After being elevated into the empty state, the electron interacts with the potentials of the the neighboring atoms. Quantum mechanically the outgoing photoelectron can be represented as a spherical wave, defined as

$$\lambda = \frac{2\pi}{k} \tag{2.11}$$

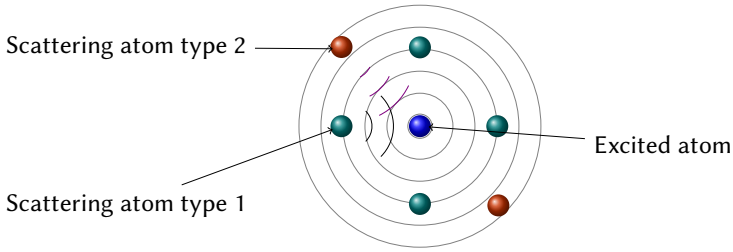

Figure 2.10: Schematic drawing of the wavefunction generated from the excited electron (grey) and the backscattered wave from two different neighboring atoms (black and violet).

with wavelength λ and wave-vector k, which is expressed by

$$k = \sqrt{\left(\frac{8\pi^2 m}{h^2}\right) h\nu + E_0 - E_{edge}} \tag{2.12}$$

m being the electron mass and h the Planck quantum. The backscattered wavefunction of the electron generates positive and negative interference with the outgoing wavefunction (see figure 2.10. Constructive interference of this wavefunction near the nucleus promotes X-ray photoabsorption, destructive interference reduces absorption. In conclusion an oscillation becomes visible in the slowly decreasing intensity of the absorption coefficient. Information on the local structure is contained in this oscillation, $\chi(k)$. It is assumed, that only elastically scattered electrons contribute to the EXAFS spectra. Also that the multiple-scattering of the electron can be neglected as the resulting signal is weak and only contributes very little. It can be given as superposition over all interference pattern:

$$\chi(k) = \sum_{j=1}^{n} A_j(k) sin\Phi_j(k) \tag{2.13}$$

where $A_j(k)$ is the amplitude of the interference wave-function $sin\Phi_j(k)$. The interatomic distance as well as a phase factor are contained in the argument, $\Phi_j(k)$, of the sin function. The properties of the oscillation (amplitude, frequency) strongly depend on the type, number and oxidation state of the neighboring atoms.

$$A_j(k) = \frac{N_j}{kR_j^2} S_0^2 F_j(k) \cdot e^{-2k^2\sigma_j^2} \cdot e^{-2R_j/\lambda k} \tag{2.14}$$

The amplitude, $A_j(k)$, contains the coordination number, N and disorder, σ, which is the fluctuation in R_j due to thermal motion or structural disorder. $F_j(k)$ is the backscattering amplitude, which is element specific and S_0^2 an amplitude reduction factor (usually between 0.8 – 1).[73] For non-oriented, dilute samples (like solutions or powders) the combination of equations 2.13

and 2.14 represents $\chi(k)$ from the oscillation:[74]

$$\chi(k) = \frac{1}{k} \cdot S_0^2 \sum_{j=1}^{n} \frac{N_j}{R_j^2} \cdot F_j(k) \cdot e^{-2k^2\sigma_j^2} \cdot e^{-2R_j/\lambda k} sin\Phi_j(k) \tag{2.15}$$

Bond lengths (from $sin\Phi_j(k)$) and order as well as coordination number, N, can be retrieved from this. Further, the exponential term $e^{-2k^2\sigma_j^2}$ takes account of the Gaussian distribution of distances of one shell due to a structural and/or thermal disorder, assuming that the displacements are only small. The second exponential term $e^{-2R_j/\lambda k}$ considers the finite mean free path of a photoelectron with wavelength $\lambda(k)$.

Spectra interpretation

As shown in figure 2.11 the retrieved spectra is composed of the Pre-edge region, the X-ray Absorption Near Edge Structure (XANES) and the Extended X-ray Absorption Fine Structure region (EXAFS) which extends up to several 1000 eV. The Pre-edge region usually ought to be flat, especially when using synchrotron radiation. However, lower energy absorption processes of the structure take place (similar to the processes involved in EELS), generating a background. In the XANES region the linear absorption coefficient is dominated by Fermi's Golden rule, which gives the probability of an electron to transient from an initial state to a given final state. The most intense features are due to electric-dipole allowed transitions (i.e. Δl = $\pm$ 1) to unfilled orbitals. For example, the most intense features of the K-edge are due to 1s $\rightarrow$ np transitions, while the most intense features of the L_3-edge are due to 2p $\rightarrow$ nd transitions. The lifetime of the transitions of the K-edge is shorter than that of the corresponding L-edge of a given element. The XANES region of the L-edge therefore usually has more distinct features than that of the K-edge. All the scattering pathways, classified according to the number of scattering events, contribute to the absorption cross section in XANES. Also the XANES region corresponds directly to the density of states (DOS) and therefore contains specific information on the oxidation state and the bonding of the nucleus. While the photoelectron interacts through multiple-scattering events in the XANES, it is assumed, that it is scattered only by a single neighbor atom in EXAFS.[73] The EXAFS spectrum is dominated by forward scattering. Long oscillations with very low frequency underlay the EXAFS information and need to be removed by applying a background spline function to the post-edge region. This function is used to extrapolate the value of the absorption coefficient to E_0. The range of this function determines the lower limit R_{bkg} for interpretation in the Fourier transform.

Data Analysis

While the XANES data often can be interpreted needing only minor extraction steps, EXAFS data requires processing before relevant information can be extracted from the spectra. The

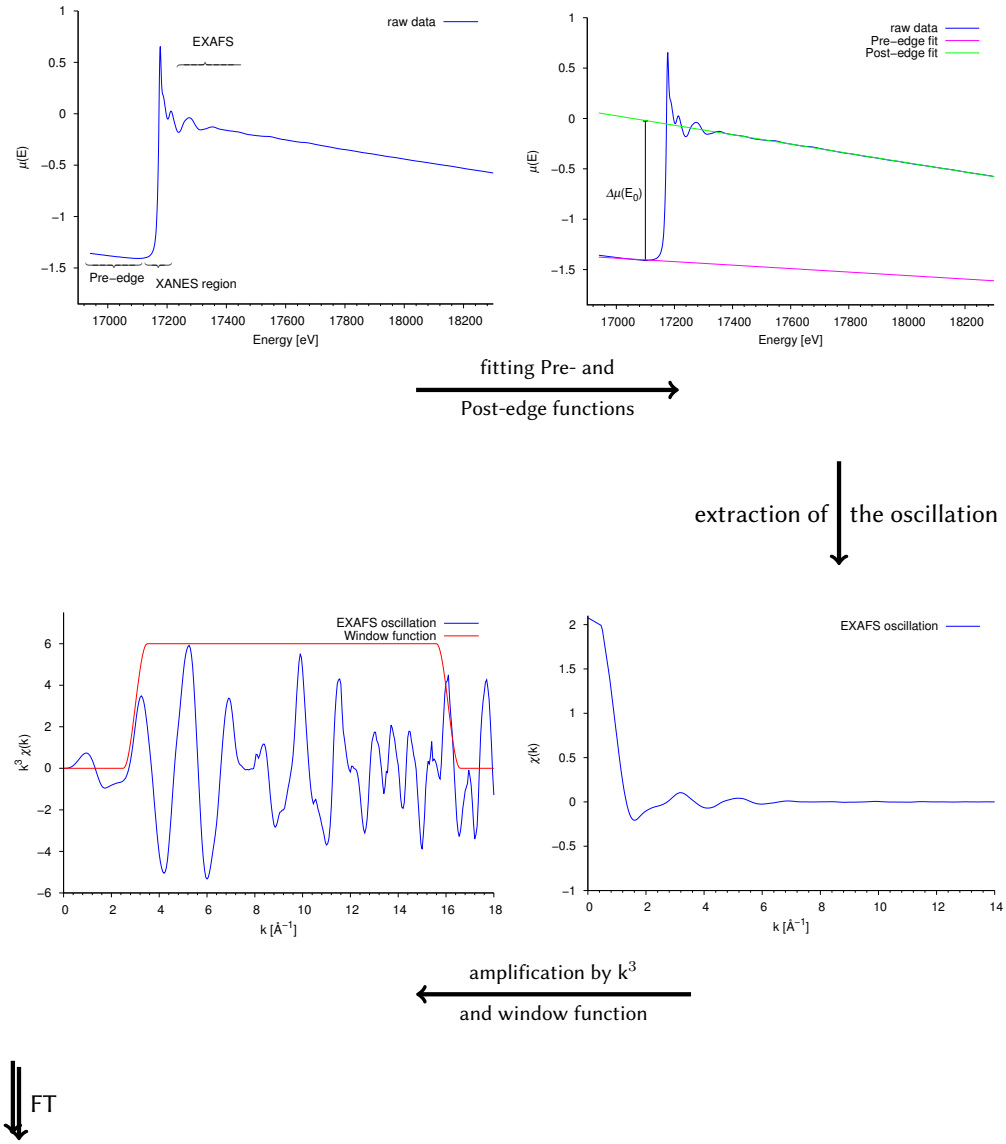

Figure 2.11: Schematic flow chart of the data reduction process for EXAFS.

data-reduction process is illustrated in figure 2.11. First the background of the spectra needs to be stripped in order to obtain just the oscillation $\chi(k)$, which then is Fourier transformed to give the radial distribution function in real space. To minimize distortions and appearance of ripples (peak side-lobes which arise from the truncated integration)[44] in the FT modulus, $\chi(k)$ is multiplied by a window function $W(k)$. This yields a "peak pattern" with the peaks

corresponding to the shells of atoms distributed around the probed atom. This radial distribution function then needs to be compared and fit to a calculated model. In this context the limits of the EXAFS investigation technique become apparent. Phase purity with respect to the probed element are mandatory to generate a reliable fit on the obtained data. Also the number of visible shells is limited, usually to 5 Å in distance. It however depends on the probed elements and the material. Especially if an absorption edge is very close to the EXAFS region and there is overlap, then extractable information from the oscillation significantly decreases. Starting from the atomic coordinates programs like FEFF or ifeffit[75;76] are used to calculate the amplitude and phases of scattering paths up to a given order and intensity. The separate forward scattering paths under investigation are then selected and used as model and the EXAFS spectrum. A least squares algorithm is employed to fit this theoretical $\chi(k)_{theo}$ which is build-up using the selected scattering paths, to the experimental $\chi(k)_{exp}$ function. If reference materials exist, it is also possible to use $\chi(k)_{ref}$ as starting value. Low frequency oscillations resulting from a misfit of the real atomic background and the approximation by the spline function (used to determine the atomic background) would appear as peaks at low ($<$ 1 Å) intensity vs. R values due to the Fourier transform. There are no real distances related to this signal, of course. The $\chi(k)$ function should oscillate symmetrically around the zero line. For the fitting process the residual in R space for frequencies below R_{bkg} is hence minimized. Errors are usually about 0.01–0.02 Å for interatomic distances, and 5–15 % for coordination numbers.[72]

Sample Preparation

For measurements dilute homogeneous samples are needed. Material with roughly 20 mg of the sample, with respect to the nuclid(s), are finely ground and combined with 250 mg Teflon powder. This mixture is cooled to 153 K (LN_2) and mixed in a vibration mill for 5 minutes. This cycle is repeated 4 – 5 times. The so homogenized powder then is pressed into a platelet using a force of 10 bar. For the measurement this platelet is put into a plastic mount and sealed with Kapton tape. Measurements at 15 K were performed using a closed cycle He cryostat. EXAFS measurements were carried out on the BM-20 beamline (ROBL) at the European Synchrotron Radiation Facility (ESRF) in Grenoble, France. A Si(111) double-crystal monochromator and a pair of collimating and focusing rhodium-coated mirrors was used to align the beam. Data were collected in transmission mode at Th L_3 ($E_{k=0}$ = 16310 eV) and U L_3 ($E_{k=0}$ = 17185 eV) edges. Energy was calibrated using the K edge (E = 17038 eV) of an yttrium metal foil. For each X-ray absorption fine structure (EXAFS) measurement, the spectra of the reference foil was systematically collected at the same time. Several sweeps were performed during the measurement on the same sample to improve the signal-to-noise ratio. The EXAFS oscillations were extracted from the raw absorption spectra by using WinXAS 3.1[77] and the edge step extracted with ATHENA from the demeter package.[76] Curve fitting was done using the EXAFSPAK software[78] for the $U_xTh_{(1-x)}SiO_4$, x = 0 – 1, samples. The interatomic scattering paths were calculated using the

ab initio code FEFF8.[75] Since the theoretical backscattering phases of U and Th are almost identical no effort was made to generate mixed scattering phases. Studtite and metastudtite samples were fitted employing the ARTEMIS suite.[76] The related error in the interatomic distance R is less than the standard deviation. The data analysis was conducted by fixing the coordination numbers, N, to the crystallographic values and refining the distances, R, and Debye-Waller factors, σ^2, simultaneously. The amplitude reduction factor (S_0^2) was set at 0.90 and the shift in the threshold energy (E_0) was linked during the fit for all paths of a data set.

2.5.4 Incoherent Inelastic Neutron Scattering - IINS

Incoherent inelastic neutron scattering (IINS) provides the advantages of deep penetration of neutrons in most samples and extreme sensitivity to hydrogen. IINS is suited very well to study the librations of water in synthetic compounds and minerals distinguishing well between bulk water, water in crystallographic positions, water on surfaces and occluded water. The key advantage of IINS is that the phonon density of states (PDOS) can be calculated qualitatively as well as quantitatively from the data gathered.

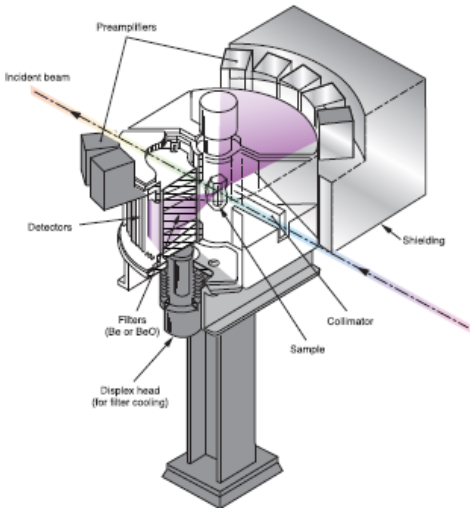

Figure 2.12: Setup of the Filter Difference Spectrometer (FDS) of the LANSCE, Lujan Center.[79]

IINS spectra were collected on the Filter Difference Spectrometer (FDS) at the LANSCE, Manuel Lujan, Jr. Center at Los Alamos National Laboratory, Los Alamos, New Mexico, USA. FDS uses the time-of-flight method to determine initial neutron energy and cooled Be filters to constrain the final energy of the scattered neutrons to 5.22 meV. Spectra obtained with FDS have a range of 40 to 4000 cm^{-1} with resolution varying from 2 to 4 %.

Sample Preparation

IINS samples were sealed in aluminum sample holders under He and cooled to 15 K by a closed cycle He cryostat during measurements to reduce the thermal broadening of the vibrational bands. The background contributions of FDS and the sample holder were accounted for by subtracting the spectrum of a vanadium rod in an identical aluminum sample holder from the sample spectrum.

2.6 ICP-MS

Inductive coupled plasma mass spectrometry, ICP-MS, is a highly sensitive method for the quantitative analysis of elements and even isotopes. The liquid sample is fed through a thin quartz-capillary around which a high-frequency field is applied by magnetic induction. Around the quartz tubing is a multi-walled system of metal tubes which feed the carrying gas and the plasmagas. For both purposes Ar is employed. This setup comprises the plasma tip. The high-frequency coil ionizes Ar, which in turn ionizes the sample. During the ionization process, the temperature in the center of the plasmatip can reach 6000 – 8000 K.[80] The ionized sample is then carried through a quadrupol mass-spectrometer, where the ions are deflected by the magnet field according to their *m/z - ratio* and detected. ICP-MS operates with very dilute samples with the concentration of the investigated isotope is in the ppb (parts per billion) range. This way, even trace-elements can be qualitatively and quantitatively measured.

Sample Preparation

All ICP-MS samples were prepared by dissolving an aliquot of the initial sample in 1 % HNO_3. Samples were measured by Fabian Sadowski at the IEK-6 in Jülich and by Aline Ritter at the HZDR.

Chapter 3

Experimental section

3.1 Investigations in the System $USiO_4$–$ThSiO_4$

3.1.1 Previous studies

Uranium silicate, coffinite, was first discovered in 1954 by Stieff, Stern, and Sherwood[14;81] in numerous ore deposits. It is one of the two most abundant U^{4+} containing phases, the other being UO_2. Large interest in $USiO_4$ results from its potentially important role in a geologic repository for nuclear waste, specifically regarding the interactions of nuclear waste with the environment such as the pore water. It is supposed that under reducing conditions UO_2 in contact with silica-rich groundwater ($10^{-4}\,{}^{\mathrm{mol}}/_{\mathrm{L}}$) reacts to coffinite (Langmuir's criterion).[19] As spent nuclear fuel (SNF) consists to > 90 % of UO_2, coffinite needs to be taken into account in the safety assessment as a secondary phase. It is therefore necessary to gather reliable and well established thermodynamic data on this substance. The structure of $USiO_4$ is tetragonal with space group symmetry $I\,4_1/amd$ and Z = 4.

It is an orthosilicate isostructural to zircon ($ZrSiO_4$) and thorite ($ThSiO_4$). Alternating, chains of edge-sharing SiO_4-tetrahedra and UO_8 (or ThO_8/ ZrO_8) triangular dodecahedra run parallel to the c axis. The UO_8-polyhedra however is slightly distorted, as the equatorial U-O-bonds are longer than those in axial position. While coffinite has been studied extensively, many investigations rely on the use of natural samples.[27;81] However these natural samples are often metamict [†] and associated with uraninite (UO_2), thorianite (ThO_2), rare earth elements, arsenic, selenide, and organic matter. These significant amounts of impurities has hindered the accurate determination of physical properties. Therefore, a significant effort has been undertaken to synthesize coffinite. A first successful experiment was reported in 1956[83], while a more recent synthesis has been reported by Pointeau et al.[25] Because the presence of the ν(OH)–stretching vibration

[†] Metamictization means, that the crystal lattice has been destroyed over time. This happens when α-emitters are present. The high-energy and highly charged recoil nucleus, displaces the atoms from their position in the lattice in large displacement cascades. As a result, the material is in a glass -like state, where only short range order exists.[82]

can be detected in the absorption infrared-spectra the molecular formula $U(SiO_4)_{(1-x)}(OH)_{4x}$ is sometimes assigned. The cavities in the zircon structure are large enough to accommodate water molecules and the substitution of the SiO_4^{4-}-group by OH^--groups is known to happen in many silicates.[14;68] However, the actual presence of bonded water or hydroxyl-groups could not be confirmed by DSC-TG or simply from weight loss upon heating. In thorite these substitutions have been confirmed and an influence of the substitution on the lattice parameters has been found.[84]

Whereas $ThSiO_4$ can easily be synthesized in the thorite[85] as well as in the huttonite[86] modification, synthesis of pure coffinite, $USiO_4$ proves to remain rather challenging. By applying the original hydrothermal procedure developed by Hoekstra and Fuchs[83] samples often turn out to contain the oxide UO_2 and be of rather poor crystallinity.[85;25] The data provided[87] shows that the synthesis only takes place in a range between pH = 8 and 10.5. The temperature and pressure-range are rather narrow and a carbonate buffer improves the reaction. For the last decades attempts to obtain synthetic $USiO_4$ by other methods (solid–state,[88;89] electrochemical[90]) have failed. The possibility of solid solutions between $USiO_4$ and $ThSiO_4$ was already predicted by Goldschmidt[91] and first synthesis were made by Fuchs and Gebert.[92] From this very limited data it seems that solubility follows Vegard's Law and complete miscibility between the two phases should be possible. Förster[93] has investigated natural uranothorites and found a maximum solubility of 30 mol% Th in coffinite and max. 36 mol% U in thorite. In this study the influence of carbonate, CO_2^{-3} and fluoride, F^- and their role during genesis of U/Th silicates is also discussed. DFT calculations employing modeling with VASP followed by Monte-Carlo simulation conducted by Ferriss et al.[94] suggest that the maximum amount of Th in $USiO_4$ or U in $ThSiO_4$ should not exceed 12 mol% at 500 K and there should be a complete miscibility gap at 1000 K. Costin et al.[95] on the other hand assigned the problems associated to the synthesis of pure coffinite to kinetics and studied the synthesis behavior of the solid solutions. While they were able to synthesize $U_xTh_{(1-x)}SiO_4$ solutions up to x = 0.61, the uranium rich products were associated with an oxide phase, $U_yTh_{(1-y)}O_2$.

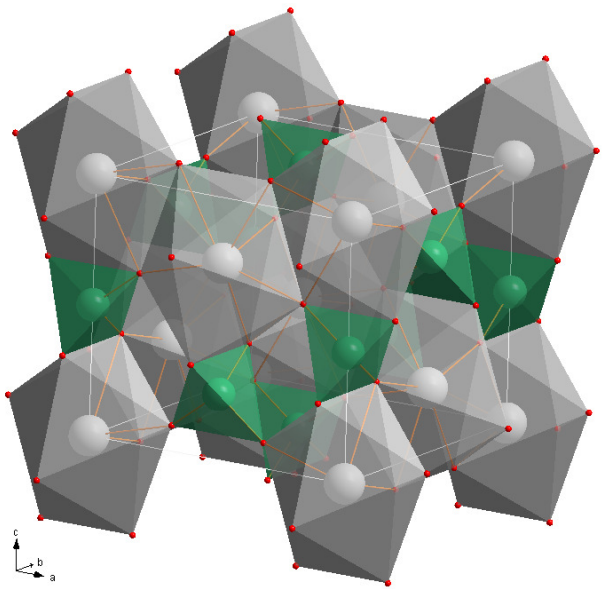

Figure 3.1: Unit cell with the coordination polyhedra of coffinite; grey U–, green Si–atoms and coordination polyhedra, red O–atoms and coordination polyhedra.

Model calculations including actinides are not as simple to perform due to the large number of electrons, f-orbital hybridization, and relativistic effects. On the other hand, pressure increases can be included rather simply in DFT calculations. The data gathered in high-pressure investigations can be compared to ab-initio calculations and help to benchmark actual models. This allows for improvements towards more realistic models. Very little is known about the properties of uranium silicate under elevated pressures. A comparative study by Liu from 1982[96] suggests amorphization of $USiO_4$ above 10 GPa, while current investigations from Zhang et al.[97] state that coffinite is stable up to at least 14 GPa. It then, similar to zircon, transforms into a scheelite-type structure before undergoing amorphization at 45 GPa. While high pressures are not of relevance in repository scenarios on the macroscopic scale, they can exist locally. During α-decay the recoil nucleus deposits it's energy through a collision cascade in which the situation is similar to that under high-temperature and high-pressure.[98] High-pressure and/or high-temperature phases therefore, might exist to a certain extent under repository conditions. Even while they will exist only in very limited spaces they could either act as a stabilizing component or as a hazard in nuclear waste. The study of the behavior of coffinite under elevated pressures furthermore allows insight on general phase stability.

3.1.2 Synthesis

Thorite

Thorium stock solutions (0.1 M and 0.5 M) were prepared by dissolving the desired amount of $Th(NO_3)_4 \cdot 5H_2O$ in millipore H_2O. A 0.1 M silica solution was prepared by dissolving $Na_2SiO_3 \cdot 9H_2O$ demineralized water. Carbonate buffer solution was prepared by adding 0.5 M $NaHCO_3$ to 1 L of millipore water and dissolving it. All chemicals were analytical grade and either from Merck KGaA Darmstadt or Sigma-Aldrich. Thorite samples, $ThSiO_4$, were prepared by adding the thorium stock solution to the of silica solution. The pH is then adjusted to $\sim$ 8 and the white precipitate centrifuged. The clear supernatant is pipetted off and the remaining green slurry mixed with $NaHCO_3$ buffer solution. This mixture is transferred into an autoclave equipped with a Teflon inlet and hydrothermally treated. The used autoclave is shown in figure 3.3b. After cooling the product is washed several times with water and dried at 200 °C.

Coffinite and $U_xTh_{(1-x)}SiO_4$ Solid Solutions

All experimental steps are performed in an anoxic glovebox under N_2 atmosphere (O_2 below 10 ppm). The UCl_4 stock solution was prepared by dissolution of uranium metal turnings in 6 M HCl. Before dissolution the uranium turnings were washed in EtOH abs. to remove remains of oil from cutting. The oxide layer is removed by washing the turnings with 0.1 M HNO_3. As soon as the hydrogen evaporation has seized the obtained solution is filtered to remove any possibly remaining solids. The uranium concentration is then determined by ICP-MS and the

oxidation state is confirmed through UV-VIS. $ThCl_4$ solution was prepared by weighing in the desired amount of $Th(NO_3)_4 \cdot 5H_2O$ and dissolving it in 6 M HCl. Afterwards several steps of dissolution and evaporation are performed to boil out the nitrate as nitreous gases. Ultimately, the concentration of thorium in solution is measured by ICP-MS. The A 0.1 M silica solution was prepared by dissolving $Na_2SiO_3 \cdot 9H_2O$ in carbonate free demineralized water. $Na_2SiO_3 \cdot 9H_2O$ and $NaHCO_3$ were analytical grade from Merck KGaA Darmstadt.
UCl_4 (s) was self prepared from amorphous UO_3 by reaction with C_3Cl_6 under reflux. A three neck bottle, equipped with circulation cooler, thermometer, and flushed by N_2 is filled with 25 mL (0.177 M) C_3Cl_6 and 5 g (0.017 M) UO_3. The mixture is continuously stirred and heated to 80 °C. After some time the suspension suddenly turned into a dark-red solution and temperature increases, indicating the start of the reaction. The heat is removed and cooling is applied so that the temperature does not go over 150 °C. After this first strongly exothermic reaction has stopped, the solution is again heated under reflux for at least 6 hrs. Dark green precipitate occurs, which is filtered under protective atmosphere and washed with CCl_4.[99] UF_4 (s) was of unknown origin and a gift of RWTH Aachen.

Co-Precipitation route Synthetic coffinite, $USiO_4$, was prepared by adding UCl_4 solution to an excess amount of silica solution. For two samples (C 1-1 and C 1-6) solid UCl_4 or UF_4 (D1-1 and D1-6) respectively was used and directly added to silica solution. The pH is then adjusted to $\sim$ 8 and the greenish precipitate centrifuged. The clear supernatant is pipetted off and the remaining green slurry mixed with $NaHCO_3$ buffer. This mixture is transferred into a glass ampule and sealed. A picture of these sealed ampules can be seen in figure 3.2. The sealed ampules are hydrothermally treated at 250 °C for 7 d and cooled down to room temperature with a rate of 20 °C/d. After cooling the product is washed several times with water and dried. The solid solutions were prepared employing the same procedure, but using a mixture of the UCl_4 and $ThCl_4$ stock solutions in the desired stochiometry.

Carbonate route As before, UCl_4 solution is added to an excess amount of silica solution. The still highly acidic mixture is then rapidly overthrown to alkaline pH by adding $\sim$ 2.5 g of $NaHCO_3$ to the solution. After the gas evolution has seized the pH is adjusted to 7 – 8 by dropwise addition of 6 M HCl. The precipitate is further processed hydrothermally as described earlier.

Figure 3.2: Photograph of the sealed ampules prior to the synthesis.

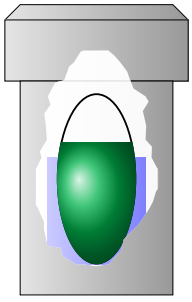

(a) Schematic drawing of the autoclave with the ampule, during hydrothermal treatment.

(b) Picture of one of the used steel autoclaves.

Figure 3.3: Photograph and schematic drawing of the autoclave used for the hydrothermal syntheses.

3.1.3 Thorite

The main focus of this work is the synthesis of coffinite, $USiO_4$. As this turned out to be rather challenging, the hydrothermal synthesis procedure and the parameters, which could significantly influence it, are first studied on the easier obtainable thorite, $ThSiO_4$. Especially, the influence of reaction time and temperature on the crystallinity of the product are investigated. Synthesis were conducted at 100 – 200 °C, over a duration of usually 3 – 7 days (few samples were treated longer) and with stock solutions of 0.1 and 0.5 M Th concetration. Besides this, the buffer solution also was varied exchanging the $NaHCO_3$-buffer for K_2CO_3-, $(NH_4)_2(CO_3)_2$-, and an 0.01 M $(NH_4)_2Mo_2O_7$-solution. Increase of the pH value after the reaction of the remaining liquid could be found. Depending on initial concentration $\sim$ 300 – 1300 mg of a fine white powder are obtained. A complete list of samples and reaction parameters can be found in table I on page ii of the appendix.

X-ray diffraction The XRD pattern shows the reflections expected for a zircon-type structure (space group $I\,4_1amd$). As the thorite samples were not synthesized using excess silica, no amorphous silica is present in the diffraction pattern. The lattice parameters are increased along a- and b-axis with a = b = $\sim$ 7.16 Å, while the c-axis is often shortened to c = $\sim$ 6.29 Å, compared to those of flux grown thorite (a = b = 7.13 Å, c = 6.31 Å [100]). This phenomena has been reported by several authors,[84;85] supposedly substitution of SiO_4^{4-}-groups by OH^--groups plays a major role. This also leads to the modification of the sum formula to $Th(SiO_4)_{(1-x)}(OH)_{4x}$. In figure 3.4 the lattice parameter lengths are set in relation to reaction time and temperature, as well as the concentration of the initial Th-stock solution. Samples hydrothermally treated at 100 °C did not show a good crystalline phase in the XRD pattern, of the batch processed at 125 °C only one sample established a good pattern. While there are individual observations made concerning the dependence to one of the synthesis parameters on one specific series, in the evaluation of the whole, no straight trend is observable. Concerning crystallinity, the samples processed at 200 °C proved to yield the best quality. By substituting the $NaHCO_3$-buffer for a K_2CO_3- or $(NH_4)_2(CO_3)_2$-buffer, no measurable change on lattice parameters or crystallinity appears. However, when completely discarding the buffer, the precipitation of ThO_2 tends to appear, this also happens, when the pH is set higher than 9. Using a 0.01 M $(NH_4)_2Mo_2O_7$-solution as buffer, however, leads to precipitation of an additional scheelite-type phase (cf. figure 3.5. Scheelite-type materials $(A,Ln)MoO_4$, with A = NH_4, Na, K, Cs and Ln = La – Lu, are known to exist for most of the lanthanides. As the early actinides, especially as Th^{4+}, act very similar to the lanthanides [101] this result is in fact not too surprising, yet it directly excluded the use of a molybdate buffer for the later coffinite synthesis. Formation of the scheelite-type phase seamed to be favored by Th at 150 °C as according to the refinement only 25.2 wt.% of $ThSiO_4$ are found in the sample. The sample processed at 200 °C, did not feature such a good quality, that Rietveld refinement was feasible. As this route was no of too high interest, and hence not further pursued

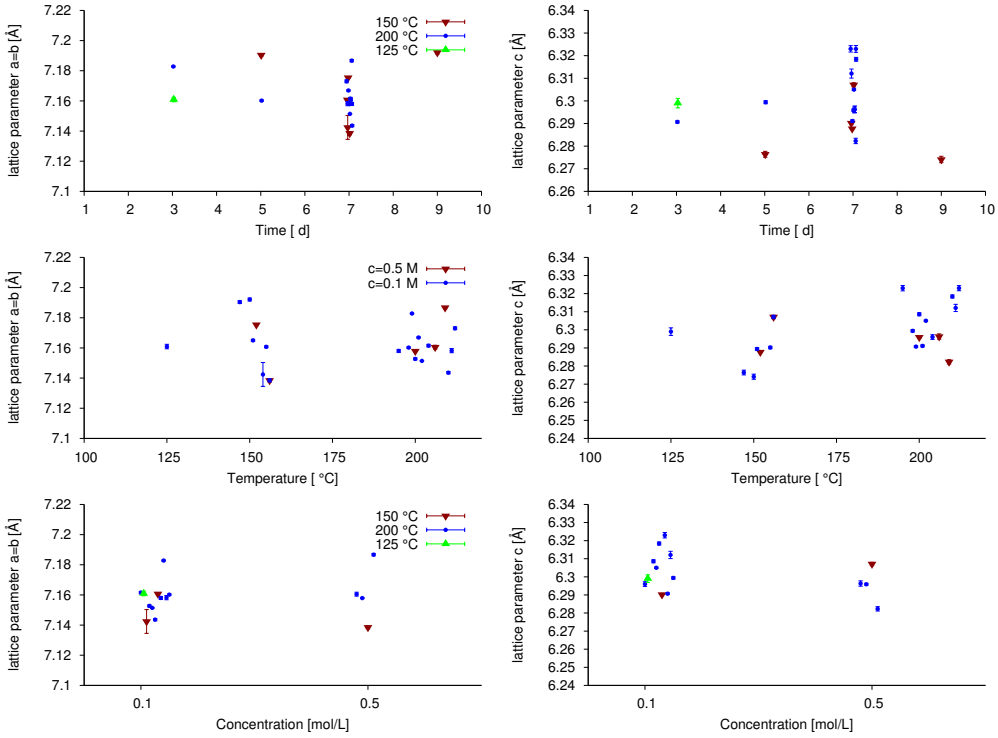

Figure 3.4: Dependence of the lattice parameters a=b, and c to reaction time, temperature and concetration of the stock solution.

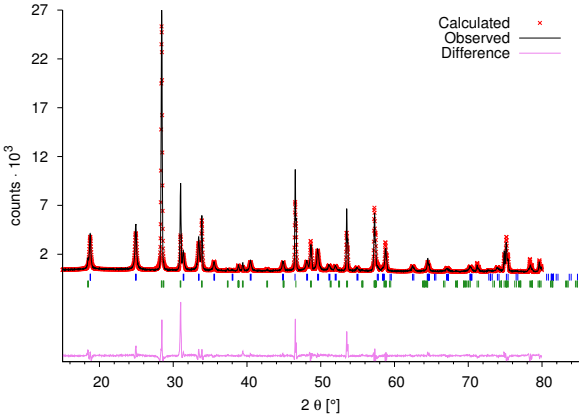

Figure 3.5: Refinement of the X-ray diffraction pattern of the thorite sample, processed with $(NH_4)_2Mo_2O_7$ buffer. Observed (red), calculated (red) and difference (purple) curve; reflections of $ThSiO_4$ (blue) and scheelite-type phase (green) shown.

no further quantitative conclusions can be drawn.

IR-spectroscopy The IR spectra of the synthetic thorite samples (one example shown in figure 3.6) were collected and compared to that of natural thorite, seen in figure 3.7. The band positions and assignment are listed in table 3.1. Generally, the different syntheses parameters

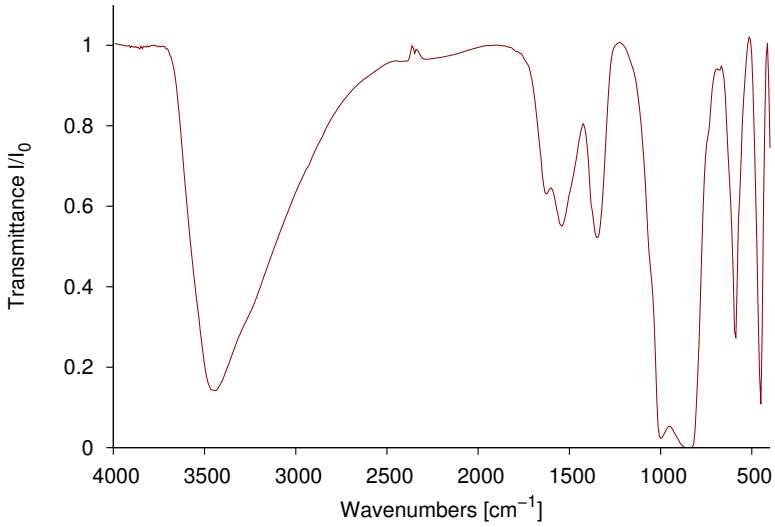

Figure 3.6: IR spectrum of synthtic thorite, $ThSiO_4$.

do not show any influence on the IR spectra, supposing that the short range order does not depend on the preparation route. In all spectra the bending and stretching modes of water can be observed. The strongest signals, however derive from the modes of the SiO_4^{4-}-tetrahedron at 600 – 1000 cm^{-1}. Indeed, the synthesized thorite still contains a lot water, through DSC-TG measurements (cf. figure VI) it could be established that $\sim$ 5 wt.% water are still present in the samples, even after drying at 200 °C for 48 hrs. The A_{2u} (ν_4) mode of the silica tetrahedron is hardly notable in the natural sample, it is barely distinguishable as very weak shoulder.

Additionally to the strong δ(HOH) bending mode, two additional modes at $\sim$ 1530 cm^{-1} and $\sim$ 1360 cm^{-1} are present. These modes cannot be attributed to vibrations of the SiO_4^{4-}-tetrahedron, neither are they lattice modes, as those should only appear in the lower wavenumber region.[41] Through the observations made concerning the lattice parameters and while the phenomena of substitution of SiO_4^{4-}- for OH^--groups is known for thorite, it is reasonable to assume, that these might be bending and stretching vibrations of type δ(Th-OH) and δ(Th-O-Th). According to Wang and Andrews[102] however, those modes appear more in the region around 600 cm^{-1}. Because of the selection rules no other modes are expected from the SiO_4^{4-}-tetrahedron and to the best of my knowledge have not been observed in synthetic thorite so

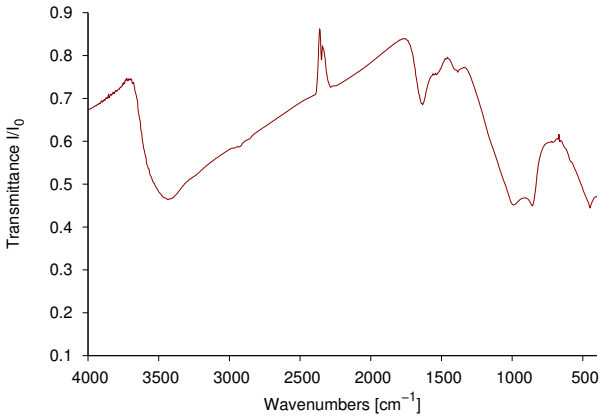

(a) IR spectrum of natural thorite.

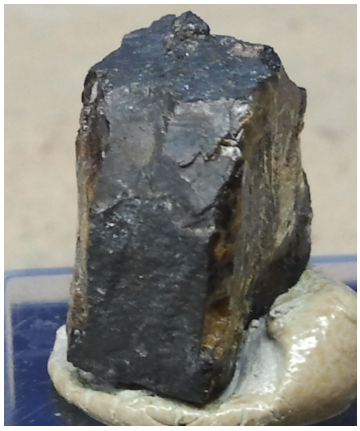

(b) Natural Thorite sample from Ösbe, Norway.

Figure 3.7: Natural thorite sample (b) and corresponding IR spectrum (a). IR spectrum collected on Bruker *Equinox 55* TGA-IR, natural thorite sample kindly provided by the Radioactivity Control (S) department.

far.[103] These vibrations consistently appear and are also present in the natural sample. If they are not associated to δ(Th-OH) or any of the SiO_4^{4-}-modes, they might result from ν(H-O-Si)- and δ(H-O-Si)-vibrations. It is, however, also possible, that these are also δ(HOH) but resulting from water in different position in the structure.

Table 3.1: Band positions in wavenumbers [cm^{-1}] in the IR spectra of the $ThSiO_4$ thorite samples.

sample name	ν(OH)	δ(HOH)	δ(HOH)?	δ(HOH)?	A_{2u} (ν_3)	E_u (ν_3)	A_{2u} (ν_4)	E_u (ν_4)
nat. sample	3427	1636	1536	1397	994	861	592 vw s	455
SL-Th-17	3439	1629	1548+1471	1355	1004	842	590	450
DG-Th-1	3440	1625	1527	1354	997	832	588	453
DG-Th-2	3435	1627	1540	1357	1005	839	588	450
DG-Th-3	3446	1626	1538	1359	1002	841	589	452
DG-Th-4	3440	1625	1529	1357	996	846	587	453
DG-Th-5	3443	1630	1537	1356	1002	833	590	452
DG-Th-6	3441	1630	1537	1353	995	834	587	454
DG-Th-8	3441	1629	1541	1351	1000	846	591	453
DG-Th-9	3441	1626	1542	1349	999	840	590	454
DG-Th-12	3434	1626	1541	1350	1001	841	589	452
DG-Th-14	3439	1631	1542	1351	1002	843	591	451
DG-Th-15	3430	1632	1549	1345	1002	830	587	448
DG-Th-16	3435	1627	1540	1351	1005	830	590	451
DG-Th-17	3431	1632	1552	1349	996	851	589	448

Morphology studies All obtained thorite samples were investigated concerning their morphology with SEM. While samples processed at temperatures below 125 °C already only showed the presence of amorphous material in the XRD pattern, very few particles could be observed in the samples synthesized below 150 °C in the SEM. Mostly glassy bigger grained material is found. However, other synthesis attempts yielded homogeneous lentil shaped particles as shown in figure 3.8. Particle sizes were measured on at least 20 specimen (usually even 30; 10 for the 100 °C samples) and an overview with dependencies to reaction time, reaction temperature, and initial stock solution concentration is given in figure 3.9. While a certain dependence on tem-

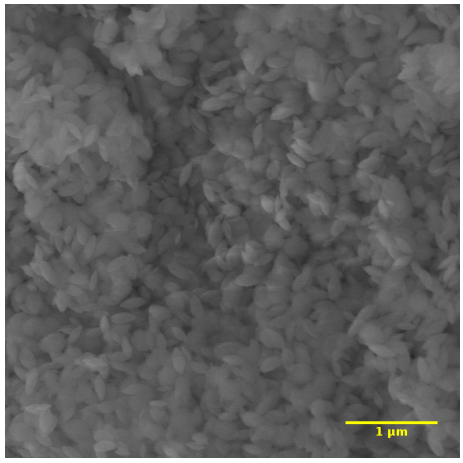

Figure 3.8: Exemplary SEM micrograph of one thorite sample.

perature and reaction time can be observed, all particle sizes are in the range of 150 – 375 nm. Standard derivatives are however, lower for the samples processed at 200 °C. (The lower derivatives for the 100 and 125 °C samples is due to the fact, that here less particles were found for measurement.) In general, the particle size remains rather stable. It appears though, that other influences, like the rate at which the autoclav is cooled down, also contribute to the particle size distribution.

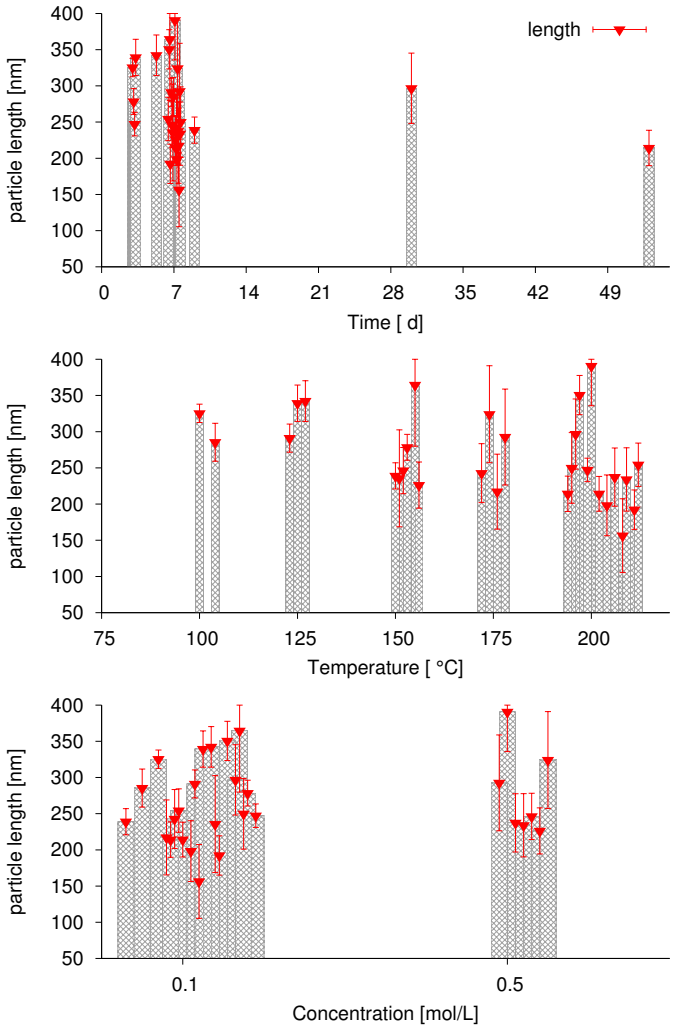

Figure 3.9: Particle sizes from SEM analysis of the Thorite samples. Influence of the synthesis parameters time, temperature and concentration of the stock solution shown. Data point staggered represented for better visibility.

Also syntheses employing the molybdate buffer solution were studied with SEM. The appearing scheelite phase, already determined by XRD, can easily be visually distinguished in the synthesis run at 150 °C as large particles of cubic shape with $\sim$ 10 μm edge length (cf. figure 3.10b). On closer investigation, also smaller particles with the familiar lentil shape, sometimes laying on the larger particles, are found. Further EDS analysis determines, that the smaller particles are solely thorite, while the large particles also contain Na and Mo. The same synthesis at 200 °C

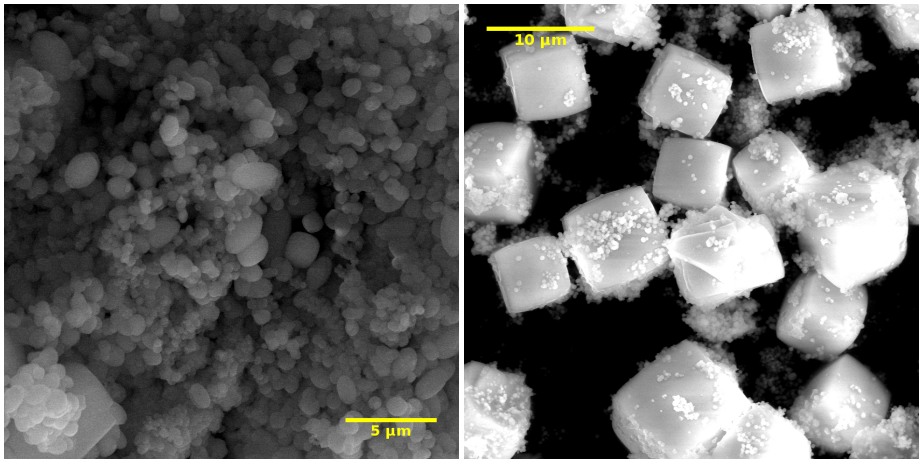

(a) SEM micrograph of the thorite sample, processed with the molybdate buffer with T = 200 °C.

(b) SEM micrograph of the thorite sample, processed with the molybdate buffer with T = 150 °C.

Figure 3.10: SEM micrographs of the thorite samples, processed with the molybdate buffer. The additional Th-containing scheelite phase can be distinguished visually as large particles of cubic shape.

produced particles of a round shape in the range of 3–5 μm in diameter. From the EDS spectrum, it could be confirmed, that all particles contained Na and Mo from the buffer solution.

3.1.4 Coffinite and Uranothorite

Diffraction Studies

Coffinite The influence of excess silica on the reaction

$$U^{4+}(aq) + SiO_4^{4-}(aq) \rightleftharpoons USiO_4(s) \tag{3.1}$$

during the initial precipitation step was qualitatively studied. X-ray diffraction pattern of the products obtained at different U/Si - ratios is shown in figure 3.11. It is apparent, that samples processed with identical or close to equimolar U/Si - ratio always yield UO_2 as accompanying or main product under the given parameters. The tendency observed in the experiments cor-

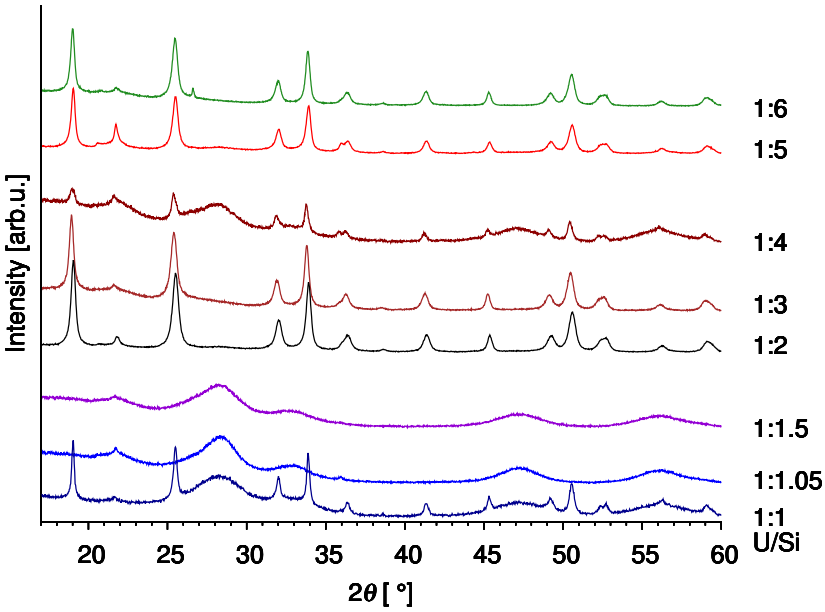

Figure 3.11: Influence of the silica amount on the coffinite synthesis. From bottom to top, the U/Si-ratio increases.

responds to one of the oldest principles in chemistry, the Equilibrium Law - commonly called Le Chatelier's Principle. By applying more force through excess silica $USiO_4$ will form more readily than at equimolar ratio, a detailed list of experiments performed and the yielded products is given in the appendix in table 5.1.1. What can be observed on the one hand is that even at equimolar ratio it is possible to synthesize coffinite, however with a serious amount of UO_2 attached to it. On the other hand the use of excess silica per se does not completely rule out the formation of the oxide phase. From the experiences made in this study an U/Si -ratio of 1:6 always leads to formation of the silicate phase and suppresses the precipitation of the oxide

phase. However, also leaving a significant amount of gelatinous SiO_2 or α-quartz attached to the product.

The synthesis via the carbonate route was not as successful as the co-precipitation route. One of the biggest problems was breaking of the glass ampules during hydrothermal treatment. The samples recovered from intact ampules however led to a similar observation like the one from the standard synthesis route, i.e. an excess of silica promotes the silicate formation. Additionally, in two synthesis a yet undetermined crystalline phase, which also contains a high amount of sodium in it's structure, has been discovered (cf. figure 3.12). A similar diffraction pattern, but with slightly shifted reflection positions, has also been obtained for an uranothorite sample. During the present no structure solution for this material could be found. Both samples are gray – green in color (the thorium containing one is much lighter though) and judging from the XANES spectra only U(IV) is present. As seen in figure 3.12b from SEM investigation it appears that the material crystallizes as long rods, which agglomerate and form four-fold star like structures. EDS analysis yields a composition of U = 8.3 at.%, Na = 20.4 at.%, and Si = 71.2 at.%.

The experiments using solid UCl_4 led to similar results as those with UCl_4 solution. On the other hand those, which used the fluoride, UF_4, increasingly led to UO_2 as a product. In this synthesis attempt the slurry already was inhomogenous during the co-precipitation step. This result is not too surprising, as inorganic fluorides (with exception of the alkalifluorides) in general are rather stable. Even if reaction or simply hydrolysis takes place, in a silica-rich environment the F^- will in part react to SiF_4 or H_2SiF_6. This will reduce the amount Si available, even if only slightly, and hence have influence on the equilibrium of the reaction. After first synthesis results showed that this synthesis route employing fluorides was not as feasible it was no longer pursued.

After qualitative investigation concerning phase purity Rietveld refinement of the diffraction pattern was carried out. The region between 2θ = 20.45° - 22.55°, where a broad peak resulting from glassy silica dominates the pattern, was excluded from the refinement for better agreement between experimental and calculated data.

In table 3.2 the lattice parameters and oxygen bond legths of the coffinite samples characterized during this work are compared to those of synthetic coffinite reported in literature. The values differ slightly from those reported by Pointeau et al.[25] but otherwise are in very good agreement for all prepared samples. From the earlier values of Fuchs and Gebert a Si-O bond length of 1.58 Å can be calculated, which would be extraordinary short for a silicate. In α-SiO_2 the Si-O distances are 1.61 Å and bond lengths of the actinide and rare earth silicates are typically in the range of 1.61 – 1.80 Å.[106;107;108] Usually, lengths below 1.61 Å in tetrahedral conformation are common only to the silicon halides.[101] Especially, when taking into account that U-O bonds ought to establish significant parts of covalent bonding behavior, a distance larger than 1.61 Å seems more probable. Yet the reliable determination of the oxygen-position next to

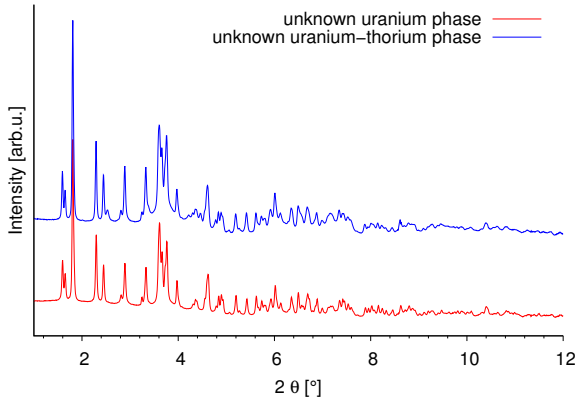

(a) Synchrotron X-ray powder diffraction pattern of the uncharacterized phases obtained through the carbonate route.

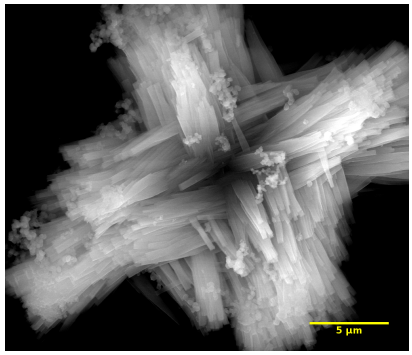

(b) SEM micrograph of the unknown uranium phase obtained through the carbonate route.

Figure 3.12: Synchrotron powder diffraction pattern and SEM micrograph of the unknown phases obtained through the carbonate route.

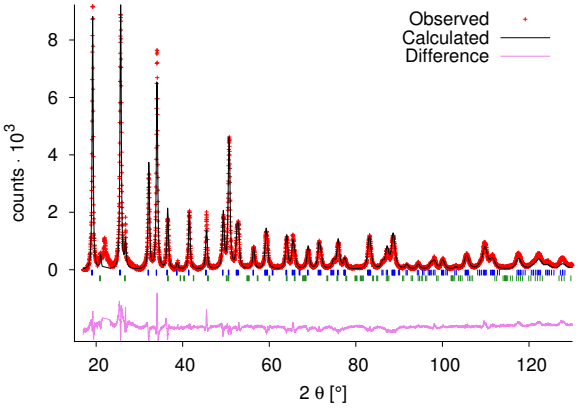

Figure 3.13: Rietveld refinement of one $USiO_4$ sample (C1-6). Calculated pattern (red), observed pattern (black) and difference curve (purple). Positions of the $USiO_4$ (blue) and α-SiO_2 phase (green) are marked; Rp = 7.89 %, wRp = 8.28 %.

such a heavy element as uranium is nearly impossible from laboratory X-ray diffraction. It has to be noted, hat most authors therefore don't even bother to undertake these parameters a diligent

Table 3.2: Comparison between the crystallographic data on coffinite obtained by XRD in this study and reported in literature. Data from Hoekstra & Fuchs and Fuchs & Gebert were determined via Weissenberg photographs.

author		Parameter [Å]		bond type [Å]			
		a = b	c	U-O_1	U-O_2	U-U_1	Si-O_1
Hoekstra & Fuchs[83†]		6.991	6.320	-	-	-	-
Fuchs & Gebert[87]		6.995(4)	6.263(5)	2.3194	2.5117	3.8320	1.582
Keller[104]		6.992(4)	6.262(4)	-	-	-	-
Mulak[105]		6.986(2)	6.268(2)	-	-	-	-
Pointeau et al.[25]		7.0135(4)	6.2669(6)	2.36	2.38	-	-
Reynolds[26]		6.9979(2)	6.2720(2)	-	-	-	-
this study	A 1-2	6.9864(3)	6.2606(3)	2.301(6)	2.477(8)	3.826(1)	1.607(5)
	A 1-5	6.9825(4)	6.2557(4)	2.300(1)	2.434(9)	3.828(1)	1.638(8)
	C 1-6	6.9831(3)	6.2631(4)	2.347(5)	2.445(6)	3.827(1)	1.577(4)

analysis. The same problems were observed for $ThSiO_4$, where oxygen positions were uncertain until Taylor and Ewing successfully determined them from single crystal measurements. The Si-O distance then was found to be 1.63 Å. Data on the atomic positions of oxygen is rather scarce, an overview for $USiO_4$ and $ThSiO_4$ is given in table 3.3. Values for $ThSiO_4$ were determined from Rietveld refinement (see figure 3.14) and are in fair agreement with the single crystal data.

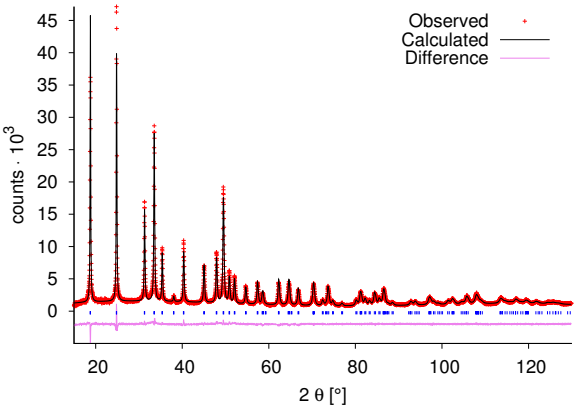

Figure 3.14: Rietveld refinement of the $ThSiO_4$ sample (DG-Th-09). Calculated pattern (red), observed pattern (black) and difference curve (purple). Positions of the $ThSiO_4$ (blue) reflections are marked; Rp = 6.73 %, wRp = 8.74 %.

[†]In the original articles by Hoekstra & Fuchs[83] and Fuchs & Gebert[87] the lattice parameters are given in KX units, not Å. Often the mistake is made to not convert these factors or mix up converted an non converted values. Even in the ICSD databank the kX values are erroneously listed as Å[87] where a = b = 6.981 kX and c = 6.250 kX. Using the conversion factor of 1 kX = 1.00202 Å as reported in the original article by Bragg[109;110] the kX values have been converted in this table. It also has to be noted that Hoekstra & Fuchs[83] in a following article[92] correct their original values to a = b = 6.995(4) Åand c = 6.263(5) Å, i.e. the values then referenced also in Fuchs & Gebert[87].

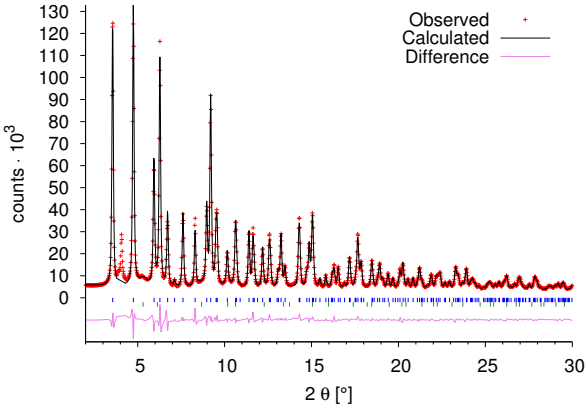

Figure 3.15: Rietveld refinement of the Synchrotron measurement conducted at the ECB (P02.2, λ = 0.2895 Å beam size 1.6 μm x 1.6 μm). Calculated pattern (red), observed pattern (black) and difference curve (purple). Positions of the $USiO_4$ (blue) and UO_2 phase (green) are marked; Rp = 3.90 %, wRp = 5.26 %.

Coffinite sample A 1-2 could be studied with synchrotron powder diffraction and the obtained pattern was treated by Rietveld refinement, a plot of the refinement is shown in figure 3.15. Due to the much higher intensity of the beam, even minor impurities become observable. In this particular case a small reflection for UO_2 becomes evident at 2θ = 3.75°. The refinement shows that ca. 4.4 wt.% of UO_2 (taking into account only the uranium phases) are still present in the sample, which could not be detected with the usual laboratory X-ray. It was

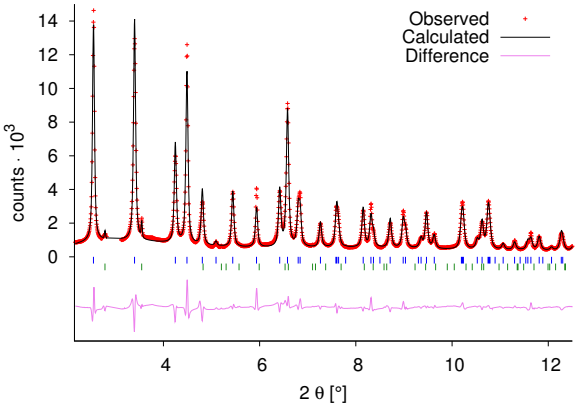

Figure 3.16: Rietveld refinement of the Synchrotron measurement conducted at the HRPD (λ = 0.2071 Å). Calculated pattern (red), observed pattern (black) and difference curve (purple). Positions of the $USiO_4$ (blue) and α-SiO_2 phase (green) are marked; the angular range between 2.82 – 3.12° where only glassy silica is present, was excluded from the fitting procedure Rp = 8.53 %, wRp = 6.81 %.

possible to study also coffinite sample C 1-6 with synchrotron powder diffraction. The obtained pattern was treated by Rietveld refinement, a plot of the refinement is shown in figure 3.16. No UO_2 impurities are observable this time, yet the amount of crystalline α-SiO_2 is can be estimated from the refinement that ca. 60(2) wt.% of α-SiO_2 present in the sample.

The oxygen positions for $USiO_4$ from these measurements are y = 0.069 and z = 0.208 and comparable to those reported by Fuchs and Gebert, y = 0.070(1) and z = 0.222(1) within the typical error limits. The resulting uranium-oxygen bond distances from this refinement are U-O_1 = 2.30(1) Å and U-O_2 = 2.44(1) Å, whereas the silicon-oxygen bond length is Si-O = 1.64(1) Å. This is comparable to the value found for $ThSiO_4$ by Taylor and Ewing and a more plausible value than the result obtained by Fuchs and Gebert.

Table 3.3: Overview of the crystallographic data on $USiO_4$ and $ThSiO_4$ obtained in this study and reported in literature.

$USiO_4$	Atomic positions		Bond distance [Å]		
	y	z	U-O_1	U-O_2	Si-O
Fuchs & Gebert	0.070(1)	0.222(1)	2.32(8)	2.52(9)	1.58(9)
Bose et al.*	0.076	0.212	-	-	-
A 1-2	0.0691(2)	0.2087(1)	2.298(1)	2.439(1)	1.64(1)
C 1-6	0.069(2)	0.207(2)	2.28(1)	2.44(1)	1.646(9)

$ThSiO_4$					
	y	z	Th-O_1	Th-O_2	Si-O
Fuchs & Gebert	0.084(1)	0.222(1)	2.46(8)	2.50(9)	1.55(9)
Sinha & Prasad	0.081	0.232	2.45	2.51	1.56
Taylor & Ewing	0.0732(1)	0.2104(2)	2.37(1)	2.47(1)	1.63(1)
Bose et al.*	0.079	0.215	-	-	1.627
this study	0.0706(8)	0.2092(8)	2.363(5)	2.467(6)	1.658(9)

* calculated values

While the intensity and highly monochromatic radiation supplied through synchrotron allow for a better resolution than laboratory X-ray, in this case the measurement was in part carried out on a beamline not dedicated to high resolution powder diffraction with a small beamsize and a regular resolution detector. To truly clarify oxygen positions either single crystal or at least high resolution synchrotron data should be used. Neutron diffraction would be even more suitable, if water/OH-groups in the crystal lattice can be excluded (this on the other hand requires an anhydrous synthesis route). Another possibility is to perform the synthesis with completely deuterated reagents.

$USiO_4$ could be synthesized as a pure phase from UCl_4 solution and from solid UCl_4 by hydrothermal synthesis. The precipitation of a second U(IV) phase could be suppressed by applying an excess amount of silica during the synthesis. This in turn leads to formation of glassy

silica and α-quartz. Synthesis attempts employing UF_4 as a reagent were not as successful, yet showed that formation of $USiO_4$ in principle is possible. The atomic positions of oxygen were determined from Rietveld refinement and compared to those known in literature for $ThSiO_4$ and $USiO_4$. Results hereof yield a Si-O bond length of 1.64(1) Å, that is supposedly closer to the true value than the data reported so far.

Solid Solutions By qualitative analysis of the X-ray diffraction pattern the synthesized $U_xTh_{(1-x)}SiO_4$ uranothorite solid solutions, regardless of composition, exhibit the expected pattern for spacegroup *I* 4_1*/amd*. While the presence of the dioxide, $U_yTh_{(1-y)}O_2$, can be excluded, amorphous silica, and in some samples α-SiO_2, are observed as additional phases. The lattice parameters of the uranothorite samples were determined by the Le Bail method and are listed in table 3.4. For the refinement the amorphous silica was treated as a virtual phase with symmetry *P* $m\bar{3}m$; in samples with x < 0.4 α-SiO_2 (space group *P* 3_2 2 1) was also included as a phase.

Table 3.4: Unit cell parameters, cell volume and reliability factors from Le Bail refinement of the $U_xTh_{(1-x)}SiO_4$ uranothorite solid solutions.

$\nu(U)_{XAS}$	a [Å]	c [Å]	V [Å^3]	R_{wp} [%]	R_p [%]
0.12(1)	7.1129(8)	6.3301(8)	321.39(5)	8.09	5.67
0.26(1)	7.0949(8)	6.3194(8)	318.10(5)	8.10	5.82
0.36(1)	7.0775(6)	6.3103(7)	316.09(3)	8.34	6.05
0.42(1)	7.0697(7)	6.3106(7)	315.41(5)	7.74	5.67
0.55(1)	7.0450(4)	6.2904(6)	312.20(4)	10.42	7.81
0.56(1)	7.0410(5)	6.2844(6)	311.81(4)	9.70	7.33
0.71(1)	7.0180(3)	6.2802(4)	309.32(2)	5.73	4.50
0.75(1)	7.0105(4)	6.2680(6)	308.06(2)	10.49	8.12
0.84(1)	7.0017(2)	6.2636(3)	307.07(1)	10.74	8.42
0.92(1)	6.9952(4)	6.2727(5)	306.94(3)	12.28	8.38

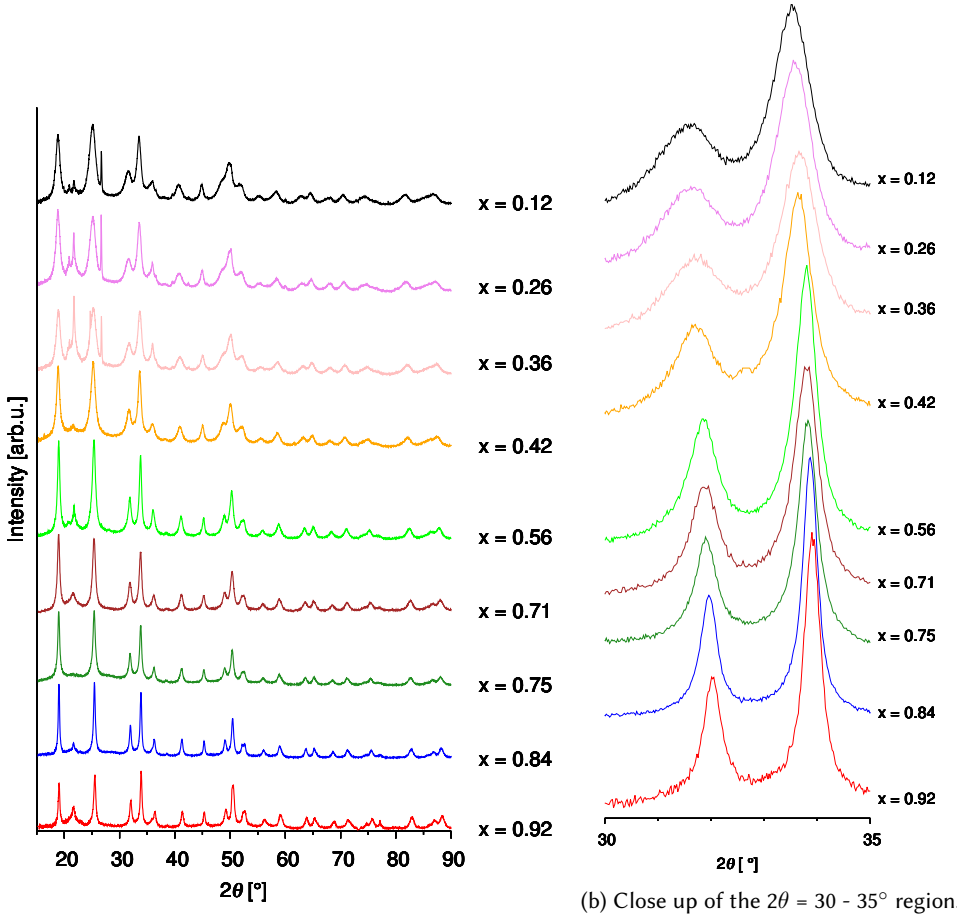

(a) Comparison of X-ray diffraction pattern with increasing x, range 2θ = 15 - 90° shown.

(b) Close up of the 2θ = 30 - 35° region. The shift of the (211) and (112) reflections is observable and the peak broadening becomes evident.

Figure 3.17: X-ray diffraction pattern of $U_xTh_{(1-x)}SiO_4$ solid solutions.

A small overview of the X-ray pattern is shown in figure 3.17. The unit cell of thorite, $ThSiO_4$ is, larger then the one of coffinite, $USiO_4$. As expected, reflections in the pattern move to slightly larger 2θ values with increasing uranium mole fraction x. While amorphous silica (a rather broad reflection at $2\theta \approx 21°$) is observable in all samples, especially phases with a $x < 0.4$ also show the presence of α-quartz. It appears that reflections additionally experience a significant broadening in the thorium rich phases. This effect can be a result of crystallite size (i.e. the length of the coherent scattering domains), internal stress and strain and stacking faults. Special interest is laid on the diffraction pattern considering splitting and additional reflections, as these could be signs of segregation into two separate silicate phases or superstructure phenomena. None of these however are observed. It is evident, that only a single pattern in each composition of the $U_xTh_{(1-x)}SiO_4$ solid solutions is present. It should be kept in mind though, if two $U_xTh_{(1-x)}SiO_4$ phases with very similar composition were present it might not be possible to separate the reflection profiles. Especially, when difference in lattice parameters is very small and reflection profiles are very similar (e.g. same size of the coherent scattering domains, similar strain on the structure), one broad peak would be observed instead of two "sharper" ones. Chances to detect such overlap with poor crystallinity of the sample in conventional laboratory XRD, is very low.[†] The possible deviation of the composition yet cannot be large for such a merging of reflection profiles. In principle it is possible to determine the quantity of α-SiO_2 in the mixture from a Rietveld refinement. It is also possible to determine the amount of an amorphous phase, when the sample is mixed with a certain amount of a standard with known amorphous content. In this case, however, the sample amounts were very low ($\leq$ 100 mg per synthesis). The quantity of α-SiO_2 was not determined, as the samples were afterwards needed for further investigations including calorimetric measurements. Especially for the calorimetric measurements it is not desirable to mix the samples with further material. It has to be noted, that even when applying the method described, only the total amorphous content is obtained. This means, any amorphous $USiO_4$ or $U_xTh_{(1-x)}SiO_4$ in the samples would be accounted for as amorphous SiO_2. With uranium as a heavy atom present in a mixed amorphous phase, this can also lead to significant errors.[111]

[†] Meanwhile HRPD synchrotron measurements on selected samples of the $U_xTh_{(1-x)}SiO_4$ solid solutions have been performed late January 2014 at P02.1 of the PETRA III facility (DESY). After preliminary data analysis no hint towards the formation of two separate phases could be observed.

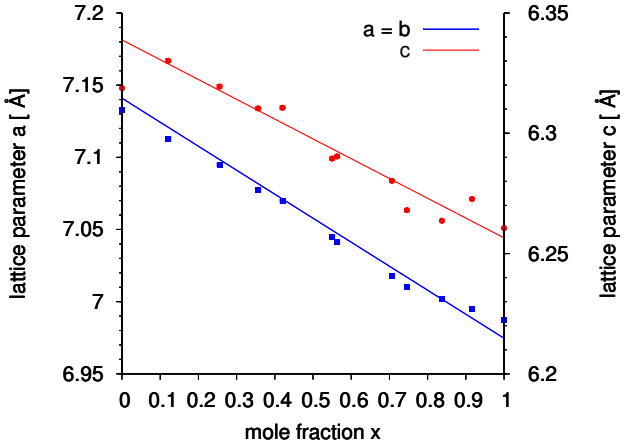

(a)

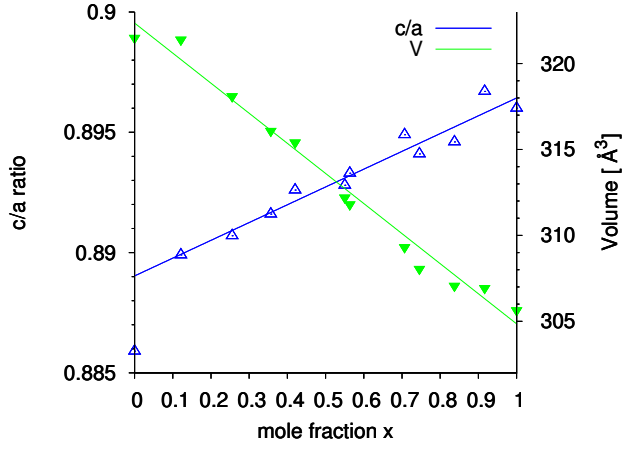

(b)

Figure 3.18: Overview of the change of the lattice parameters a = b and c vs. mole fraction x (a) and c/a-ratio and cell volume vs. mole fraction x (b).

Both lattice parameters as well as the cell volume decrease linearly with increasing uranium content (cf. figures 3.18a and 3.18b). The $USiO_4$ – $ThSiO_4$ – system hence follows Vegard's law. The latest works[28;95] reported mainly data on the thorium rich members of the system up to x = 0.61. In those works the desired silica phase was also accompanied by a mixed dioxide phase $U_yTh_{(1-y)}O_2$ above x = 0.24. Above x = 0.61 the dioxide phase dominated the samples. This observation initially led Costin to the assumption, that the involved kinetics hindered the precipitation of the uranium rich phases and that pure $USiO_4$, i.e. x = 1.00, could "probably only be synthesized with a reaction time of several weeks".[95]

The values from Costin et al.[95] and Szenknect et al.[28] are compared to the obtained data of

this study in table 3.5, the data is plotted together in figures 3.19b and 3.19a. The trends and differences of the data are clearly visible. It appears, that some fluctuations of the lattice parameters appear in the Th-rich members especially for the c lattice parameter. This behavior can be observed in the data of Costin et al.[95] and Szenknect et al.[28] as well.

Table 3.5: Comparison of lattice parameters a = b and c of the $U_xTh_{(1-x)}SiO_4$ solid solutions obtained in this study and reported in literature.

this work			Costin et al.[95]			Szenknect et al.[28]		
$x(U)_{XAS}$	a = b[Å]	c [Å]	$x(U)_{XRD}$	a = b[Å]	c [Å]	$x(U)_{XRD}$	a = b[Å]	c [Å]
0	7.1816(1)	6.2946(1)	0	7.148(1)	6.309(1)	0	7.148(1)	6.309(1)
0.12(1)	7.1129(8)	6.3301(8)	0.09(1)	7.119(1)	6.317(1)	0.09(1)	7.119(1)	6.317(1)
0.26(1)	7.0949(8)	6.3194(8)	0.17(1)	7.095(1)	6.320(1)	0.17(1)	7.095(1)	6.320(1)
0.36(1)	7.0775(6)	6.3103(7)	0.24(1)	7.085(2)	6.310(1)	0.24(1)	7.085(2)	6.310(1)
0.42(1)	7.0697(7)	6.3106(7)	0.33(2)	7.069(3)	6.305(1)	0.34(3)	7.069(3)	6.305(1)
0.55(1)	7.0450(4)	6.2904(6)	0.42(3)	7.056(1)	6.299(1)	0.45(1)	7.051(1)	6.303(1)
0.56(1)	7.0410(5)	6.2844(6)	0.43(4)	7.049(1)	6.296(1)	0.46(2)	7.048(1)	6.294(1)
0.71(1)	7.0180(3)	6.2802(4)	0.61(4)	7.028(1)	6.286(1)			
0.75(1)	7.0105(4)	6.2680(6)						
0.84(1)	7.0017(2)	6.2636(3)						
0.92(1)	6.9952(4)	6.2727(5)						
1	6.9842(2)	6.2606(2)						

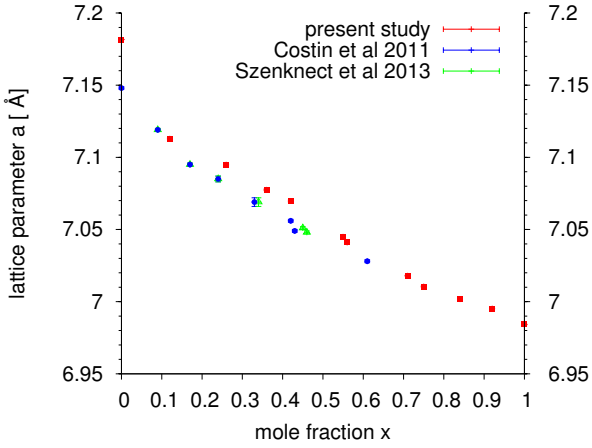

(a)

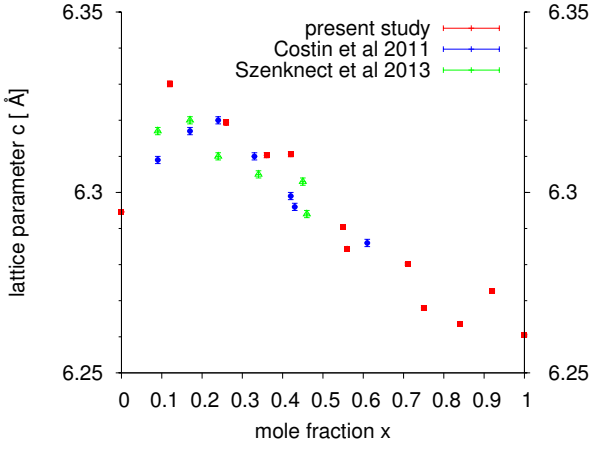

(b)

Figure 3.19: Comparison of the lattice parameters a = b (a) and c (b) observed in this study and from literature.[95;28]

In the present work the formation of the dioxide was suppressed through the use of silica in excess. In addition to the thorium rich (x $<$ 0.60) also the uranium rich members with x = 0.64, 0.71, 0.75, 0.84 and 0.92 could be synthesized. The crystallite size was calculated from the breadth of the reflections in the XRD pattern using the Williamson-Hall method.[112] Detailed data can be found in 5.1.2 and table IV on pages vi and viii in the appendix. One big advantage of the Williamson-Hall method is, that size of the coherent scattering domains as well as "strain" can be obtained from the Williamson-Hall plot. Both microstructural causes: small crystallite size and microstrain occur together in the reflection broadening. When plotting $cos\theta$ over $4sin\theta$ the size can be calculated from the intercept; the strain ϵ is derived from the slope. Crystallite sizes

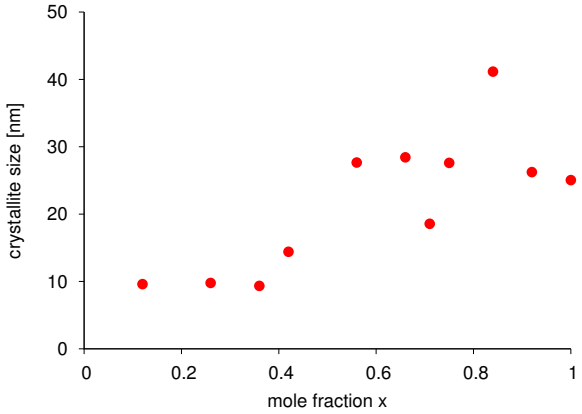

Figure 3.20: Crystallite size as derived from Williamson-Hall plot vs. mole fraction x for the solid solutions.

according to composition are shown in figure 3.20, a list of the derived strain is given in table 3.6. From the data shown in figure 3.20 it appears, that the crystallite sizes decrease from 30 nm with decreasing uranium content to at about 9 nm below x = 0.4. Below x = 0.4 the crystallite size nearly remains constant at about 9 nm. Costin et al. as well as Szenknect et al. both report that crystallite sizes are in between 10 – 30 nm with no further information on correlation to the composition. Looking at the contribution of strain to the peak broadening, it appears that even the pure end members of the $U_xTh_{(1-x)}SiO_4$ uranothorite solid solutions contain internal strain. The amount is comparable to that of nanoscale ZnO.[113] When increasing the Th content in the solid solutions to $\sim$ x = 0.3 the strain only increases little (x = 0.75 is assumed to be an exception). Above x = 0.4 strain increases strongly to $\epsilon \sim 5$, which is comparable to ZnO accompanying 10% Fe(III).[114] However, this is only a qualitative comparison and cannot be used for special interpretation.

Table 3.6: Distortion and stress induced strain ϵ of the $U_xTh_{(1-x)}SiO_4$ uranothorite solid solutions derived by the Williamson Hall method.

$\chi(U)_{XAS}$	ϵ [a.u. 10^{-3}]
0	1.562
0.12(1)	5.394
0.26(1)	4.311
0.36(1)	3.496
0.42(1)	5.992
0.55(1)	4.711
0.56(1)	6.060
0.60	6.048
0.71(1)	3.047
0.75(1)	6.026
0.84(1)	2.943
0.92(1)	2.127
1	2.041

reference	ϵ [a.u. 10^{-3}]
Fe doped ZnO [114]	
0.1Fe:ZnO	5.531
0.08Fe:ZnO	4.214
0.02Fe:ZnO	2.031
ZnO (50 nm) [113]	1.32

Determination of the Sample Composition A priori it cannot be presumed that the composition of the initial solution is the same in the precipitated sample. Therefore, it is necessary to determine the composition of the obtained samples experimentally. The mass photoabsorption cross section μ of a specific element (e.g. Th) is directly related to the corresponding edge step (ThL_3) in the EXAFS spectrum. From the edge step of the EXAFS spectra it is hence possible to determine the absolute amounts of nuclids in the sample and hence also the U/Th - ratio. Assuming homogeneity of the sample and bearing in mind, that phase purity has been determined by complementary methods, it is possible to determine the composition of the $U_xTh_{(1-x)}SiO_4$ solid solutions. That is, to determine x from the relations of the edge-step of the XANES region in the XAS spectra.

$$m = \frac{K \cdot A}{\Delta\mu} \tag{3.2}$$

A being the surface area of the sample pellet,
K the edge step
and $\Delta\mu$ the photon cross section [115],
with $\Delta\mu Th$ = 62.95 $\frac{cm^2}{g}$
and $\Delta\mu U$ = 64.4 $\frac{cm^2}{g}$.

As the area of the sample is known, the absolute mass of U in the sample can be calculated from the edge step of the spectra collected at the UL_3-edge, the mass of Th from the from the edge step of the spectra collected at the ThL_3-edge respectively. Division of these values by the corresponding molar masses yields the molar ratio. Prior to this, $\Delta\mu$ have been determined from the photoabsorption cross sections μ just before the edge step and after the XANES region. From database the mass photoabsorption cross section μ is always presented with four significant digits without any error. The mole fractions therefore were calculated to four significant digits. Simultaneously these values were confirmed by SEM-EDS and results are listed in table 3.7.

The uranium amount in the product phases is always higher than expected from the initial ratio, as can be seen in table 3.8. This is in contradiction to the experiences of Costin et al. who usually found less uranium in the desired silicate phase than calculated. However, in their case the missing uranium could be found in the accompanying dioxide phase. The stability of colloidal $ThSiO_4$ and $USiO_4$ is strongly increased at high silica concentrations (see Dreissig et al. [116]), yet there are no big differences in the stability of $ThSiO_4$ and $USiO_4$ colloids. The amount of liquid in the ampules after reaction is negligible small and hardly retrievable through filtration. An analysis of the liquid phase after washing and filtration could not determine amounts of U or Th by ICP-MS. However ampules are heavily corroded on inside and outside surface after the hydrothermal treatment. A whitish layer covers the inside of the ampule. It has to be assumed, that Th to a certain amount reacts with the surface of the ampule or even diffuses into the glass. A thorough investigation of the ampule surfaces after reaction has not been undergone. While

Table 3.7: SEM - EDS analysis of the composition of the uranothorite samples and comparison with values calculated from edge step from XAS.

	EDS analysis			XAS edge step		
$x(U)_{expected}$	U (at. %)	Th (at. %)	$x(U)_{EDS}$	U (at. %)	Th (at. %)	$x(U)_{XAS}$
0.10	14(1)	86(1)	0.14(1)	12.12	88.88	0.12
0.20	27(1)	73(1)	0.27(1)	25.54	74.46	0.26
0.30	40(1)	61(1)	0.40(1)	35.67	64.43	0.36
0.40	43(1)	57(1)	0.44(1)	42.01	58.99	0.42
0.50	55(1)	45(1)	0.55(1)	55.02	44.98	0.55
0.50	58(1)	43(1)	0.58(1)	56.34	43.66	0.56
0.60	66(1)	33(1)	0.66(1)	-	-	-
0.66	17.8(7)*	8.0(5)*	0.69(1)	70.67	29.33	0.71
0.70	75(1)	25(1)	0.74(1)	74.55	26.45	0.75
0.80	82(1)	19(1)	0.82(1)	83.74	16.26	0.84
0.90	90(1)	10(1)	0.90(1)	91.63	8.37	0.92

)* value from TEM-EDS

the relative difference with respect to the U content seems rather big, a close look onto the absolute values reveals, that these remain constant in the range of 0.02 – 0.06. This supports the thesis, that the Th loss can be explained by reaction with the ampule's surface, as all ampules have the same dimensions and hence the same surface area on the inside.

Table 3.8: Comparison between the uranium and thorium mole fractions before reaction and in the corresponding product.

sample ID	U:Th-ratio before	U:Th-ratio after	absolute difference	relative difference
UTh13-09	0.10 : 0.90	0.12 : 0.88	+ 0.02	+ 20 %
UTh13-08	0.20 : 0.80	0.26 : 0.74	+ 0.06	+ 30%
UTh13-07	0.30 : 0.70	0.36 : 0.64	+ 0.06	+ 20%
UTh13-06	0.40 : 0.60	0.42 : 0.58	+ 0.02	+ 5%
UTh13-05	0.50 : 0.50	0.56 : 0.44	+ 0.06	+ 12%
UTh13-10	0.50 : 0.50	0.55 : 0.45	+ 0.05	+ 10%
UTh12-03	0.66 : 0.33	0.71 : 0.29	+ 0.05	+ 7.6%
UTh13-03	0.70 : 0.30	0.75 : 0.25	+ 0.05	+ 7.1%
UTh13-02	0.80 : 0.20	0.84 : 0.16	+ 0.04	+ 5%
UTh13-11	0.90 : 0.10	0.92 : 0.08	+ 0.02	+ 2.2%

SEM and EDS analysis

Through SEM investigation the morphology and particle size has been studied. Special interest was layed on the influence of composition of the $U_xTh_{(1-x)}SiO_4$ solid solutions on size and shape of the particles. Excess silica appears in all samples as spherical particles with > 20 μm diameter. These sometimes are covered with the much smaller $U_xTh_{(1-x)}SiO_4$ silicate phase particles, which can be well distinguished from the spheres (cf. fig. 3.21). The composition of the micro-spheres has been confirmed by EDS.

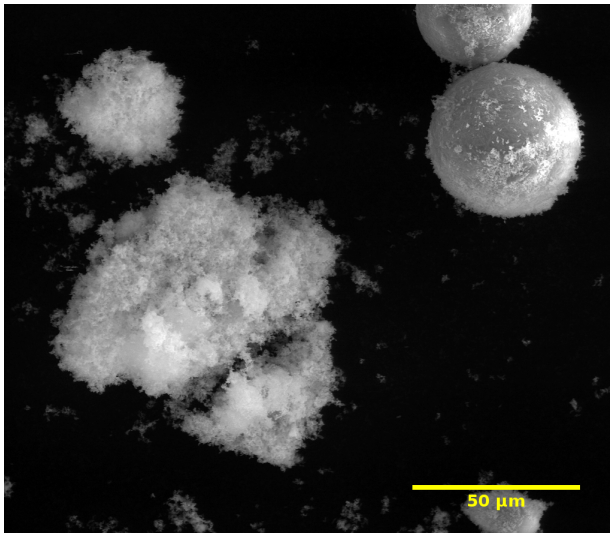

Figure 3.21: SEM micrograph showing approx. 40 μm silica sphere with attached $U_xTh_{(1-x)}SiO_4$ particles (upper right corner) and an agglomerate of $U_xTh_{(1-x)}SiO_4$ particles.

All samples were synthesized under the same conditions, i.e. same temperature regime and same reaction time. The particle sizes and morphology are hence comparable and can be correlated to the composition of the samples. As in the pure $ThSiO_4$, $USiO_4$ and the $U_xTh_{(1-x)}SiO_4$ likewise exhibit a lentil like shape. Particles of samples with a high uranium mole fraction are significantly smaller than those with high thorium content. However, while those samples with high uranium content (see figures 3.22a, 3.22b, 3.22c) are homogeneous in size and almost cubic grains, the thorium rich samples (cf. figures 3.22h and 3.22i) show one axis being strongly elongated, leading to a nearly acicular shape. Also the size distribution of particles in theses samples is much broader. Close to an equimolar ratio of uranium an thorium the particles are uniform in size, in the range from 800 $\pm$ 200 nm x = 0.60) to 1000 $\pm$ 150 nm x = 0.55), and show a well established lentil shape (fig. 3.22d, 3.22e, 3.22f).

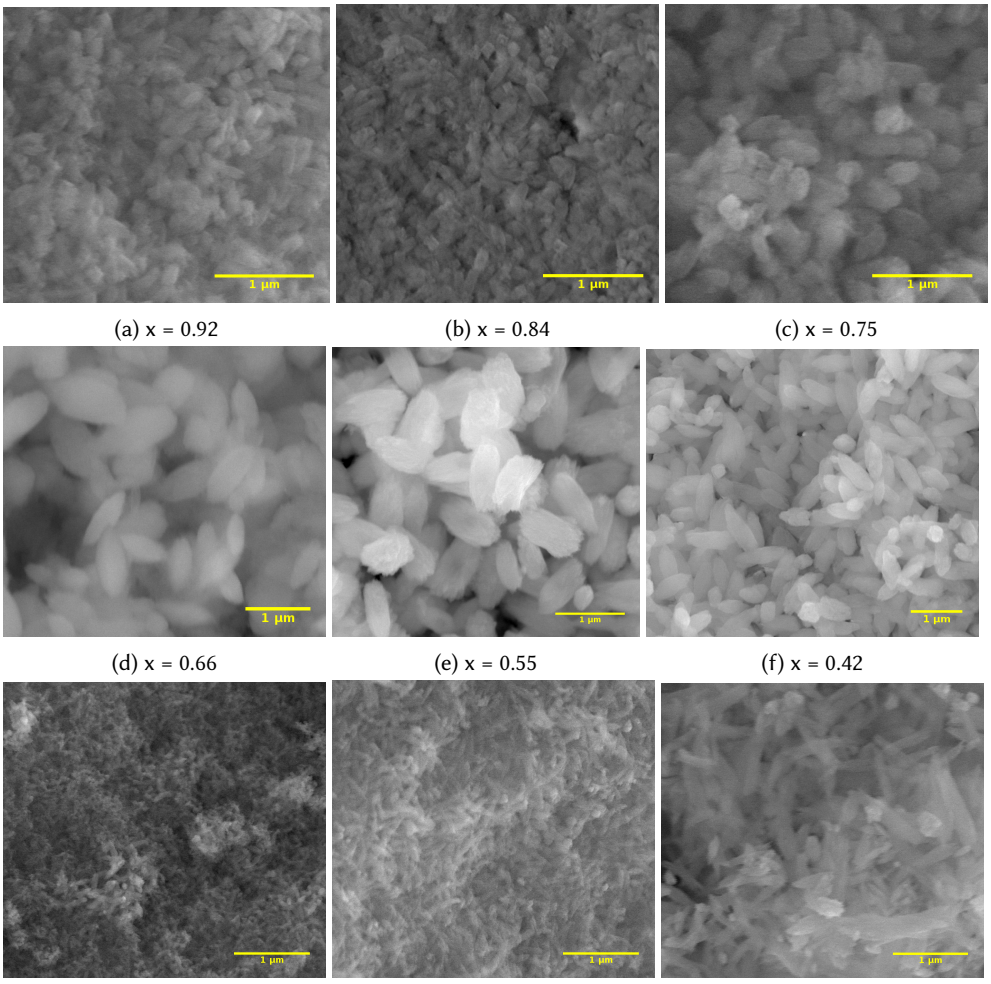

(a) x = 0.92 (b) x = 0.84 (c) x = 0.75

(d) x = 0.66 (e) x = 0.55 (f) x = 0.42

(g) x = 0.36 (h) x = 0.26 (i) x = 0.12

Figure 3.22: SEM micrographs of the $U_xTh_{(1-x)}SiO_4$ solid solutions, scale bar is 1 μm.

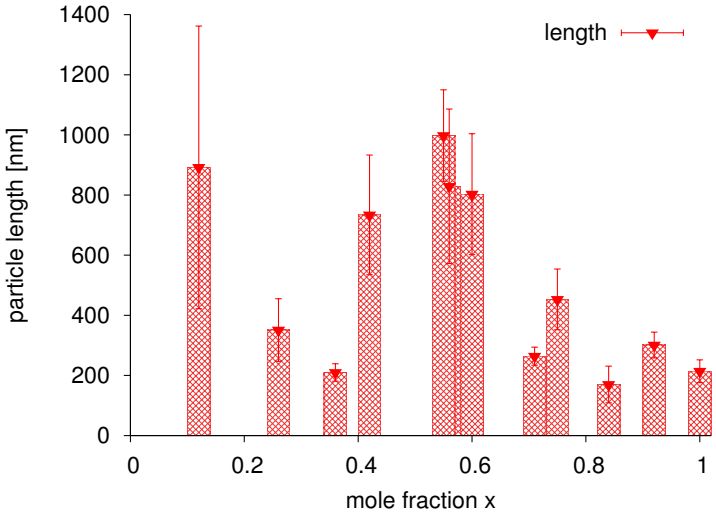

Figure 3.23: Particle size vs. mole fraction x as observable in SEM micrographs for the solid solutions.

In figure 3.23 the observed particle sizes and distributions are shown. Statistic measurements were obtained on at least 20 particles (usually > 30) led to average sizes. Costin et al. observed an increase of particle sizes in the uranium rich phases. While in their studies particles ranged from 120 $\pm$ 20 nm (x = 0.1) to 450 $\pm$ 60 nm (x = 0.7) and also showed the lentil like shape, the size variation could be not directly correlated to the uranium content, as the duration of the hydrothermal treatments was not always comparable.[117]

Particle sizes establish an opposite tendency than the crystallite size (i.e. the coherent scattering domains, which often is referred to as grain size as well), as the particles of the thorium rich phases can reach a much bigger size than those of the uranium rich. The crystallite size as derived from XRD data and the particle size differ by one order of magnitude increasing to two orders of magnitude in the thorium rich phases. It is notable, that the change in the particles' habitus could be predicted from the c/a-ratio (see figure 3.18b). As x decreases, the c/a-ratio increases. The base of the unit cell becomes smaller respectively to the main axis, like in a platelet transforming to a needle.

To provide an explanation for this odd behavior it is useful to take a look at the local environment the solid solutions. The $USiO_4$ unit cell is smaller than the $ThSiO_4$ unit cell, and for high U content the substituted Th atoms are isolated. Due to their slightly larger radius these few Th atoms are fixed in the smaller U gap. With increasing Th content the lattice opens up, so for $x \longrightarrow 0$ U atoms are confined within a rather large Th gap. This allows the U atom to shift out of the equilibrium position which increases possibilities for stacking faults, displacement of atoms. As a result crystallization is strongly disturbed and smaller crystallites form.

During the morphological investigation of the samples the composition was investigated on several spots with EDS. As measurements were carried out in low vacuum mode, employing water as atmosphere to lead off the current, values for oxygen amount are not reliable. Uranium and thorium amounts can be determined from the U L- and Th L-signals, as these are well separated and not overlaid by any other signal. Also the background in the region of interest is low (cf. figure 3.24). The determined U/Th-ratios are listed in table 3.7 and compared to

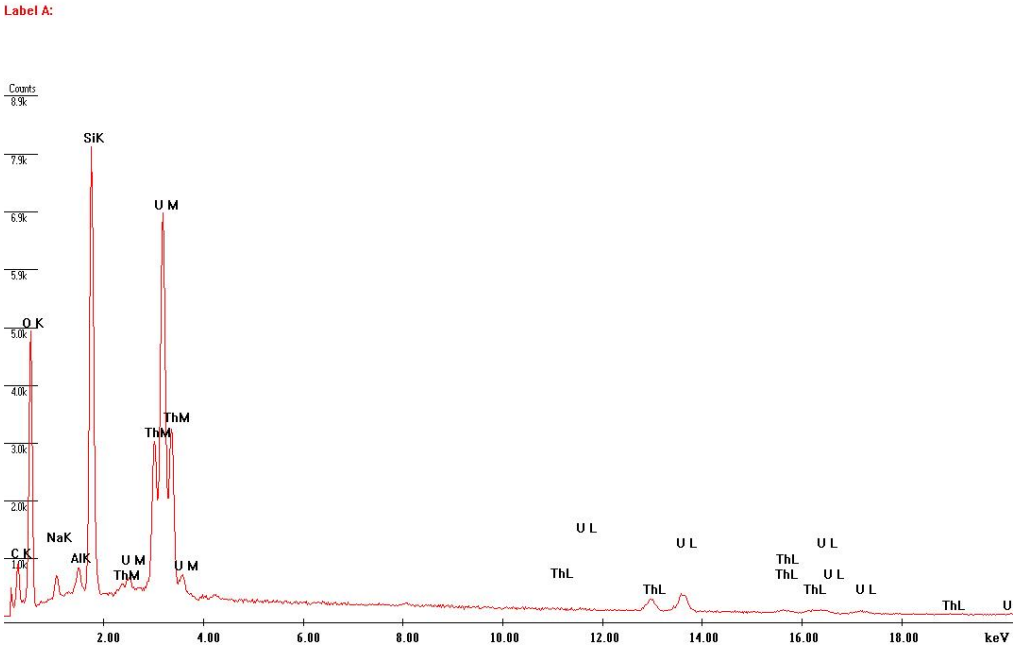

Figure 3.24: EDS spectrum of $U_{0.66}Th_{0.33}SiO_4$.

the values determined from the XANES edge-step. Within the limitations of XRD technique, the presence of two different $U_xTh_{(1-x)}SiO_4$ phases with only a small difference in x can be excluded. resulting in a gradual change of U/Th–ratio from center to shell of the precipitated particle. Considering the present samples consisted of core-shell particles with, for instance, a U-rich $U_xTh_{(1-x)}SiO_4$ core and different U-deficient $U_xTh_{(1-x)}SiO_4$ shells. In principle, it would be possible to detect such an U/Th-ratio decrease from center to rim of the particle with EDS, if
1) core and shells, which comprise the particle are large enough; and
2) the particle could be prepared in such a way, that this "bulls-eye" structure is accessible by the electron beam. The excitation volume from which the detected x-rays originate is $\sim 1\mu$m in diameter. The individual layers or shells therefore should at least be in this size range. For the present samples it is therefore not possible to detect such a gradient in the U/Th-ratio. Even the use of wavelength dispersive x-ray spectroscopy (WDS) is not feasible, as the particles only

comprise a few 100 nm. Let alone the problem of the necessary preparation. Samples would have to be suspended and embedded in hard resin, then polished to hopefully prepare nice surfaces cutting evenly through the potential shells. This dilemma could possibly be overcome by transmission electron techniques. Using electron energy loss spectroscopy (EELS) in a line scan across the particles could detect a gradient in sample composition. Energy filtered transmission electron microscopy (EFTEM) would also offer a possibility. However, resolution and detection limits need to be taken into account. Due to the similarities of U and Th, the difference in EFTEM might be only marginal. Especially if the U/Th-ratio decrease is not very large even such a sensitive method as EELS could not sufficiently solve the question.

IR spectroscopy studies

In the IR spectra of the complete $U_xTh_{(1-x)}SiO_4$ series, the stretching- and bending-mode of water can be detected. The ν(OH) stretching mode can be found at $\sim$ 3440 cm^{-1}, the bending mode δ(HOH) remains constant at 1635 $^{cm-1}$. With exception of the x = 0, i.e. hydrothermally prepared thorite, the water bands are not the strongest signals in the spectra. The spectra are dominated by the internal modes of the SiO_4^{4-}-tetrahedron in region between 800 – 1100 cm^{-1}. Two modes can be detected, which often overlap and show a strong shoulder. According to Dawson et al.[68] these correspond to A_{2u}- and E_u-modes of the SiO_4^{4-}-tetrahedron also referred to as ν_4 vibration-modes in the Herzberg notation.[67;66] A list of the band positions in the IR spectra of the $U_xTh_{(1-x)}SiO_4$ uranothorite solid solutions is given in table 3.9. Most interesting are the very sharp bands at $\sim$ 570 and $\sim$ 450 cm^{-1} which also can be attributed to internal A_{2u}- and E_u-modes, also referred to as ν_4 - vibrations, of the SiO_4^{4-}-tetrahedron. These are characteristic for the zircon-structure and values correspond to those reported by Zhang et al.[97] While all other bands remain constant within the resolution, the band attributed to the E_u (ν_4)-mode experiences a small shift towards higher wavenumbers towards the uranium rich members. However, the collected data is insufficient to draw reliable conclusions from this.

Table 3.9: Band positions in wavenumbers [cm^{-1}] in the IR spectra of the $U_xTh_{(1-x)}SiO_4$ uranothorite solid solutions.

$x_{(U)}$	ν(OH)	δ(HOH)	A_{2u} (ν_3)	E_u (ν_3)	A_{2u} (ν_4)	E_u (ν_4)
0	3345	1632	1000	848	590	459
0.12(1)	3447	1636	1072	910	577	456
0.36(1)	3436	1635	1069	908	576	448
0.42(1)	3446	1635	1097	916	575	468
0.56(1)	3435	1635	1079	907	574	450
0.66*	3446	1636	1071	908	573	450
0.71(1)	3447	1638	1090	910	575	447 s
0.84(1)	3435	1636	1075	908	574	446
1	3443	1634	1046	904	571	444

The strong signal for the ν(OH) vibrations, however cannot be loosely bound surface water. Even after the sample had been dried at 200 °C and the signal is rather narrow. Keller[104] reports on the lattice parameters becoming slightly smaller (- 0.002 Å, it has to be noted, that this is within the error limits) and a weight loss of 0.2 % in coffinite after heating for 6 hrs. at 500 °C under Ar. Also the reflections according to Keller "become sharper". Keller, however, argues that this is rather an effect of better ordering in the crystal lattice, than loosing water. From a DSC-TG measurement of one coffinite sample (A1-2) up to 400 °C in air a weight loss of -1.47 % could be measured (cf. figure V on page xi in the appendix) above 400 °C the mass started to increase due to the starting oxidation to U_3O_8. The weight loss of corresponding thorite samples up to 400 °C is usually in the range of $\sim$ 5 % (compare in figure VI) and continues up to 600 °C.

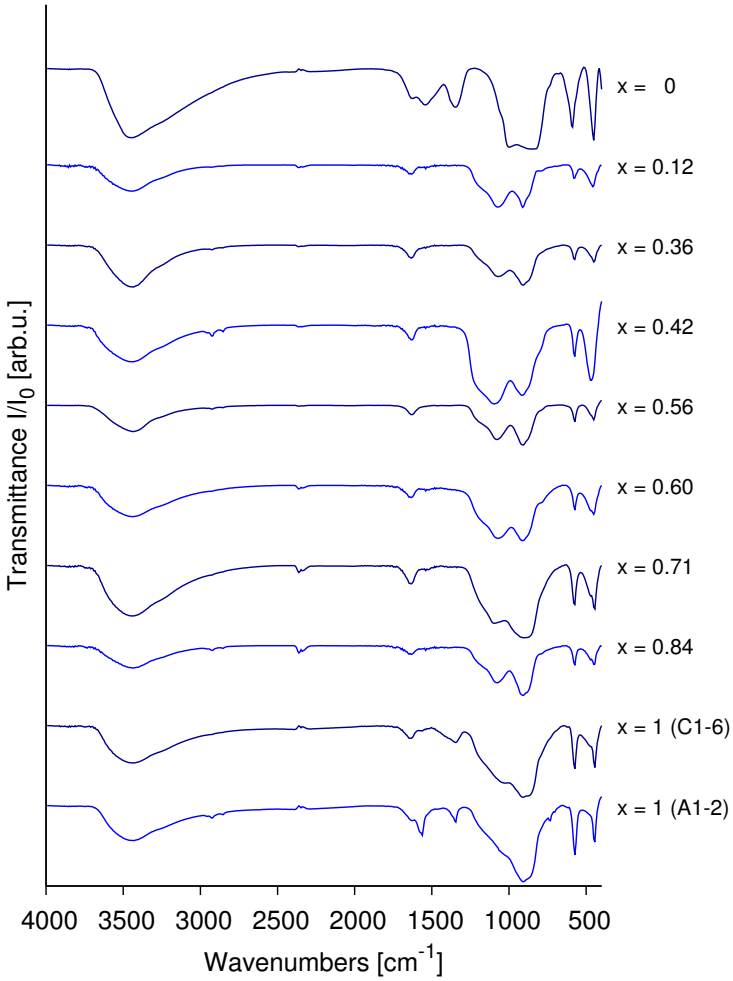

Figure 3.25: IR spectra of the $U_xTh_{(1-x)}SiO_4$ uranothorite solid solutions, [Bruker *Equinox 55* TGA-IR, KBr pellet].

Still none of the spectra shows big similarities to UO_2 as can be seen from comparison with figure 3.26. In the region up to 1000 cm^{-1} two strong modes can be observed at 530 cm^{-1} and 920 cm^{-1}, up to higher wavenumbers the characteristic signals for water can be seen. The band at 530 cm^{-1} is characteristic for UO_2 (uraninite),[26;102] whereas the band at 920 cm^{-1} is common for UO_2^{2+}-stretching vibrations. (The latter could be a sign of oxidation of the UO_2 sample and the presence of U(VI).) More important, the distinct band at 530 cm^{-1} is not observed in the IR spectra for coffinite and the $U_xTh_{(1-x)}SiO_4$ solid solutions. It can be assumed that no significant amount of UO_2 or $U_yTh_{(1-y)}O_2$ is present in these samples.

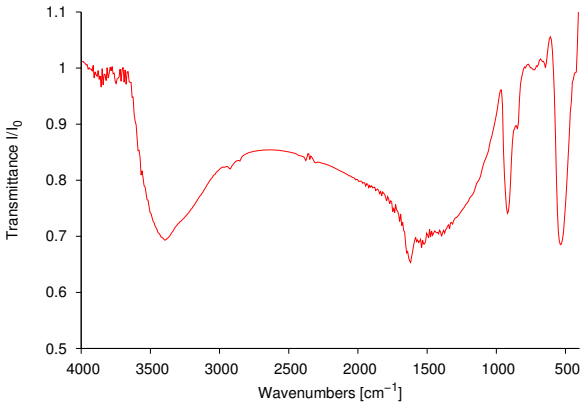

Figure 3.26: IR spectrum of UO_2 sample (commercial reagent, Merck KGaA), [Bruker *Equinox 55* TGA-IR, KBr pellet].

The coffinite sample A1-2 in was first washed in 6 M HNO_3 to leach off the remaining oxide phase, detected in the synchrotron X-ray diffraction and rinsed with water. Then the sample afterwards was washed in 0.1 M KOH solution to remove excess silica and dried for 2d at 200 °C to remove any attached water. After this procedure IR spectroscopy was also employed to confirm the absence of UO_2 and UO_2^{2+}. Even over longer time of heating at 200 °C, the coffinite samples do therefore not decompose as can be seen in figure 3.27. However, the mode at 1470 cm^{-1}, which can be detected in the coffinite sample prior to washing and drying, has significantly increased in intensity. This type of mode was attributed to δ(HOH) of water in a different position during evaluation of the thorite data (see page 53). However, the signal of ν(OH) at $\sim$ 3400 cm^{-1} remains.

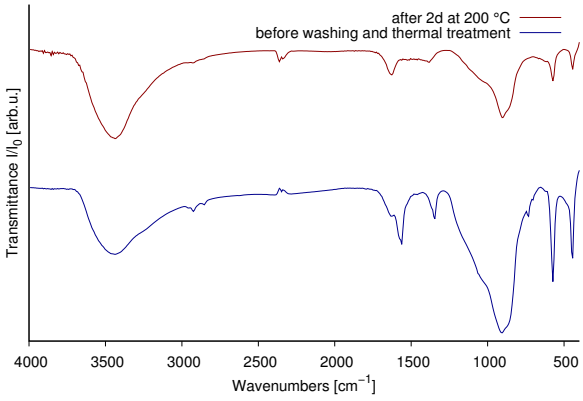

Figure 3.27: IR spectrum of coffinite sample as prepared and after washing procedure and drying at 200 °C for 2d. [Bruker *Equinox 55* TGA-IR, KBr pellet]

Concluding from the IR spectra, even after heating at 200 °C for longer periods of time, water cannot be completely removed from the $U_xTh_{(1-x)}SiO_4$ solid solutions. For thorite the substitution of hydroxyl-groups for silicate is well known. Hence the composition of hydrothermally grown $ThSiO_4$ should indeed be considered as $Th(SiO_4)_{(1-x)}(OH)_{4x}$. It might be the same case with coffinite and the $U_xTh_{(1-x)}SiO_4$ solid solutions. In literature, the composition of hydrothermally synthesized coffinite as being $U(SiO_4)_{(1-x)}(OH)_{4x}$ is often discussed, yet no alternative synthesis to obtain pure "$USiO_4$" with no water in the structure for comparison is known.

TEM investigation

It is not always trivial to answer the question, whether a sample is pure or not. Even if an XRD pattern does not show any unassigned reflections, it is possible that up to 5 wt.% (depending on atomic mass difference and scattering properties) of another crystalline phase are overlooked. Another problem is the amorphous content of a sample. One aim of his work is to establish a reproducible synthesis route for $USiO_4$ so reliable thermodynamic data of the substance can be collected. In order to get reliable thermodynamic data, it must be certain that other secondary phases – especially the oxide – are not present. As the sample mass from these syntheses is limited, transmission electron microscopy is a productive technique to investigate the samples for amorphous components. Coherent scattering domains are visible first hand in the TEM. These values can be used to confirm the crystallite sizes derived from XRD.

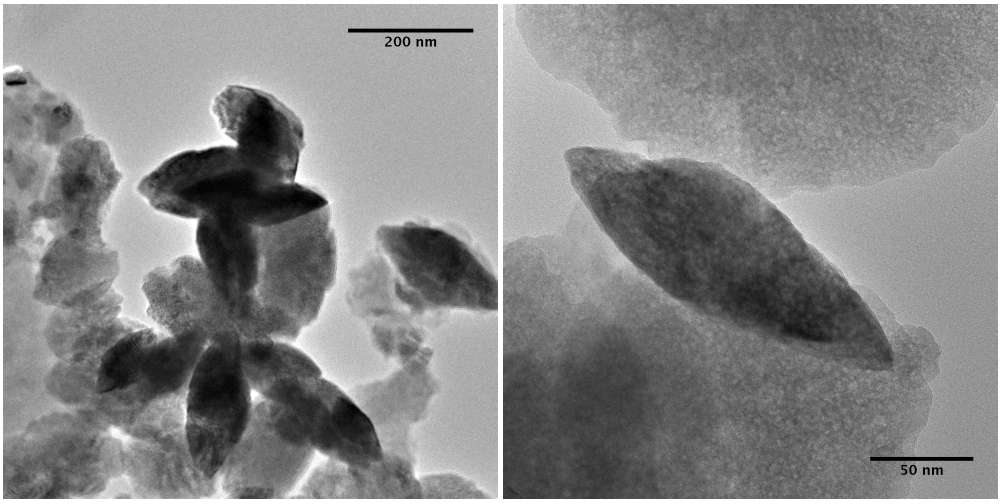

(a) Overview TEM micrograph of thorite, $ThSiO_4$, scale bar 200 nm.

(b) Close-up TEM micrograph of thorite, $ThSiO_4$, scale bar 50 nm.

Figure 3.28: Bright field TEM micrographs of the thorite, $ThSiO_4$, sample. The overview shows the agglomerated particles (a), the lentil shape is particularly evident in the close-up (b).

The high resolution transmission electron microscopy (HRTEM) measurements show, that

the lentil shaped $USiO_4$ particles, of which the morphology could already be observed by SEM, are not single crystal. Instead the lentils appear to be an agglomeration of smaller particles, which are again covered in an amorphous layer (see figure 3.29a). The uranium containing particles are not as sharp and the edges not as clean cut as those known from hydrothermally synthesized α-$ThSiO_4$ 3.28a. Of the solid solutions it was only possible to investigate $U_{0.71}Th_{0.29}SiO_4$ by TEM. As the pure $USiO_4$ sample, it exhibits agglomerated, lentil shaped particles, see figure 3.29c.

From the high angular annular dark field (HAADF) TEM investigations, figure 3.29b, it is confirmed that the amorphous layer around the particles indeed is amorphous SiO_2 and does not contain heavy elements. While the SEM images mainly give information about the particle sizes and morphology, the TEM investigations give an insight on the crystallite sizes. The observable crystallites are in the size of $\sim$ 20 nm, which is in considerably good accordance with the crystallite size derived through the Williamson-Hall method[112] from XRD. Upon closer investigation the lattice planes in the particles become visible. In the FFT of the TEM image of coffinite (fig. 3.30a) the characteristic distances d(020) = 0.34 nm and d(011) = 0.45 nm can be found. Distances of the (020) lattice planes can also be detected in the real space image with value d(020) = 0.346 nm. The diffraction pattern from FFT corresponds to view along $[11\bar{1}]$. Lattice planes of the same type are exhibited in the $U_{0.71}Th_{0.29}SiO_4$ sample as well, as can be seen in figure 3.30b. Due to the larger unit cell also the distances of the lattice planes should increase. Indeed, as expected they are slightly larger, with d(011) = 0.456 nm and d(020) = 0.352 nm.
TEM investigation reveals, that neither the $ThSiO_4$ nor $USiO_4$ or the $U_{0.71}Th_{0.29}SiO_4$ solid solutions are single crystal particles. All appear to consist of smaller grains as already expected from the reflection breadths in the XRD pattern. The size determination through the Williamson-Hall method has it's difficulties. In particular the method requests spherical particle shape and a cubic spacegroup to be fully reliable. It is however proven, that the crystallite size values from Williamson-Hall plots and observed in the TEM micrographs are in very good agreement. Since the crystallite sizes now have been qualitatively acknowledged for four samples by TEM, the crystallite sizes estimated from XRD for the remaining $U_xTh_{(1-x)}SiO_4$ solid solutions can be regarded as validated. No other uranium phase could be observed as nanocrystalline material, nor did the amorphous layer contain a notable amount of heavy elements. Of course, it is only possible to investigate a random part of the whole sample with TEM but from what can be considered the presence of another uranium phase, especially the oxide, can be excluded.

EXAFS study

Bond distances and angles can be calculated from the powder XRD pattern of the samples through Rietveld refinement with a remarkable small standard deviation. This error is derived from the fit and suggest an accuracy in the laboratory X-ray measurements, which is in fact "too good". Besides, it has to be taken into account, that from XRD only an overall average of a cer-

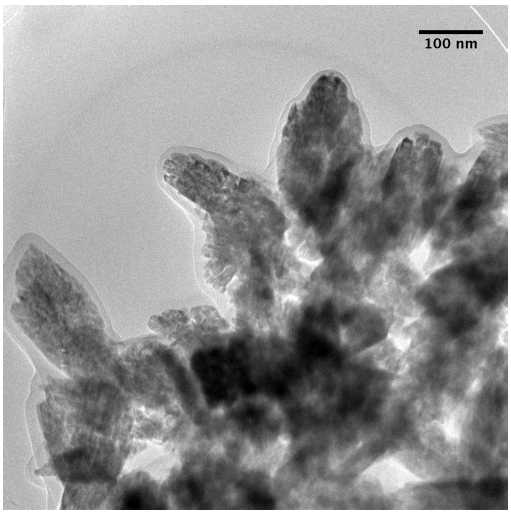

(a) Overview TEM image of the pure $USiO_4$ sample, scale bar 100 nm.

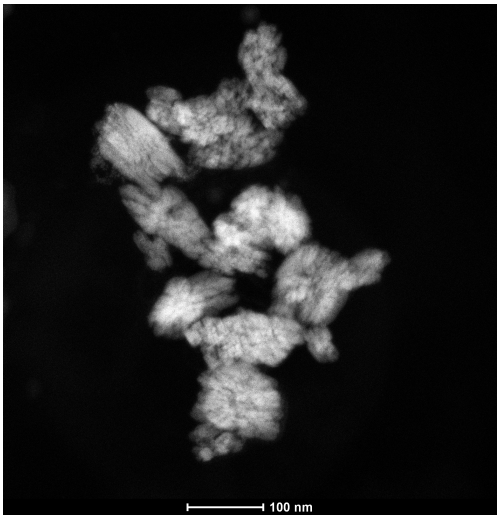

(b) Corresponding HAADF image of $USiO_4$ sample, scale bar 100 nm.

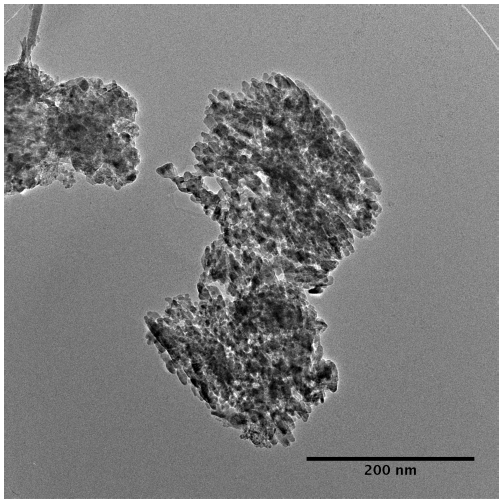

(c) Overview TEM image of the $U_{0.71}Th_{0.29}SiO_4$ sample, scale bar 200 nm.

Figure 3.29: Overview TEM micrographs of pure $USiO_4$ and the $U_{0.71}Th_{0.29}SiO_4$ sample. In the HAADF image the amorphous layer is not evident.

tain bond is obtained. For instance, when the length of the metal–oxygen distance of the axial oxygen atoms M-O_1 in the [MO_8]-polyhedron is calculated, no difference between Th-O_1 and U-O_1 bonds is made. In principle it is possible to investigate occupancy of the atomic species in solid solutions with the Rietveld method. However, to determine the occupancy and through

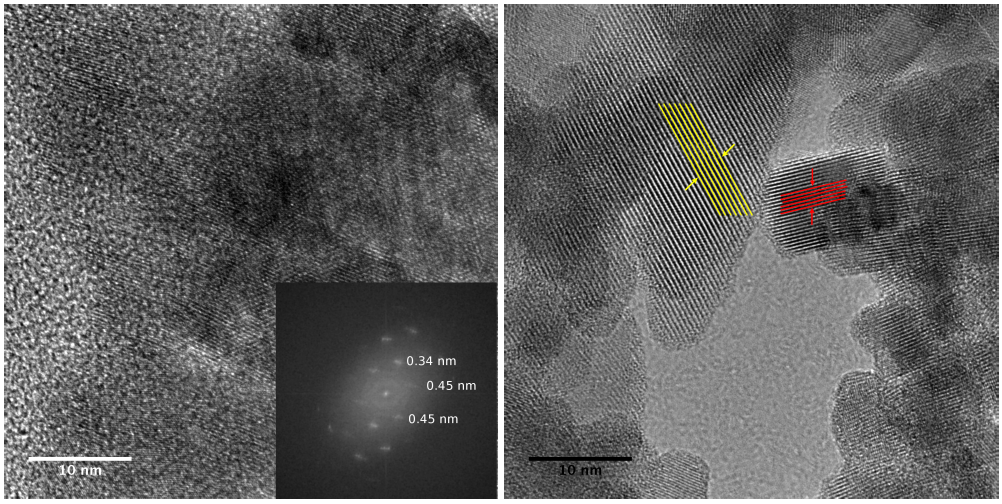

(a) HRTEM micrograph of coffinite, $USiO_4$. From FFT the lattice planes with d(011) = 0.45 nm and d(020) = 0.34 nm can be assigned.

(b) HRTEM micrograph of $U_{0.71}Th_{0.29}SiO_4$. Lattice planes with d(011) = 0.456 nm (yellow) and d(020) = 0.352 nm (red) are observed.

Figure 3.30: HRTEM micrographs of pure $USiO_4$ and the $U_{0.71}Th_{0.29}SiO_4$ sample. For $USiO_4$ the FFT is shown as inset, in the $U_{0.71}Th_{0.29}SiO_4$ sample the lattice planes can be directly observed and evaluated (emphasized for two directions).

this the formula of a crystal will lead to satisfactory and reliable results only if differences in the atomic number and hence the electron hull are large enough.[45] To determine occupancy from powder furthermore requests a certain quality of the XRD pattern and in conclusion also the sample. For uranium and thorium the differences of the electron configurations are just too small to be distinguishable from XRD. The stoichiometry of the $U_xTh_{(1-x)}SiO_4$ solid solutions cannot be confirmed or refined by XRD. There is also no reliable way to investigate the existence of a superstructure or ordering – phenomena. While EXAFS in principle is not as accurate in the determination of bond lengths in a crystal structure as XRD,[72] it offers the opportunity to investigate the short range order of materials with regard to a distinct central atom very accurately. The error in distances obtained from EXAFS is the deviation of the distance in real space and not the error of the mathematical fit. For a pure material the interatomic distances from XRD and EXAFS should of course be the same within the error range. A comparison of the XRD and EXAFS data from the end members of the $U_xTh_{(1-x)}SiO_4$ solid solution is given in 3.10.

EXAFS spectra were collected at the European Synchrotron Radiation Facility (ESRF) in Grenoble at beamline BM-20 (ROBL) during two beamtimes in November 2012 and April 2013 (ESRF CRG proposal No.: 20-01-723). The spectra were collected at room temperature, while of the measurements of two endmembers and $U_{0.71}Th_{0.29}SiO_4$ took place at 15 K. As motion of the atoms is nearly stopped at such low temperatures this directly influences the scattering ampli-

Table 3.10: Comparison between interatomic distances of $ThSiO_4$ and $USiO_4$ obtained by XRD and measured with EXAFS.

$USiO_4$			$ThSiO_4$		
Bond type [Å]	XRD	EXAFS	Bond type [Å]	XRD	EXAFS
U-O_1	2.276(1)	2.272(4)	Th-O_1	2.3499(4)	2.336(3)
U-O_2	2.407(1)	2.395(6)	Th-O_2	2.4695(6)	2.434(4)
U-Si_1	3.1304(2)	3.126(4)	Th-Si_1	3.140(1)	3.177(4)
U-Si_2	3.8277(1)	3.879(6)	Th-Si_2	3.9130(7)	3.940(7)
U-U_1	3.8277(1)	3.830(2)	Th-Th_1	3.9130(7)	3.918(2)

The true error of atomic distances derived from EXAFS spectra is to be considered with $\pm$ 0.02 Å.

tudes. This difference can be observed in the FT-magnitudes of the spectra, especially on the peak of the M-M distance. The higher temperature also has impact on the Debye-Waller factors. It does not however change the absolute position of the peak. A complete list of the obtained distances by EXAFS from the ThL_3-edge is given in table V and from UL_3-edge in table VI in the appendix on pages xii and xiii.

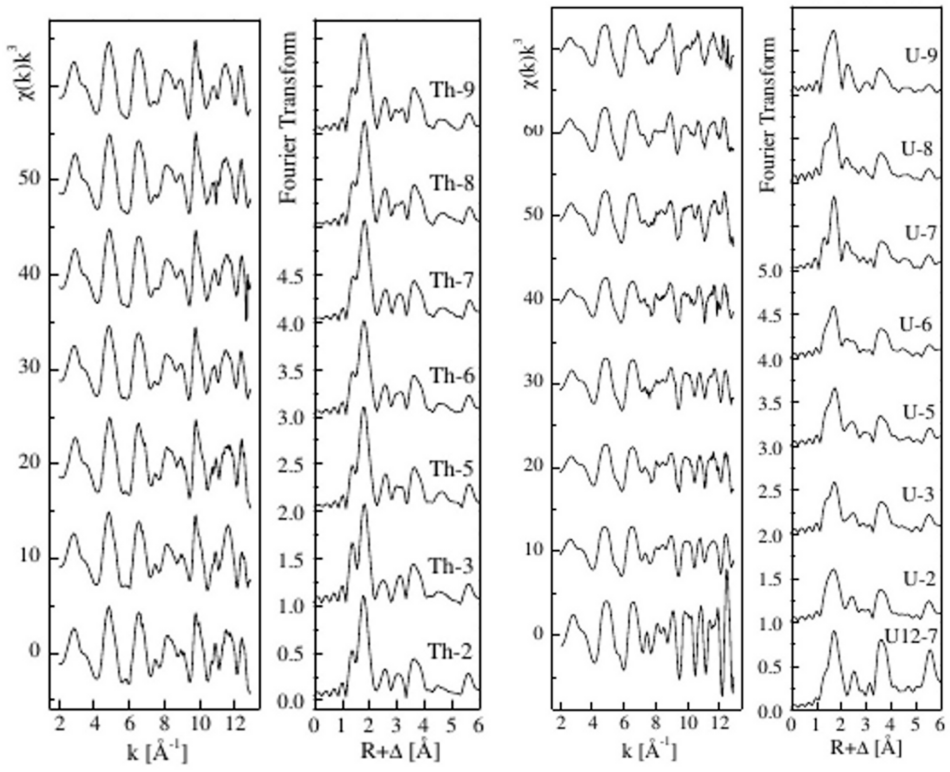

Figure 3.31: Overview of the k^3 weighed FT-magnitudes of the EXAFS from the ThL_3-edge (a) and the UL_3-edge (b).

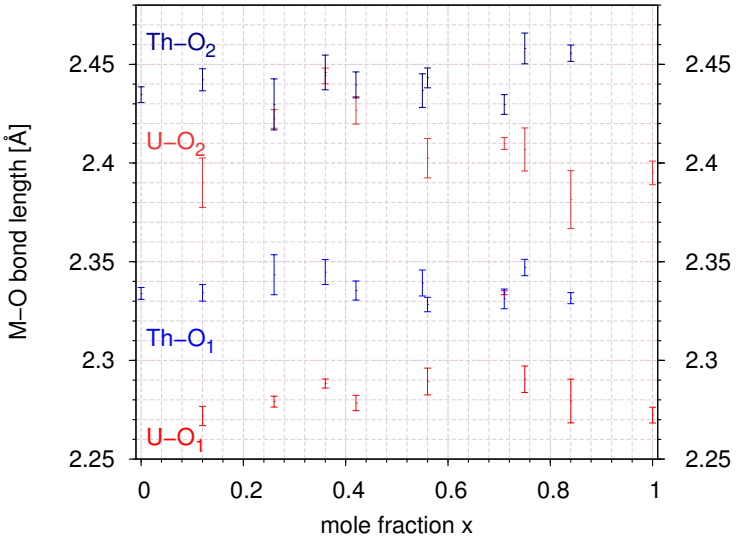

Figure 3.32: U/Th-$O_{1/2}$ distances and standard deviation of the $U_xTh_{(1-x)}SiO_4$ uranothorite solid solutions from EXAFS measurements of the UL_3 and ThL_3-edge respectively.

Over the complete range of the solid solutions the M-O_1 and M-O_2 distances remain nearly constant within the standard deviation as can be seen in figure 3.32. This is not surprising as these distances rely mostly on the central atom (U(IV) or Th(IV)), hence the Th-O distances are always larger than the corresponding U-O distances. To study the behavior of the $USiO_4$ – $ThSiO_4$ – system, especially regarding the miscibility, these results are not suitable. For this purpose the first shell metal – metal distance, which is R_{M-M} (cf. figure 3.33), is better applicable.

In order to correctly interpret the results of the measurements, it is useful to first take a look at the possible scenarios for this system. In general, for the $U_xTh_{(1-x)}SiO_4$ solid solutions three different possibilities can be distinguished:

1. no miscibility is possible,
2. complete miscibility exists[86],
3. solid solutions of $USiO_4$ - $ThSiO_4$ are only possible within a limited range[93;118;95] (miscibility gap).

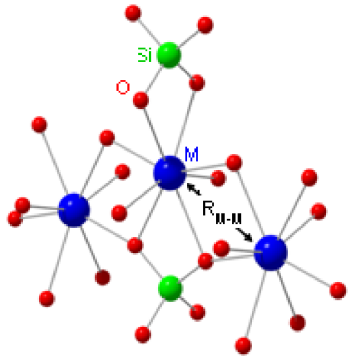

Figure 3.33: Schematic drawing of the metal coordination of the excited metal cation in $U_xTh_{(1-x)}SiO_4$. R_{M-M} represents the three possible distances R_{Th-Th} and R_{Th-U} and R_{U-U} under discussion.

No miscibility between the endmembers

In this case the detected intensities would result completely from R_{U-U} an R_{Th-Th}-distances. Neither distance should change over the range of the solid solutions. The R_{Th-Th} distances always being larger than those of R_{U-U}

Complete solid solution

For an ideal solid solution of $USiO_4$ – $ThSiO_4$ U(IV) and Th(IV) are statistically distributed in the crystal lattice. On first thought the R_{M-M} distances should be identical when measured from either ThL_3-edge or UL_3-edge and linearly decrease with increasing x. This model however does not take into account the difference of the slightly larger Th(IV) atom on the local environment. Indeed, in the ideal solid solution distances of type R_{U-U}, R_{Th-Th} and R_{U-Th} are present. While R_{U-U}, R_{Th-Th} are obtained from the measurements of the endmembers, R_{U-Th} is unknown (it has to be noted, that R_{U-Th} is of course equivalent to R_{Th-U}). The approximation as

$$R_{U-Th} = \frac{R_{U-U} + R_{Th-Th}}{2} \tag{3.3}$$

should suit this purpose. It can be argued, that this simplification does not take into account the contribution of the subsequent neighbors, i.e. like the Madelung factor which is applied in the calculation of lattice energies.[35] For binary halide solid solutions, in oxides or alloys, the influence of the higher coordination spheres to the bond distance can be large enough to be detectable. For instance, the disordering of oxygen in wuestite, FeO_2, can be envisaged this way.[119] In the present case, where large SiO_4^{4-}–anions separate the individual U(IV) and Th(IV)–cations, this effect can be neglected. The resolution of the EXAFS technique is $\pm$ 0.02 Å in distances and hence larger than the contribution of the next-neighbor effect to the distances.[35;33] In the spectra obtained from UL_3-edge R_{U-U} and R_{U-Th} can be detected. With increasing uranium content, the signal results mainly from R_{U-U} and only small amount of R_{U-Th} until in pure coffinite, x = 1

solely R_{U-U} is detected. For x $\longrightarrow$ 0, the opposite case, with increasing thorium content, R_{U-Th} distances dominate the spectra as the few isolated uranium atoms all have a thorium environment. It is hence impossible for any R_{U-M} distance measured on the UL_3-edge to be larger than R_{U-Th} as derived from equation 3.3. The same applies to R_{Th-U} and R_{Th-Th} distances measured on the ThL_3-edge respectively.

Limited miscibility

If a miscibility gap between $USiO_4$ - $ThSiO_4$ exists and it is not too small, then this ought to be detectable from these measurements. The obvious case would be, if R_{M-M} distances experienced a sudden change, and above a certain uranium mole fraction only R_{U-U}, R_{Th-Th} as in the pure coffinite and thorite were found. This would correspond to a complete phase separation. The more complicated situation though includes a mixture of thorite, coffinite and possible uranothorite solid solutions with all signals overlapping in the spectra. In this case for x $\longrightarrow$ 0 a significant amount of the R_{U-U} is still present and the average R_{U-M} distances would be in fixed between R_{U-U} and R_{Th-U} and smaller. The difference between R_{U-M} and R_{Th-M} would be larger than in the ideal solid solution.

For example, if uranothorite solutions were only possible up to x = 0.8 as Costin et al.[95] experienced, then above this value the R_{U-M} distance should be significantly shorter than observed in these measurements.

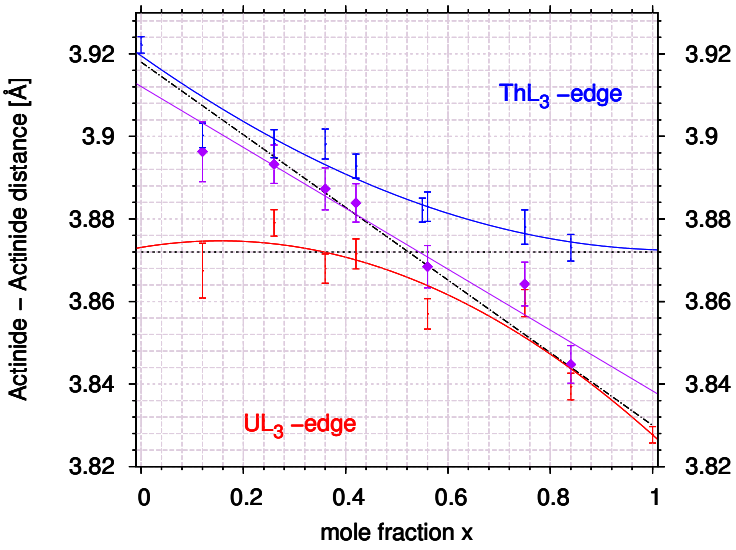

Figure 3.34: U/Th-Th/U distances and standard deviation of the $U_xTh_{(1-x)}SiO_4$ uranothorite solid solutions and the weighed averages (purple). The measurements at the UL_3 (red) and ThL_3 (blue) absorption edges were performed successively with the same sample.

Figure 3.34 shows the measured R_{M-M} distances with an approximation of $\bar{R}_{ThL_3}$ and $\bar{R}_{UL_3}$

by Gaussian normal distribution functions. The weighed mean cation-cation distances vary linearly with composition and are close to the Vegard line, implying a complete solid solution without notable clustering. Measurements from the both edges follow the expected trend for complete mixing. The data from ThL_3-edge measurements are following the fit better than those from the UL_3-edge. Because of the closeness of ThL_3-edge (16300 eV) and UL_3-edge (17185 eV) the background ot the EXAFS of the UL_3-edge is to a certain extend influenced by the remaining EXAFS on the ThL_3, which explains this slight derivation.

In conclusion, the difference of Th(IV) and U(IV) is visible in the short range order of the solid solutions. Such a phenomenon is observed in other solid solution systems as well.[120;121] In this case it acts as reminder that, while on the macroscopic scale for the bulk material U and Th appear to be the same, they can well be distinguished on the local scale. The measurements of the local cation interactions support the hypothesis of an ideal mixing behavior in the system $USiO_4$ – $ThSiO_4$. The existence of a miscibility gap can be excluded. Which means that the tendency already observed from the XRD data is largely confirmed through these results.

Here $USiO_4$ and the complete range of $U_xTh_{(1-x)}SiO_4$ solid-solutions were synthesized via a hydrothermal route. To suppress the formation of the oxide phase, $U_yTh_{(1-y)}O_2$, an excess of silica was used, employing Le Chatelier's principle. By this means it was possible to synthesize $USiO_4$ in good crystallinity, with no additional uranium phase present and within short reaction times. Significant amounts of α-SiO_2 and amorphous silica in the product however have to be taken into account. Quartz reflections are easily distinguished from those of $USiO_4$ in the XRD, and furthermore silica does not disturb the EXAFS spectra, therefore this additional phase does not cause problems analyzing the structure of $USiO_4$. According to X-ray diffraction data $U_xTh_{(1-x)}SiO_4$ forms a complete solid solution under hydrothermal conditions. Refined lattice parameters of the $U_xTh_{(1-x)}SiO_4$ phases as well as cell volume follow Vegard's Law and regularly decrease with increasing uranium content. This observation is well supported by the small difference in ionic radii of U^{4+} (1.00 Å) compared to Th^{4+} (1.05 Å).[122] This tendency can directly be observed in the TEM micrographs. Also it is visible that the synthesized particles are not single crystalline but that the over all lentil shaped particles consist of smaller crystallites, i.e. coherent scattering domains. Crystallite sizes observed in the TEM micrographs are in very good accordance with those derived from the XRD data by the Williamson-Hall method and one to two magnitudes smaller than the size of the particles observed by SEM. Pure $ThSiO_4$, $USiO_4$ and the $U_xTh_{(1-x)}SiO_4$ likewise exhibit a lentil like shape in the SEM investigations. Samples with a high uranium mole fraction are significantly smaller than those with high thorium content. Samples with high uranium content are homogeneous in size, smaller and almost of cubic shape, while the thorium rich samples show one axis being strongly elongated, leading to a nearly acicular shape. The mole fractions, which originally were calculated from the XANES edge-step could largely be confirmed by EDS. Even after longer heating treatment at 200 °C water or at least OH-groups are still present in the coffinite and $U_xTh_{(1-x)}SiO_4$ samples as is evident from the IR investigation. This allows for the discussion if these hydroxylgroups are essential for the structure and cannot be removed. Results from EXAFS measurements of ThL_3- and UL_3-edge feature a continuous correlation between increasing uranium content and decreasing metal-metal distances. This confirms the presence of a complete solid solution in the system $USiO_4$ – $ThSiO_4$. This work offers extensive data for this system and moreover a congruent set of measurements as useful base for further investigation into the involved kinetics of formation for coffinite and the uranothorites.

3.1.5 High-pressure studies of $USiO_4$

High-pressure phase transitions from zircon- to scheelite-type are known for many ABO_4 (A = Sc, Y, REE; B = V, As) compounds like vanadates or chromates.[123] It is also observed in orthosilicates with zircon structure, like zircon, $ZrSiO_4$,[124] hafnon, $HfSiO_4$,[125] and has recently been reported for coffinite, $USiO_4$.[97] Thorite, α-$ThSiO_4$, first establishes the monoclinic huttonite phase at elevated pressures before transforming into another unknown phase.[96] Calculations by Bose et al.[126] suggest, that thorite also will transform to the scheelite phase at even higher pressures. The phase transition of zircon under dynamic or hydrostatic pressures and at room or elevated temperatures has been extensively studied.[124;127;1;128;129] At room temperature the phase transition usually takes place between 20 – 30 GPa, while the transition pressure is strongly influenced by impurities and radiation damage.[98;130;131;132;133;134] Hafnon is reported to undergo the transition at 19.6 GPa,[125] while the critical pressure for coffinite is considerably lower at 15 – 17 GPa.[97] It

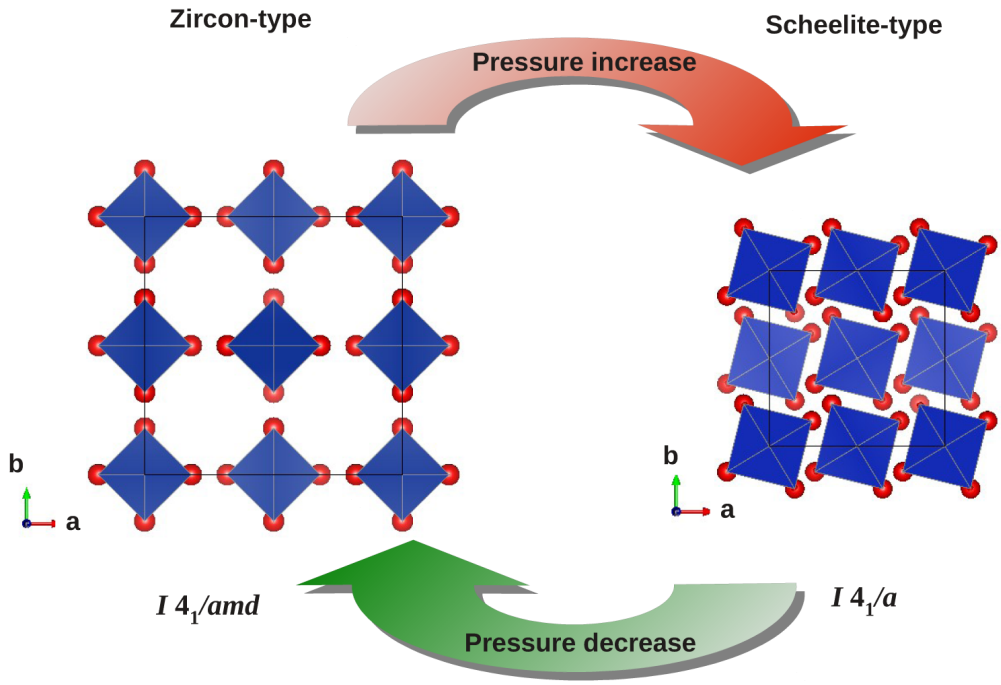

Figure 3.35: Schematic diagram of the structural relationship between the zircon type structure and the high pressure scheelite type structure. To avoid confusion only the SiO_4^{4-} tetrahedra are depicted.

is established, that the high pressure scheelite structure is space group $I\,4_1/a$, which is a maximal subgroup of $I\,4_1/amd$ and 10 % more dense. The structural relationship of the crystal structures seems obvious, when looking at the scheme in figure 3.35. It requires only a deformation of the

SiO_4-tetrahedra to transform from one structure type to the other. It is therefore tempting to assume that the phase transition is of second order. During the phase transition the cell volume however abruptly drops, the dimension of the c-axis nearly doubles while the a-axis is shortened by a third. This as well as the fact that these high-pressure phases are quenchable, indeed classifies the phase transition to be of first order. The group–subgroup relationship therefore is by classic interpretation[35] coincidental. Attempts to consolidate group-subgroup relationships to so called soft first-order phase transitions are widely discussed. For the zircon-scheelite phase transition this has been done by Smirnov et al.[128], who proposed the route via a cubic intermediate phase. The model developed by O'Keeffe[135] specially regards the cations of a structure. According to this, the driving force in zircon for this pressure induced phase transition is the elimination of cation – cation – repulsions, that is Zr - Si repulsions.

While Zhang et al. proposed in their work, that the high-pressure phase was stable and the phase transition irreversible,[97] in this work clearly the transformation back from scheelite to zircon type was observed in the synchrotron X-ray diffraction pattern. No signs of decomposition to UO_2 and SiO_2 are found in the samples. From the present Raman spectra up to 18.7 GPa the

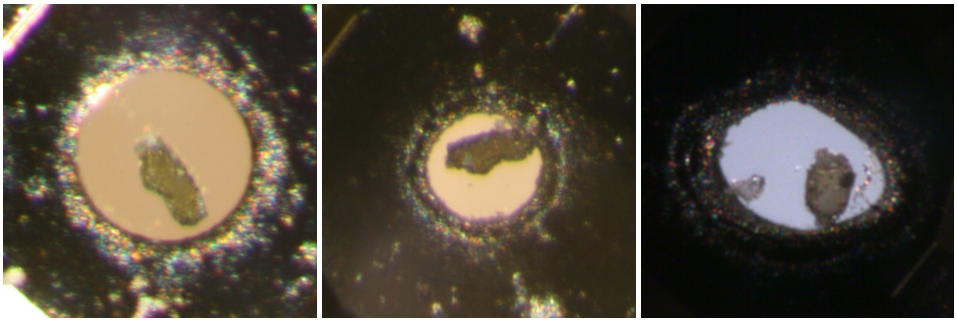

(a) DAC27 at 0.0001 GPa (b) DAC27 at 14.5 GPa (c) DAC09 at 23 GPa

Figure 3.36: Coffinite sample inside DAC, the color of the coffinite sample gets darker upon pressure increase.

zircon-scheelite phase transition cannot sufficiently be distinguished. However, in here high-pressure Raman spectra of coffinite, $USiO_4$, are collected for the first time. The derived pressure shifts are in the range of those measured for zircon and hafnon. A negative value of the pressure shift for the first observed lattice mode, does agree with a strengthening of the lattice. Also the green color of the sample intensifies and gets darker during compression, see figure 3.36. A pressure induced $U^{4+} \rightarrow U^{5+}$ transition as proposed by Zhang et al.[97] cannot be confirmed and has to remain speculative.

Synchrotron Powder Diffraction

High-pressure synchrotron powder diffraction measurements were conducted under proposal I - 20120681 at P02.2 beamline at the PETRA III facility, DESY Hamburg. Data was collected on two samples, DAC09 and DAC27, on pressures up to 35 GPa and on decompression. In total, diffraction pattern of 25 pressure points were investigated. Starting pressure of DAC27 for the powder diffraction series was 20.2 GPa. At this pressure the pattern already shows the scheelite phase. Unfortunately, also a significant amount of α-SiO_2 is always present in this sample, which results from pressure induced crystallization of the amorphous silica present in the sample from the synthesis. This makes it difficult to fit the lattice parameters of the high-pressure phase. With further increase of pressure the reflections experience broadening until they become nearly unresolvable at 35 GPa, due to starting pressure induced amorphization of the sample. In figure 3.39 the compression and decompression of DAC27 is shown. The reflections become resolvable again upon decompression.
The second sample, DAC09, solely exhibits the pattern for coffinite at the starting pressure of 2.24 GPa. At about 18 GPa the high-pressure phase is observed and becomes dominating in the diffraction pattern further on (see figure 3.37). Above 23 GPa the zircon pattern can no longer be recognized, judging from the intensities of the coffinite (020) and (211) reflections. At this pressure the completion of the phase transition was also reported by Zhang et al. The XRD pattern of coffinite were refined over the complete range of pressure though. When the pressure of the cell is slowly decreased, allowing the sample to relaxate, the zircon type phase is completely recovered. The transformation from scheelite to zircon phase is be accompanied by hysteresis, as the scheelite phase still is present in the diffraction pattern at 12.6 GPa during the decompression.

Table 3.11: Lattice parameters from the Le Bail refinements of the X-ray powder diffraction measurements of $USiO_4$ at high pressure. *Data points measured during pressure decrease.

Pressure [GPa]	Lattice parameters [Å]			
	low-pressure phase zircon-type, $I4_1/amd$		high-pressure phase scheelite-type, $I4_1/a$	
	$a = b$	c	$a = b$	c
0.0001*	6.9960(8)	6.2709(9)		
2.24	6.9584(6)	6.2488(7)		
6.4	6.9015(4)	6.2119(5)		
9.4	6.8627(7)	6.1890(8)		
11.1	6.844(10)	6.176(11)		
12.5	6.8269(8)	6.1660(8)		
14.8	6.815(10)	6.157(11)		
15.4	6.7988(9)	6.149(10)		
18.1	6.730(13)	6.129(12)		
12.6*	6.800(12)	6.201(11)	4.801(3)	11.09(1)
20	6.590(3)	6.157(2)	4.768(3)	10.988(8)
22.2	6.552(3)	6.133(2)	4.761(4)	10.91(1)
24.6	6.531(18)	6.137(2)	4.743(2)	10.883(4)
26.6	6.508(2)	6.121(3)	4.712(2)	10.910(4)
28.2	6.508(15)	6.120(2)	4.711(1)	10.90(3)
31.3	6.43(2)	6.15(2)	4.648(6)	10.85(2)
35	6.402(2)	6.129(2)	4.625(1)	10.887(3)
30.2*	6.448(5)	6.136(6)	4.688(4)	10.93(1)
21.9*	6.558(3)	6.179(4)	4.743(3)	10.999(7)
15.0*	6.701(7)	6.137(8)	4.783(3)	11.091(8)
9.4*	6.827(3)	6.189(5)	4.865(3)	11.138(7)

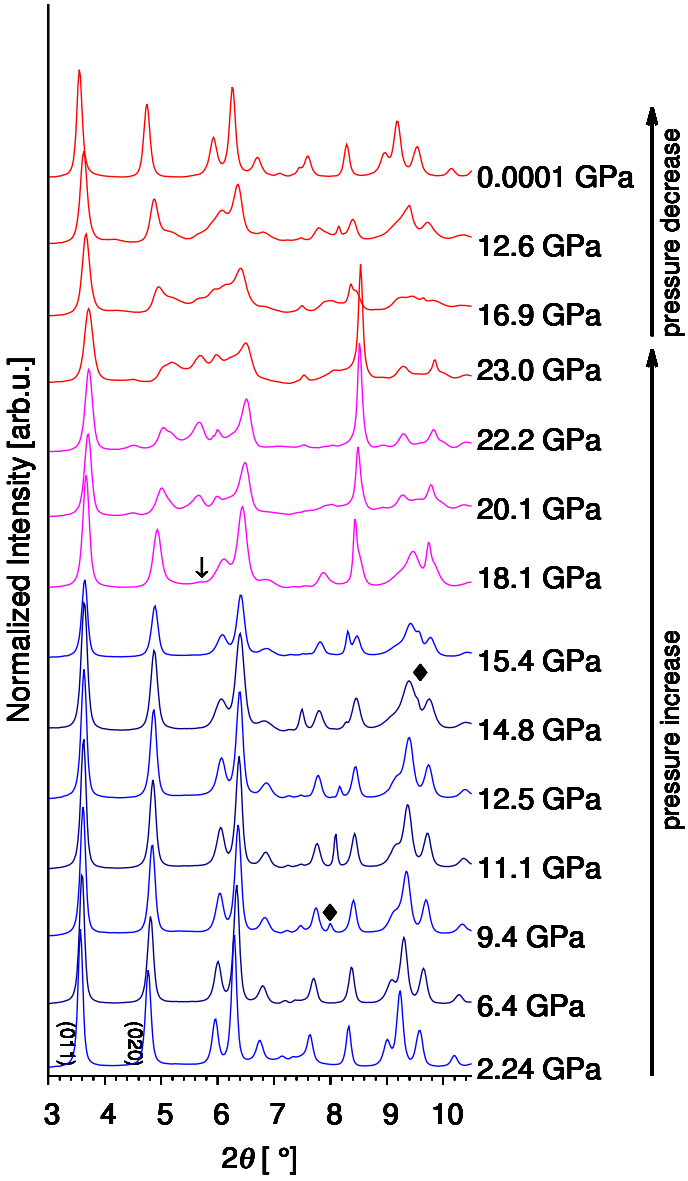

Figure 3.37: Compression-decompression series of DAC09, range 2.4 – 10.5° 2θ shown. Appearance of the scheelite phase at 18.1 GPa in (a) is indicated with an ↓. Sharp reflections, belonging to Ne indicated with an ♦, visible α-SiO_2 reflection marked with a ★.

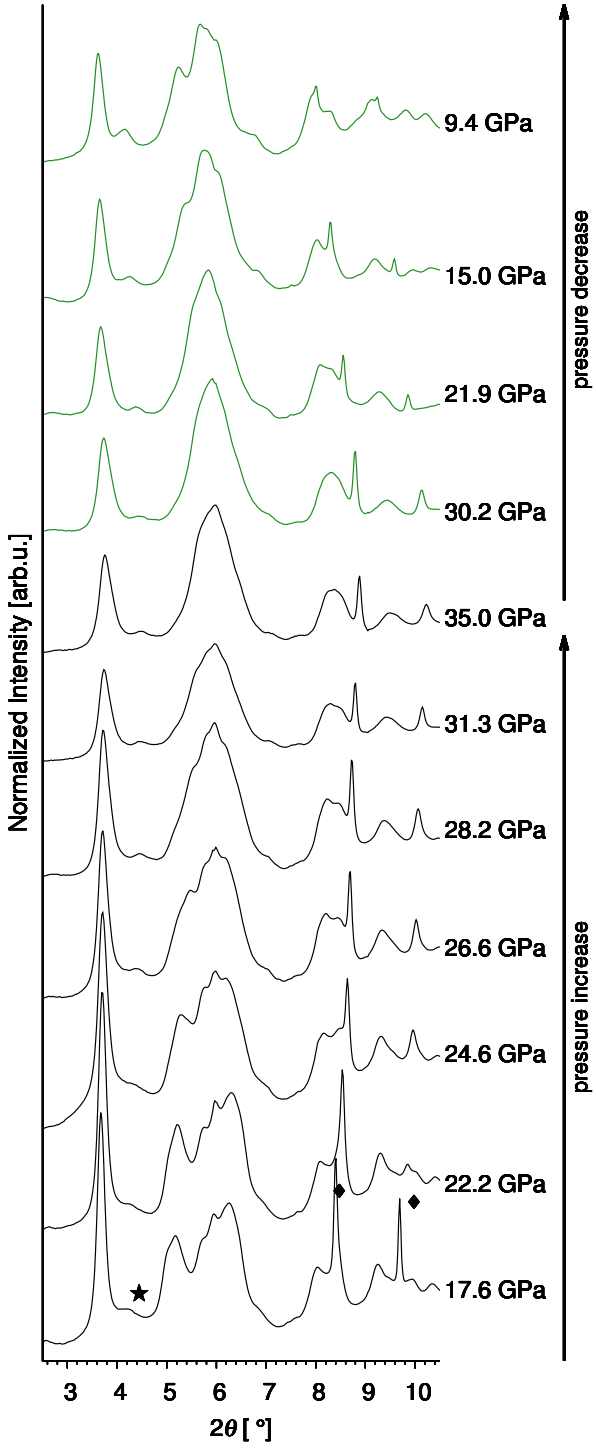

Figure 3.38: Compression-decompression series of DAC27, range 2.4 – 10.5° 2θ shown. Appearance of the scheelite phase at 18.1 GPa in (a) is indicated with an ↓. Sharp reflections, belonging to Ne indicated with an ♦, visible α-SiO_2 reflection marked with a ★.

The complete process of the phase transition from zircon to scheelite structure and the starting amorphization is shown in figure 3.39. During compression reflections shift to higher 2θ values (emphasized for (011) and (020) with dashed lines) corresponding to a decrease of the cell volume. At 20 GPa the shift of the zircon (011) reflection seizes. It seems to remain at the same position, just becoming broader with further pressure increase. Yet at the same time the (020) reflection disappears and the scheelite phase is beginning to dominate the diffraction pattern. Due to the similarities of normal and high-pressure phase the (011) reflection of the scheelite phase is at the same position as the zircon (011) reflection.

The pressure dependence of the unit cell volume is shown in figure 3.40. At 15 GPa the cell volume collapses from 283.3 $Å^3$ in the zircon phase to 253.7 $Å^3$ in the scheelite phase. This is a 10.6 % drop and corresponds to the expected higher density in the high pressure phase. An examination of the lattice parameters with increasing pressure shows the anisotropic behavior. The unit cell of the zircon-type is more compressible along a- and b-axis than along c-axis, therefore the c/a-ratio increases with increasing pressure (cf. figure 3.41a). From what is known for the reidite[1], it is expected, that the c/a-ratio of the high-pressure scheelite-type phase should decrease with increasing pressure. As can be observed in figure 3.41b though, the values are more scattered and an increase in the c/a-ratio becomes evident.

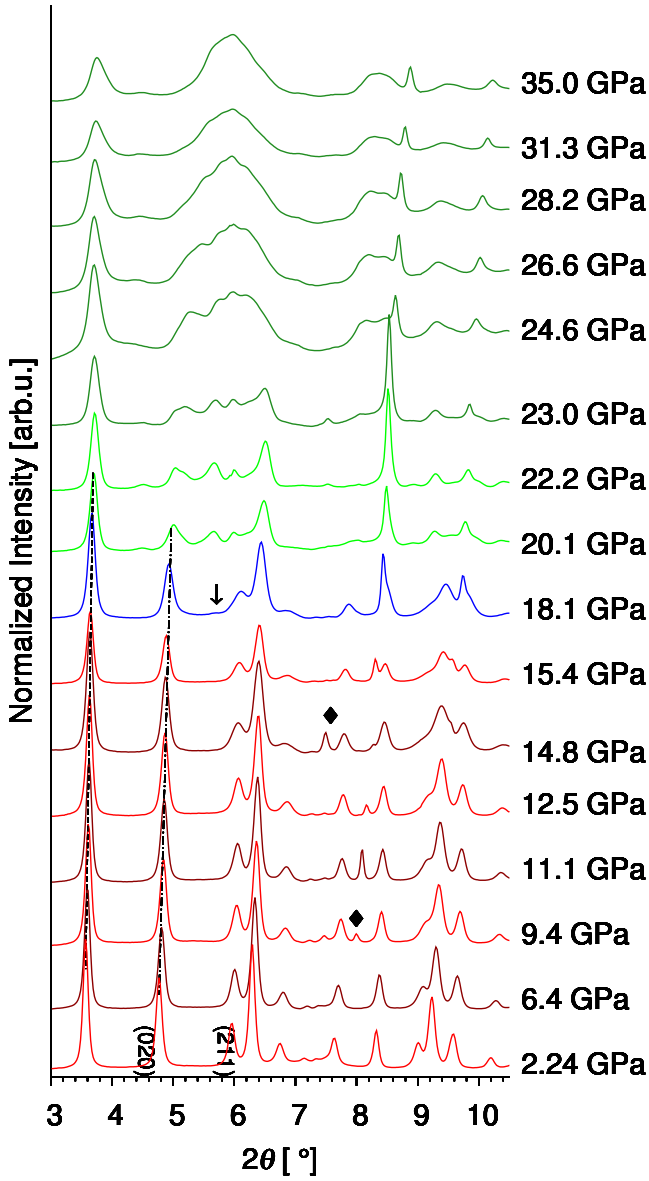

Figure 3.39: Compression series of $USiO_4$ (DAC09 and DAC27, range 3 – 8° 2θ shown). Appearance of the scheelite phase at 18.1 GPa is indicated with an ↓, the strong reflection at ∼ 7.5° 2θ at 14.8 GPa is indicated with a ♦ and assigned to Ne.

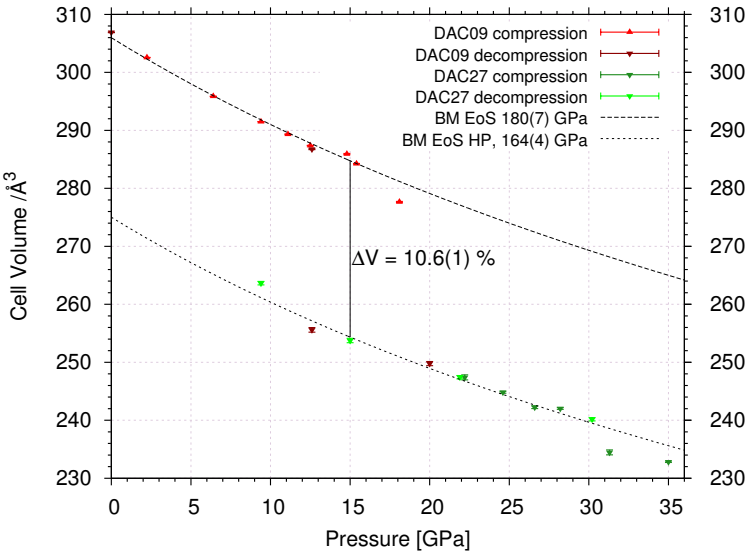

Figure 3.40: Unit cell volume vs. pressure of $USiO_4$. At $\sim$ 15 GPa the zircon-phase unit cell collapses and the scheelite-phase becomes more favorable.

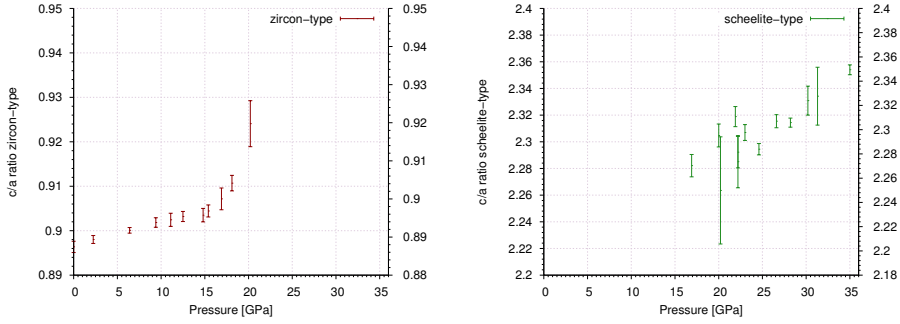

(a) c/a-ratio of the $USiO_4$ zircon phase vs. pressure, upon compression.

(b) c/a-ratio of the high pressure $USiO_4$ scheelite phase vs. pressure, measured upon compression and pressure decrease.

Figure 3.41: c/a-ratio of the low-pressure zircon (a) and high-pressure scheelite (b) phase of $USiO_4$ vs. pressure, measured upon compression and pressure decrease.

Above 15 GPa the data starts to derive from the Birch-Murnaghan model. ‡ [136;137] The phase transition is already taking place and neither low-pressure nor high-pressure phase can be satisfactory be described by the model. Trying to fit the data in this area would only result in a bad fit and erroneous values. Therefore 15 GPa is regarded as the critical pressure. By fitting *p-V* curve of coffinite below 15 GPa with a second order Birch-Murnaghan equation of state, yields a bulk modulus of K_0 = 180 ± 7 GPa (K_p, the pressure derivative of the bulk modulus, is fixed at 4).

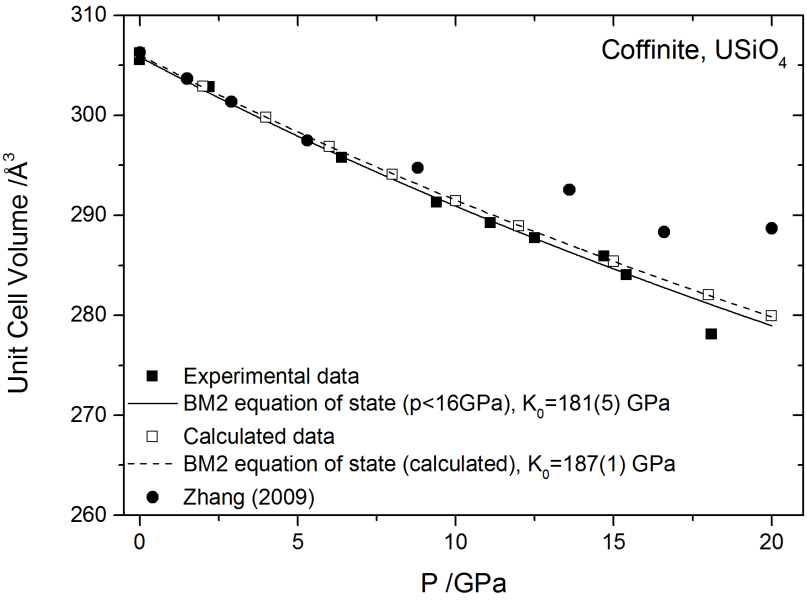

Figure 3.42: Birch-Murnaghan 2^{nd} order Equation of State fitted to coffinite *p-V* data. Comparison to the values presented by Zhang et al. (2009)[97] and *ab initio* DFT calculations performed by the group of Prof. Winkler. [138]

In figure 3.42 the data gathered in this study are compared to that from previous investigations and with the calculated equation of state. The value for the bulk modulus for coffinite is slightly lower than the 188(4) GPa calculated by Zhang. It has to be noted though, that in their study a methanol/ethanol/water mixture was used as pressure medium, which is known to not act ideally hydrostatic in higher pressure ranges. [39] This of course has impact on the pressure at which the phase transition is observed and in following consequence also on the bulk modulus.

‡The Murnaghan equation of state assumes the linear decrease of the unit cell volume (and lattice parameters) with increasing pressure, but taking into account a pressure dependent stiffening. The Birch-Murnaghan model ascribes this pressure dependency to the free energy F. After Taylor series expansion, the 2^{nd} order Birch-Murnaghan EoS with K_0' = 4 is derived as: $P(V) = K_0 \cdot \frac{3}{2}(\frac{V}{V_0}^{-\frac{7}{3}} - \frac{V}{V_0}^{-\frac{5}{3}})$. One advantage of the Birch-Murnaghan EoS over the simple Murnaghan model is that it is possible to easily obtain the internal energy.

Applying the linear relationship from Errandonea et al.[123]:

$$K_0 = 610(11) \cdot \frac{Z_A}{d_{A-O}^3} \tag{3.4}$$

(with Z_A being the formal charge of the metal cation, d_{A-O} is the average A-O distance in Å inside the AO_8 polyhedron and K_0 the bulk modulus in GPa) with the mean U-O distance d_{U-O} = 2.3685 Å for $USiO_4$ as determined by EXAFS measurements, and Z_A = 4 yields a bulk modulus $K_{0,calc1}$ of 184(33) GPa. This value also is in surprisingly good agreement with the gathered data. It is either way significantly less than the bulk modulus of zircon [227(2) GPa (Hazen et al.[139]), 205(8) GPa (Ono et al.[1])]. This corresponds also to Birch's Law[140] which states that because of the bigger unit cell it is more probable for coffinite to have a smaller bulk modulus than zircon.

Fitting the *p-V* data of the high-pressure scheelite phase above 15 GPa with a yields a bulk modulus of 164 ± 4 GPa. For the fit V_0, the unit cell volume at ambient pressure for the high-pressure scheelite phase, is fixed at 275.4 $Å^3$. This corresponds to the unit cell volume at ambient pressure of the zircon-phase minus 10% volume decrease as expected by the denser structure type $I4_1/a$. The value of the bulk modulus of the high pressure phase is significantly lower than that of 275(16) GPa calculated by Zhang et al.[97] and lower than that for reidite (high-pressure $ZrSiO_4$ phase; 305 GPa[1]). The bulk modulus of the high pressure scheelite phase is also lower than that of the zircon phase, which is rather unusual. Calculations expect the bulk modulus of the scheelite phases generally to be higher than those of the corresponding zircon phases.[126] For instance, the bulk modulus of the high pressure phase of $HfSiO_4$ has not been determined experimentally, though calculations by Bose et al.[126] predict it to be about 314 GPa. When applying equation 3.4 on the found bulk modulus of 164(4) GPa, an estimated mean U-O distance of $d_{(A-O)_{HP}}$ = 2.46 Å results. This is larger than the mean U-O distance of the zircon phase at ambient pressure and therefore not reasonable. The value of 164(4) GPa hence must be too low. The other bulk moduli of Zhang et al. ($K_{0,Zhang}$= 275(16) GPa) and Bose et al. ($K_{0,Bose}$=314 GPa) yield estimates of $d_{(A-O)_{Zhang}}$ = 2.07 Å and $d_{(A-O)_{Bose}}$ = 1.98 Å respectively. The formula given in equation 3.4 can only be applied under very limited aspects. It is not valid for formal charge $Z_A \geq 4$, meaning a possible $U^{4+} \longrightarrow U^{5+}$ transition. However, it is useful to illustrate a tendency for the average A-O distance and bulk modulus. The gathered data on the high pressure phase is not of the best quality. Additionally, it was not possible to quench the high-pressure phase and determine V_0, which has a big influence on the fit and the derived bulk modulus. The derived value therefore must be regarded as erroneous and surely too small.

Confocal micro-Raman

Raman spectra were collected in a range of 150 cm^{-1} to 1200 cm^{-1} and up to 18.7 GPa on the DAC27 sample. Under ambient pressure, five distinct peaks can be observed in the Raman spectra of $USiO_4$ (cf. figure 3.43), an additional very weak peak can be observed at 585 cm^{-1}. Deriving from group theory 12 Raman active modes are expected in the spectrum: $2A_{1g}$ + B_{1g} + B_{2g} + $5E_g$. It is not too surprising that not all possible modes are observed in this work. For hafnon eight modes have been observed at most,[125;141] studies on uranium doped zircon from Chernobyl "lava"[142] are missing modes in the spectra and in their high-pressure investigation of zircon Knittle and Williams[127] could not distinguish all modes either. In total all 12 possible modes have been documented by different investigators on these orthosilicates. High-quality Raman data on zircon[143;68] and thorite[144] allow a complete assignment of the spectra and are given in table 3.12.

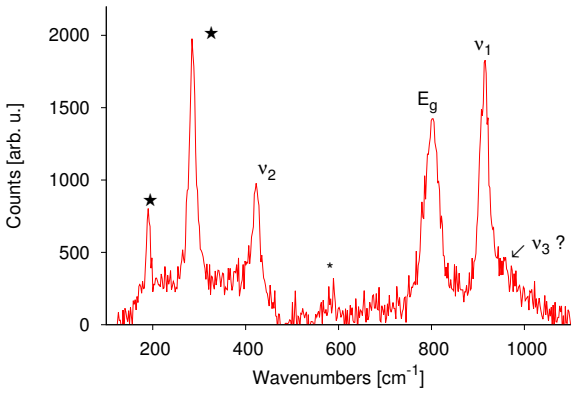

Figure 3.43: Raman spectra of coffinite, $USiO_4$, at ambient pressure and 300 K.

The region between 400 cm^{-1} – 1100 cm^{-1} is dominated by the internal stretching and bending modes of the SiO_4^{4-} tetrahedron, while the modes detected at 192 cm^{-1} and 290 cm^{-1} result from lattice modes, that is mainly motion of the U^{+4} cation.

The collected spectra up to pressures of 18.7 GPa are shown in figure 3.44. The mode at 914 cm^{-1} splits up into two sharp signals with increasing pressure. At 3 GPa a slight shoulder in the peak's form can be detected. Above 7 GPa there are undoubtedly two rather sharp peaks present (see figure 3.44). There are several possible explanations for this behavior. One is that the evolving shoulder above 3 GPa is a completely new lattice mode. From XRD data there is, however, no sign of a new phase at this time. As the other modes and pressure shifts remain unchanged, this also seems rather unlikely. Another possibility is that the assignment is wrong and the peak indeed belongs to a degenerate mode, where degeneracy is lost with pressure increase due to deformation of the lattice. This explanation also is more than unsatisfactory, as

Table 3.12: Ambient pressure frequencies and the calculated pressure dependencies of the Raman modes of coffinite, in comparison with those of hafnon[125] and zircon.[127] The peak assignements are made according to Syme et al.[144]

ν^0 [cm^{-1}]	$\frac{d\nu}{dp}$ [$\frac{cm^{-1}}{GPa}$] coffinite	$\frac{d\nu}{dp}$ [$\frac{cm^{-1}}{GPa}$] zircon	$\frac{d\nu}{dp}$ [$\frac{cm^{-1}}{GPa}$] hafnon	assignment
192	- 0.67 ± 0.12	-	-0.5	lattice mode E_g + B_{1g}
290	3.78 ± 0.13	3.2	2.7	lattice mode E_g
423	1.41 ± 0.07	1.1	1.1	A_{1g} (ν_2)
585	2.32 ± 0.27			B_{1g} (ν_4)
800	0.78 ± 0.23			E_g
914	4.42 ± 0.14	4.1	4.1	A_{1g} (ν_1)
924*	5.02 ± 0.13	4.8	4.6	B_{1g} (ν_3)

* ν^0 as derived from linear fit.

the next degenerate mode of the silicate-tetrahedron of E_g-type is not expected in so close to the stretching vibration. Furthermore, the pressure shift of the new peak is by any means too large for the E_g-mode. In fact it perfectly matches the expected value for the $\nu_2(SiO_4)$-mode. The B_{1g}- and the A_{1g}-mode overlap and at ambient conditions it nearly impossible to separate both. Taking now into account that an additional mode is expected here and knowing that the signal at 800 cm^{-1} does not belong to the A_{1g}-mode, it is to speculate if the broadening of the signal at 923 cm^{-1} towards the base can already be regarded as a sign of the B_{1g}-mode (see figure 3.43). Positions of the Raman mode frequencies from Geisler et al. suggest, that distance between $\nu_1(SiO_4)$ and $\nu_3(SiO_4)$-modes should decrease from hafnon over zircon to coffinite. The modes associated to the Si-O stretching vibration are lower than in the other orthosilicates. As the mode frequency is affected by the equilibrium Si-O bond length, it indicates that the Si-O bond is longer in coffinite than in zircon. This supports the longer Si-O distance, which has been found in the Rietveld refinement (see page 61).

The peak at 800 cm^{-1} attributed to E_g-mode barely shifts but broadens upon pressure increase and is hardly resolvable above 16 GPa. Knittel and Williams observed the same effect in their sample at 15 GPa, but argued that in their case the freezing of the pressure medium significantly contributed to this.

While all other modes drift to higher wavenumbers with increasing pressure, the first lattice mode experiences a negative pressure shift. This is conclusive with a general compression of the lattice and hence stronger intermolecular bonding. Above 10 GPa the peak becomes broader and the position appears to stop shifting. For hafnon similar behavior is reported.[125] Manoun et al. argued that this peak ought to be an overlap of E_g + B_{1g} modes, who have slightly different pressure shifts and split up at pressures higher than 14.3 GPa. Knittle and Williams only observed positive pressure dependence of modes in their spectra. Yet the estimated thermodynamic Grüneisen parameter showed a strong difference from the average spectroscopic

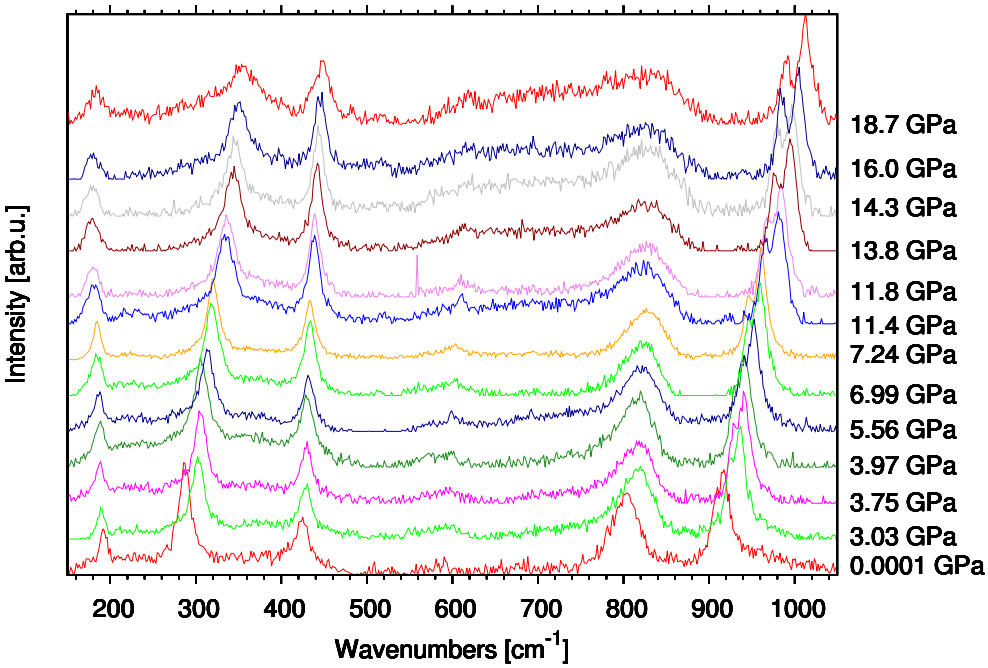

Figure 3.44: Raman spectra of coffinite, $USiO_4$, in the pressure range from 0 to 18.7 GPa

Grüneisen parameter. The only plausible explanation for this observation was an unobserved external mode in zircon with a negative pressure shift. Taking this all into account it can be concluded, that this is exactly what is observed here. An overlay of two external modes, with at least one showing a negative pressure dependence. From the quality of the gathered data it is not sensible to try to distinguish both peaks from each other and separately calculate their shifts. There are no obvious sudden changes or discontinuities in the spectra detectable up to 18.7 GPa. The pressure shifts for the $\nu_1(SiO_2)$ bending and the $\nu_3(SiO_4)$ and $\nu_1(SiO_4)$ stretching modes follow the tendency of hafnon and zircon (cf. table 3.12) and are well in the range for orthosilicates. Raman spectra collected from DAC27 after quenching the high-pressure phase unfortunately only showed amorphous scattering. DAC09 after relaxation established the spectra known of coffinite, but with slightly broader peaks, indicating small partial amorphization of the sample. Additional samples have been prepared in a DAC to collect high-pressure Raman spectra above 18 GPa and measurements have been undertaken but so far yielded data of only bad quality.

In this study the first high pressure investigation of synthetic $USiO_4$ without impurities of UO_2 is presented. Raman spectra of synthetic $USiO_4$ at ambient conditions and at high pressures up to 18.7 GPa were measured. The phase transition from zircon-type to scheelite-type was dis-

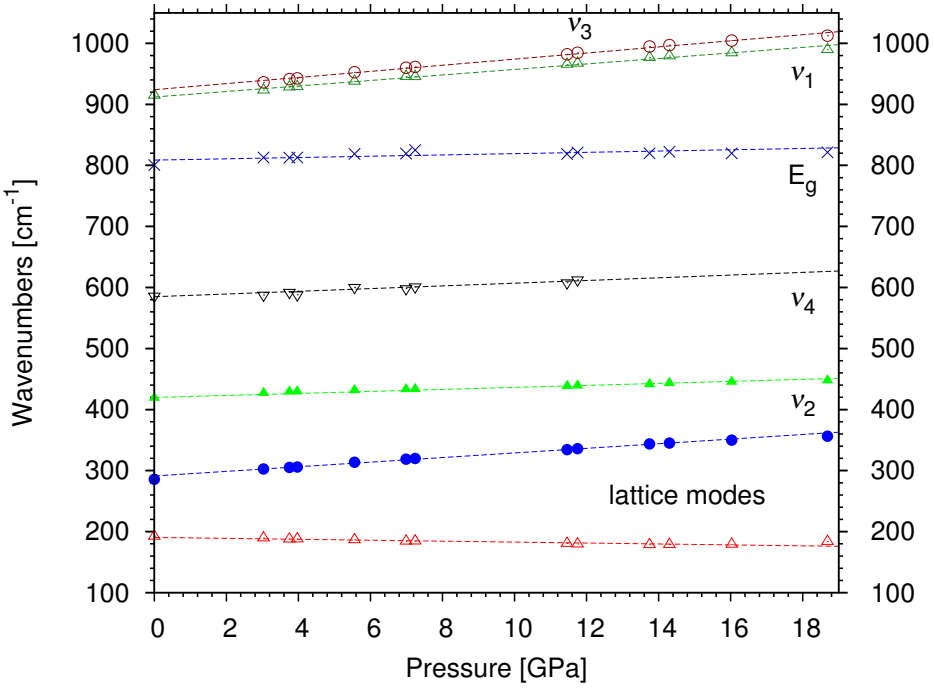

Figure 3.45: Raman frequencies as a function of pressure and linear fits shown. Errorbars are omitted.

tinctively studied and shown to happen at 15.5 GPa. The zircon-type $USiO_4$ phase completely disappears above 23 GPa, yet can be completely recovered when slowly releasing the pressure again. The phase transition, therefore, can be regarded as completely reversible. It is merely that, when the sample is compressed to pressures at about 35 GPa, partial amorphization takes place. This amorphous fraction, of course, cannot reverse into the zircon-type $USiO_4$. The reversibility has been observed not only in the X-ray diffraction pattern but also in the Raman spectra. From the pressure dependence of the cell volume the bulk modules for coffinite $USiO_4$ and scheelite-type $USiO_4$ were derived by second order Birch-Murnaghan equation of state fit. The bulk modulus for coffinite $USiO_4$ is 180(7) GPa and hence lower than those of $ZrSiO_4$ and $HfSiO_4$, as would be expected. The pressure dependence of the Raman modes was studied up to 18 GPa, yet no obvious changes appear. Furthermore, it could be established, that the B_{1g}- and the A_{1g}-modes of the SiO_4^{4-}-tetrahedron in the Raman spectrum are very close and overlap at ambient conditions.

3.2 Charcterization of Studtite and Metastudtite

3.2.1 Previous Studies

The minerals studtite ($UO_4{\cdot}4H_2O$) and metastudtite ($UO_4{\cdot}2H_2O$) are the only natural occurring peroxide minerals. These natural analogues of the uranium(VI)peroxides were not discovered until 1964 by Debets et al.[145] Well defined uranium(VI)peroxide was first synthesized in 1944 by Zachariasen[146] and its structural behavior during decomposition to UO_3 initially studied by Cordfunke and van der Giessen in 1963.[147] The interest in studtite, $UO_4{\cdot}4H_2O$ is from its potentially important role in a geologic repository for nuclear waste, specifically regarding the interactions of nuclear waste with the environment such as the pore water. In a nuclear waste repository the high alpha dosage will be the dominating factor after the first thousand years of storage. In combination with groundwater the α-radiation will lead to formation of H_2O_2. These very localized oxidative conditions could trigger the genesis of studtite or metastudtite even if the overall conditions are reducing. The formation of metastudtite on UO_2 samples as a direct effect of α-radiolysis of water was observed by Sattonay et al. in 2001.[148] $UO_4{\cdot}4H_2O$ (studtite) and $UO_4{\cdot}2H_2O$ (metastudtite) could be identified by Hanson et al.[149] as the only secondary phases left in a two year corrosion experiment on spent nuclear fuel (SNF). Also $UO_3{\cdot}xH_2O$ ($x<2$), metaschoepite, was found to form as an oxidation product on the surface of UO_2 samples. Upon leaching with aqueous H_2O_2 solution however, it is found to be completely replaced by studtite. The reaction mechanisms by which either phase forms are still largely unknown. Most studies on the safety assessment of nuclear waste repositories regarding the uranium component emphasize on the role of the silicates, oxides and oxyhydroxides. However, Forbes et al.[150] were able to demonstrate, that some of these earlier formed phases are susceptible to alteration to studtite. Recently Rey et al.[151] investigated the thermal decomposition of uranium peroxide with DSC-TG measurements. Hereby some old values could be precised and exact temperatures and enthalpy values for the following reactions could be established:
$UO_4{\cdot}4H_2O \rightarrow UO_4{\cdot}2H_2O$ (- 42 $^{kJ}/_{mol}$; studtite to metastudtite)
$UO_4{\cdot}2H_2O \rightarrow UO_3{\cdot}xH_2O$, $x<2$ (- 46.26 $^{kJ}/_{mol}$; metastudtite to amorphous metaschoepite).[151]
The standard enthalpy of formation for studtite was measured by Kubatko et al.[152] in 2003 to be -2344.7 $^{kJ}/_{mol}$. So far, no mechanism regarding the dehydration (e.g. water molecules exiting preferably parallel to b/c-plane) has been proposed. Burns and Hughes determined the crystal structure of studtite from a natural sample by single crystal diffraction.[153] The structure consists of chains of edge sharing [UO_8]-polyhedra. In between these chains water molecules are located. While there are different, yet very similar models for metastudtite,[154;2] so far no reliable structure has been found, no empirical solution is reported. It is highly probable that metastudtite, like studtite, consists of chains of edge sharing [UO_8]-polyhedrons though.

3.2.2 Synthesis

Studtite was synthesized from an acidic (pH $\sim$ 3) aqueous UO_2 suspension by very slowly adding 30 % H_2O_2 solution. The mixture is continuously stirred over night. After reaction the light yellow precipitate was filtered and washed several times with demineralized water and then dried at ambient temperature. Metastudtite was obtained by dehydrating the prepared studtite at 90 °C for 48 hrs.

Figure 3.46: Studtite, Metastudtite and the amorphous dehydration product (UO_3).

Deuterated samples were prepared in a glovebox continuously flushed with Ar. UO_2, which previously was dried for 48 hrs. at 90 °C under vacuum, was suspended in D_2O, 98 % and the mixture acidified with DCl, 6 M. Simultaneously the peroxide solutions was prepared by dissolving Na_2O_2, 98 % in D_2O. The peroxide solution is then very slowly added to the suspension and the mixture stirred over night. The yellow precipitate is filtered and washed several times with D_2O. The obtained material is dried at ambient temperature. Metastudtite was obtained by dehydrating the prepared studtite at 90 °C under Ar. Remaining Na in the samples was excluded by X-ray fluorescence.

3.2.3 Powder Diffraction

Initially studtite was described as a hydrated uranyl carbonate by Vaes in 1947.[155] After qualitative chemical analysis and XRD investigation Walenta[156] determined studtite to be identical to synthetic uranyl peroxide with monoclinic symmetry and either spacegroup *C* 2, *C m* or *C* 2/*m* with *a* = 11.85 Å, *b* = 6.80 Å, *c* = 4.25 Å, β = 93.51°, and Z = 2. Synthetic uranyl peroxide was first reported by Fairley[157] in 1877 as $UO_4 \cdot 4H_2O$. While different values for the amount of water (from 2 – 4.6 moles) were reported in earlier works,[158;159;160] Sato in 1961[161;162] demonstrated from IR and thermogravimetry studies, that two modifications, $UO_4 \cdot 4H_2O$ and $UO_4 \cdot 2H_2O$, of uranyl peroxide existed. The structure of studtite could finally be solved from single crystal diffraction by Burns and Hughes in 2003[153] to be monoclinic with spacegroup *C* 2/*c* with *a* = 14.068(6) Å, *b* = 6.721(3) Å, *c* = 8.428(4) Å, β = 123.356(6)°, and Z = 4. The real unit cell is hence double the size as determined earlier. Burns and Hughes reported, that in this case particular interest was laid on the investigation of weaker reflections. Furthermore, two different positions for water were found. According to analysis studtite consists of long chains of $[UO_8]$-polyhedra, which are connected via an O_2^{2-} - dumbbell. The chains run parallel to the c-axis (cf. figure 3.47c. In these chains U(VI) is present as UO_2^{2+} group, where the O atoms are in axial position. Four equal peroxide O atoms are positioned in the equatorial plane, with a U – O distance of $\sim$ 2.365 Å. In the equatorial plane two water molecules are also bound to the U atom, with a U – O distance of $\sim$ 2.395 Å. In between the chains crystal water is located, which is arranged along the a-axis as can be observed in figure 3.47a. The individual $[UO_8]$-polyhedra are tilted towards each other. Along the b-axis (see figure 3.47b) the chains therefore take a zig-zag-shape. Resulting from these information as molecular formula $UO_2(O_2)(OH_2)_2 \cdot 2H_2O$ is better suited to describe the structure of studtite, as it represents the peroxide group and the two types of water. Synthetic uranyl peroxide dihydrate, corresponding to metastudtite, was first structurally characterized by Zachariasen in 1944[146] as an orthorhombic unit cell with lattice parameters *a* = 6.50(3) Å, *b* = 4.21(2) Å, and *c* = 8.74(5) Å. Debets further investigated the structure and assigned it to spacegroup *I mmm*. By studying the thermal decomposition of studtite, Walenta[156] observed the dehydration to $UO_4 \cdot 2H_2O$ when heating the material to 60 °C. When he discovered, that the dehydration was irreversible, Walenta suggested, occurence of a natural analogon as possible. In 1983 Deliens and Piret[163] first described a natural mineral with composition $UO_4 \cdot 2H_2O$, which proved to be equivalent to synthetic $UO_4 \cdot 2H_2O$ and named it metastudtite. After the structure determination of studtite by Burns and Hughes, the authors suggested, that similar $[UO_8]$-polyhedra chains may as well be present in metastudtite (cf. figure 3.48). Since the repeat length of these chains, corresponding to two connected $[UO_8]$-polyhedra, is 8.428 Å,a lattice parameter of *c* = 4.21 Å is too short. The structure model with space group *I mmm* can hence definitely regarded as erroneous. First-principle calculation studies by Ostanin and Zeller[154] proposed an orthorhombic unit cell with space group *P nma* and lattice parameters *a* = 8.677 Å, *b* = 6.803 Å,

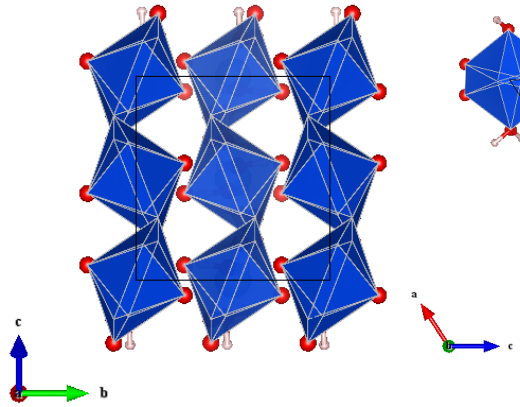

(a) Illustration of the structure of studtite in [100] direction. Tilted $[UO_8]$-chains can be observed.

(b) Illustration of the structure of studtite in [010] direction. The long $[UO_8]$-chains || to the c-axis are visible.

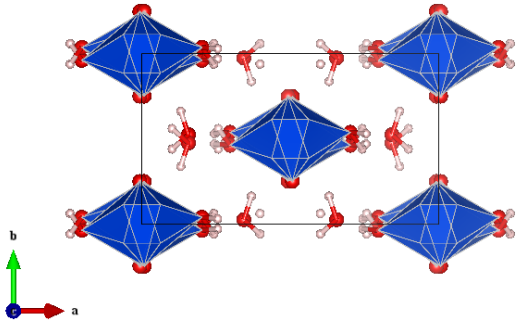

(c) Illustration of the structure of studtite in [001] direction. Note the position of the crystal water on the a-axis.

Figure 3.47: The structure of studtite according to single crystal diffraction measurements by Burns and Hughes.[153] Atoms and coordination polyhedra are shown, with U in blue, O in red and H in white.

and c = 8.506 Å, yet no atomic positions were given. Finally in 2012 Weck et al.[2] systematically studied the structural properties of studtite and metastudtite using DFT calculations. Therefrom metastudtite is supposed to crystallize in the orthorhombic space group *P nma* with a = 8.45 Å, b = 8.72 Å, and c = 6.75 Å. The work of Weck et al. is the first to report, i.e. in fact predict, atomic positions for the structure. To the best of my knowledge no empirical structure solution for metastudtite has been reported so far. As in studtite the U is hexagonal bipyramidally coordinated by six O atoms. The axial O comprise the UO_2^{2+} group with two short axial U=O bonds calculated to be 1.80 Å and 1.85 Å long, with a nearly linear angle ($\sim$ 179°. Equatorial O atoms are calculated at distances of 2.39 Å for the peroxo O atoms and 2.42 Åfor water O atoms.

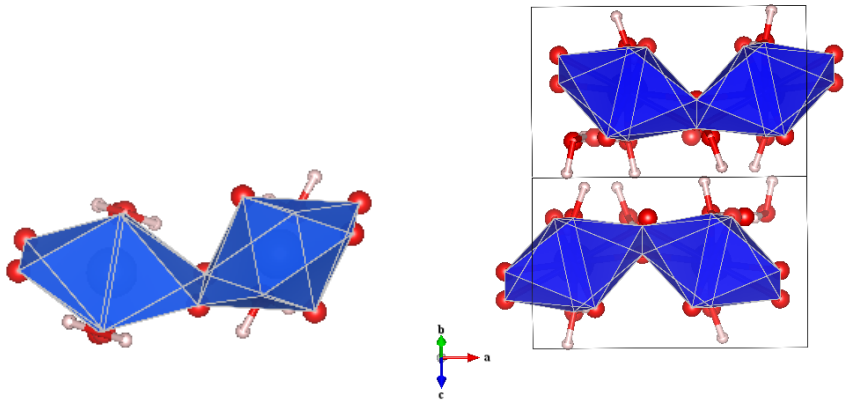

(a) Illustration of two connected coordination polyhedra, the smallest building block in the structure of studtite (acc. to Burns and Hughes [153]).

(b) Illustration of two connected coordination polyhedra, the smallest building block expected in the structure of metastudtite (acc. to Weck et al.[2], view along [011]).

Figure 3.48: Illustration of the smallest building block common to many polyoxouranylates [164]; present in studtite and suggested to be contained in metastudtite.

Again, the polyhedra are tilted towards each other and linked through the O_2^{2-} - group. In analogy to studtite being $UO_2(O_2)(H_2O)_2{\cdot}2H_2O$, metastudtite is best represented by the molecular formula $UO_2(O_2)(H_2O)_2$. The long $[UO_8]$ chains now run parallel to the b-axis in the proposed structure (see figure 3.49c). Crystal water is no longer present, and the chains are supposedly connected through hydrogen-bridging from the bound water, e.g. for instance distances between H and peroxo O atoms are $\sim$ 1.75 Å. Also coordination to the uranyl O appears probable (cf. figure 3.49a). According to the calculations, the tilting of the polyhedra towards each other slightly increases, the U–O–U angle decreases from 126 ° in studtite to 123 ° in metastudtite. A selection of the calculated values from Weck et al. is listed in table 3.19.

Structure Analysis

HRPD High resolution synchrotron powder diffraction measurements were conducted under proposal I - 20120660 at P02.1 beamline at the PETRA III facility, DESY Hamburg. After treating the collected data by Rietveld refinement employing the structure determination from Burns and Hughes,[153] lattice parameters could be refined to:

$C\,2/c$

a = 14.161(1) Å

b = 6.7865(5) Å

c = 8.5013(6) Å

β = 123.265(5) °

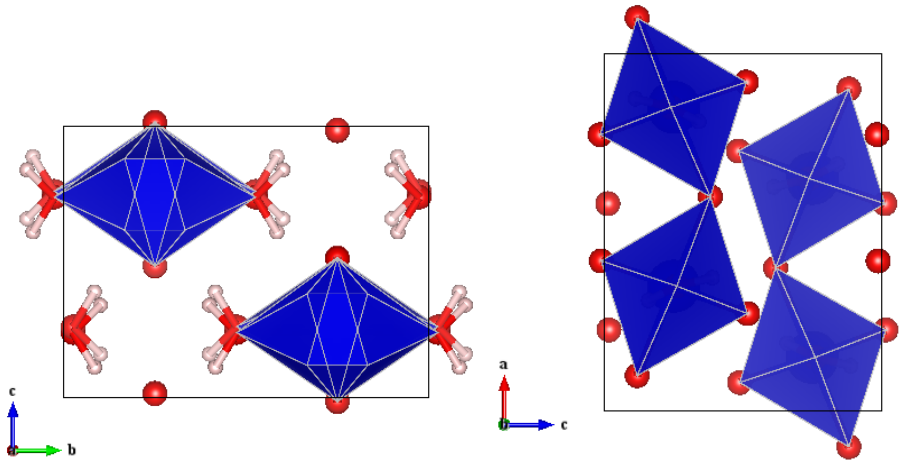

(a) Illustration of the structure of metastudtite in [010] direction (acc. to Weck et al.[2]).

(b) Illustration of the structure of metastudtite in [010] direction (acc. to Weck et al.[2]).

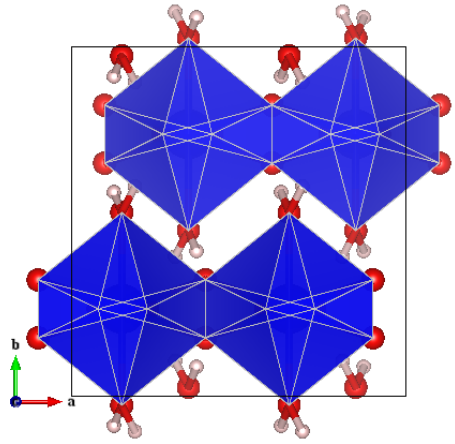

(c) Illustration of the structure of metastudtite in [100] direction (acc. to Weck et al.[2]).

Figure 3.49: The structure of metastudtite as proposed from DFT calculations by Weck et al.[2]).

*w*Rp = 7.22 %, Rp = 5.02 %.

The collected diffraction pattern and fit are shown in figure 3.50.

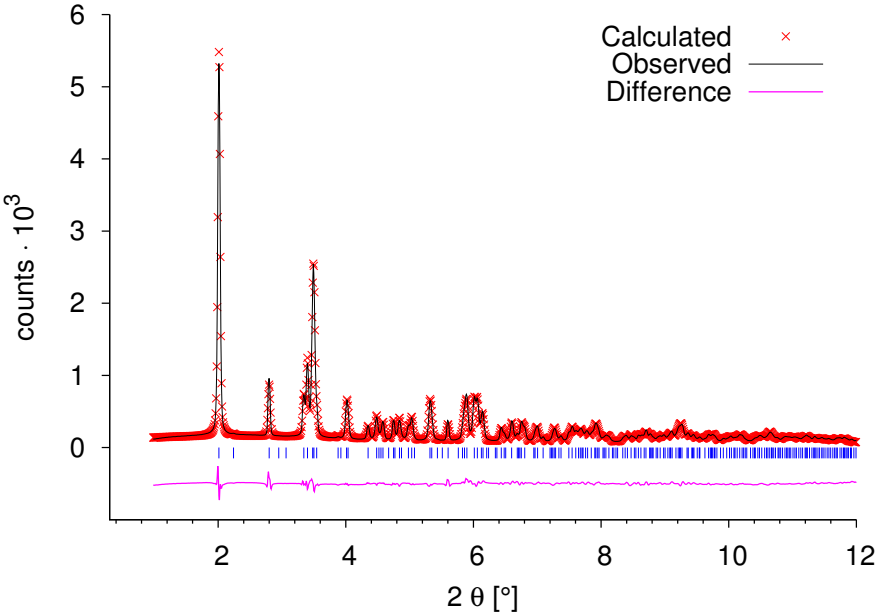

Figure 3.50: Rietveld refinement of studtite sample, calculated (red), observed (black) and difference (purple) curves shown. Reflection positions of studtite marked (blue). High resolution synchrotron measurement carried out om PETRA III P02.1, λ = 0.2073 Å.

Table 3.13: Refined atomic positions and fractional coordinates of studtite derived from Rietveld refinement of the HRPD data.

	Wyckoff position	*x*	*y*	*z*	U_{iso}
U1	4a	0	0	0	0.017
O1	8f	0.0081	0.750	0.063	0.008
O2	8f	0.0560	0.114	0.3027	0.008
O3	8f	0.1957	0.038	0.170	0.042
O4	8f	0.8455	0.4857	0.0667	0.019
H1	8f	0.255	0.03	0.317	0.03
H2	8f	0.242	-0.06	0.15	0.03
H3	8f	0.898	0.56	0.06	0.03
H4	8f	0.869	0.338	0.08	0.03

Hydrogen positions and isotropic displacement parameters were not refined. It appears, that displacement parameters for oxygen atoms O1 and O2 are too small.[45] Both atoms belong to the uranyl group, the U=O–bond length in this is group is typically between 1.6 – 1.9 Å. Determined from IR data, it should be $\sim$ 1.80 Å.[165] As oxygen is a light atom, it is very difficult to get good,

reliable U_{iso} next to such an extremely heavy atom as uranium from X-ray data, even when heavy damping during the fitting process is applied.

The collected data for the metastudtite sample was refined using he structure model of Weck et al.[2], listed in table 3.14. Diffraction pattern and fit are shown in figure 3.51 and the derived atomic coordinates from the refinement are listed in table 3.15. Lattice parameters could be refined to:

P nma

a = 8.4117(5) Å

b = 8.7631(5) Å

c = 6.4921(4) Å

*w*Rp = 7.15 %, Rp = 5.16 %.

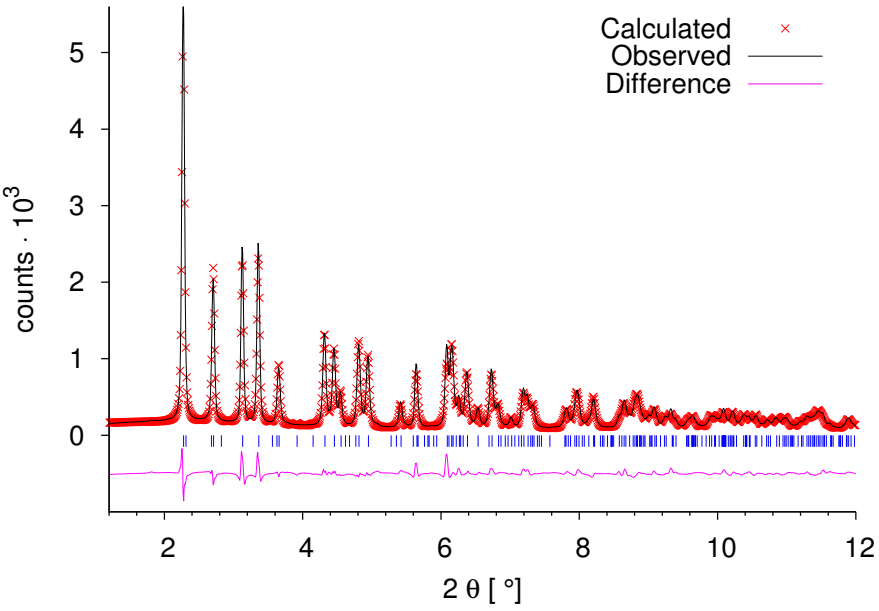

Figure 3.51: Rietveld refinement of metastudtite sample, calculated (red), observed (black) and difference (purple) curves shown. Reflection positions of metastudtite in proposed *P nma* structure marked (blue). High resolution synchrotron measurement carried out on PETRA III P02.1, λ = 0.2073 Å.

In this case it appears, that displacement parameters for oxygen atoms O2 and O4 are too small, while that of O3 (the peroxo group) is rather large. It has to be noted also, that the refinement of the U_{iso} of oxygen does not contribute much to a better fit and smaller wR_p and R_p values. However, this illustrates one of the biggest problems associated to these substances. Studtite and metastudtite consist only of the heavy atom and strong scatterer U and the very

Table 3.14: Atomic positions and fractional coordinates of metastudtite as derived from DFT calculations by Weck et al.[2] (space group *P nma*, Z = 4;*a* = 8.42, *b* = 8.78, *c* = 6.51 Å)

	Wyckoff position	*x*	*y*	*z*
U1	4c	0.150	0.250	0.750
O1	4c	0.227	0.250	0.016
O2	4c	0.080	0.250	0.488
O3	8d	0.599	0.833	0.382
O4	8d	0.150	0.974	0.761
H1	8d	0.127	0.584	0.889
H2	8d	0.190	0.600	0.659

Table 3.15: Refined atomic positions and fractional coordinates of metastudtite derived from Rietveld refinement of the HRPD data employing the model of Weck et al.[2] (space group *P nma*, Z = 4;*a* = 8.4114, *b* = 8.7641, *c* = 6.4923 Å)

	Wyckoff position	*x*	*y*	*z*	U_{iso}
U1	4c	0.127	0.250	0.744	0.011
O1	4c	0.110	0.250	0.032	0.030
O2	4c	0.115	0.250	0.473	0.002
O3	8d	0.610	0.867	0.332	0.139
O4	8d	0.050	0.986	0.771	0.006
H1	8d	0.218	0.544	0.806	0.013
H2	8d	0.303	0.654	0.952	0.013

light atoms O and H. As soon as the uranium positions in the structure are refined, the majority of the electron density is assigned; making a structure solution from powder data merely impossible [‡]. While the general surrounding of U in metastudtite is most certainly the same as in studtite, the long range order cannot be proven this easily. The fact, that the proposed $[UO_8]$–chains lie even closer in studtite and probably are connected through hydrogen bridging, further impedes this. Nevertheless, the interatomic distances derived from the synchrotron powder diffraction data are compared to those known from single crystal (studtite) or proposed by DFT calculation (metastudtite) in tables 3.16 and 3.19. To illustrate the distances and angles in question, a ball-and-stick representation of the $(UO_2)O_2(H_2O)_2$ complex, the common building block composing studtite and metastudtite, is shown in figure 3.52. The distances and angles derived for studtite seem in very good accordance to literature data. Yet, the peroxide O–O bond causes problems. The derived value is certainly too small for studtite, it is too long in the metastudtite refinement. The O–O distances in studtite and metastudtite are supposed to be the same, judging from Raman studies.[166] A possible explanation might be sought in the employed method. The used X-rays interact with the electron density in the structure. In the O–O group the bonding situation is such, that not not only the bonding molecular orbitals are occupied, but

[‡]Attempts to do this using EXPO2009[54] were not successful so far. Maybe employing the Patterson-method will turn out as frugal, as the general situation is similar to that in organic structures containing heavy metal atoms, like e.g. some organometallic complexes.

also the $2\pi_x^*$ and $2\pi_y^*$-orbitals. This means, that even more electron density is located between the oxygen atoms and lacking at the individual O atoms, making the distance appear shorter. On the other hand, if in metastudtite the $[UO_8]$-chains are interconnected by strong hydrogen bridging on the peroxo oxygen atoms, this might shift and smear the electron density more towards the outer edges of the O_2^{2-}-dumbbell. Consecutively, the O–O distance appears longer than expected.

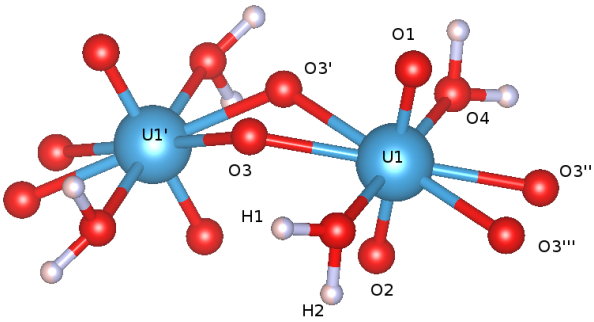

Figure 3.52: Ball-and-stick representation of the $(UO_2)O_2(H_2O)_2$ complex composing studtite and metastudtite.

Table 3.16: Selected interatomic distances [Å], angles [°] in the structures of studtite derived from HRPD and NPDF data and reported in literature.

Parameters	Studtite		
	exp. Burns [153]	from HRPD	from NPDF
U1–O1	1.769(7)	1.7619(1)	1.8014(2)
U1–O2	1.769(7)	1.7619(1)	1.8014(2)
U1–O3	2.351(6)	2.3447(1)	2.3418(2)
U1–O3”	2.365(6)	2.3677(2)	2.3586(2)
U1–O4	2.395(7)	2.3335(2)	2.3363(3)
U1–U1	4.214	4.251	4.2073(4)
O3–O3’	1.46(1)	1.326	1.4675(2)
O4–H1	0.976	1.061(1)	1.0165(1)
O4–H2	0.975	1.011(1)	1.0250(1)
O2–H_2O	2.0136(1)	1.9221(1)	1.805(1)
O3–H_2O	1.8109(1)	1.7849(1)	1.869(1)
O1–U1–O2	180.00	180.00	180.00
O1–U1–O3	89.76	86.87	89.85
O1–U1–O4	86.53	86.45	89.77
O2–U1–O3	90.27	93.14	90.15
O2–U1–O4	93.47	93.55	90.23
O3–U1–O3’	36.17	32.69	36.38
O3–U1–O3”	180.00	180.00	180.00
O3–U1–O3”’	143.83	147.31	143.62
O3–U1–O4	71.32	73.51	70.70
U1–O3–U1’	126.60	128.85	127.04

NPDF As stated before, one of the major difficulties in the structure determination from X-ray powder diffraction is the presence of a very heavyweight atom next to a lightweight atom. The atomic form factors in X-ray diffraction are related to the electron number of an atom, as well as to the angle at which a reflection appears. In neutron diffraction, this is different as neutrons interact with the atoms core and not the electron hull. Therefore, the scattering behavior is different to that of X-rays. With neutron diffraction it is possible to detect lightweight atoms next to heavyweight atoms, even the determination of hydrogen positions in a structure is possible. However, as hydrogen itself has an enormous scattering cross section and leads largely to incoherent scattering, deuterated samples are necessary for this technique. Deuterated studtite and metastudtite were prepared for neutron powder diffraction on the NPDF instrument at the Los Alamos Neutron Science Center (LANSCE) - Manuel Lujan, Jr. Center. After preparation the general crystallinity of the samples was checked with XRD, while the deuteration of the samples was confirmed by IR spectroscopy. Due to technical reasons however, samples could not be measured at the designated beam time in Aug. 2012, but not until Feb. 2013. Samples were kept in closed V vials, flushed with Ar but not in a glovebox or under completely protective atmosphere. During the measurements it appeared, that the samples now contained a noticeable amount of hydrogen, leading to a big background signal. The H/D-ratio could be refined from the data to be 0.55/0.45, meaning that significant hydrogen exchange possibly from humidity in the air has taken place. Also reflections of UO_2, not reacted reagent, were visible. Rietveld refinement was carried out by first refining the bank 2 and 4, i.e. at 90 and 148 °, then subsequently adding bank 3 and 1, i.e. 119 and 46 °. As it showed, bank 1 suffered from a very miserable background, has the least resolution, and did not contribute any valuable information into the fitting process, hence it was again discarded for the refinement. The background subtracted diffraction pattern of the studtite sample is shown in figure 3.53, the derived atomic positions are listed in table 3.17. A comparison between the atomic distances and angles from the different refinements and the literature data for studtite are shown in table 3.16.

Table 3.17: Refined atomic positions and fractional coordinates of studtite derived from Rietveld refinement of the NPDF data; space group $C\,2/c$ with Z = 4, a = 14.011(1), b = 6.7151(7), c = 8.4147(8), and β = 123.23.

	Wyckoff position	x	y	z	U_{iso}
U1	4a	0	0	0	0.0055
O1	8f	0.0079(7)	0.7460(10)	0.0751(10)	0.0169
O2	8f	0.0626(5)	0.1114(11)	0.3060(10)	0.0058
O3	8f	0.2012(7)	0.02051(12)	0.1832(12)	0.0288
O4	8f	0.8413(5)	0.4795(11)	0.0525(8)	0.0052
H1	8f	0.263(4)	0.085(6)	0.308(7)	0.0151
H2	8f	0.231(4)	-0.122(9)	0.224(7)	0.0213
H3	8f	0.915(4)	0.586(6)	0.103(6)	0.0092
H4	8f	0.870(4)	0.363(7)	0.120(7)	0.0116

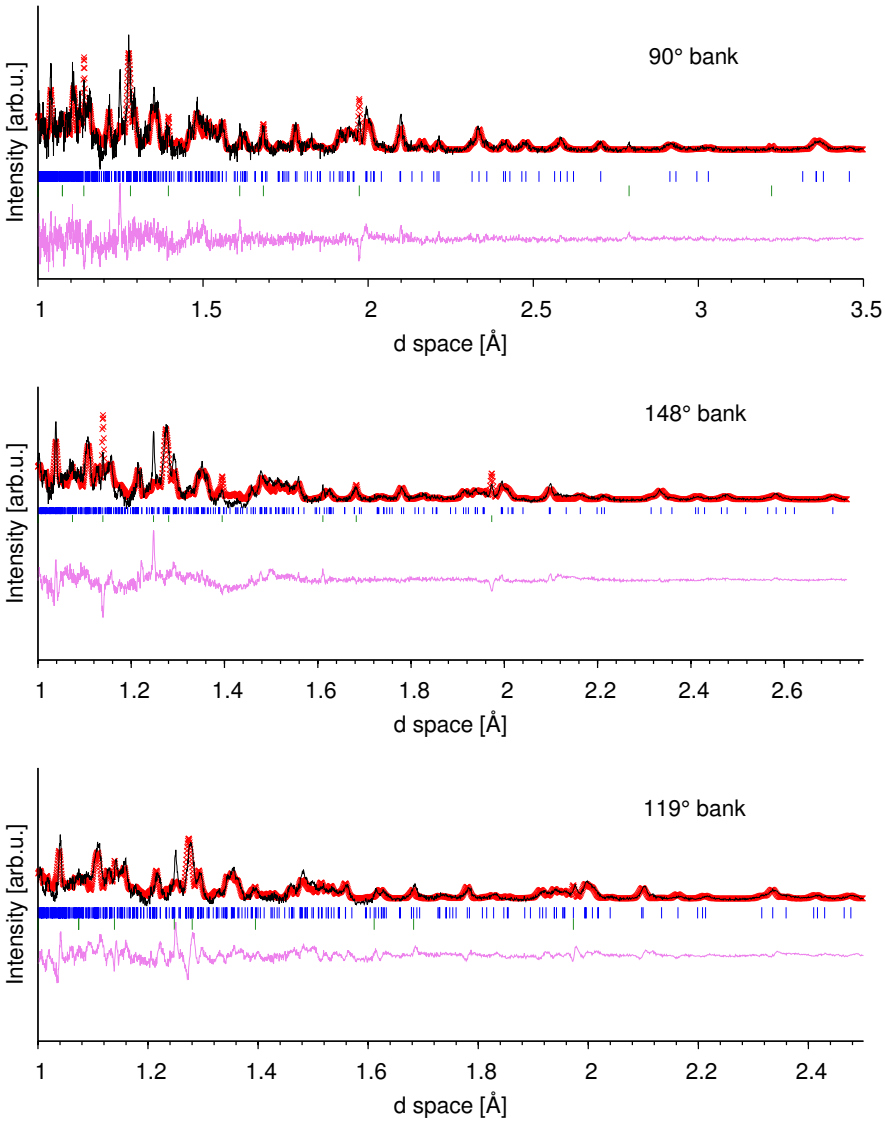

Figure 3.53: Rietveld refinement of studtite sample, calculated (red), observed (black) and difference (purple) curves shown. Data from banks at 90, 119 and 148 ° are shown in the range 1 – 2.5 Å. Neutron powder diffraction measurement carried out at NPDF, LANSCE Lujan Center.

The metastudtite sample was even more problematic concerning the hydrogen exchange. Here the H/D-ration was refined to roughly 80/20, meaning even after 14 hrs. of measuring, the reflection profile was rather poor. The collected data was nevertheless treated with Rietveld refinement, employing the structure model, proposed from Weck et al.[2], but using the refined lattice parameters and fractional coordinates obtained from the HRPD measurement as starting values. While this time no remaining UO_2 could be observed, unidentified reflections are found at $\sim$ 2.13 Å and 2.32 Å (cf. figure 3.54, marked with an asterisk).

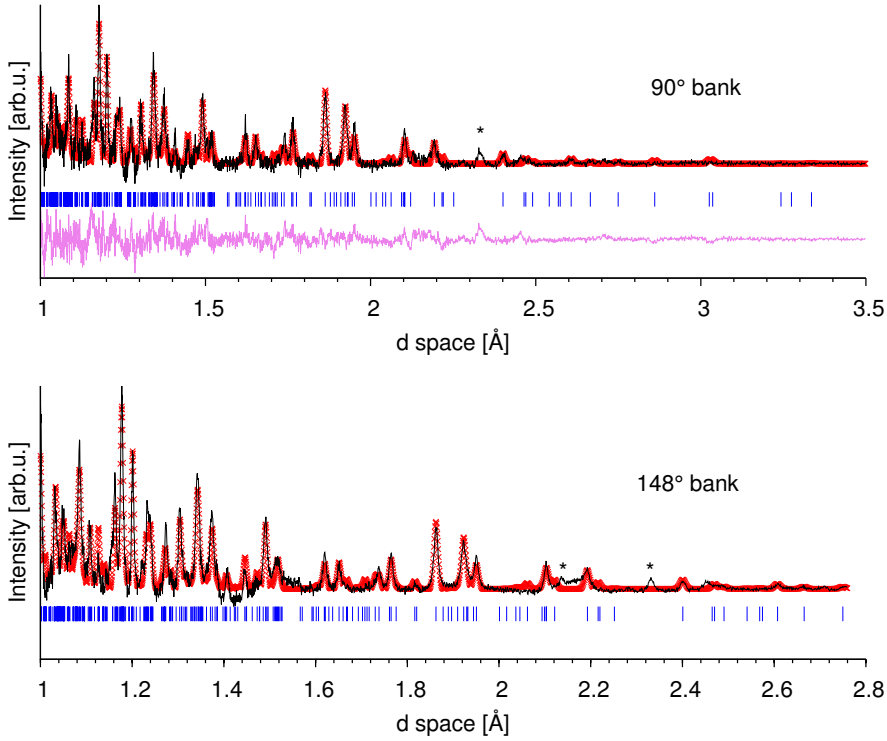

Figure 3.54: Rietveld refinement of metastudtite sample, calculated (red), observed (black) and difference (purple) curves shown. Reflection positions of metastudtite in proposed *P nma* structure marked (blue). Data from Banks at 90 and 148 ° are shown, neutron powder diffraction measurement carried out on the NPDF instrument, LANSCE Lujan Center.

The analysis of this specific dataset proved to be particularly difficult. During refinement it was observed, that, if no strong damping was applied, the atomic displacement parameter for U tended to become negative, which is a most unusual behavior. Also, when refining atomic positions, oxygen O1 would tend to shift too close towards U, resulting in unreasonably short U-O distances even below 1.5 Å. Owing to the data quality only banks 2 and 4, i.e. at 90 and 148 ° were used in the refinement. After converging the lattice parameters a = 8.4142 Å, b

Table 3.18: Refined atomic positions and fractional coordinates of metastudtite derived from Rietveld refinement of the NPDF data employing the model of Weck et al.[2] space group *P nma*, Z = 4 with *a* = 8.4142 Å, *b* = 8.7711 Å, and *c* = 6.4854 Å.

	Wyckoff position	*x*	*y*	*z*	U_{iso}
U1	4c	0.112(1)	0.250	0.745(2)	0.007
O1	4c	0.037(2)	0.250	0.028(3)	0.068
O2	4c	0.072(7)	0.250	0.500(2)	0.023
O3	8d	0.646(1)	0.8305(6)	0.381(1)	0.014
O4	8d	0.127(2)	0.9730(5)	0.756(2)	0.013
H1	8d	0.118(4)	0.604(2)	0.864(3)	0.014
H2	8d	0.203(2)	0.585(2)	0.730(4)	0.014

= 8.7711 Å, and *c* = 6.4854 Å and the fractional coordinates listed in table 3.18 are retrieved, selected bond distances and angles are compared in table 3.19. The resulting structure from the neutron diffraction data is quite interesting. While one U–O bond (U1–O2) is extremely shortened, the other (U1–O1) is enlarged and tilted toward the peroxo group. The uranyl group (O1–U1–O2) is no longer linear or slightly bend as suggested from the DFT calculations or the HRPD data, instead an angle of 143 ° is now obtained. On the one hand, this value so strongly derives from the expected near 180 °, that the complete result could be discarded, attributed to the bad data quality. Kubatko on the other hand reports several polyoxouranylate structures with uranyl angles as low as 160 – 145 °[164]. It is therefore not impossible for the uranyl group to establish such a strongly bend formation. The resulting structure should nevertheless be treated with extreme caution.

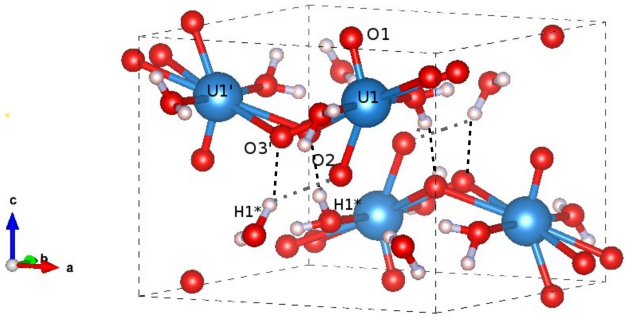

Figure 3.55: Ball-and-stick representation of the unit cell of metastudtite in the modified model. The black dashed lines represent probable hydrogen-bridging, the grey dashed lines probable coordination.

Taking the new model for further structure refinement on the collected HRPD data for metastudtite improves the fit to wR_p = 6.88 % and R_p = 5.62 % with *a* = 8.4251 Å, *b* = 8.7772 Å, and *c* =

Table 3.19: Comparison of selected interatomic distances [Å], angles [°] in the structures of metastudtite retrieved from HRPD and NPDF measurements and proposed in literature.

Parameters	Metastudtite			
	DFT Weck[2]	from HRPD	from NPDF	HRPD new model
U1–O1	1.85	1.8261(1)	1.973(2)	1.8274(1)
U1–O2	1.80	1.8804(1)	1.643(1)	1.8149(1)
U1–O3	2.39	2.3743(1)	2.31(1)	2.3647(1)
U1–O3”	-	2.4054(1)	2.45(1)	2.4353(1)
U1–O4	2.42	2.4269(1)	2.432(4)	2.4179(1)
U1–U1’	4.21	4.2061(2)	4.2077(4)	4.2128(3)
O3–O3’	1.46	1.5781(1)	1.41(1)	1.5648(1)
O4–H1	1.00	1.045	0.97(2)	0.9882
O4–H2	1.00	0.976	0.84(2)	0.9178
O1–U1–O2	178.8	172.97	143	149.47
O1–U1–O3	88.2	88.04	47.5	54.44
O1–U1–O4	88.4	88.91	88.7	85.42
O2–U1–O3	92.9	91.17	98.3	96.98
O2–U1–O4	91.7	90.81	91.9	92.99
O3–U1–O3’	35.5	38.82	35.7	37.48
O3–U1–O3”	179.9	179.17	176.6	180.00
O3–U1–O3”’	144.5	141.43	145.3	141.97
O3–U1–O4	71.6	73.00	72.3	74.97
U1–O3–U1’	123.7	123.29	124.52	122.72

6.5028 Å and reasonable bond lengths (cf. last column in table 3.19). Also the angle of the uranyl group has increased to $\sim$ 150 °, which again is in a possible range.[164] The distance between H1 and O3 is short enough for hydrogen bridging to appear. Strong hydrogen bridging between O3–H1 with a distance of 1.745 Å seems highly probable. Through the tilt of O2 towards the peroxo group, coordination of H1$\cdots$O2 ($\sim$ 2.05 Å) as illustrated in figure 3.55 by the grey-dashed lines, is reasonable. This structure for metastudtite appears heavily connected, leading to high stability. Furthermore, it gives a reasonable explanation to why it is not possible to obtain "water free" uranium peroxide.

In addition to the pure plausibility of the models, the congruence with the diffraction pattern needs to be taken into account. Here, the absence or unexpected appearance of reflections is of significance. Upon closer investigation of the diffraction pattern the small (220) reflection at $\sim$ 3.90° 2θ (λ = 0.2073 Å) is expected from the Weck as well as the modified model, but not observed. It has to be noted, that the expected intensity of this unobserved reflection is smaller when using the Weck model. The shoulder of the reflection at 5.09° 2θ is not indexed by either model.

EXAFS While the EXAFS data alone are not too conclusive for the structure, they allow for a more detailed investigation of the local environment of studtite and metastudtite. EXAFS spectra were collected on the BM-20 (ROBL) at ESRF in Grenoble at a temperature of 15 K. In table 3.20 the obtained interatomic distances are compared to those very recently reported by Walshe et al.[167] For comparison the EXAFS spectra of metastudtite was fitted employing a structure model based on the local coordination studtite, the modified structure model and the *ab-initio* model from Weck et al.[2] When fitting the spectrum by employing the scattering paths

Table 3.20: Atomic distances [Å] in studtite and metastudtite from EXAFS measurement and reported in literature.

	Studtite		
Bond type	this study	Walshe et al.[167]	
U–O	1.80	1.78	
U–O_{peroxo}	2.37	2.36	
U–O_{aquo}	2.46	2.50	
U–U	4.26	–	
	Metastudtite		
Bond type	this study	Walshe et al.[167]	Weck et al.[2]
U–O	1.79	1.79	1.81
U–O_{peroxo}	2.33	2.32	2.36
U–O_{aquo}	2.43	2.52	2.42
U–U	4.23	–	4.21

of studtite, the resulting atomic distances are the same as using the modified model as a base. It strongly impacts the fit, however, when the Weck model is used, the overall fit is unsatisfactory; the U–O_{peroxo} distance appears too long, U–O_{aquo} too short. The uranyl-bond appears to remain the same in studtite as in metastudtite within the experimental error. The distance of U–O_{peroxo} has decreased from the dehydration of studtite to metastudtite. This observation has also been made in the study of Walshe et al.[167] Yet the authors report extremely long U–O_{aquo} distances for both materials. It is a pity that the authors have not reported the U–U distances in their study. With the good scattering properties of U this would have been easily to include in the fit. In studtite, as well as in metastudtite, the U–U bond appears at 4.26 Å and 4.23 Å, respectively. In the k^3 weighed FT-magnitudes shown in figure 3.56 it can be well observed, that the signal of metastudtite differ however from that of studtite. Instead of one peak, it appears as if two features are present. The earlier peak, indicated with an asterisk, does not belong to the U, but must result from a heavy backscatterer at that distance. This leads to the assumption of two different U in the second coordination sphere. But a sufficient explanation is lacking at present. This information should be further investigated and taken into account, when evaluating other structure models for metastudtite. A complete summary of the EXAFS results is given in table VIII on page xv in the appendix. The interatomic distances for studtite from EXAFS

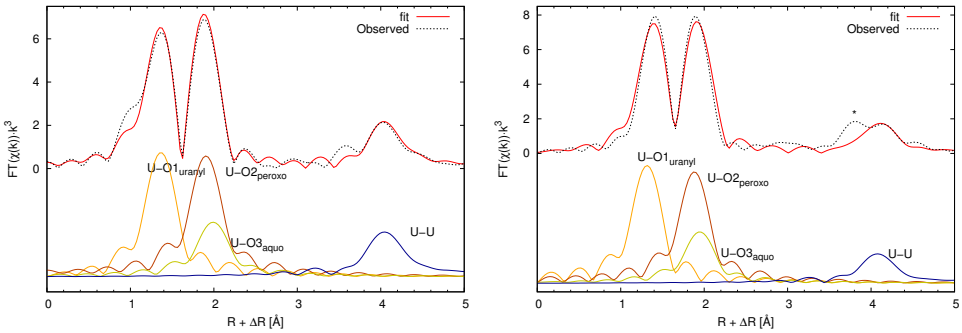

(a) FT-magnitudes of studtite, best fit with scattering paths shown below.

(b) FT-magnitudes of studtite, best fit with scattering paths shown below.

Figure 3.56: k^3 weighed FT-magnitudes of the EXAFS from the UL_3-edge of studtite (a) and metastudtite (b).

derive a bit from those of the XRD measurements. The uranyl-bond lengthened by 0.04 Å in the spectrum, even more does the U–O_{aquo} distance appear only with 2.33 Å from XRD, while it is 2.46 Å from the EXAFS spectrum. On the other hand, the datasets for metastudtite prove to correspond rather well. The U–U distance of both samples are comparable to those from XRD.

The presented data provides the positions for hydrogen in the studtite structure from the NPDF data. Furthermore, the structure model from Weck et al.[2] for metastudtite with space-group *P nma* could be validated from HRPD data. It was possible to further refine this model with the hydrogen positions derived in the NPDF investigation. EXAFS data allowed to compare these data with the local coordination sphere of both materials. Also it indicated, that the modified structure model for metastudtite is plausible. However also new features were observed, which require further attention. The performed investigations will provide a good dataset for future research on the studtite–metastudtite phase relationship. The refinement of the HRPD measurement with the structure derived from NPDF allows to discuss the bonding situation of water concerning hydrogen-bridging and coordination in metastudtite. It will allow for insight into why this material is so much more stable than studtite.

Dehydration behavior

One focus of this work is the studtite–metastudtite phase relationship. Metastudtite can be obtained by heating studtite, until it looses 2 H_2O. In order to ensure a good comparability with literature data [162;168;151] and to confirm phase purity, DSC-TG measurements on the samples of the studtite, metastudtite and amorphous dehydration product were carried out.† For studtite two weight losses, at 80 °C and 224 °C respectively, in the TG-curve can be detected. Both correspond to endothermic peaks in the DSC-curve as can be seen in figure 3.57. The first weight loss can be attributed to the dehydration reaction to metastudtite by loosing 2 H_2O, the second weight loss hence corresponds to the decomposition to the amorphous $UO_3{\cdot}xH_2O$. The DSC and TG-curves of metastudtite feature only the second weight loss at 212 °C, accompanied by an endothermic peak. The variance of temperatures, which are reported for the studtite – metastudtite reaction, is remarkable. Table 3.21 gives a small overview on the reported values. Even the last publication by Rey et al. [151] lists two different temperatures, when only taking into account the values obtained from the DSC peak maxima. All three samples show a weight loss at 555 °C, which is overall exothermic. Yet a small endothermic peak can be distinguished upon close examination in the DSC-curve. This feature is discussed controversially in literature. While it can simply be attributed to the reaction of $UO_3{\cdot}xH_2O$ to UO_3, [162;147] it has also been assigned to the subsequent reaction to U_3O_8. [168;151] Unfortunately, it was not possible to characterize the remaining sample after DSC-TG measurement. On closer investigation, it appears, that the

Table 3.21: Overview of temperatures for the reaction $UO_4{\cdot}4H_2O \rightarrow UO_4{\cdot}2H_2O \rightarrow UO_3{\cdot}xH_2O \rightarrow UO_3$ found by DSC and in literature.

$UO_4{\cdot}4H_2O$ to $UO_4{\cdot}2H_2O$	$UO_4{\cdot}2H_2O$ to $UO_3{\cdot}xH_2O$	$UO_3{\cdot}xH_2O$ to UO_3	reference
	180 °C		Duval 1949 [169]
	90–190 °C		Boggs and El–Chehabi 1957 [170]
∼ 140 °C	220 °C	320 °C	Ukazi 1959 [168]
	200 °C	500 °C	Sato [162]
80 °C	425 °C	500 °C	Cordfunke and van der Giessen 1963 [147]
75 °C 94 °C	206 °C	565°C	Rey et al. 2009 [151] (reaction to U_3O_8)
80 °C	224 °C	555 °C	this work
	212 °C	554 °C	

slope in the weight loss of studtite does increase at 500 °C. Additionally, the DSC signal features a strong shoulder. This shoulder is also present in the DSC signal of the amorphous dehydration product, yet extremely broad and the corresponding TG-curve shows no abrupt changes. In

†The weight increase below 50 °C has to be regarded as artifact. It even appears with α-Al_2O_3 and must be due to irregularities in this setup.

the metastudtite data neither of this can be noticed. It is interesting that the temperature of the amorphization in metastudtite is slightly lower than in the studtite sample, as in this case the metastudtite sample was made from part of the studtite sample. As the remaining sample in this work is of very dark and rather greenish than brown color, and no significant signal can be detected in the DSC until 700 °C, the reaction to U_3O_8 seems to have taken place in this case. If indeed, the direct reaction to U_3O_8 has taken place, reasons for this behavior are purely speculative but might be connected to the synthesis route. Most samples investigated in literature are either prepared from uranyl nitrate or uranyl acetate solution. Cordfunke et al.[147] reported, that the dehydration behavior of $UO_4{\cdot}4H_2O$ prepared from uranyl nitrate solution varies to that of $UO_4{\cdot}4H_2O$ prepared from uranyl acetate solution. The reasons for this are still not understood. As the present samples were prepared from UO_2 suspension, this might have an influence. Overall the DSC-TG measurement confirms that there is no remaining studtite in the metastudtite sample. The temperatures at which the dehydration and the amorphization take place could be ascertained and compared with literature values. These values will be especially considered during for the in-situ X-ray diffraction study.

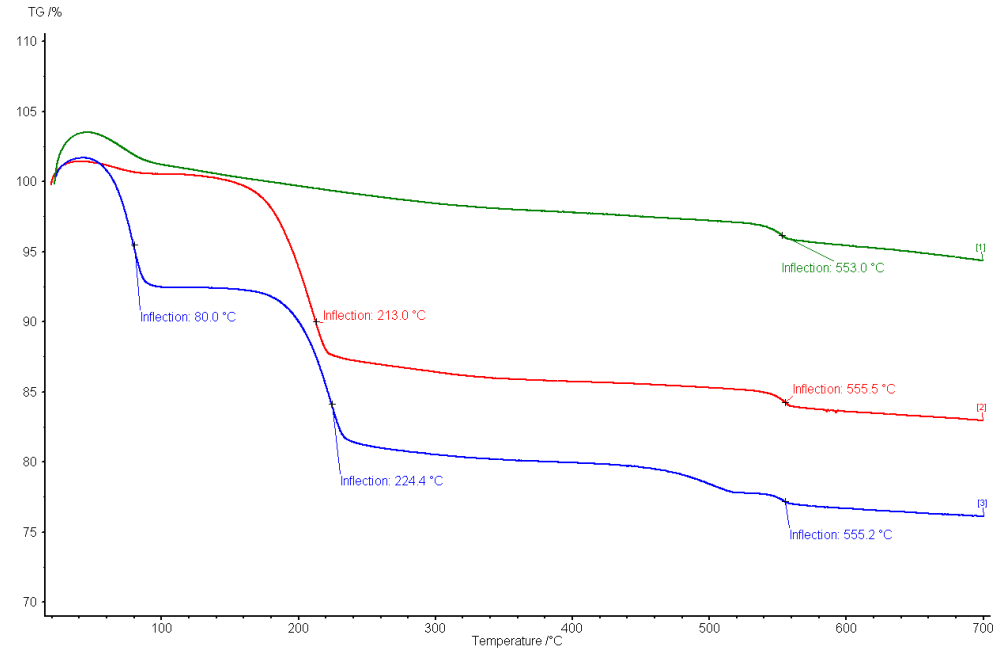

(a) TG measurement of studtite (blue), metastudtite (red) and amorphous product (green).

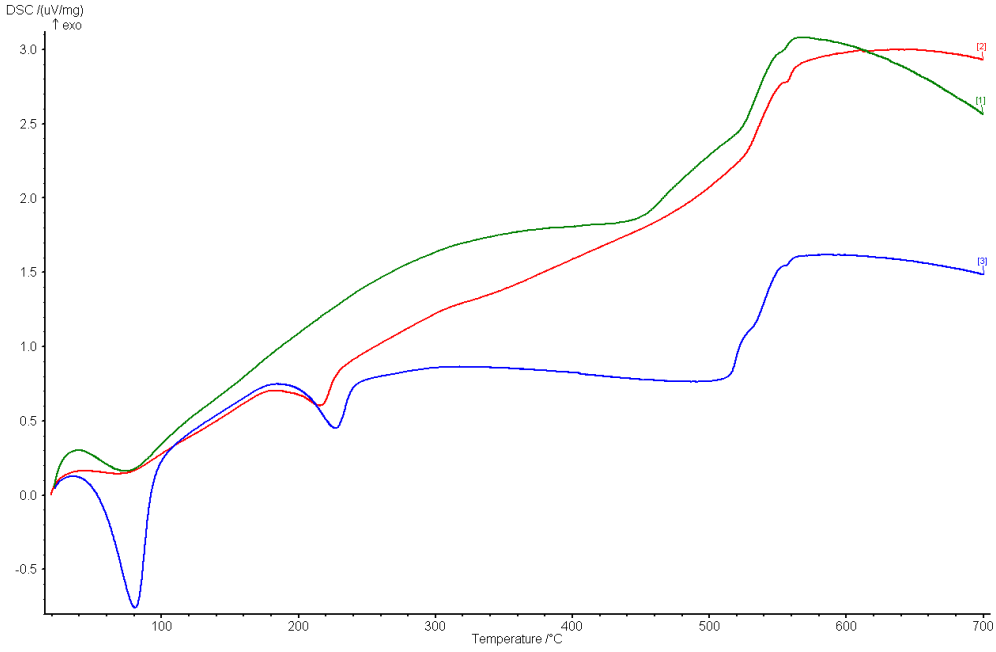

(b) Corresponding DSC measurement of studtite (blue), metastudtite (red) and amorphous product (green).

Figure 3.57: TG-DSC measurement of studtite (blue), metastudtite (red) and amorphous product (green). [NETZSCH *Jupiter STA 449C*, Al_2O_3 crucible, heating rate: 10 K/min.]

To investigate the dehydration behavior of studtite X-ray diffraction pattern were collected in the temperature range of 30 °C – 254 °C. This range covers the transformation of studtite to metastudtite as well as the subsequent amorphization. While the DSC-TG showed the reaction $UO_4{\cdot}4H_2O \rightarrow UO_4{\cdot}2H_2O$ to take place at 80 °C and the amorphization $UO_4{\cdot}2H_2O \rightarrow UO_3{\cdot}xH_2O$, x<2 at 215 °C especially the first reaction takes place much earlier in the XRD. The temperature range between 30 – 60 °C is shown in figure 3.58. Here the phase transformation already becomes evident at 39 °C, and above 56 °C studtite can no longer be detected (cf. figure 3.59 in detail). This result is not too unusual. Due to the measurement technique in DSC-TG the heat

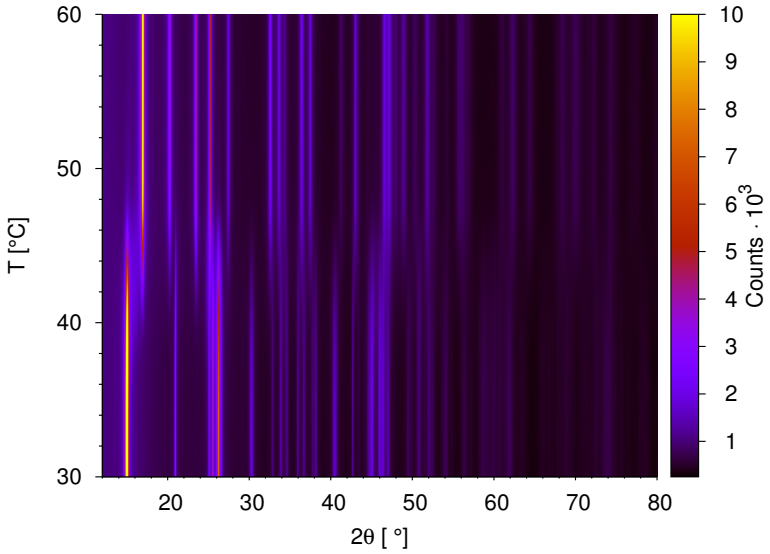

Figure 3.58: 2D in-situ X-ray diffraction study of studtite. T [°C] vs. 2θ, intensities given as colorcode

transfer of the reaction is detected with a small hysteresis. In this case the structural change might have already happened in terms of recrystallization, but the water is still adsorbed on the sample surface. Therefore, the weight loss is not detectable.

The collected diffraction pattern are treated by Rietveld refinement to extract the lattice parameters and weight fractions, U_{iso} of O and H atoms and H positions were excluded from refinement. It appears that during the phase transition the dimensions of the unit cell of studtite only change little. Figure 3.60 shows the temperature dependence of the studtite lattice parameters and linear fits. While the a-axis increases upon temperature increase ($1.5(3){\cdot}10^{-3}$ Å/K), the b-axis slightly decreases but the dimension is within the experimental errors ($-0.9(1){\cdot}10^{-4}$ Å/K). The thermal expansion of β and the c-axis is negligible. The chains of edge-sharing [UO_8]-polyhedra, which are connected via the peroxide groups and run parallel to the c-axis. These chains also exist in the metastudtite structure, now parallel to the a-axis. They remain essen-

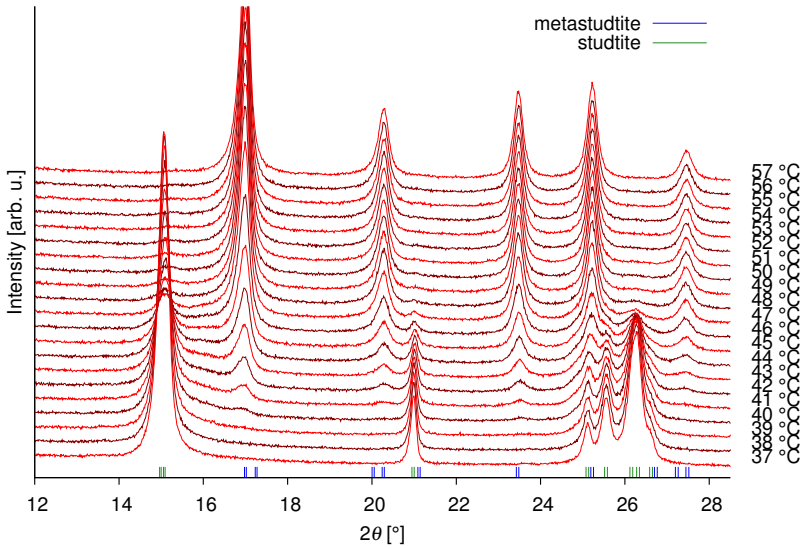

Figure 3.59: Close-up waterfall plot of the in-situ X-ray diffraction study of studtite. Range 12 – 28.5 ° 2θ, important reflection positions for studtite (green) and metastudtite (blue) are marked.

tially unchanged during the transition to metastudtite. It is therefore reasonable, that the c lattice parameter is not influenced during the heating process.

The notable elongation of a-axis with increasing temperature can be explained by the strong increase of thermal motion of the crystal water. This is located between the polyhedra chains just on the a-axis and directly influences the lattice parameter. When changing from studtite to metastudtite the distance between the polyhedra chains decreases, also chains appear to be more staggered. This yields an explanation for the decrease of the b-axis. Once the water molecules exit the structure the void is filled by the polyhedra chains moving towards each other. Closer to the phase transition lattice parameters of course experience the strongest influence.

Lattice parameters a, b, and c of metastudtite change insignificantly, the a lattice parameter slightly increases but fit values are within the experimental error. Above 120 °C the structure starts to contract again. The b-axis decreases a bit (- 1.02(7) · 10^{-4} $^{Å}/_{K}$). At the beginning, close to the phase transition, the values experience extreme fluctuations as can be seen in figure 3.61. Above 180 °C the amorphization becomes dominating, leading to strong decrease in of the a- and b-axis.

In figure 3.62 the weight fractions from Rietveld refinement of studtite and metastudtite vs. temperature are given with corresponding sigmoidal fit functions. Due to the copper sample holder, Cu-reflections are present in the diffraction pattern. They were included in the refinement, and initially set to 0.5 wt.% but included in the last refinement cycle. As the sample volume decreases the weight fraction for this "Cu-phase" increases. Leading to a decrease in the

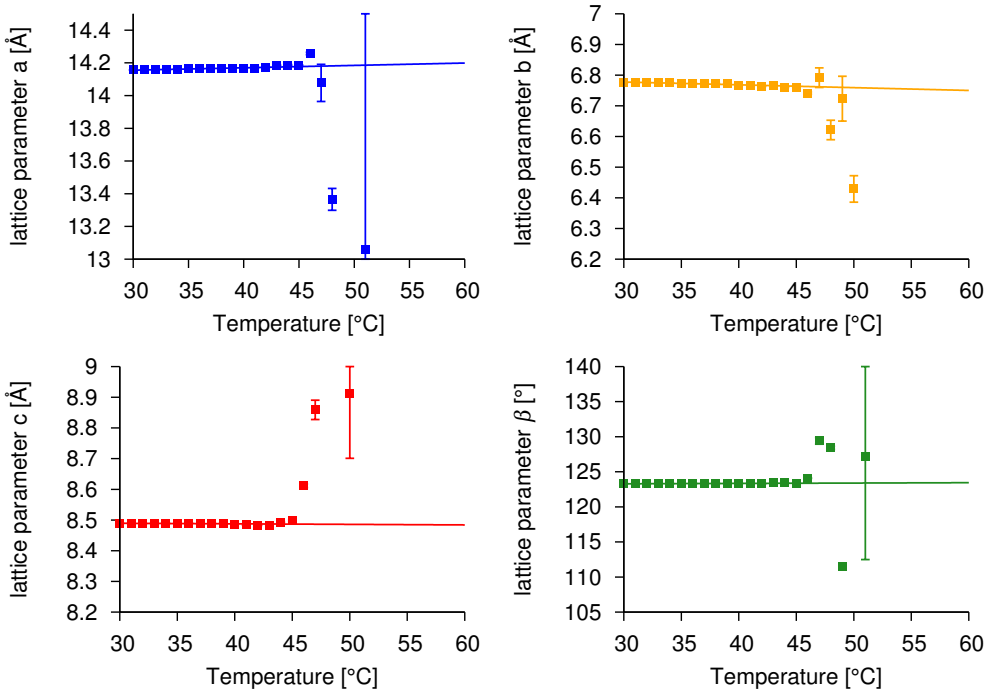

Figure 3.60: Temperature dependence of the lattice parameters a, b, c, and β with linear fits of studtite obtained by Rietveld refinement.

studtite and metastudtite fraction, respectively. In a way this linear decrease in the metastudtite fraction depicts the amorphization process. During the amorphization process of metastudtite, not all reflections decrease equally in intensity. In figure 3.63 this is exemplary shown. While the (011) reflection diminishes very fast, the (020),(201), and (002) reflections remain at rather high relative intensity. The reflection with highest intensity of studtite appears at 2θ = 15.04° and is assigned to the (011) reflection. In metastudtite the highest intensity belongs to the (011) reflection at 2θ = 16.92°. During the phase transition from 39 – 56 °C another broad intensity is visible just in between, at 2θ = ∼16°. It increases in intensity up to 43 °C, then diminishes again. This reflection must be associated with the phase transition and most likely results from some amorphous intermediate state.

The first reflection of the studtite and metastudtite phase are fitted with a Pseudovoigt function, the reflection of this amorphous intermediate is fitted with a Gaussian function, then the areas are calculated. At room temperature the sample consists solely of studtite, therefore the area calculated for the first studtite reflection is divided, i.e. normalized by the area obtained at room temperature. Every mol of studtite, will yield one mol of metastudtite above 90 °C. Therefore the same procedure is applied for the first reflection of metastudtite. The area obtained at 95 °C is

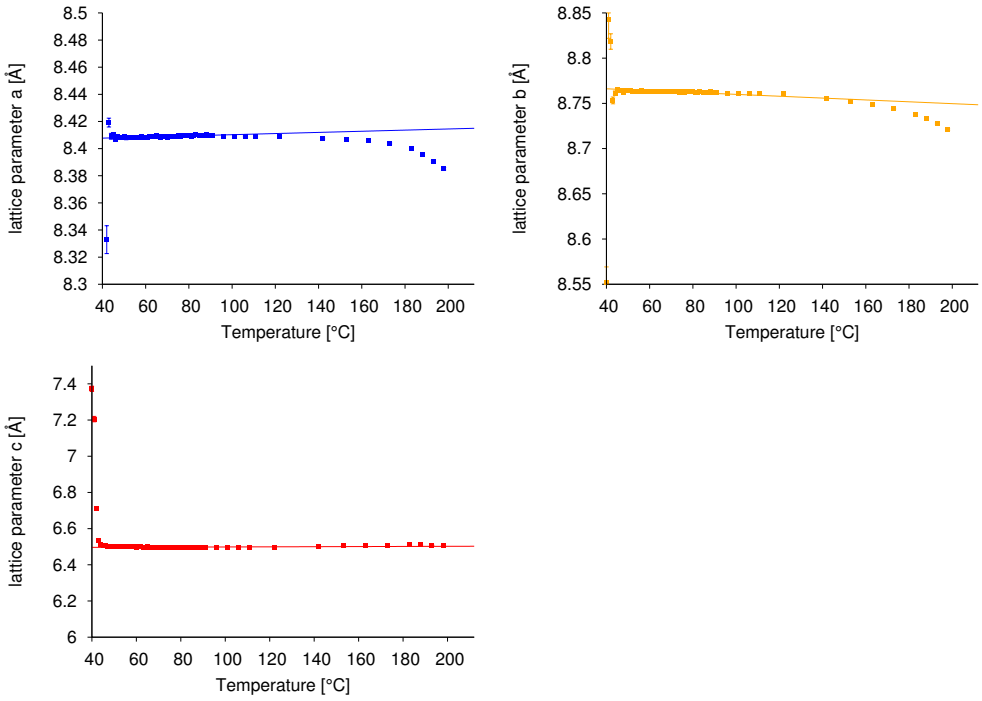

Figure 3.61: Temperature dependence of the lattice parameters a, b, and c in metastudtite obtained from Rietveld refinement and linear fits.

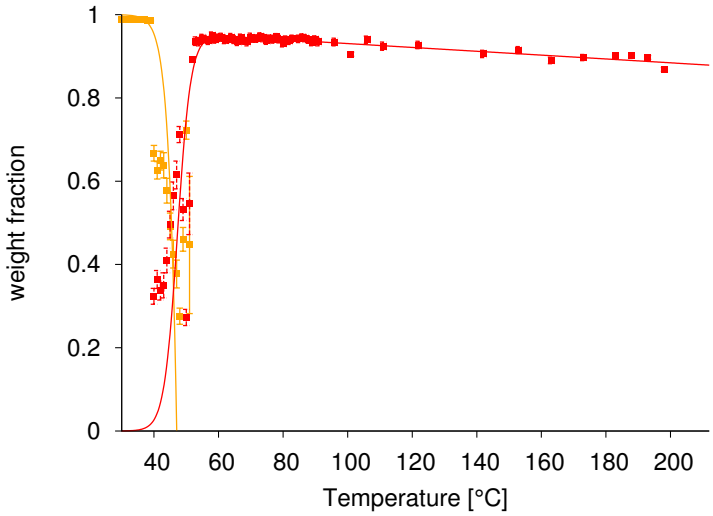

Figure 3.62: Weight fractions of studtite (yellow) and metastudtite (red) vs. temperature as calculated from Rietveld refinement and sigmoidal fit functions.

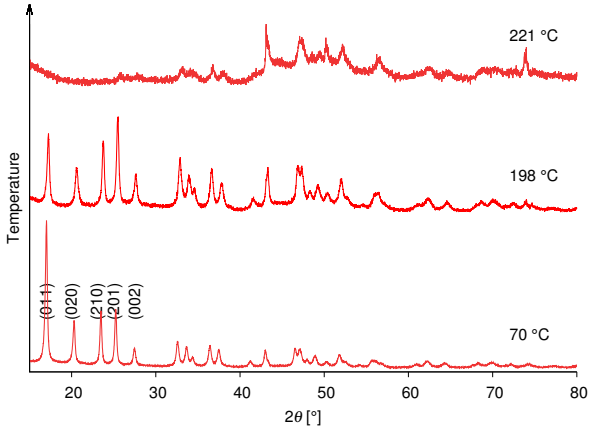

Figure 3.63: X-ray diffraction pattern illustrating the amorphization of metastudtite.

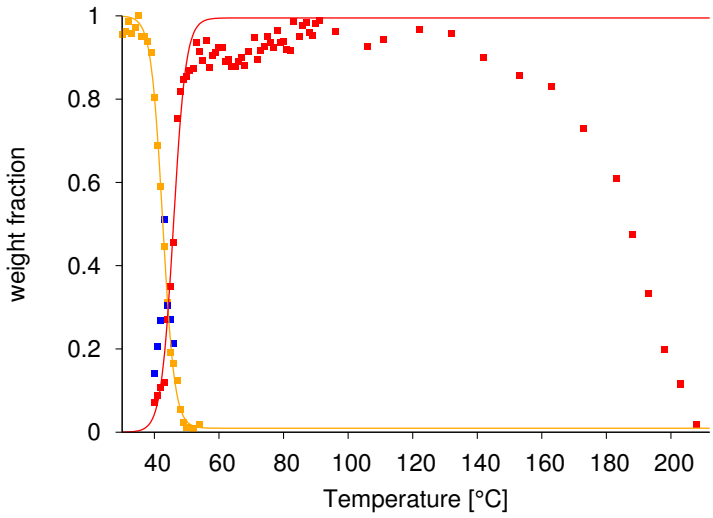

Figure 3.64: Estimated weight fractions of studtite (yellow), metastudtite (red), and amorphous phase (blue) vs. temperature as calculated from the area of the single peak fits of the first reflections. Sigmoidal fit functions have been applied for the studtite and metastudtite phase respectively.

used for normalization, as here the area of the metastudtite reflection reaches a maximum. This way the weight fractions of studtite and metastudtite are derived. The maximum weight fraction of the amorphous phase is estimated from the remaining amount at 80 °C. Values for the amorphous phase are normalized then. The result of this is presented in figure 3.64 and comparable to the results from Rietveld refinement (see figure 3.62). In the higher temperature range the applied method yields a decrease of the weight fraction. This is reasonable, as the sample starts to

decompose. Amorphization cannot be sufficiently described by the Rietveld refinement without the use of an internal standard. During the phase transition the minority phase can be better described. It is, however, due to the extremely high intensity of the first reflections in these particular materials, that this is possible. The observations made in the laboratory X-ray setup

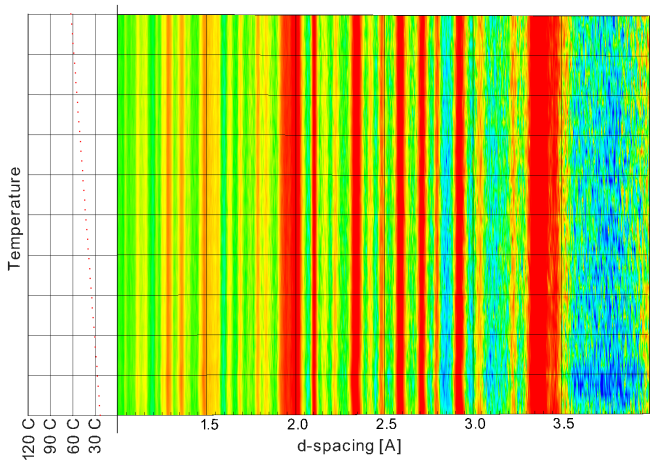

Figure 3.65: Preliminary results from the in-situ neutron diffraction of deuterated studtite. 2D plot of the in-situ neutron diffraction series, intensity as heat map. Diffraction pattern collected on the HiPPO instrument at the LANSCE Lujan Center, T_{max} = 60 °C.

could not be confirmed during an in-situ neutron diffraction study, of which an overview plot is shown in figure 3.65. In the temperature range 25 – 60 °C the reflection pattern of metastudtite could not be observed. Reflections of the studtite phase do shift insignificantly, according to the small changes in the unit cell, but the phase transition cannot be detected. During the measurement, the sample is set in a closed V container. The heat transfer of the material is good and the temperature measured and the actual temperature of the sample should not differ. It might be, that due to the closed container, the partial pressure of water during reaction plays a role. A strong stabilizing effect of D_2O on the structure seems improbable, but cannot be completely ruled out.

3.2.4 Electronmicroscopy

To study the morphology of the studtite sample, scanning electron microscopy was employed. Upon investigation the morphology of the studtite particles becomes evident as seen in figure 3.66. At low magnifications the sample appears as a voluminous agglomeration of smaller particles. In some spots distinct rods become apparent. The sample appears to consist of small elongated platelets, when switching to higher magnification.

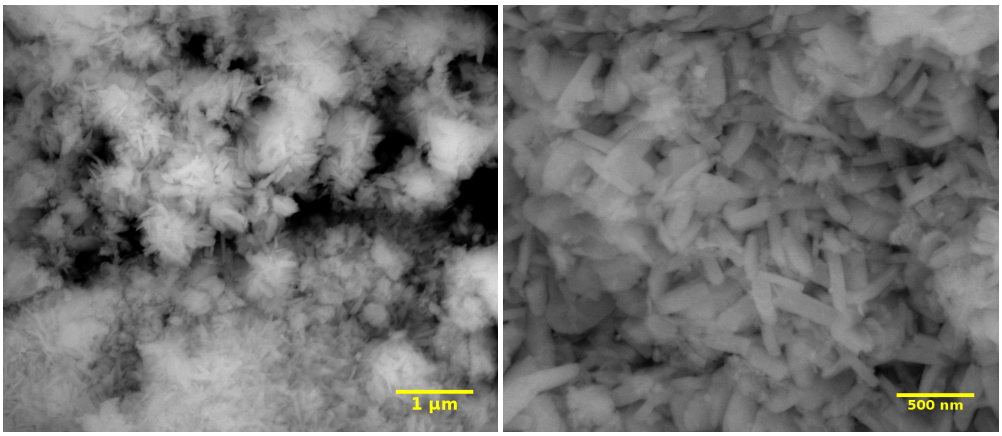

(a) (b)

Figure 3.66: Overview (a) and close up (b) SEM micrographs of studtite. The particle morphology being elongated platelets, can be nicely seen.

Difference in size or appearance of the particles in the metastudtite sample was not observed. As in studtite particles are elongated platelets, which are usually agglomerated. It would not be possible to distinguish studtite from metastudtite from morphology. To see if any change is visible during the active dehydration studtite was heated in the up to 60 °C during investigation in ESEM mode. Apart from a general shrinkage of the sample, the dehydration had no significant influence on the morphology of the studtite particles.

Figure 3.67 shows a TEM sample. Again the elongated platelets already familiar from the SEM micrographs are visible. Upon closer investigation many small grains, i.e. coherent scattering domains, become evident (cf. figure 3.68). Most of these are below 10 nm in dimensions. This is remarkable, when taking into account that reflections in the XRD pattern exhibit very small halfwidths.

While closer investigating the lattice fringes the studtite sample started to decompose to metastudtite. This process could be repeated on several fresh spots of the sample. The electron diffraction pattern of the studtite sample, directly after exposition and after changing in the lattice fringes has seized, confirm this. Due to the small crystallite size, the diffraction pattern does not show single reflections but debye-scherrer-rings. A comparison of the collected diffraction

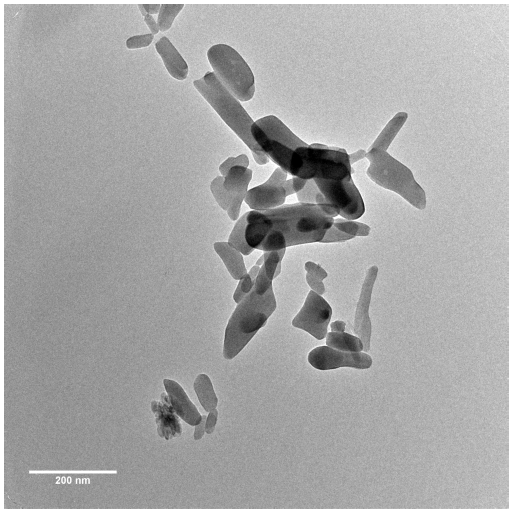

Figure 3.67: TEM micrograph of the metastudtite sample showing the specimen shape.

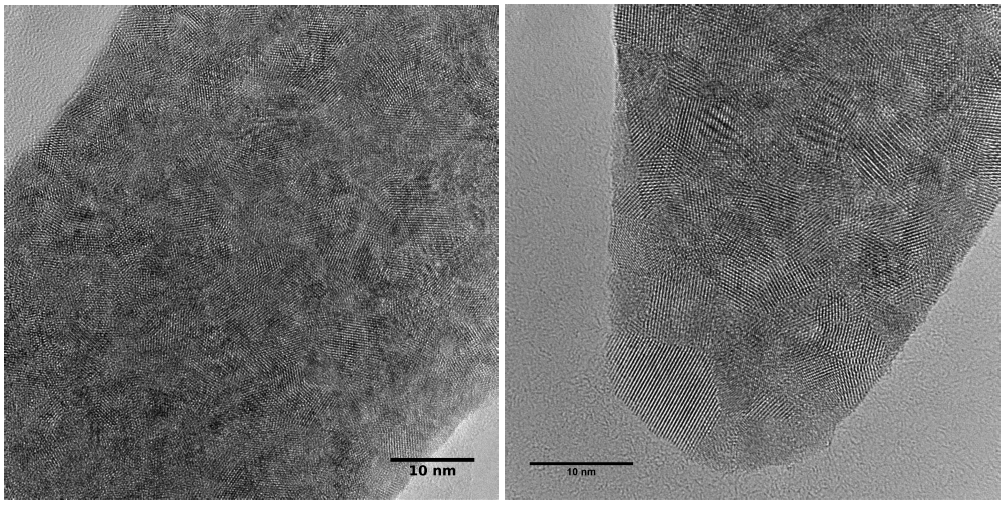

(a) HRTEM micrograph of studtite, scale bar 10 nm. (b) HRTEM micrograph of metastudtite, scale bar 10 nm.

Figure 3.68: HRTEM micrographs of studtite and metastudtite. Grain sizes of $<$ 10 nm are well visible.

pattern and the XRD pattern, as can be seen in figure 3.69, together with the lattice distances allowed to identify the metastudtite phase after being exposed to the electron beam. The shape of the particles, yet did not change. Similar observations had been made by Cordfunke et al.[147] The so dehydrated sample was investigated closely concerning changes, like pore formation or increase of grain size due to dehydration. None of these effects could be found though.

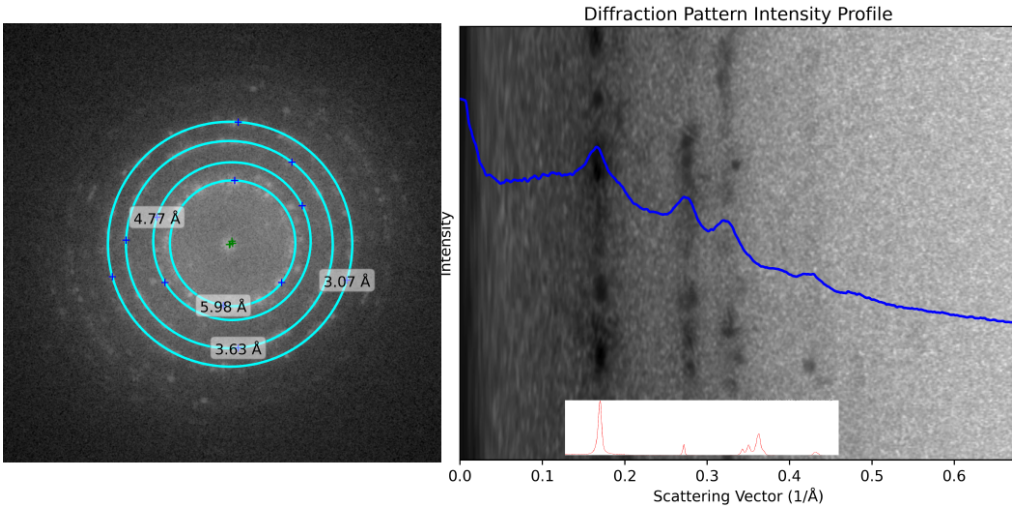

(a)

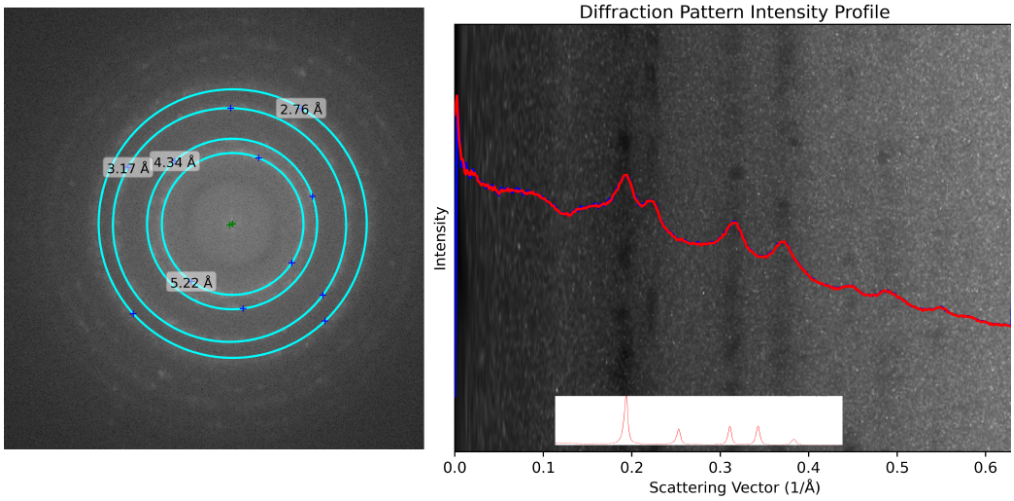

(b)

Figure 3.69: FFT of the HRTEM micrographs (left) of studtite (a) and (after irradiation) metastudtite (b) with intensity profiles are shown right. Insets are excerpts of the corresponding XRD pattern for comparison.

Even though this was not to expect from the reflections in the XRD pattern, the samples consist of extremely small crystallites; size as revealed by TEM is below 10 nm. Studtite also is far more susceptible to beam damage than metastudtite. Undergoing a pseudomorphic recrystallization it dehydrates easily in the electron beam to metastudtite, while the metastudtite samples stay stable. Signs of pore formation or growth or alignment of the coherent scattering domains could not be observed.

3.2.5 IR spectroscopy

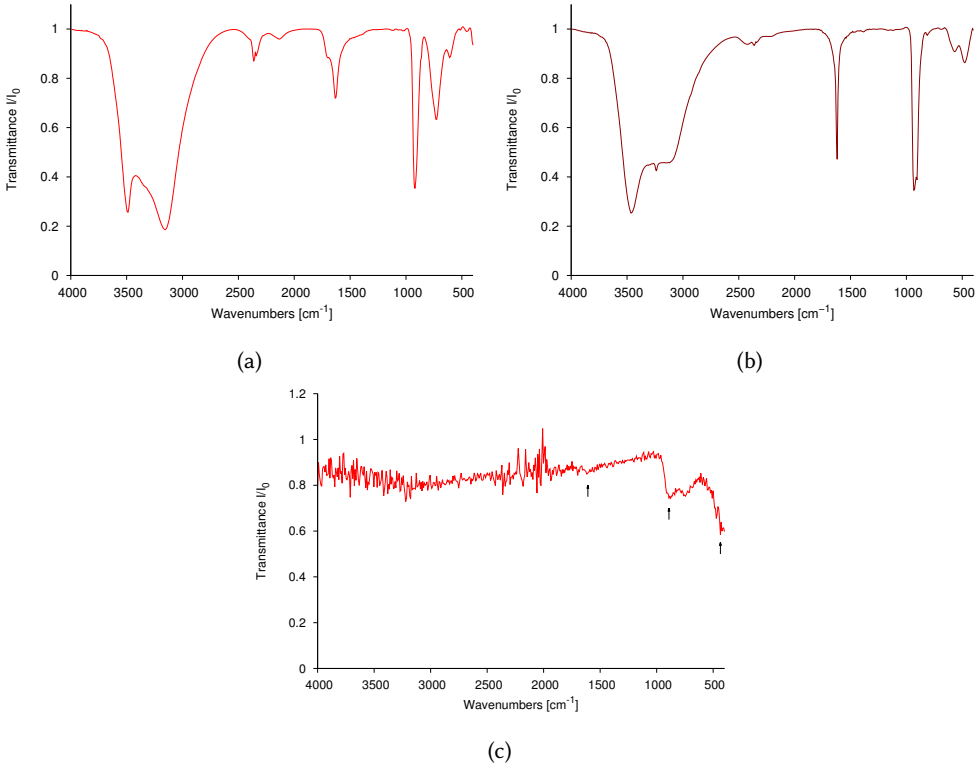

Figure 3.70: IR spectra of studtite (a) and metastudtite (b) [Bruker *Equinox 55* TGA-IR, KBr pellet, signals at $\sim$ 2400 cm^{-1} in are to be regarded as artifacts], and the amorphous dehydration product, $UO_3 \cdot xH_2O$ (c) for comparison.

FT-IR spectra of studtite (figure 3.70a) and metastudtite (figure 3.70b) and amorphous $UO_3 \cdot xH_2O$ (figure 3.70c) for comparison were collected (Indications of the weak/diffuse bands by arrows). Wavenumbers and assignments according to Bastians [166] of the bands are listed in table 3.22.

The strongest bands in the spectra arise from ν(OH) vibrations in the region above 3000 cm^{-1}. At 3153 cm^{-1} studtite features $\nu(OH)^{asym}$ band which is much weaker in metastudtite. In return, this band is sharper in metastudtite, which was already observed by Sato. [161] Supposedly, mainly the crystal water contributed to this signal in the spectrum of studtite. In studtite δ(HOH) at 1631 cm^{-1} shows a strong shoulder, which also can be attributed to the two different positions of water in the structure. The very weak δ(UOH) band can be distinguished at 1100 cm^{-1} in the studtite spectra. In the metastudtite spectra this vibration is broader and shifted to slightly higher wavenumbers; it is merely unresolved. The δ(HOH) though is intense and sharp, overall bending- and stretching vibrations of water, i.e. OH-group, are significantly sharp in the IR

spectrum of metastudtite. As expected these bands only exist as small and rather diffuse features in the IR spectrum of the dehydration product. Aside from the stretching vibrations of water, the asymmetric stretch ν(U=O)^{asym} is the dominating IR band, in studtite as well as in metastudtite. The ν(U=O)^{asym} is slightly shifted $\sim$ 10 cm^{-1} to higher wavenumbers from 921 cm^{-1} in studtite to 933 cm^{-1} in metastudtite. A sign of a stronger and so shorter U-O bond in metastudtite. In the spectrum of metastudtite also a slight splitting of this band occurs. A similar observation has been made by Bastians[166] as well in synthetic as in heated natural samples. In the dehydration product only broad bands for the uranyl ν(U=O) vibrations appear. The peroxo stretch ν(O–O) of the bridging peroxo groups is visible. As this vibration will not cause a dipole change, it should not be visible in the IR spectra at all. Through polarisation effects a small dipole change can result making the vibration visible as a very weak band.

Table 3.22: IR peak positions of studtite, metastudtite, and amorphous $UO_3 \cdot xH_2O$ (x<2) and assignments.

peak position [cm^{-1}]			assignment (acc. to Bastians[166])
studtite	metastudtite	$UO_3 \cdot xH_2O$	
3490	3451		ν(OH)^{sym}
3153	3237 s		ν(OH)^{asym}
1631	1620	1609 w	δ(HOH)
1100 vw	1100 vw		δ(UOH)
921	933	891	ν(U=O)^{asym}
	906		ν(U=O)^{asym}
	865 (shoulder)		ν(O–O)
	815 w		ν(U=O)^{sym}
730 b		743	ν(U=O)^{sym} (?)
608	568		ν(U-O$_{peroxo}$)^{asym}
455	479		ν(U-O$_{peroxo}$)^{asym}

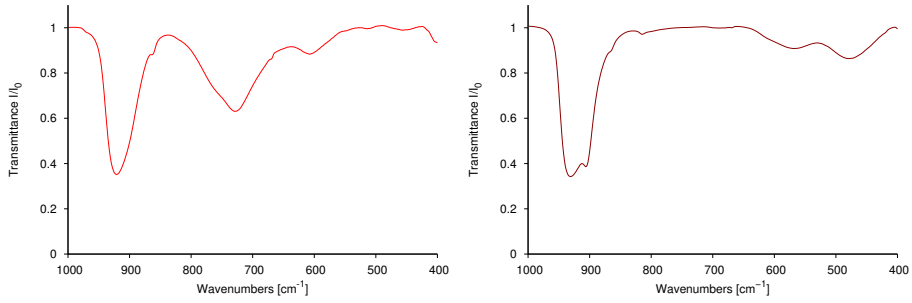

(a) (b)

Figure 3.71: Close up of the IR spectra of studtite (a) and metastudtite (b), 1000 – 400 cm^{-1} shown [Bruker *Equinox 55* TGA-IR, KBr pellet].

The low wavenumber region (1000 – 400 cm^{-1}) features one of the biggest differences between studtite and metastudtite. At 730 cm^{-1} a broad band, with a shoulder appears in studtite, which is most probably attributed to the ν(U=O)^{sym} vibration (see figure **??**). Distinct ν(U-O_{peroxo})^{asym} vibrations can also be detected at 608 and 455 cm^{-1}, however, the latter signal is rather weak. In the metastudtite spectrum the strong ν(U=O)^{sym} vibration is lost, merely a small, yet sharp signal at 816 cm^{-1} remains. The ν(U-O_{peroxo})^{asym} vibrations instead appear more intense at 568 and 479 cm^{-1}.

For the neutron powder diffraction studies also deuterated and partially deuterated studtite and metastudtite samples were prepared. To confirm the deuteration of the samples, IR spectra were collected. It appeared, that ν(OD) bands were found in the region of 2500 cm^{-1}. Bands assigned to δ(DOH) can be observed at 1400 cm^{-1}. There is no significant shift of the uranyl vibrations, ν(U=O), in neither studtite nor metastudtite visible. There are significant differences in the bands associated to water in the IR spectra of studtite and metastudtite. From the present data it can be concluded, that in studtite two different types of water (corresponding to the two different crystallographic positions) are present. In metastudtite only one type of water, or OH-groups, exist. The uranyl vibration ν(U=O)^{asym} is shifted to higher wavenumbers in than studtite, corresponding to a stronger U=O bond. Additionally the signal splits up, suggesting that two marginally different U=O bonds are present.

3.2.6 Investigation of the bonding of water with IINS

With Inelastic Incoherent Neutron Scattering it is possible to distinguish between different types of water in the crystal structure by examining the characteristic spectroscopic shifts.

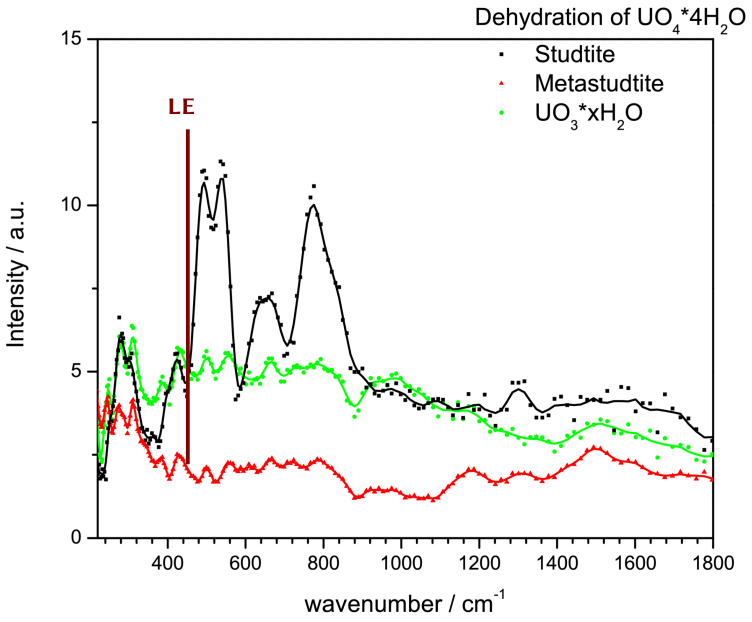

Figure 3.72: IINS spectra of studtite, metastudtite and dehydration product, range 200 – 1800 cm $^{-1}$.

The libration edge (LE) of water, usually appearing at 500 – 800 cm^{-1}, is clearly visible in the spectra of studtite and shifted toward lower wavenumbers; it already appears at at 450 cm^{-1}. The following peaks are rather sharp, making the different librational modes resolvable. This shows that the occluded water present is bound rather strong through hydrogen bonding.[171;172] As the libration edge of water is visible only in studtite, it is evident that crystal water (free water) is not present in metastudtite.

Strong signals from δ(HOH) and δ(UOH) in metastudtite are visible at 1500 cm^{-1}, yet these are not as distinguishable in studtite. In the intramolecular region δ(HOH) and δ(UOH) modes in studtite are very broad. Since no distinct peaks as in metastudtite are visible, this suggests that the vibration is restricted in metastudtite but not in studtite.

All three spectra show strong similarities at very low wavenumbers, where mainly phonons appear. While translational modes of water are present in all three spectra (shoulders at 140 cm^{-1} and 165 cm^{-1}) only the spectrum of metastudtite shows intermolecular hydrogen bending and stretching modes (215 cm^{-1} and 245 cm^{-1}).

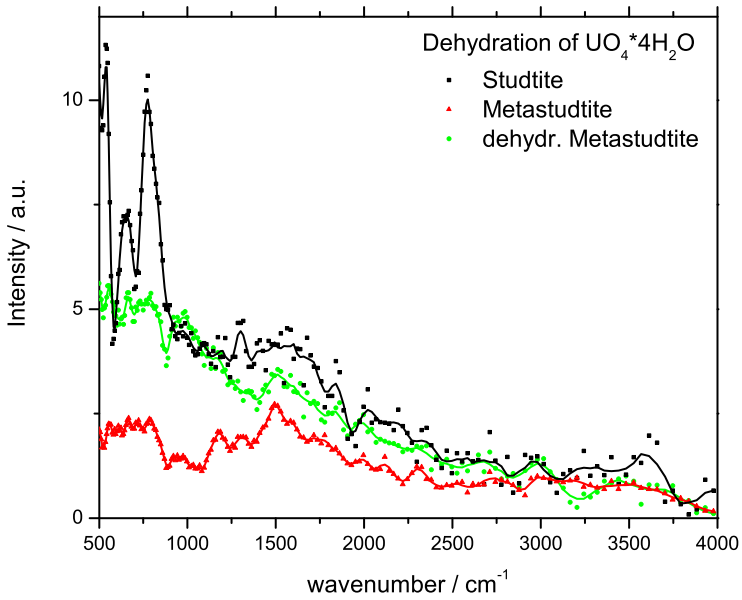

Figure 3.73: IINS spectra of studtite, metastudtite and dehydration product, range 500 – 4000 cm $^{-1}$.

Table 3.23: IINS peaks [cm^{-1}] of studtite, metastudtite, the dehydrated product, amorphous UO_3·x H_2O (x<2), and assignments.

Assignment	Studtite	Metastudtite	amorphous UO_3·x H_2O
lattice vibrations (phonons)	120 142 150	120 140 165	120 140
translational modes of water	185 280	215 245 280	 280
hydrogen bond bend and stretch	490 541		
librations of water	660 775 845		
δ(UOH) + δ(HOH)		1182 1508	

In summary the data allows for the discussion on how water is bound in the metastudtite structure. As the libration edge only exists in studtite, free water is not present in metastudtite.

In return the intermolecular hydrogen bending and stretching modes are very distinct in the metastudtite spectrum. Suggesting, that rather bridging HOH-groups are present, than actual "water". The collected IINS data hence further supports the structure model for metastudtite proposed by Weck et al.[2]

3.2.7 High-pressure Raman studies

Raman spectra of studtite and metastudtite were collected under ambient conditions and at elevated pressures up to 18 GPa. The behavior of studtite and metastudtite under pressures is investigated for the first time in this study. Samples were loaded into a Boehler-Allmax diamond-anvil-cell with neon as hydrostatic pressure transmitting medium, the pressure was monitored by standard ruby fluorescence.

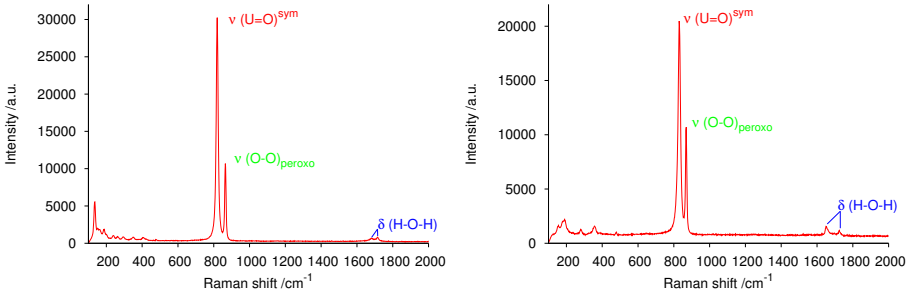

(a) Raman spectrum of studtite at ambient pressure.

(b) Raman spectrum of metastudtite at ambient pressure.

Figure 3.74: Raman spectra of studtite and metastudtite. ν(O-O$_{peroxo}$)^{sym} and ν(U=O)^{sym} vibration are visible as strongest peaks. δ(HOH) bending vibration is more distinguished in metastudtite than in studtite (assignments according to Bastians et al.[166]).

The similarities in the Raman spectra of studtite and metastudtite become evident on first sight. In the Raman spectra the symmetric uranyl ν(U=O)^{sym} stretch appears as the strongest band, followed by the symmetric ν(O-O)$_{peroxo}$ stretching vibration. In the region between 1600 – 1800 cm^{-1} the δ(HOH) bending vibrations are visible. These bands are more distinguished in metastudtite than in studtite. Significant variations between both samples appear only in the region below 600 cm^{-1}. The bands close to 430 and 405 cm^{-1} in the studtite spectrum could be asymmetric and symmetric uranium–peroxo stretching vibrations ν(U-O$_2$)^{asym} and ν(U-O$_2$)^{sym}. This type of η^2-vibration has been reported for other metal-peroxo complexes by Gresley et al.[173] On the other hand, for metastudtite only one significant signal can be found at 470 cm^{-1}. Generally, it can be observed, that the metastudtite spectrum features less signals in the region below 600 cm^{-1} than studtite.

The pressure shifts were determined for the two strongest peaks (cf. tables 3.24a and 3.24b). These can be assigned to the ν(U=O)^{sym} stretching mode and symmetric peroxide stretching mode.[166] At ambient conditions the ν(O-O$_{peroxo}$)^{sym} is basically at the same position in studtite and metastudtite, at 866 cm^{-1} and 867 cm^{-1} respectively, while the ν(U=O)^{sym} is 14 cm^{-1} higher in metastudtite (833 cm^{-1}) than in studtite (819 cm^{-1}). This corresponds to a stronger U-O

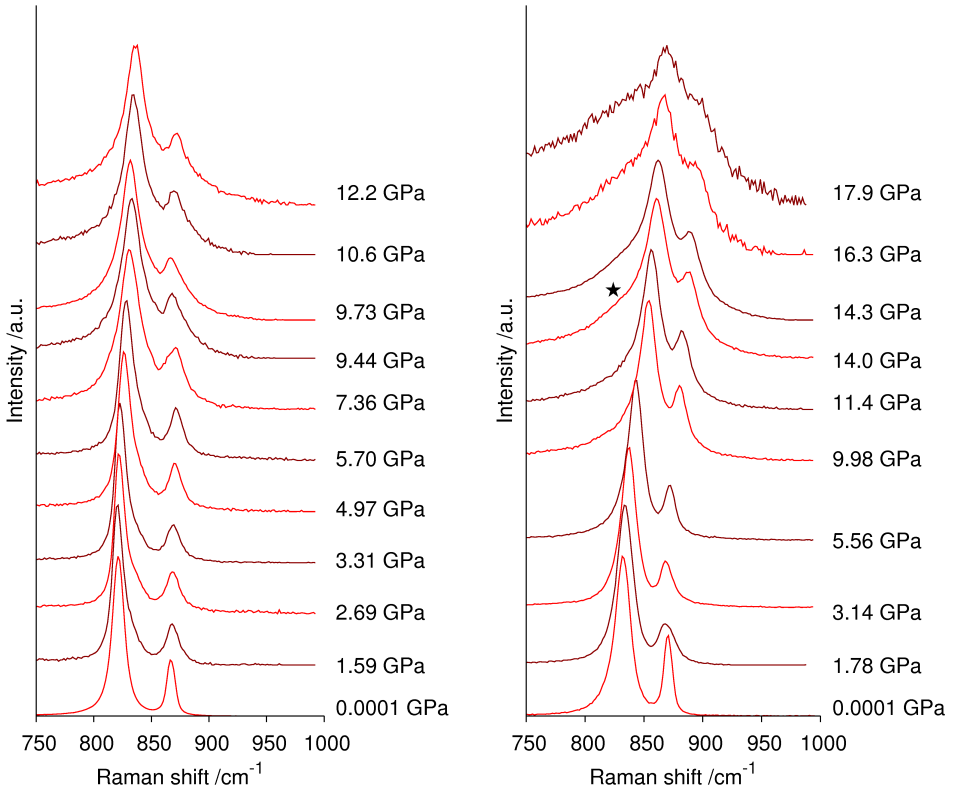

(a) Close up of the Raman spectrum of studtite in with increasing pressure, range 750 – 1000 cm^{-1} shown.

(b) Close up of the Raman spectrum of metastudtite in with increasing pressure, range 750 – 1000 cm^{-1} shown.

Figure 3.75: Close up of the Raman spectra of studtite and metastudtite, ν(O-O_{peroxo})^{sym} and ν(U=O)^{sym} vibration are studied with increasing pressure. Onset of the ν(O-U-O-U) vibration in metastudtite is marked with a ★.

bonding in metastudtite, which is in accordance to the trend observed in the IR spectra. In both samples ν(U=O)^{sym} as well as ν(O-O_{peroxo})^{sym} shift to higher wavenumbers with compression, suggesting a stronger in the U-O bond with increasing pressure. (An example for the fit of such high-pressure Raman spectra can be seen in figure VII on page xv of the appendix.)

The ν(O-U-O-U) stretching vibration appears above 1.6 GPa in studtite, yet remains unobserved in metastudtite below 14 GPa, see figure 3.75b. Onset of the decomposition indicated through the dominant ν(O-U-O-U) vibration in metastudtite is marked with a ★. This ν(O-U-O-U) mode is characteristic for UO_3 and the observed shifts are in good accordance with the values reported by Lipp et al.[174] for UO_3 at pressures up to 18 GPa. Upon compression the ν(U-O) vibration shifts to lower wavenumbers, corresponding to a weakening of the U-O bond.

Table 3.24: Pressure shifts of the ν(O-O$_{peroxo}$)^{sym} and ν(U=O)^{sym} vibration in the Raman spectra of studtite and metastudtite.

ν^0 [cm^{-1}]	$\frac{d\nu}{dp}$ [$\frac{\text{cm}^{-1}}{\text{GPa}}$]	assignment
866	0.61	ν(O-O$_{peroxo}$)^{sym}
818	1.51	ν(U=O)^{sym}

(a) Studtite

ν^0 [cm^{-1}]	$\frac{d\nu}{dp}$ [$\frac{\text{cm}^{-1}}{\text{GPa}}$]	assignment
867	1.51	ν(O-O$_{peroxo}$)^{sym}
832	2.03	ν(U=O)^{sym}

(b) Metastudtite

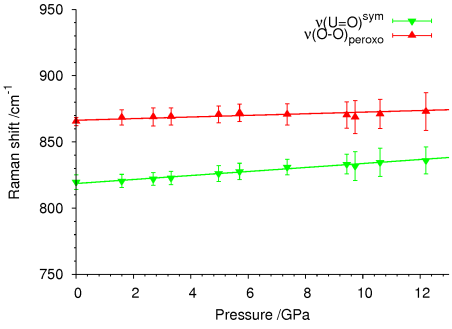

(a) ν(O-O$_{peroxo}$)^{sym} and ν(U=O)^{sym} Raman shifts of studtite vs. pressure.

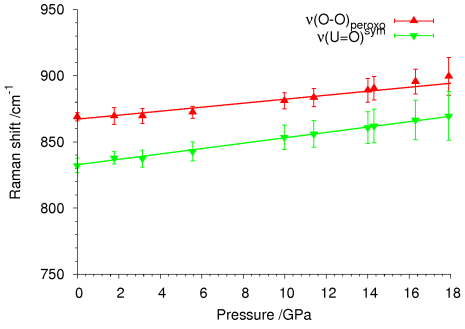

(b) ν(O-O$_{peroxo}$)^{sym} and ν(U=O)^{sym} Raman shifts of metastudtite vs. pressure.

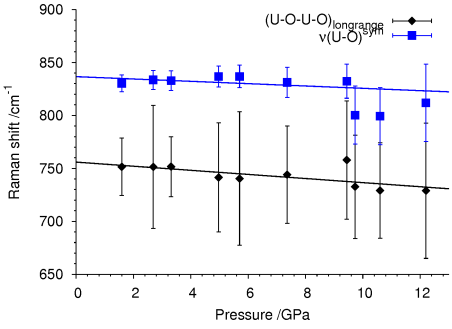

(c) ν(U-O) and ν(U-O-U-O) long range Raman shifts of studtite vs pressure.

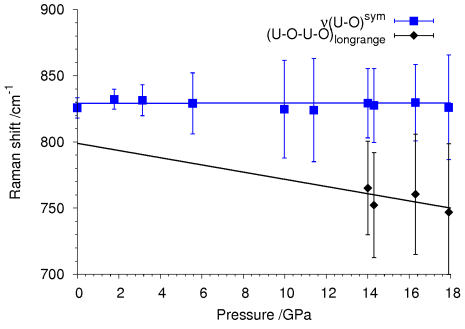

(d) ν(U-O) and ν(U-O-U-O) long range Raman shifts of metastudtite vs. pressure.

Figure 3.76: Raman shifts and linear fit of ν(U=O)^{sym} and ν(O-O$_{peroxo}$)^{sym} in studtite (a) and metastudtite (b) with increasing pressure. Weak stretching vibration ν(U-O) and ν(U-O-U-O) long range vibrations already appear at lower pressures in studtite (c) than in metastudtite (d). Especially the ν(U-O-U-O) long range vibration can be associated with beginning decomposition to UO_3.

Above 16 GPa the signals in metastudtite become significantly broader, suggesting the begin of an amorphous phase transition. There is no evidence so far for a pressure induced studtite $\longrightarrow$ metastudtite phase transition. Direct decomposition to UO_3 seems probable. Based on the late appearance of ν(O-U-O-U) vibration it can be concluded that the metastudtite phase is more stable concerning pressure increase than the studtite phase.

During this work attempts were made to also collect the corresponding XRD pattern. Unfortunately due to the small beam size at the ECB the flux of the synchrotron radiation was so high, that samples decomposed almost instantaneously. At most the diffraction pattern of metastudtite was observable for a short time. Studtite decomposed even at extremely short exposition times and only diffuse scattering from the resulting amorphous phase was detectable. While this of course cannot be regarded as conducted experimental work, it corresponds to the general observations made during this work, that metastudtite is by far more stable than studtite regarding heating, compression or irradiation.

In summary, structural investigations employing synchrotron X-ray and neutron powder diffraction allowed for a better determination of hydrogen positions in the studtite structure. Through EXAFS measurements the U–O distances of the first coordination sphere and the U–U distance were determined for both samples and compared to those reported in literature and derived from powder diffraction data. While the derived atomic distances reassured the studtite structure and were in good accordance with diffraction data, the spectrum of metastudtite showed an interesting feature in the range of the U–U distance. The structure model from Weck et al.[2] for metastudtite is generally supported by the diffraction data. Through the results derived from NPDF it was possible to amend the model, which lead to a completely different atomic position for one uranyl O atom and a strong bending of the uranyl group. While the result should be handled with caution, the derived new model seems plausible and encourages further discussion on the topic. Furthermore, it is the first comprehensive synchrotron and neutron powder diffraction study reported on studtite and metastudtite so far. The Raman spectra show no change in the ν(O-O_{peroxo})^{sym} stretching mode, implying that this distance is the same in studtite as in metastudtite. From IR spectra it can be observed, that the modes associated to water are strictly confined in metastudtite. The ν(U=O)^{asym} is split in metastudtite, a sign for two different U=O–distances. For studtite the presence of crystal water is observed in the strong ν(OH) mode in the IR spectrum, and confirmed by the observance of the librational modes of water in the IINS spectra. The IINS spectrum of metastudtite completely lacks any features of the librations of water, instead, the δ(HOH) vibrations give a strong signal. Suggesting, that metastudtite only contains directly bound water with strong O$\cdots$H coordination.

The morphology of studtite and metastudtite was investigated with SEM. Both materials appeared as small elongated platelets or rods. During heating, no change in form of the particles was visible. It could be observed in the TEM, that the particles consist of numerous nano-scaled grains, with 5 – 10 nm in dimension. While metastudtite is stable in the electron beam at 300 kV, studtite undergoes dehydration very fast. During this transition, grain sizes and particle shape remain the same, the process is hence pseudomorphic. Only the rearrangement of the lattice fringes can be seen. DSC-TG measurements showed that the dehydration of studtite to metastudtite takes place at 80 °C and that the amorphization happens at $\sim$ 215 °C. During the in-situ X-ray diffraction study, the onset of the studtite $\longrightarrow$ metastudtite transition was observed at 39 °C and the reaction was completed at 56 °C. Further amorphization was observed at 212 °C. Mass fractions of studtite and metastudtite were obtained from Rietveld refinement and by a single peak fit technique. While both methods depicted the dehydration process similarly, the Rietveld refinement does not represent the amorphization. This can, however, be nicely observed in the data from the single peak fit technique. Furthermore, this way it is possible to relatively quantify the amorphous intermediate accompanying the studtite $\longrightarrow$ metastudtite transition. Additionally the thermal expansion of the lattice parameters of studtite and metastudtite were investigated, showing that the axes perpendicular to the [UO_8]-polyhedra are least influenced

by temperature.

Concerning the pressure stability, both materials were studied with Raman spectroscopy. The pressure dependence of the ν(U=O)^{sym} and ν(O-O$_{peroxo}$)^{sym} stretching vibrations were derived. Judging from the appearance of the ν(U-O-U-O) long range mode, metastudtite undergoes amorphization to UO_3 at 14 GPa, while studtite already starts to decompose at 1.6 GPa. A pressure induced transformation from studtite to metastudtite could not be observed.

Chapter 4

Conclusion and Outlook

Comprehensive data on $USiO_4$ and the $U_xTh_{(1-x)}SiO_4$ solid solutions was obtained in this work which serves as a useful basis for further syntheses, and as reference for future investigations. Figure 4.1 represents a graphical abstract of the investigated routes for secondary phase formation and the employed characterization techniques. Lattice parameters of the solid solutions evidently follow Vegard's Law. Investigation of the local structure with EXAFS reveals small differences between U and Th environment attributed to different atomic radii of the metal atoms, the complete miscibility is confirmed. IR spectroscopy reveals the presence of water or hydroxyl-groups even in thoroughly dried samples. This work also for the first time implemented the carbonate route for synthesis of $USiO_4$ and $U_xTh_{(1-x)}SiO_4$ bulk material and yielded a unknown U(IV) phase, which should further be characterized. The data obtained from the high-pressure investigations serves great purpose for bench-marking model calculations and may aid to improve these. Synchrotron X-ray powder diffraction pattern of synthetic coffinite, $USiO_4$, show a reversible first order zircon- to scheelite-type phase transition at $\approx$ 15 GPa and room-temperature. The bulk modulus for zircon-type $USiO_4$ is derived as 180(7) GPa. Through the high-pressure Raman investigations it could be furthormore established that B_{1g}- and A_{1g}-modes of the SiO_4^{4-}-tetrahedron in the Raman spectrum are very close and overlap under ambient conditions.

Now that a reproducible and stable route for the synthesis of coffinite, $USiO_4$, and the $U_xTh_{(1-x)}SiO_4$ uranothorites has been developed, it needs to be implemented to produce enough sample mass for reproducible and reliable calorimetric measurements. Samples have been supplied to the group of Prof. Björn Winkler (University, Frankfurt am Main, Germany) for Ultra-low temperature calorimetry (PPMS) and the group of Alexandra Navrotsky (University California, Davis, CA, USA) for high-temperature drop-solution calorimetry.

Th does not significantly contribute to the inventory of SNF after burn-up and thus will most probably not play a significant role in a final repository. However, still special Th-rich fuel from the THTR pebble-bed reactor exists (the total amount nuclear waste deriving from the THTR and AVR reactor is $\sim$ 1970 $cm^{3\,8}$), which will also be disposed of in a final repository.

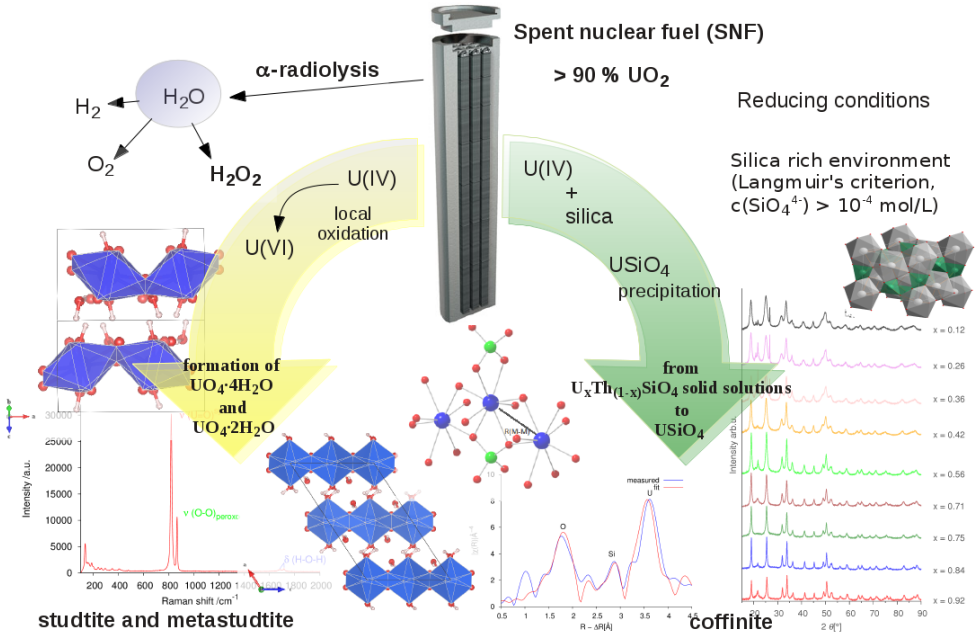

Figure 4.1: The secondary phases evolving from corrosion of spent nuclear fuel (SNF) focused on in this work, their relationship and an excerpt of the methods involved for characterization; schematic drawing.

Interaction between Th-containing an U-containing waste under reducing conditions with silica-rich groundwaterscan be discussed and the obtained data on the $U_xTh_{(1-x)}SiO_4$ solid solutions should contribute useful data for a risk assessment.

Commonly Zr is used as cladding material for the fuel rods in nuclear reactors. Zircon, $ZrSiO_4$, is a ubiquitous appearing mineral, and also an orthosilicate. In fact, it is the aristotype of the $I\,4_1/amd$ spacegroup. Formation of $U_xZr_{(1-x)}SiO_4$ solid solutions has been reported in the Chernobyl 'lavas' [142] and *ab-initio* studies do exist [175;94] on this matter. The $U_xZr_{(1-x)}SiO_4$ solid solutions hence are of even higher importance and more desirable to synthesize than the $U_xTh_{(1-x)}SiO_4$ solid solutions. A collaboration on this topic with the Helmholtz-Zentrum Dresden-Rossendorf (HZDR) within a TALISMAn project, the follow-up of ACTINET-i3, was therefore prepared. In this context it should be also considered to investigate the $U_xHf_{(1-x)}SiO_4$ and corresponding $Th_xHf_{(1-x)}SiO_4$ and $Th_xZr_{(1-x)}SiO_4$ solid solutions and establish the general tendencies towards formation. This could also prove to be of interest as benchmark for data obtained by molecular modeling and promote further reliability of predicted thermodynamic values.

For further fundamental research and to validate computer modeling techniques, the high-pressure investigation of the uranothorites, especially the nearly equimolar solid solutions, can be progressed. First experiments with $U_{0.56}Th_{0.44}SiO_4$ and $U_{0.55}Th_{0.45}SiO_4$ have been undertaken. During research on high-pressure and Raman reference data, it appeared, that almost no data exists for $HfSiO_4$ in this field and that $CeSiO_4$ is also very poorly investigated. Hf is a neutron absorber and under discussion as addition to matrix materials for Pu storage to prevent criticality. On the other hand, Ce(IV) is used as a Pu surrogate. Here is still a lot of research potential for a better understanding of the whole orthosilicate systems.
Besides this work does provide a lot of comprehensive new data on studtite, $UO_2(O_2)_2(OH_2)_2{\cdot}2H_2O$, and metastudtite, $UO_2(O_2)_2(OH_2)_2$, which can be used as references. Many rather old datasets were reevaluated and compared to the newly obtained data. As I believe, this work also contributes to solving the structure of metastudtite. Whereas the model of Weck et al.[2] can largely be validated, the structure still could benefit from further analysis. There are questions remaining and the structure has not been completely solved. From a reliable structure model, a better interpretation of adsorption data of short-lived fission products into studtite can be expected. It might turn out, that studtite indeed can act as a sink for potentially highly toxic radionuclides. Studtite has also been reported to form on gibbsite, γ-$Al(OH)_3$ substrates[176] from uranyl-containing solutions, even when no peroxide is present. This can probably be explained by photocatalytic activity of the U(VI) center, but sufficient data is lacking. Bearing in mind, that U(VI) can be leached from mine tailings this matter could be environmentally important and worth to consider for targeted research. The field still offers many opportunities for scientific investigation.

Chapter 5

Appendix

5.1 Supporting Information on Coffinite and Uranothorites

5.1.1 Syntheses parameters

Table I: List and parameters of the $ThSiO_4$ syntheses performed.

number	concentration [mol/L]	temperature [°C]	time [d]	pH	remarks
SL-Th-1	0.1	100	3	8.9	amorph
SL-Th-2	0.1	100	5	8.5	amorph
SL-Th-3	0.1	100	7	8.4	amorph
SL-Th-4	0.1	150	5	8.5	
SL-Th-5	0.1	150	9	8.6	
SL-Th-6	0.1	150	3	8.5	
SL-Th-7	0.1	200	3	8.2	
SL-Th-8	0.1	200	5	8.1	
SL-Th-9	0.1	200	7	8.3	
SL-Th-10	0.1	125	7	8.6	
SL-Th-11a	0.1	125	3	8.7	
SL-Th-11b	0.1	125	5	8.6	
SL-Th-12	0.1	200	7	8.7	double size
SL-Th-13	0.1	200	7	10	no buffer
SL-Th-14	0.1	200	30	9.6	
SL-Th-15	0.1	200	7	8.9	K_2CO_3 buffer
SL-Th-16	0.1	200	7	8.6	$(NH_4)_2(CO_3)_2$
SL-Th-17	0.1	200	53	8.6	
SL-Th-18	0.5	200	7	8.3	
DG-Th-1	0.5	200	7	7.9	
DG-Th-2	0.1	200	7	7.8	
DG-Th-3	0.1	200	7	8.4	
DG-Th-4	0.5	200	7	8.6	
DG-Th-5	0.1	200	7	8.7	Th-first
DG-Th-6	0.5	200	7	8.5	Th-first
DG-Th-7	0.1	200	7	8.5	
DG-Th-8	0.1	150	7	8.4	
DG-Th-9	0.5	200	7	8.9	
DG-Th-10	0.1	200	100	8.5	
DG-Th-11	0.1	150	7	8.4	molybdate-buffer
DG-Th-12	0.1	150	7	8.6	Th-first
DG-Th-13	0.5	150	7	8.7	Th-first
DG-Th-14	0.1	175	7	8.5	
DG-Th-15	0.5	175	7	8.5	
DG-Th-16	0.1	175	7	8.5	Th-first
DG-Th-17	0.5	175	7	8.5	Th-first

Table II: List of the refined lattice parameters a=b and c of selected $ThSiO_4$ syntheses performed.

number	a=b [Å]	sem[Å]	c[Å]	sem[Å]	V[Å^3]	sem[Å^3]
SL-Th-4	7.1904	0.0009	6.2764	0.0013	324.50	0.08
SL-Th-5	7.121	0.00098	6.2741	0.0014	324.54	0.09
SL-Th-6	7.1867	0.0008	6.2823	0.00119	324.47	0.07
SL-Th-7	7.1828	0.00035	6.2907	0.0005	324.55	0.03
SL-Th-8	7.1602	0.00047	6.29941	0.00066	322.96	0.04
SL-Th-9	7.1669	0.00039	6.29111	0.00056	323.14	0.03
SL-Th-11A	7.1609	0.0015	6.2990	0.0021	323.00	0.14
SL-Th-12	7.1582	0.0014	6.3121	0.0020	323.44	0.12
SL-Th-15	7.158	0.001	6.323	0.0015	324.02	0.09
SL-Th-16	7.173	0.00097	6.323	0.0014	325.39	0.09
DG-Th-1	7.1579	0.00034	6.2959	0.00051	322.58	0.03
DG-Th-2	7.1514	0.00026	6.3050	0.0004	322.45	0.02
DG-Th-3	7.1615	0.00085	6.2960	0.00129	322.91	0.08
DG-Th-4	7.1605	0.00129	6.2963	0.00147	322.82	0.16
DG-Th-7	7.1436	0.00075	6.3184	0.00085	322.44	0.09
DG-Th-9	7.1754	0.0002	6.2877	0.0003	323.73	0.02
DG-Th-10	7.1527	0.00071	6.3086	0.00082	322.76	0.09
DG-Th-11	7.1424	0.0079	6.220	0.011	317.30	0.73
DG-Th-12	7.1607	0.00062	6.2902	0.0007	322.54	0.07
DG-Th-13	7.1385	0.001	6.3071	0.00092	321.15	0.05

Table III: List of the syntheses performed in cooperation with Stephan Weiss at HZDR. All samples of the M, N, and O batch also contained glassy silica.

number	M/Si-ratio	U/Th-ratio	precursor	route/special	product (acc. to XRD)
A 1:1	1:1	1:0	UCl_4 (l)	standard	UO_2 and $USiO_4$
A 1:2	1:2	1:0	UCl_4 (l)	standard	$USiO_4$
A 1:3 b	1:3	1:0	UCl_4 (l)	standard	$USiO_4$ and UO_2
A 1:6	1:6	1:0	UCl_4 (l)	standard	$USiO_4$, SiO_2, and some UO_2
A 1:2/1:6	1:5	1:0	UCl_4 (l)	standard	$USiO_4$
B 1:2 a	1:6	1:2	MCl_4 (l)	standard	$MSiO_4$ and MO_2
B 1:2 c	1:6	1:2	MCl_4 (l)	standard	$MSiO_4$
B 1:1 a	1:6	1:1	MCl_4 (l)	standard	$MSiO_4$ and MO_2
B 1:1 b	1:6	1:1	MCl_4 (l)	standard	$MSiO_4$ and MO_2
B 2:1 a	1:6	2:1	MCl_4 (l)	standard	$MSiO_4$ and MO_2
B 2:1 b	1:6	2:1	MCl_4 (l)	standard	$MSiO_4$
B 2:1 c	1:6	2:1	MCl_4 (l)	standard	$MSiO_4$
C 1:1	1:1	1:0	UCl_4 (s)	standard	$USiO_4$ and UO_2
C 1:6	1:6	1:0	UCl_4 (s)	standard	$USiO_4$, SiO_2
D 1:1	1:1	1:0	UF_4 (s)	standard	$USiO_4$ and UO_2
D 1:6 a	1:6	1:0	UF_4 (s)	standard	$USiO_4$, SiO_2, and UO_2
D 1:6 b	1:6	1:0	UF_4 (s)	standard	UO_2 and SiO_2
D 1:6 c	1:6	1:0	UF_4 (s)	standard	$USiO_4$ and SiO_2
E 1:4	1:4	1:0	UF_4 (l)	standard	U(VI)-oxyhxdroxid
F 1:1	1:1	1:0	UF_4 (s)	silica first	UO_2
A 1:1.05	1:1.05	1:0	UCl_4 (l)	standard	UO_2
A 1:1.5	1:1.5	1:0	UCl_4 (l)	standard	UO_2
A 1:3	1:3	1:0	UCl_4 (l)	standard	$USiO_4$ and SiO_2
B 1:1.1	1:1.05	1:0	UCl_4 (l)	carbonate	UO_2
B 1:4	1:4	1:0	UCl_4 (l)	carbonate	unknown phase
M 9:1I	1:6	9:1	MCl_4 (l)	standard	$MSiO_4$
M 9:1II	1:6	9:1	MCl_4 (l)	standard	$MSiO_4$ and spurious MO_2
M 4:1I	1:6	4:1	MCl_4 (l)	standard	$MSiO_4$
M 4:1II	1:6	4:1	MCl_4 (l)	standard	$MSiO_4$
M 7:3I	1:6	7:3	MCl_4 (l)	standard	$MSiO_4$
M 7:3II	1:6	7:3	MCl_4 (l)	standard	$MSiO_4$ and spurious MO_2
M 6:4I	1:6	6:4	MCl_4 (l)	standard	$MSiO_4$ and spurious MO_2
M 6:4II	1:6	6:4	MCl_4 (l)	standard	$MSiO_4$ and spurious MO_2
M 6:4III	1:6	6:4	MCl_4 (l)	standard	$MSiO_4$ and some MO_2
M 1:1I	1:6	1:1	MCl_4 (l)	standard	$MSiO_4$
M 1:1II	1:6	1:1	MCl_4 (l)	standard	$MSiO_4$
M 1:1III	1:6	1:1	MCl_4 (l)	standard	$MSiO_4$
M 4:6I	1:6	4:6	MCl_4 (l)	standard	$MSiO_4$
M 4:6II	1:6	4:6	MCl_4 (l)	standard	$MSiO_4$
M 3:7I	1:6	3:7	MCl_4 (l)	standard	$MSiO_4$
M 3:7II	1:6	3:7	MCl_4 (l)	standard	$MSiO_4$
M 1:4I	1:6	1:4	MCl_4 (l)	standard	$MSiO_4$

Continued on next page

Table III – continued from previous page

number	M/Si-ratio	U/Th-ratio	precursor	route/special	product (acc. to XRD)
M 1:4II	1:6	1:4	MCl_4 (l)	standard	$MSiO_4$
M 1:9I	1:6	1:9	MCl_4 (l)	standard	$MSiO_4$
M 1:9II	1:6	1:9	MCl_4 (l)	standard	$MSiO_4$
O 1:1	1:4	1:1	MCl_4 (l)	standard	$MSiO_4$
N 9:1	1:4	9:1	MCl_4 (l)	carbonate	MO_2 and spurious $MSiO_4$
N 3.5:1	1:4	3.5:1	MCl_4 (l)	carbonate	unknown phase
N 1:1	1:4	1:1	MCl_4 (l)	carbonate	$MSiO_4$
N 1:4	1:4	1:4	MCl_4 (l)	carbonate	$MSiO_4$
N 1:9	1:4	1:9	MCl_4 (l)	carbonate	$MSiO_4$

UV-VIS spectra of the used UCl_4 - solution and reference from the PhD thesis of Opel.

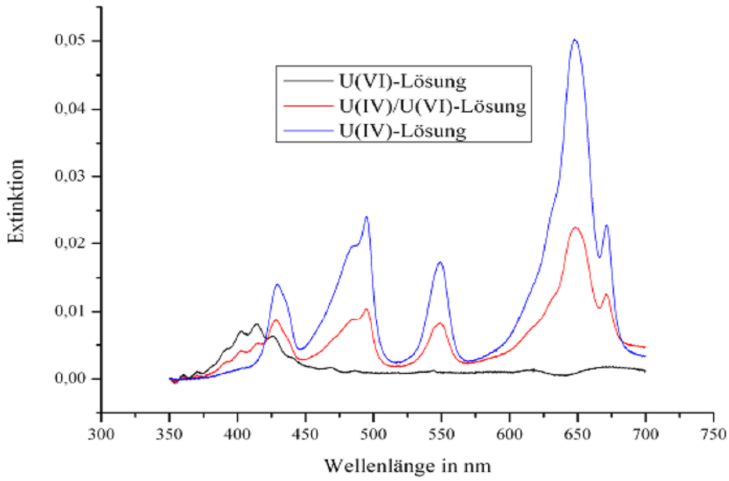

Figure I: Reference UV-VIS spectra of U(IV) and U(VI)-solutions from Opel (2006)[177].

5.1.2 Crystallite size determination and strain analysis using the Williamson–Hall method

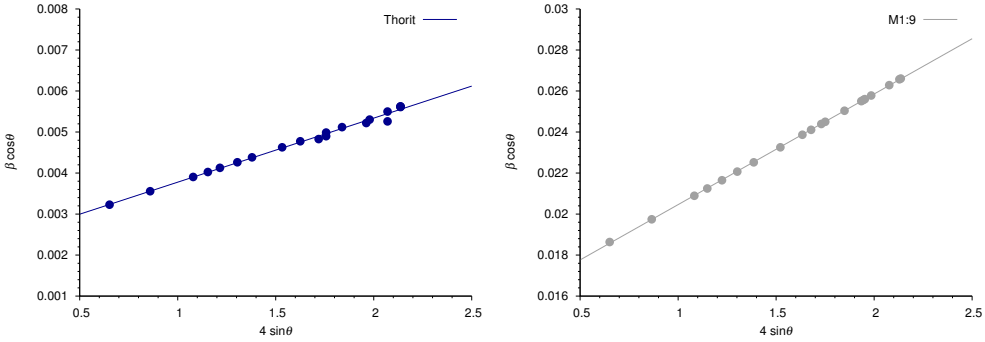

(a) x = 0

(b) x = 0.12

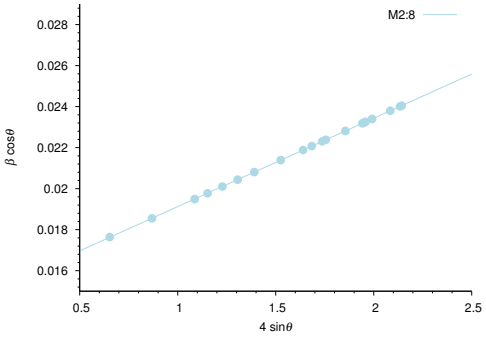

(c) x = 0.26

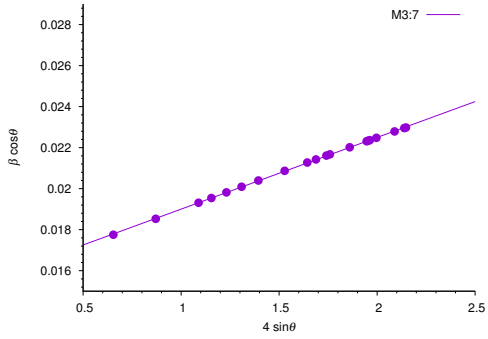

(d) x = 0.36

Figure II: Williamson-Hall plots of the $U_xTh_{(1-x)}SiO_4$ solid solutions used to estimate crystallite size and strain.

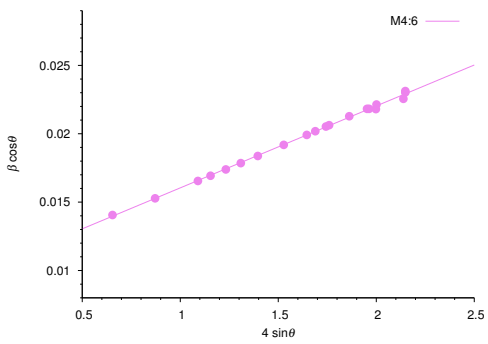

(e) x = 0.42

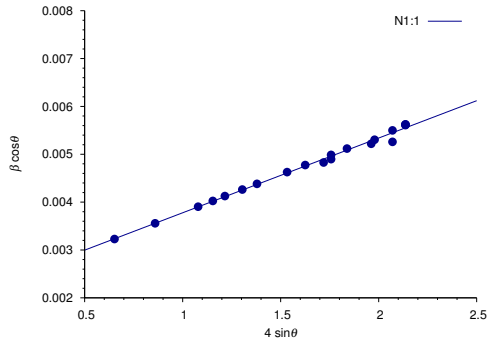

(f) x = 0.55

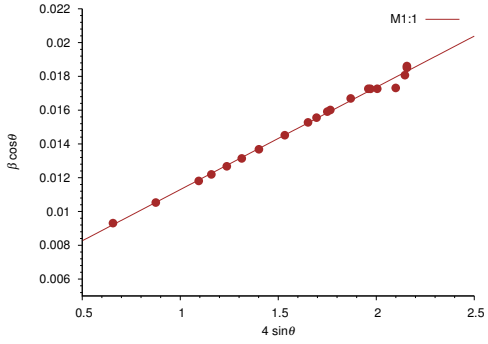

(g) x = 0.56

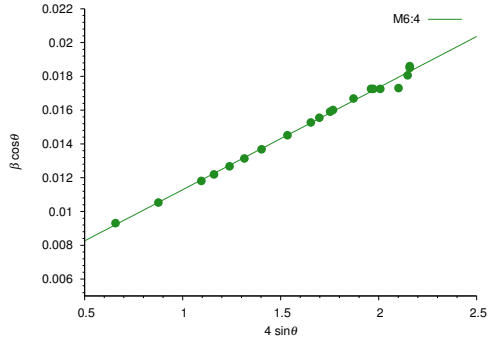

(h) x = 0.60

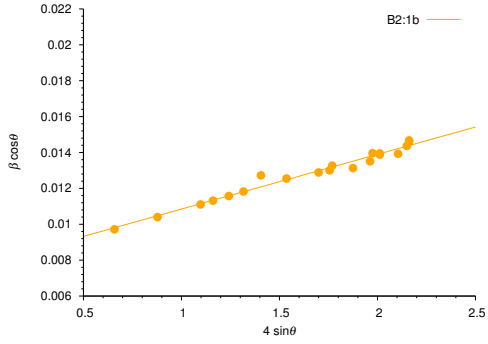

(i) x = 0.71

Figure II: **II – continued from previous page**

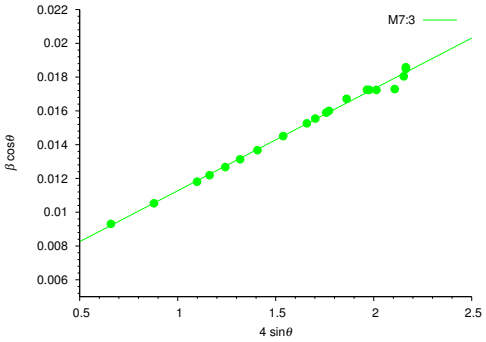

(j) x = 0.75

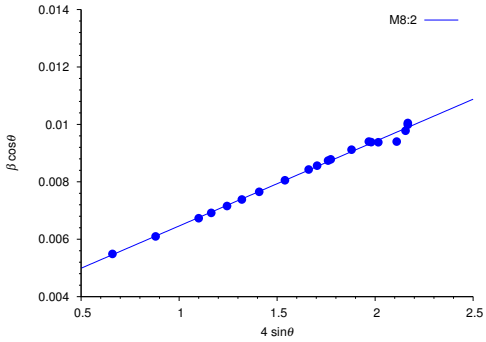

(k) x = 0.84

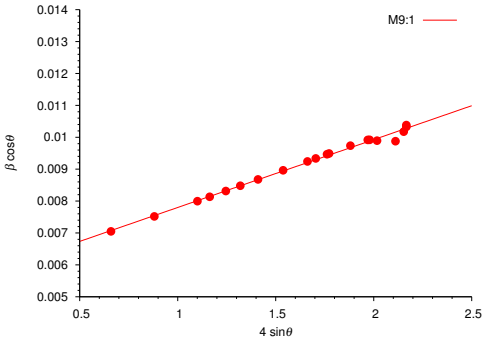

(l) x = 0.92

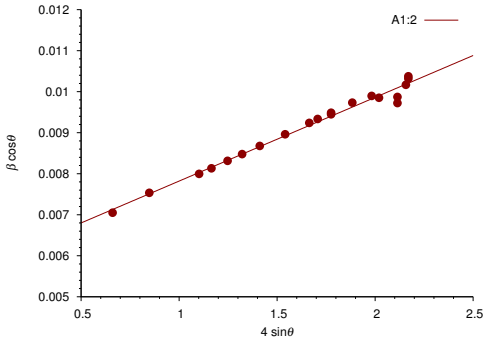

(m) x = 1

Figure II: **II – continued from previous page**

Table IV: Parameters of the linear fit functions derived from Williamson–Hall plot.

χ(U) sample	slope [a.u. 10^{-3}]	intercept [a.u. 10^{-3}]	R^2
0 $ThSiO_4$ (DG-Th-9)	1.562	2.216	0.9930
0.12(1) M1:9	5.394	15.07	0.9999
0.26(1) M1:4	4.311	14.81	1.000
0.36(1) M3:7	3.496	15.51	0.9999
0.42(1) M4:6	5.992	10.05	0.9983
0.55(1) N1:1	4.711	3.658	0.9892
0.56(1) M1:1	6.060	5.235	0.9952
0.60 M6:4	6.048	5.240	0.9952
0.71(1) B2:1b	3.047	7.801	0.9755
0.75(1) M7:3	6.026	5.245	0.9948
0.84(1) M4:1	2.943	3.519	0.9948
0.92(1) M9:1	2.127	5.672	0.9930
1 $USiO_4$ (A1-2)	2.041	5.780	0.9839

5.1.3 Interpretation of the IR and Raman spectra

Vibrations of the SiO_4^{4-}-tetrahedron. The SiO_4^{4-}-tetrahedron belongs to point group T_d. According to symmetry, the four normal modes are expected, see figure III: When moving from point

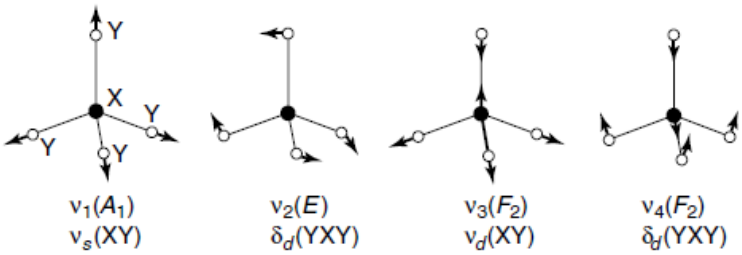

Figure III: Expected normal modes of a pentaatomic XY_4 molecule with tetrahedral symmetry.[67]

group symmetry T_d to lattice symmetry D_{4h} (via site symmetry D_{2d}) these modes split up into the vibrations shown in figure IV.[68;144]

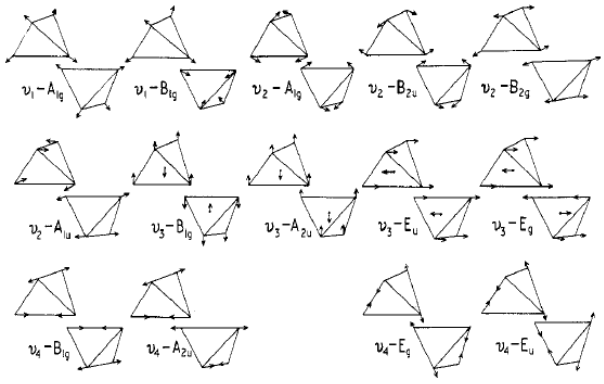

(a)

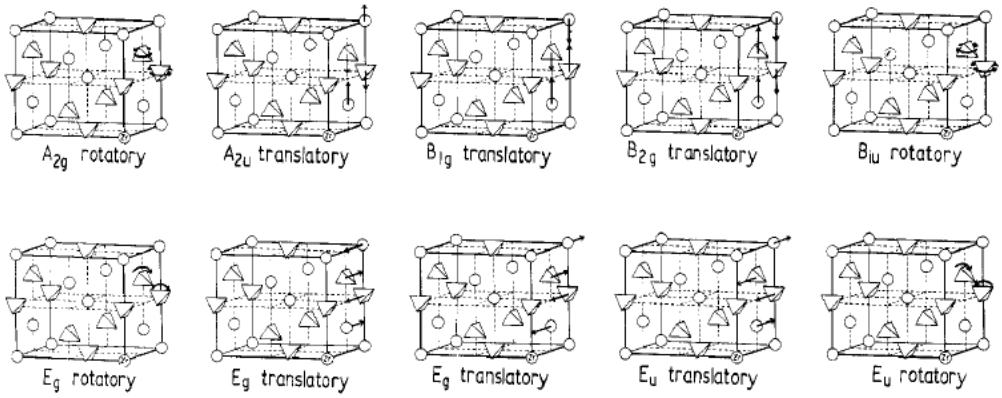

(b)

Figure IV: Illustration of the internal vibrational modes of the SiO_4^{4-} tetrahedron in zircon. In the u (g) modes corresponding atoms of the two SiO_4^{4-} ions in the primitive unit cell move opposite (equivalent) directions. Taken from Dawson et al. (1971).[68]

5.1.4 DSC-TG measurements of $USiO_4$ and $ThSiO_4$

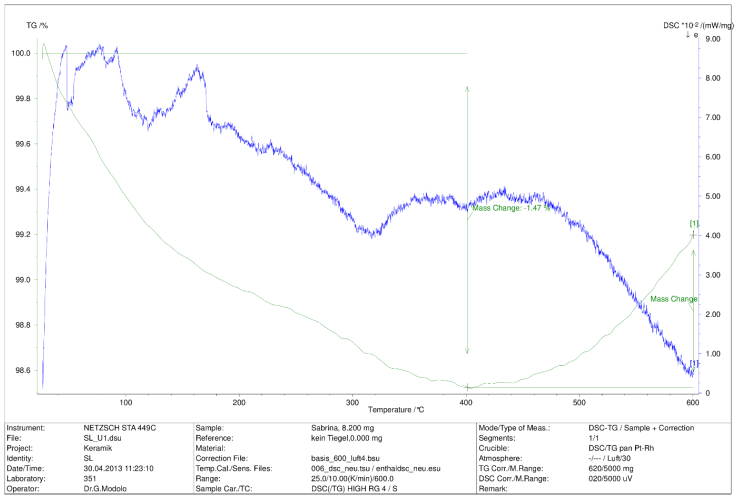

Figure V: DSC-TG measurement of as prepared coffinite sample (A1-2).

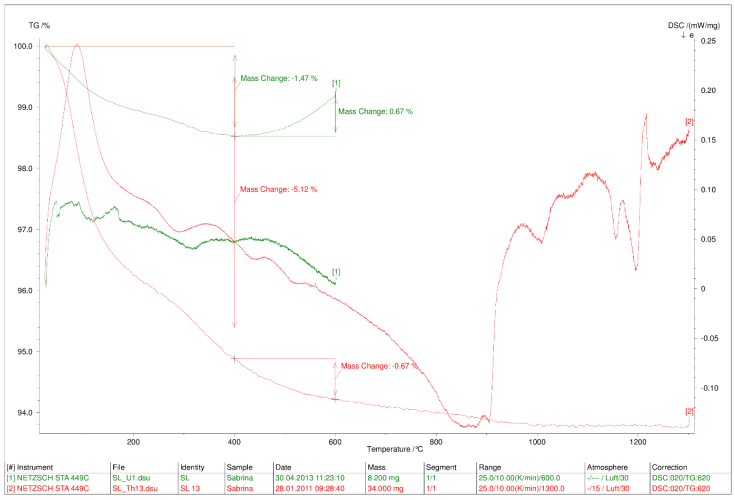

Figure VI: DSC-TG measurements of as prepared thorite and coffinite (A1-2) samples.

5.1.5 EXAFS data

Table V: EXAFS fit parameters of $U_xTh_{(1-x)}SiO_4$ solid solutions at the Th L_3 edge. Coordination numbers are taken from the crystallographic data of $ThSiO_4$ and fixed during the fit procedure. The standard deviations are given in parentheses. Errors in distances R are $\pm$ 0.02 Å, errors in coordination numbers are $\pm$15%.

Sample	Scattering path	N	R [Å]	σ^2 [^{2}]	$\Delta E_{k=0}$ [eV]	F
ThSiO4	Th-O1	4	2.336(3)	0.0012(5)	+ 0.3	0.31
	Th-O2	4	2.434(4)	0.0004(4)		
	Th-Si1	2	3.177(4)	0.0031(4)		
	Th-Si2	4	3.940(7)	0.0057(7)		
	Th-Th	4	3.918(2)	0.0029(2)		
UTh13-9	Th-O1	4	2.334(4)	0.0027(6)	- 4.1	0.21
	Th-O2	4	2.442(6)	0.0036(8)		
	Th-Si1	2	3.181(4)	0.0030(4)		
	Th-Si2	4	3.942(8)	0.0069(9)		
	Th-Th	4	3.900(3)	0.0041(2)		
UTh13-8	Th-O1	4	2.343(10)	0.0034(9)	- 2.6	0.25
	Th-O2	4	2.430(12)	0.0051(2)		
	Th-Si1	2	3.177(4)	0.0027(4)		
	Th-Si2	4	3.945(9)	0.0068(9)		
	Th-Th	4	3.898(3)	0.0043(2)		
UTh13-7	Th-O1	4	2.344(6)	0.0030(7)	- 1.9	0.32
	Th-O2	4	2.446(9)	0.0049(14)		
	Th-Si1	2	3.193(5)	0.0030(4)		
	Th-Si2	4	3.956(13)	0.0088(16)		
	Th-Th	4	3.898(4)	0.0046(3)		
UTh13-6	Th-O1	4	2.335(5)	0.0033(6)	- 3.7	0.18
	Th-O2	4	2.440(6)	0.0047(10)		
	Th-Si1	2	3.186(4)	0.0032(3)		
	Th-Si2	4	3.943(8)	0.0070(9)		
	Th-Th	4	3.893(3)	0.0043(2)		
UTh13-5	Th-O1	4	2.328(3)	0.0018(5)	- 2.3	0.32
	Th-O2	4	2.447(5)	0.0033(7)		
	Th-Si1	2	3.179(4)	0.0024(4)		
	Th-Si2	4	3.943(9)	0.0058(10)		
	Th-Th	4	3.883(4)	0.0038(2)		
UTh13-3	Th-O1	4	2.347(4)	0.0018(4)	- 3.3	0.39
	Th-O2	4	2.458(8)	0.0058(2)		
	Th-Si1	2	3.190(6)	0.0042(6)		
	Th-Si2	4	3.944(2)	0.0070(2)		
	Th-Th	4	3.878(4)	0.0041(3)		
UTh13-2	Th-O1	4	2.332(3)	0.0011(3)	- 3.7	0.25
	Th-O2	4	2.456(4)	0.0031(4)		
	Th-Si1	2	3.179(4)	0.0027(4)		
	Th-Si2	4	3.948(8)	0.0054(9)		
	Th-Th	4	3.873(3)	0.0038(3)		

Table VI: EXAFS fit parameters of $U_xTh_{(1-x)}SiO_4$ solid solutions at the U L_3 edge. Coordination numbers are taken from the crystallographic data of $USiO_4$ and fixed during the fit procedure. The standard deviations are given in parentheses. Errors in distances R are $\pm$ 0.02 Å, errors in coordination numbers are $\pm$15%.

Sample	Scattering path	N	R [Å]	σ^2 [^{2}]	$\Delta E_{k=0}$ [eV]	F
USiO4	U-O1	4	2.272(4)	0.0033(7)	- 3.4	0.45
	U-O2	4	2.395(6)	0.0040(10)		
	U-Si1	2	3.126(4)	0.0018(4)		
	U-Si2	4	3.879(6)	0.0034(6)		
	U-U	4	3.830(2)	0.0027(2)		
UTh13-9	U-O1	4	2.272(5)	0.0040(4)	- 9.8	0.39
	U-O2	4	2.390(12)	0.012(2)		
	U-Si1	2	3.120(10)	0.0073(11)		
	U-Si2	4	3.86(2)	0.013(3)		
	U-U	4	3.867(7)	0.0072(4)		
UTh13-8	U-O1	4	2.279(3)	0.0037(3)	- 7.2	0.14
	U-O2	4	2.422(5)	0.0067(7)		
	U-Si1	2	3.137(5)	0.0059(5)		
	U-Si2	4	3.883(13)	0.014(2)		
	U-Th	4	3.879(3)	0.0062(2)		
UTh13-7	U-O1	4	2.288(2)	0.0016(2)	- 5.1	0.19
	U-O2	4	2.444(4)	0.0046(5)		
	U-Si1	2	3.135(5)	0.0054(5)		
	U-Si2	4	3.911(10)	0.0085(12)		
	U-Th	4	3.868(4)	0.0055(2)		
UTh13-6	U-O1	4	2.278(4)	0.0051(5)	- 6.2	0.21
	U-O2	4	2.427(7)	0.0091(9)		
	U-Si1	2	3.154(7)	0.0067(7)		
	U-Si2	4	3.899(18)	0.014(3)		
	U-Th	4	3.871(4)	0.0058(3)		
UTh13-5	U-O1	4	2.289(7)	0.0059(7)	- 4.7	0.16
	U-O2	4	2.402(9)	0.0097(2)		
	U-Si1	2	3.134(5)	0.0047(5)		
	U-Si2	4	3.887(12)	0.0102(9)		
	U-Th	4	3.857(4)	0.0056(2)		
UTh13-3	U-O1	4	2.290(6)	0.0066(7)	- 5.2	0.20
	U-O2	4	2.406(10)	0.0124(3)		
	U-Si1	2	3.144(5)	0.0053(5)		
	U-Si2	4	3.915(2)	0.0114(2)		
	U-Th	4	3.859(3)	0.0052(2)		
UTh13-2	U-O1	4	2.28(1)	0.0073(2)	- 7.9	0.16
	U-O2	4	2.38(2)	0.0093(3)		
	U-Si1	2	3.125(4)	0.0045(4)		
	U-Si2	4	3.884(9)	0.0090(2)		
	U-Th	4	3.839(3)	0.0052(2)		

5.1.6 High-pressure Raman data

Table VII: List of peak positions [cm^{-1}] in the Raman spectra of $USiO_4$ under elevated pressures. Assignment according to Syme et al.[144] FWHM given in brackets.

pressure [GPa]	lattice modes [cm^{-1}]		ν_2 [cm^{-1}]	ν_4 [cm^{-1}]	E_g [cm^{-1}]	ν_3 [cm^{-1}]	ν_1 [cm^{-1}]
0.00	192(35)	286(24)	419(5)	586(28)	801(39)	915(30)	
3.03	189(10)	302(26)	427(31)	588(51)	813(50)	923(8)	936(18)
3.75	188(12)	305(15)	429(16)	592(29)	813(48)	928(9)	941(16)
3.97	188(13)	306(16)	429(19)	588(29)	813(47)	929(9)	943(17)
5.56	186(13)	314(15)	431(13)	600(17)	819(50)	938(12)	953(18)
6.99	184(14)	319(17)	433(15)	598(33)	819(36)	945(9)	960(16)
7.24	184(9)	320(16)	433(14)	601(38)	825(44)	945(9)	961(15)
11.46	180(15)	335(20)	438(15)	608(38)	819(58)	965(11)	982(15)
11.75	180(13)	336(25)	439(14)	613(53)	821(56)	968(12)	985(16)
13.75	179(13)	344(28)	442(14)	668(145)	820(60)	977(10)	995(13)
14.30	179(13)	345(26)	443(14)	676(185)	822(70)	979(12)	997(14)
16.03	179(10)	350(21)	445(16)	667(191)	820(72)	984(7)	1005(13)
18.69	184(23)	356(47)	448(19)	699(151)	821(82)	990(11)	1013(15)

5.2 Supporting Information on Studtite and Metastudtite

5.2.1 EXAFS

Table VIII: EXAFS fit parameters of studtite, $UO_2(O_2)(H_2O)_2{\cdot}2H_2O$, and metastudtite, $UO_2(O_2)(H_2O)_2$, at the U L_3 edge. Coordination numbers are taken from the crystallographic data of $UO_2(O_2)(H_2O)_2{\cdot}2H_2O$ [153] and fixed during the fit procedure. The standard deviations are given in parentheses. Errors in distances R are $\pm$ 0.02 Å, errors in coordination numbers are $\pm$15%, k-Range 3.6 – 13.

Sample	Scattering path	N	R [Å]	σ^2 [^{2}]	$\Delta E_{k=0}$ [eV]	R
Studtite	U-O1	2	1.8011(6)	0.0020(4)	- 1.29	0.014
	U-O2	4	2.372(6)	0.0020(4)		
	U-O3	2	2.461(15)	0.0020(4)		
	U-U	2	4.25(12)	0.002(1)		
Metastudtite	U-O1	2	1.795(5)	0.0015(4)	+ 9.2	0.024
	U-O2	4	2.374(6)	0.0015(4)		
	U-O3	2	2.48(1)	0.0015(4)		
	U-U	2	4.23(15)	0.003(1)		

5.2.2 High-pressure Raman data

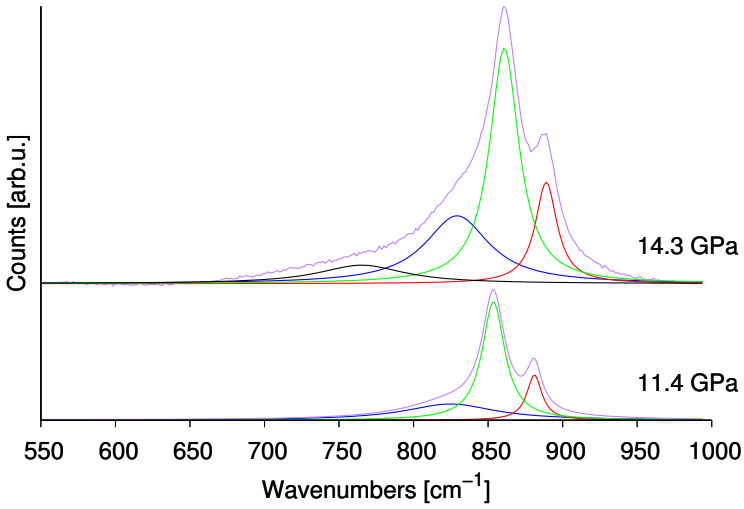

Figure VII: Example fits of the high-pressure Raman spectra of studtite and metastudtite.

Table IX: List of peak positions [cm^{-1}] in the Raman spectra of studtite under elevated pressures. Assignment according to Bastians[166] FWHM given in brackets.

pressure [GPa]	ν(U-O-U-O) [cm^{-1}]	ν(U=O)^{sym} [cm^{-1}]	ν(U-O) [cm^{-1}]	ν(O-O)^{sym} [cm^{-1}]
0.0001	-	820(11)	-	865(6)
1.59	752(54)	821(10)	830(16)	868(11)
2.69	751(116)	822(10)	834(18)	869(13)
3.31	752(56)	823(10)	833(18)	869(13)
4.97	741(103)	826(12)	837(20)	871(13)
5.70	740(126)	828(12)	837(21)	872(13)
7.36	744(92)	831(12)	831(28)	871(16)
9.44	758(111)	832(32)	833(15)	870(20)
9.73	733(97)	800(54)	832(22)	869(25)
10.6	729(90)	799(54)	835(21)	871(22)
12.2	729(127)	812(73)	836(20)	873(29)

Table X: List of peak positions [cm^{-1}] in the Raman spectra of metastudtite under elevated pressures. Assignment according to Bastians[166] FWHM given in brackets.

pressure [GPa]	ν(U-O-U-O) [cm^{-1}]	ν(U-O) [cm^{-1}]	ν(U=O)^{sym} [cm^{-1}]	ν(O-O)^{sym} [cm^{-1}]
0.0001	-	826(15)	832(11)	869(6)
1.78	-	832(15)	838(9)	870(13)
3.14	-	831(23)	837(13)	870(11)
5.56	-	829(46)	843(14)	872(9)
9.98	-	825(74)	854(18)	881(12)
11.40	-	824(78)	856(20)	883(14)
14.00	765(71)	829(52)	861(24)	889(18)
14.30	752(79)	828(55)	862(25)	890(18)
16.30	760(91)	830(58)	867(30)	896(19)
17.90	747(103)	826(79)	870(37)	900(28)

5.3 In-situ X-ray diffraction

Table XI: Lattice parameters and mass fractions from the Rietveld refinement of the studtite, $UO_2(O_2)(H_2O)_2{\cdot}2H_2O$, in-situ X-ray dehydration experiment.

	Studtite						Metastudtite						
T [°C]	a[Å]	b[Å]	c [Å]	β [°]	wt.	V [Å^3]	a [Å]	b [Å]	c [Å]	wt.	V [Å^3]	Rp [%]	wRp [%]
30	14.157(1)	6.7755(5)	8.4891(6)	123.295(5)	0.988(1)	680.61(5)						7.73	10.72
31	14.157(1)	6.7758(5)	8.4899(6)	123.302(5)	0.989(1)	680.59(5)						7.78	10.69
32	14.158(1)	6.7756(5)	8.4883(6)	123.300(5)	0.989(1)	680.59(5)						7.71	10.59
33	14.160(1)	6.7749(5)	8.4889(6)	123.304(5)	0.988(1)	680.62(5)						7.83	10.75
34	14.161(1)	6.7748(5)	8.4890(6)	123.310(5)	0.988(1)	680.62(5)						7.83	10.75
35	14.163(1)	6.7740(5)	8.4890(6)	123.314(6)	0.988(1)	680.60(5)						7.94	10.84
36	14.165(1)	6.7731(5)	8.4891(7)	123.325(6)	0.988(1)	680.53(5)						8.09	10.98
37	14.166(1)	6.7727(6)	8.4898(7)	123.336(6)	0.988(1)	680.53(6)						8.17	11.13
38	14.163(2)	6.7725(6)	8.4898(8)	123.339(7)	0.987(1)	680.45(7)						8.36	11.47
39	14.167(2)	6.7725(7)	8.4894(9)	123.342(8)	0.986(1)	680.46(7)						8.59	11.80
40	14.167(1)	6.7668(5)	8.4860(6)	123.327(5)	0.67(2)	679.72(5)	8.85(3)	8.55(2)	7.37(1)	0.32(2)	558(2)	7.70	9.90
41	14.169(1)	6.7670(6)	8.4837(7)	123.332(6)	0.63(2)	679.60(6)	7.85(2)	8.84(2)	7.21(1)	0.36(2)	500(1)	8.05	10.24
42	14.172(2)	6.7635(8)	8.483(1)	123.298(8)	0.65(2)	679.59(8)	8.33(1)	8.818(9)	6.712(6)	0.34(2)	493.2(7)	9.52	12.47
43	14.184(3)	6.77(1)	8.484(2)	123.47(2)	0.64(3)	679.2(1)	8.419(3)	8.753(4)	6.534(2)	0.35(3)	481.5(2)	8.57	11.89
44	14.186(3)	6.76(15)	8.492(2)	123.41(2)	0.58(3)	679.9(2)	8.409(2)	8.76(2)	6.513(1)	0.41(3)	479.9(1)	8.63	11.80
45	14.183(4)	6.761(2)	8.497(3)	123.39(2)	0.49(3)	680.3(2)	8.410(1)	8.765(1)	6.5047(9)	0.50(3)	479.48(9)	8.30	11.40
46	14.257(7)	6.742(4)	8.612(6)	124.09(4)	0.42(3)	685.5(4)	8.407(1)	8.764(1)	6.5060(7)	0.56(3)	479.37(7)	8.48	11.28
47	14.10(10)	6.79(3)	8.86(3)	129.4(5)	0.38(3)	654	8.4092(7)	8.7639(8)	6.5026(6)	0.61(3)	479.23(6)	7.84	10.05
48	13.37(6)	6.62(3)	9.98(4)	128.4(2)	0.28(2)	692(2)	8.4078(7)	8.7615(7)	6.5017(5)	0.71(2)	478.95(5)	8.00	10.36
49	15.8(1)	6.72(7)	8.09(7)	111.5(5)	0.46(3)	801(6)	8.4082(6)	8.7644(6)	6.5017(5)	0.53(3)	479.13(4)	8.57	10.88
50	15.1(1)	6.43(4)	8.9(2)	72(1)	0.72(2)	825(14)	8.4088(6)	8.7644(6)	6.5005(5)	0.27(1)	479.08(4)	8.68	10.81
51	13(3)	5.9(4)	9.2(5)	127(14)	0.45(2)	561(80)	8.408(1)	8.7642(1)	6.500(1)	0.55(7)	478.99(9)	23.38	26.22
52							8.4079(6)	8.7630(6)	6.4990(5)	0.89(5)	478.83(4)	7.98	10.29
53							8.4080(5)	8.7635(6)	6.4996(4)	0.94(1)	478.92(4)	7.65	9.80
54							8.4078(5)	8.7628(6)	6.4993(4)	0.94(1)	478.85(4)	7.64	9.78
55							8.4081(5)	8.7629(6)	6.4995(4)	0.94(1)	478.88(4)	7.58	9.72

Continued on next page

Table XI – continued from previous page

	Studtite						Metastudtite						
T [°C]	a[Å]	b[Å]	c [Å]	β [°]	wt.	V [Å^3]	a [Å]	b [Å]	c [Å]	wt.	V [Å^3]	Rp [%]	wRp [%]
56							8.4086(5)	8.7637(6)	6.4992(4)	0.941(9)	478.93(4)	7.58	9.77
57							8.4083(5)	8.7634(5)	6.4984(4)	0.94(1)	478.83(4)	7.57	9.71
58							8.4089(5)	8.7636(5)	6.4991(4)	0.95(1)	478.94(4)	7.61	9.79
59							8.4085(5)	8.7632(5)	6.4986(4)	0.941(9)	478.85(4)	7.59	9.79
60							8.4084(5)	8.7630(5)	6.4982(4)	0.945(9)	478.81(4)	7.51	9.67
61							8.4083(5)	8.7627(5)	6.4984(4)	0.946(9)	478.80(4)	7.66	9.83
62							8.4087(5)	8.7632(5)	6.4984(4)	0.94(1)	478.85(4)	7.52	9.70
63							8.4089(5)	8.7633(5)	6.4982(4)	0.941(9)	478.85(4)	7.51	9.69
64							8.4090(5)	8.7631(5)	6.4981(4)	0.94(1)	478.84(4)	7.58	9.74
65							8.4093(5)	8.7633(5)	6.4983(4)	0.94(1)	478.89(4)	7.51	9.62
66							8.4092(5)	8.7630(5)	6.4975(4)	0.935(9)	478.79(4)	7.52	9.64
67							8.4084(5)	8.7627(5)	6.4973(4)	0.94(1)	478.72(4)	7.40	9.52
68							8.4090(5)	8.7630(5)	6.4974(4)	0.938(9)	478.78(4)	7.53	9.64
69							8.4092(5)	8.7632(5)	6.4974(4)	0.935(9)	478.80(4)	7.44	9.56
70							8.4081(5)	8.7632(5)	6.4976(4)	0.95(1)	478.81(4)	7.52	9.62
71							8.4091(5)	8.7630(5)	6.4971(4)	0.942(9)	478.76(4)	7.55	9.64
72							8.4088(5)	8.7630(5)	6.4967(4)	0.943(9)	478.72(4)	7.48	9.56
73							8.4088(5)	8.7628(5)	6.4970(4)	0.948(9)	478.73(4)	7.40	9.49
74							8.4089(5)	8.7624(5)	6.4969(4)	0.944(9)	478.71(4)	7.47	9.53
75							8.4096(5)	8.7630(5)	6.4968(4)	0.937(9)	478.77(3)	7.36	9.50
76							8.4091(5)	8.7625(4)	6.4966(4)	0.943(8)	478.70(3)	7.35	9.40
77							8.4095(5)	8.7626(5)	6.4966(4)	0.941(9)	478.73(3)	7.45	9.48
78							8.4099(5)	8.7628(5)	6.4966(4)	0.947(9)	478.76(3)	7.46	9.52
79							8.4093(5)	8.7626(5)	6.4967(4)	0.941(9)	478.72(3)	7.46	9.48
80							8.4095(5)	8.7627(5)	6.4967(4)	0.932(9)	478.75(3)	7.36	9.39
81							8.4091(5)	8.7623(5)	6.4964(4)	0.940(9)	478.67(3)	7.40	9.43
82							8.4095(5)	8.7624(5)	6.4969(4)	0.937(9)	478.74(3)	7.36	9.41
83							8.4101(5)	8.7627(5)	6.4965(4)	0.942(9)	478.76(3)	7.30	9.33
85							8.4095(5)	8.7622(5)	6.4961(4)	0.942(9)	478.66(3)	7.49	9.49
86							8.4094(5)	8.7623(5)	6.4965(4)	0.945(8)	478.70(3)	7.30	9.30

Continued on next page

Table XI – continued from previous page

	Studtite					Metastudtite						
T [°C]	a[Å]	b[Å]	c [Å]	β [°]	wt.	V [Å^3]	a [Å]	b [Å]	c [Å]	wt.	V [Å^3]	Rp [%]	wRp [%]
87							8.4097(5)	8.7624(5)	6.4966(4)	0.944(9)	478.73(3)	7.36	9.41
88							8.4100(5)	8.7626(5)	6.4971(4)	0.940(9)	478.80(3)	7.38	9.33
89							8.4098(5)	8.7619(5)	6.4965(4)	0.934(9)	478.70(3)	7.43	9.44
90							8.4098(5)	8.7623(5)	6.4967(4)	0.941(8)	478.73(3)	7.33	9.34
91							8.4095(5)	8.7616(5)	6.4969(4)	0.934(9)	478.69(3)	7.41	9.42
96							8.4090(5)	8.7612(5)	6.4969(4)	0.934(9)	478.64(3)	7.40	9.41
101							8.4089(5)	8.7612(5)	6.4969(4)	0.905(5)	478.65(3)	7.49	9.50
106							8.4091(5)	8.7605(5)	6.4973(4)	0.940(9)	478.65(3)	7.48	9.45
111							8.4092(5)	8.7605(5)	6.4981(4)	0.92(1)	478.70(3)	7.53	9.53
122							8.4091(5)	8.7605(5)	6.4973(4)	0.927(9)	478.65(3)	7.48	9.45
142							8.4073(5)	8.7552(5)	6.5019(4)	0.906(9)	478.59(3)	7.51	9.50
153							8.4065(5)	8.7518(5)	6.5042(4)	0.915(8)	478.53(4)	7.50	9.51
163							8.4060(5)	8.7486(5)	6.5070(4)	0.890(8)	478.53(4)	7.26	9.25
173							8.4038(5)	8.7438(5)	6.5092(4)	0.897(7)	478.30(4)	7.26	9.10
183							8.3999(5)	8.7379(6)	6.5110(4)	0.901(6)	477.89(4)	7.26	9.18
188							8.3955(6)	8.7330(6)	6.5102(5)	0.902(5)	477.31(4)	7.12	8.92
193							8.3906(7)	8.7277(7)	6.5079(6)	0.897(5)	476.57(5)	7.50	9.41
198							8.3851(9)	8.721(1)	6.5081(7)	0.869(5)	475.91(7)	8.20	10.48

Table XII: [Peak positions, FWHM and normalized area ≡ mass fractions from the single peak fit of the studtite, $UO_2(O_2)(H_2O)_2{\cdot}2H_2O$, in-situ X-ray dehydration experiment.

	Studtite			Intermediate			Metastudtite		
T [°C]	position[2θ]	FWHM [2θ]	Norm. area	position[2θ]	FWHM [2θ]	Norm. area	position[2θ]	FWHM [2θ]	Norm. area
30	15.0397	0.270533	0.955						
31	15.0401	0.270545	0.963						
32	15.0397	0.26959	0.987						
33	15.0397	0.2753	0.957						

Continued on next page

	Studtite			Intermediate			Metastudtite		
T [°C]	position[2θ]	FWHM [2θ]	Norm. area	position[2θ]	FWHM [2θ]	Norm. area	position[2θ]	FWHM [2θ]	Norm. area
34	15.0411	0.275414	0.971						
35	15.0439	0.275195	1.00						
36	15.0471	0.286642	0.950						
37	15.0522	0.292735	0.950						
38	15.0579	0.294822	0.938						
39	15.0659	0.29783	0.911						
40	15.0677	0.310336	0.804	15.794	1.26111	0.146	16.9199	0.597284	0.001
41	15.0727	0.318709	0.687	15.8417	1.32847	0.213	16.9377	0.398466	0.089
42	15.0791	0.33032	0.589	15.9356	1.42447	0.276	16.9451	0.361908	0.109
43	15.0868	0.346866	0.446	16.2903	1.9737	0.527	16.9596	0.330987	0.120
44	15.0885	0.367497	0.311	16.021	1.50783	0.313	16.9618	0.347246	0.272
45	15.0886	0.381431	0.192	16.1306	1.48931	0.280	16.9617	0.343126	0.350
46	15.0937	0.400907	0.166	16.4548	1.15944	0.219	16.9632	0.326752	0.455
47	15.1164	0.495533	0.124				16.9584	0.317444	0.754
48	15.1049	0.453108	0.055				16.9634	0.308328	0.819
49	15.1017	0.502439	0.023				16.9684	0.305909	0.847
50	15.1645	0.0893978	0.012				16.9703	0.3049	0.854
52	15.1101	0.440202	0.009				16.9718	0.302436	0.869
54	15.2303	0.657064	0.019				16.9735	0.301882	0.875
55							16.975	0.294647	0.937
56							16.974	0.299387	0.914
57							16.9774	0.298279	0.894
58							16.9778	0.298345	0.940
59							16.9778	0.302276	0.877
60							16.9794	0.302002	0.904
61							16.9791	0.300792	0.913
62							16.9809	0.300248	0.925
63							16.9824	0.297146	0.925
64							16.983	0.302746	0.890

Continued on next page

	Studtite			Intermediate			Metastudtite		
T [°C]	position[2θ]	FWHM [2θ]	Norm. area	position[2θ]	FWHM [2θ]	Norm. area	position[2θ]	FWHM [2θ]	Norm. area
65							16.9838	0.301464	0.894
66							16.9834	0.306835	0.877
67							16.985	0.306743	0.878
68							16.9854	0.301593	0.891
69							16.9862	0.299371	0.899
70							16.9877	0.304763	0.882
71							16.989	0.30028	0.915
72							16.9891	0.286858	1.00
73							16.9908	0.301769	0.896
74							16.9916	0.301056	0.917
75							16.9919	0.300017	0.927
76							16.9948	0.294561	0.949
77							16.9942	0.296812	0.936
78							16.9959	0.295805	0.923
79							16.9972	0.292952	0.966
80							16.9982	0.296291	0.937
81							16.9975	0.294945	0.940
82							16.9986	0.294172	0.919
83							16.998	0.295658	0.917
85							17.0001	0.287936	0.986
86							17.0006	0.29307	0.949
87							17.0015	0.287285	0.985
88							17.0025	0.293605	0.961
89							17.0033	0.288761	0.954
90							17.0043	0.287607	0.981
91							17.0051	0.284561	0.989
96							17.006	0.289759	0.963
101							17.0083	0.284247	1.00
106							17.0115	0.287514	0.927

Continued on next page

	Studtite			Intermediate			Metastudtite		
T [°C]	position[2θ]	FWHM [2θ]	Norm. area	position[2θ]	FWHM [2θ]	Norm. area	position[2θ]	FWHM [2θ]	Norm. area
111							17.0136	0.291207	0.944
122							17.0178	0.287106	0.966
132							17.0205	0.287567	0.958
142							17.0259	0.291296	0.900
153							17.0303	0.293943	0.858
163							17.0385	0.294678	0.830
173							17.0527	0.301921	0.729
183							17.082	0.310914	0.601
188							17.1272	0.315001	0.476
193							17.1769	0.31399	0.334
198							17.2213	0.337503	0.200
203							17.2659	0.451773	0.117
208							17.3264	0.455174	0.017
213							17.422	1.57881	0.052

Publications

Parts of this work have been submitted for publication to scientific journals or have been presented at international conferences.

Journal Contributions
S. Labs, S. Weiss, C. Hennig, H. Curtius, H. Zänker, D. Bosbach; Synthesis of coffinite, $USiO_4$, and structural investigations of the $U_xTh_{(1-x)}SiO4$ solid solutions, *Envir. Sci. Tech.* **2013**
J.D. Bauer, S. Labs, S. Weiss, L. Bayarjargal, W. Morgenroth, V. Milman, A. Perlov, H. Curtius, D. Bosbach, H. Zänker, and B. Winkler. High-pressure phase transition of coffinite, $USiO_4$ *Phys. Rev. B* **2014** (in review).

–

J.D. Bauer, S. Labs, S. Weiss, L. Bayarjagal, H. Curtius, W. Morgenroth, D. Bosbach, C. Hennig, B. Winkler; Raman Spectroscopy and Powder Diffraction Study of Synthetic Coffinite ($USiO_4$) at High Pressures, *Mineralogical Magazine*, (5) 668 **2013**. (Abstract - Talk, invited)
S. Labs, M. Hartl, L. Daemen, H. Curtius, D. Bosbach; Investigation of the Dehydration Process of Uranium Peroxide, *Z. Anorg. Allg. Chem.* 638 (10) 1606 **2012**. (Abstract - Poster)
S. Labs, H. Curtius, D. Bosbach; Synthesis of lentil shaped $ThSiO_4$ nanoparticles by a hydrothermal route, *Mineralogical Magazine* 75(3) 1262 **2011**. (Abstract - Poster)

Reports
D. Bosbach, C. Hennig, A. Scheinost; *Investigations of Th(IV) and U(IV) Silicates: colloid formation – alterations – solid state characteristics* ACTINET-i3 report, AC4-JRP04 **2013**. S. Labs, C. Hennig; *Investigations of Th(IV) and U(IV) Silicates: colloid formation – alterations – solid state characteristics* ESRF experimental report 20-01-723 **2013**.

Posters
S. Labs, S. Weiss, C. Hennig, H. Curtius, D. Bosbach; *Structural investigation of solid Solutions in the System $USiO_4$ – $ThSiO_4$*, Migration Conference 2013, 08. – 13.09.2013, Brighton, UK.
S. Labs, S. Weiss, C. Hennig, R. Hübner, H. Curtius, D. Bosbach; *Synthesis and structure investigation of $USiO_4$ – comparison between local structure and bulk*, EMRS spring meeting, 27. – 31.05.2013, Strasbourg, France.
S. Labs, J. D. Bauer, B. Winkler, L. Bayarjargal, H. Curtius, D. Bosbach; *High-pressure behavior of studtite, $UO_4 \cdot 4H_2O$, and metastudtite, $UO_4 \cdot 2H_2O$ – a Raman investigation*, EMRS spring meeting, 27. – 31.05.2013, Strasbourg, France.
S. Labs, M. Hartl, L. Daemen, H. Curtius, D. Bosbach; *Investigations regarding the dehydration mechanism of $UO_4 \cdot 4H_2O$*, 16^{th} Conference of the GdCh Division for Solid State Chemistry and Materials Research, 17. – 19.09.2012 Darmstadt, Germany.
S. Labs, H. Curtius, D. Bosbach; *Synthesis of lentil shaped $ThSiO_4$ nanoparticles by a hydrothermal route*, Goldschmidt Conference 2011 Prague, Czech Republic.

Talks – Conference
S. Labs, M. Hartl, L. Daemen, A. Neumann, H. Curtius, D. Bosbach; *Structural Investigation of Metastudtite, $UO_4 \cdot 2H_2O$*, **EUROMAT2013** conference, 08. – 13.09.2013, Sevilla, Spain.
S. Labs, A. Neumann, M. Hartl, H. Curtius;*Baking Yellow Cake*, Hemdsärmelkolloquien 2013, 07.

– 09.03.2013, Albert-Ludwigs-Universität Freiburg im Breisgau, Germany.

Talks – Contribution

J.D. Bauer, S. Labs, S. Weiss, L. Bayarjagal, H. Curtius, W. Morgenroth, D. Bosbach, C. Hennig, B. Winkler; *Raman Spectroscopy and Powder Diffraction Study of Synthetic Coffinite ($USiO_4$) at High Pressures*, Goldschmidt Conference 2013, 25. – 30.08.2013, Florence, Italy. (invited)

J.D. Bauer, S. Labs, B. Winkler, H. Curtius, D. Bosbach; *Temperature dependent X-ray study of the transformation of studtite, $UO_4 \cdot 4H_2O$, to metastudtite, $UO_4 \cdot 2H_2O$*; 22. Jahrestagung der DGK, 17. – 21.03.2014, Berlin, Germany.

Bibliography

[1] S. Ono, Y. Tange, I. Katayama, and T. Kikegawa. Equations of state in $ZrSiO_4$ phases of the upper mantle. *Am. Mineral.*, 89:185–188, 2004.

[2] Philippe F. Weck, Eunja Kim, Carlos F. Jove-Colon, and David C. Sassani. Structures of uranyl peroxide hydrates: a first-principles study of studtite and metastudtite. *Dalton Trans.*, 41(32):9748–9752, 2012.

[3] Jordi Bruno and R.C. Ewing. Spent Nuclear Fuel. *Elements*, pages 343–349, December 2006.

[4] Freiesleben, H. Final disposal of radioactive waste. *EPJ Web of Conferences*, 54:01006, 2013.

[5] U. Fischer and H.W. Wiese. Verbesserte konsistente Berechnung des nuklearen Inventars abgebrannter DWR-Brennstoffe auf der Basis von Zell-Abbrand-Verfahren mit KORIGEN. Technical Report KfK 3014, Forschungszentrum Karlsruhe, 1983. ORNL-tr-5043.

[6] Dirk Bosbach. 50 Jahre Endlagerforschung im IEK-6. Vortrag zum 50 jährigen Institutsbestehen, 2014.

[7] Gregory R. Choppin, Jan-Olov Liljenzin, and Jan Rydberg. *Radiochemistry and Nuclear Chemistry*. Butterworth-Heinemann, 3 edition, 2001.

[8] Lutz Ebermann. Jahresbericht 2012 des Bundesamt für Strahlenschutz. Technical report, Bundesamt für Strahlenschutz, 2012.

[9] Naoto Takeno. Atlas of Eh-pH diagrams Intercomparison of thermodynamic databases. Geological Survey of Japan Open File Report 419, National Institute of Advanced Industrial Science and Technology Research Center for Deep Geological Environments, 2005.

[10] Kaname Miyahara. Sensitivity of Uranium Solubility to Variation of Ligand Concentrations in Groundwater. *Journal of Nuclear Science and Technology*, 30(4):314–332, 1993.

[11] M. Chijimatsu, L. Jing, Ko. De Jonge, M. lmeier, T. S. Nguyen, A. Milard, A. Rejeb, J. Rutqvist, M. Souley, and Y. Sugita. Numerical study of the THM effects on the near-field safety of a hypothetical nuclear waste repository BMT1 of the DECOVALEX III project. Part 1: Conceptualization and characterization of the problems and summary of results. *International journal of rock mechanics and mining sciences*, 42(5-6):720–730, 2005.

[12] Yueting Chen. Using reactive transport modeling to evaluate the source term at Yucca Mountain . *Computers & Geosciences*, 29(3):385–397, 2003. Reactive Transport Modeling in the Geosciences.

[13] Olivia Roth. *Redox Chemistry in Irradiation Induced Dissolution of Spent Nuclear Fuel - from elementary reactions to predictive modeling*. PhD thesis, KTH - Chemical Science and Engineering Nuclear Chemistry, 2008.

[14] L. R. Stieff, T. W. Stern, and A. M. Sherwood. Preliminary Description of Coffinite - a New Uranium Mineral. *Science*, 121:608–609, 1955.

[15] J. Janeczek and R.C. Ewing. Dissolution and alteration of uraninite under reducing conditions. *J. Nucl. Mater.*, 190:157–173, August 1992.

[16] Maozhong Min Min, Changquan Fanga, and Mostafa Fayek. Petrography and genetic history of coffinite and uraninite from the Liueryiqi granite-hosted uranium deposit, SE China. *Ore Geology Reviews*, (26):187â197, 2005.

[17] D.G. Brookins. Geochemistry of Clay Minerals for Uranium Exploration in the Grants Mineral Belt, New Mexico. *Miner. Deposita*, 17:37–53, 1982.

[18] K. A. Jensen and R.C. Ewing. The Okélobondo natural fission reactor, southeast Gabon; Geology, mineralogy, and retardation of nuclear-reaction products. *Geological Society of America Bulletin*, 113(1):32–62, 2001.

[19] Donald Langmuir. Uranium solution-mineral equilibria at low temperatures with applications to sedimentary ore deposits. *Geochim. Cosmochim. Acta*, 42(6, Part 1):547–569, June 1978.

[20] Janusz Janeczek, Rodney C. Ewing, Virginia M. Oversby, and Lars O. Werme. Uraninite and UO_2 in spent nuclear fuel: a comparison. *J. Nucl. Mater.*, 238(1):121–130, October 1996.

[21] Robert J. Baker. Uranium minerals and their relevance to long term storage of nuclear fuels. *Coordination Chemistry Reviews*, (0):–, 2014.

[22] Rodney C. Ewing. Safe management of actinides in the nuclear fuel cycle: Role of mineralogy . *Comptes Rendus Geoscience*, 343(2-3):219–229, 2011.

[23] D. Arcos, L. Pérez del Villar, J. Bruno, and C. Domènech. Geochemical modelling of the weathering zone of the "Mina Fe" U deposit (Spain): A natural analogue for nuclear spent fuel alteration and stability processes in radwaste disposal. *Appl. Geochem.*, 23(4):807–821, April 2008.

[24] L. Pérez del Villar, J. Bruno, R. Campos, P. Gómez, J. S. Cózar, A. Garralón, B. Buil, D. Arcos, G. Carretero, J. Ruiz Sánchez-Porro, and P. Hernán. The uranium ore from Mina Fe (Salamanca, Spain) as a natural analogue of processes in a spent fuel repository. *Chem. Geol.*, 190(1-4):395–415, October 2002.

[25] V. Pointeau, A.P. Deditius, F. Miserque, D. Renock, U. Becker, J. Zhang, N. Clavier, N. Dacheux, C. Poinssot, and R.C. Ewing. Synthesis and characterization of coffinite. *J. Nucl. Mater.*, 393(3):449–458, September 2009.

[26] Hailey Sonja Reynolds. *SYNTHESIS, CHARACTERISATION AND DISSOLUTION STUDIES OF THE URANIUM MINERAL COFFINITE*. PhD thesis, School of Applied Sciences Royal Melbourne Institute of Technology (RMIT) UNIVERSITY Melbourne, Victoria, Australia, April 2013.

[27] B.S. Hemingway. United States Geology Survey Open-File Report. Technical Report 90, 1982. 82-619.

[28] Stéphanie Szenknect, Dan T. Costin, Nicolas Clavier, Adel Mesbah, Christophe Poinssot, Pierre Vitorge, and Nicolas Dacheux. From Uranothorites to Coffinite: A Solid Solution Route to the Thermodynamic Properties of $USiO_4$. *Inorg. Chem.*, 2013.

[29] Christopher R. Armstrong, May Nyman, Tatiana Shvareva, Ginger E. Sigmon, Peter C. Burns, and Alexandra Navrotsky. Uranyl peroxide enhanced nuclear fuel corrosion in seawater. *Proc. Natl. Acad. Sci. U. S. A.*, 109(6):1874–1877, February 2012.

[30] Jie Qiu and Peter C. Burns. Clusters of Actinides with Oxide, Peroxide, or Hydroxide Bridges. *Chemical Reviews*, 113(2):1097–1120, 2013.

[31] Colm Mallon, Aurora Walshe, Robert J. Forster, Tia E. Keyes, and Robert J. Baker. Physical Characterization and Reactivity of the Uranyl Peroxide $[UO_2(\eta^2\text{-}O_2)(H_2O)_2]\cdot 2H_2O$: Implications for Storage of Spent Nuclear Fuels. *Inorg. Chem.*, 51(15):8509–8515, August 2012.

[32] Albrecht Rabenau. Die Rolle der Hydrothermalsynthese in der praïparativen Chemie. *Angewandte Chemie*, (97):1017–1032, 1985.

[33] Anthony R. West. *Solid State Chemistry and its Applications*. Wiley – VCH, 1992.

[34] Gérard Demazeau. High pressures: Recent trends in materials science. *High Pressure Research*, 18(1-6):203–212, 2000.

[35] Ulrich Müller. *Anorganische Strukturchemie*. Teubner Studienbücher, 5 edition, 2006.

[36] P. Perlin, T. Suski, C. Skierbiszewski, and P. Wisniewski. Pressure studies of band structure, defects and impurities in group III nitrides. *High Pressure Research*, 18(1-6):21–28, 2000.

[37] J. M. Besson. Validation of computations by high pressure measurements: Solutions to problems that experiments cannot solve. *High Pressure Research*, 18(1-6):01–11, 2000.

[38] R. Boehler. New diamond cell for single-crystal x-ray diffraction. *Rev. Sci. Instrum.*, 77:115103, 2006.

[39] S. Klotz, J.-C. Chervin, P. Munsch, and G. Le Marchand. Hydrostatic limits of 11 pressure transmitting media. *J. Phys. D: Appl. Phys.*, 42(7):075413, 2009.

[40] Wilfried B. Holzapfel. Refinement of the ruby luminescence pressure scale. *Journal of Applied Physics*, 93(3):1813–1818, 2003.

[41] Agnes Dewaele, Frederic Datchi, Paul Loubeyre, and Mohamed Mezouar. High pressure-high temperature equations of state of neon and diamond. *Physical Review B*, 77(9):094106, March 2008.

[42] Johannes Kepler. *Vom sechsekigen Schnee*. Hellerau-Verlag, 1 edition, 2005.

[43] Harald Garcke. Kepler, Kristalle und Computer. Mathematik und numerische Simulationen helfen Kristallwachstum zu verstehen. *Mitteilungen der Deutschen Mathematiker-Vereinigung*, 20(4):219–228, 2012.

[44] D. S. Sivia. *Elementary Scattering Theory*. Oxford University Press, 2011.

[45] Werner Massa. *Kristallstrukturen*. Teubner Studienbücher, 4^{th} edition, 2005.

[46] Th. Hahn, editor. *INTERNATIONAL TABLES for CRYSTALLOGRAPHY - Volume A: Space-group symmetry*. Springer, 2005.

[47] A. Le Bail, H. Duroy, and J.-L. Fourquet. Ab-initio structure determination of $LiSbWO_6$ by X-ray powder diffraction. *Mater. Res. Bull.*, 23:447–452, 1988.

[48] H. M. Rietveld. A profile refinement method for nuclear and magnetic structures. *Journal of Applied Crystallography*, 2(2):65–71, Jun 1969.

[49] H.P. Liermann, W. Morgenroth, A. Ehnes, A. Berghäuser, B. Winkler, H. Frantz, and E. Weckert. The extreme conditions beamline at PETRA III, DESY: Possibilities to conduct time resolved monochromatic diffraction experiments in dynamic and laser heated DAC. *J. Phys., Conf. Ser.*, 215:012029, 2010.

[50] A. P. Hammersley. Fit2D: An Introduction and Overview. ESRF Internal Report ESRF97HA02T, European Synchrotron Radiation Facility, 1997.

[51] A. P. Hammersley, S. O. Svensson, M. Hanfland, A. N. Fitch, and D. Häusermann. Two-Dimensional Detector Software: From Real Detector to Idealised Image or Two-Theta Scan. *High-Pressure Research*, 14:235–248, 1996.

[52] M. Wojdyr. Fityk: a general-purpose peak fitting program. *J. Appl. Cryst.*, 43:1126, 2010.

[53] Tine Straasø, Ann-Christin Dippel, Jacob Beckerc, and Jens Als-Nielsen. Model-independent structure factors from powder X-ray diffraction: a novel approach. *J. Synchrotron Rad.*, 21:119 – 126, 2014.

[54] A. Altomare, M. Camalli, C. Cuocci, C. Giacovazzo, A. Moliterni, and R. Rizzi. EXPO2009: structure solution by powder data in direct and reciprocal space. *Journal of Applied Crystallography*, 40:1197 – 1202, 2009.

[55] A.C. Larson and R.B. von Dreele. General Structure Analysis System (GSAS). Technical Report LAUR 86-748, Los Alamos National Laboratory, 2000.

[56] B. H. Toby. EXPGUI, a graphical user interface for GSAS. *J. Appl. Crystallogr.*, 34:219–221, 2001.

[57] S. C. Vogel. gsaslanguage: a GSAS script language for automated Rietveld refinements of diffraction data. *J. Appl. Crystallogr.*, 44:873–877, 2011.

[58] Illustration of the NPDF Instrumental Setup. webpage, February 2014.

[59] O. Scherzer. Über einige Fehler von Elektronenlinsen. *Z. Phys.*, 101:593–603, 1936.

[60] Markus Lentzen. Progress in Aberration-Corrected High-Resolution Transmission Electron Microscopy Using Hardware Aberration Correction. *Microsc. Microanal.*, 12:191–205, 2006.

[61] Manfred von Heimendahl. *Einführung in die Elektronenmikroskopie*. vieweg, 1970.

[62] C. Kisielowski, B. Freitag, M. Bischoff, H. van Lin, S. Lazar, G. Knippels, P. Tiemeijer, M. van der Stam, S. von Harrach, M. Stekelenburg, M. Haider, S. Uhlemann, H. MÃ¼ller, P. Hartel, B. Kabius, D. Miller, I. Petrov, E.A. Olson, T. Donchev, E.A. Kenik, A.R. Lupini, J. Bentley, S.J. Pennycook, I.M. Anderson, A.M. Minor, A.K. Schmid, T. Duden, V. Radmilovic, Q.M. Ramasse, M. Watanabe, R. Erni, E.A. Stach, P. Denes, and U. Dahmen. Detection of Single Atoms and Buried Defects in Three Dimensions by Aberration-Corrected Electron Microscope with 0.5 ÅInformation Limit. *Microscopy and Microanalysis*, 14:469–477, October 2008.

[63] G. Cliff and G.W. Lorimer. The quantitative analysis of thin specimens. *J. Microsc.*, 103(2):203–207, 1975.

[64] Manfred Hesse, Herbert Meier, and Bernd Zeeh. *Spectroscopic Methods of Organic Chemistry*. Georg Thieme Verlag, 1997.

[65] P. W. Atkins. *Physikalische Chemie*. VCH Weinheim, 2 edition, 1990.

[66] D. L. Rousseau, R. P. Bauman, and S. P. S. Porto. Normal mode determination in crystals. *Journal of Raman Spectroscopy*, 10(1):253–290, 1981.

[67] Kazuo Nakamoto. *Infrared and Raman Spectra of Inorganic and Coordination Compounds*, chapter 5. John Wiley & Sons, Ltd, 2006.

[68] P. Dawson, M. M. Hargreave, and G. R. Wilkinson. The vibrational spectrum of zircon ($ZrSiO_4$). *Journal of Physics C: Solid State Physics*, 4(2):240, 1971.

[69] P. W. Atkins and R. S. Friedman. *Molecular Quantum Mechanics*. Oxford University Press, 1997.

[70] P. A. Temple and C.E. Hathaway. Multiphonon Raman Spectrum of Silicon. *Phys. Rev. B*, 7:85, 1973.

[71] H.K. Mao and P.M. Bell. Calibration of the ruby pressure gauge to 800 kbar under quasi-hydrostatic conditions. *J. Geophys. Res.*, 91:4673, 1986.

[72] Gilberto Vlaic and Luca Olivi. EXAFS Spectroscopy: a Brief Introduction. *Croatica Chemica Acta*, 77(3):427–433, 2004.

[73] D.C. Koningsberger, B.L. Mojet, G.E. van Dorssena, and D.E. Ramaker. XAFS spectroscopy: fundamental principles and data analysis. *Topics in Catalysis*, 10:143–155, 2000.

[74] Edward A. Stern. Theory of the extended x-ray-absorption fine structure. *Phys. Rev. B*, 10:3027–3037, Oct 1974.

[75] J.J. Rehr, J.J. Kas, F.D. Vila, M.P. Prange, and K. Jorissen. Parameter-free calculations of X-ray spectra with FEFF9. *Phys. Chem. Chem. Phys.*, 12(21):5503–5513, 2010.

[76] B. Ravel and M. Newville. ATHENA, ARTEMIS, HEPHAESTUS: data analysis for X-ray absorption spectroscopy using IFEFFIT. *Journal of Synchrotron Radiation*, 12:537–541, 2005.

[77] T. Ressler. WinXAS. *Journal of Synchrotron Radiation*, 5:118, 1998.

[78] G. N. George and I. J. Pickering. EXAFSPAK - A Suite of Computer Programs for Analysis of X-ray Absorption Spectra. Technical report, Stanford Synchrotron Radiation Laboratory, 1995.

[79] Illustration of the FDS Instrumental Setup. webpage, February 2014.

[80] Georg Schwedt. *Taschenatlas der Analytik*. Thieme, 1992.

[81] L.R. Stieff, T.W. Stern, and A.M. Sherwood. Coffinite, a Uranous Silicate with Hydroxyl Substitutions: A New Mineral. *Am. Mineral.*, 41(9 and 10):675–689, 1956.

[82] A. Pabst. The Metamict State. *Am. Mineral.*, 37:137–158, March 1952.

[83] H.R. Hoekstra and L.H. Fuchs. Synthesis of Coffinite - $USiO_4$. *Science*, 123:105, 1956.

[84] J. A. Speer. The actinide orthosilicates. *Reviews in Mineralogy and Geochemistry*, 5:113–135, 1980.

[85] F.A. Mumpton and R. Roy. Hydrothermal stability studies of the zircon-thorite group. *Geochim. Cosmochim. Acta*, 21(3-4):217–238, January 1961.

[86] L. H. Fuchs and H. R. Hoekstra. THE PREPARATION AND PROPERTIES OF URANIUM (IV) . *Am. Mineral.*, 44(September-October):1057–1063, 1959.

[87] L. H. Fuchs and Elizabeth Gebert. X-RAY STUDIES OF SYNTHETIC COFFINITE, THORITE AND URANOTHORITES. *Am. Mineral.*, 43:243–248, 1958.

[88] S. Lungu. ETUDE DES COURBES DE LIQUIDUS ET DES PROPRIETES THERMODYNAMIQUES DES SYSTEMES SiO_2-ThO_2 ET SiO_2-ThO_2-UO_2. *J. Nucl. Mater.*, 19:155–159, 1966.

[89] S. Lungu. SOME THEORETICAL ASPECTS IN THE SPINODAL DECOMPOSITION AND CRYSTALLIZATION OF SILICATE MELTS. EXPERIMENTAL RESULTS FOR THE UO_2 - SiO_2 SYSTEM. *J. Nucl. Mater.*, 48:165–171, 1973.

[90] V. Robit, C. Poinssot, K. Spahiu, and H. Cui. Materials research society symposium proceedings. *Mater. Res. Soc. Symp. Proc.*, 932(489):489, 2006.

[91] V.M. Goldschmidt. *Geochemistry*. Oxford University Press, 1954.

[92] L. H. Fuchs. FORMATION AND PROPERTIES OF SYNTHETIC THORITE CRYSTALS. *Am. Mineral.*, 43(-):367–368, March 1958.

[93] H.-J. Förster. Composition and origin of intermediate solid solutions in the system thorite-xenotime-zircon-coffinite. *Lithos*, 88(1-4):35–55, May 2006.

[94] E.D.A. Ferriss, R.C. Ewing, and U. Becker. Simulation of thermodynamic mixing properties of actinide-containing zircon solid solutions. *Am. Mineral.*, 95(2-3):229–241, 2010.

[95] D. T. Costin, A. Mesbah, N. Clavier, N. Dacheux, C. Poinssot, S. Szenknect, and J. Ravaux. How To Explain the Difficulties in the Coffinite Synthesis from the Study of Uranothorite? *Inorg. Chem.*, 50:11117–11126, 2011.

[96] Lin-gun Liu. Phase transformations in $MSiO_4$ compounds at high pressures and their geophysical implications. *Earth Planet. Sci. Lett.*, 57(1):110–116, January 1982.

[97] F.X. Zhang, V. Pointeau, L.C. Shuller, D.M. Reaman, M. Lang, Zhenxian Liu, Jingzhu Hu, W.R. Panero, U. Becker, C. Poinssot, and R.C. Ewing. Structural transitions and electron transfer in coffinite, $USiO_4$, at high pressure. *Am. Mineral.*, 94(7):916–920, 2009.

[98] A. Meldrum, S. J. Zinkle, L. A. Boatner, and R. C. Ewing. A transient liquid-like phase in the displacement cascades of zircon, hafnon and thorite. *Nature*, 395(6697):56–58, September 1998.

[99] John A. Hermann, John F. Suttle, and Henry R. Hoekstra. *Uranium(IV) Chloride*, pages 143–145. John Wiley & Sons, Inc., 2007.

[100] M. Taylor and R. C. Ewing. The Crystal Structures of the $ThSiO_4$ Polymorphs: Huttonite and Thorite. *Acta Crystallogr.*, (34):1074–1079, 1978.

[101] Wiberg Nils. *Lehrbuch der Anorganischen Chemie*. De Gruyter, Berlin, Boston, 101 edition, 2008.

[102] Xuefeng Wang and Lester Andrews. Infrared spectra and structures of the $Th(OH)_2$ and $Th(OH)_4$ molecules. *Phys. Chem. Chem. Phys.*, 7:3834–3838, 2005.

[103] M.P. Lahalle, J.C. Krupa, M. Lepostollec, and J.P. Forgerit. Low-temperature raman study on $ThSiO_4$ single crystal and related infrared spectra at room temperature. *J. Solid State Chem.*, 64(2):181–187, September 1986.

[104] Cornelius Keller. Investigations of germanates and silicates of the type ABO_4 with quadrivalent elements thorium to americium. *Nukleonik*, 5(2):41–50, 1963.

[105] J. Mulak. Crystal Field Parameters in $USiO_4$ from Temperature Dependence of Paramagnetic Susceptibility. *J. Solid State Chem.*, -(21):117–126, 1977.

[106] G. E. Brown, G. V. Gibbs, and P. H. Ribbe. THE NATURE AND THE VARIATION IN LENGTH OF THE Si-O AND AI-O BONDS IN FRAMEWORK SILICATES. *Am. Mineral.*, 54:1044–1061, July 1969.

[107] G. E. Brown and G. V. Gibbs. OXYGEN COORDINATION AND THE Si-O BOND. *Am. Mineral.*, 54:1528–1539, November 1969.

[108] W. H. Baur. Bond length variation and distorted coordination polyhedra in inorganic crystals. *Transactions of the American Crystallographic Association*, 6:129, 1970.

[109] W. L. Bragg. The conversion factor for kX units to Ångström units. *Journal of Scientific Instruments*, 24(1):27, 1947.

[110] Elizabeth Armstrong Wood. The Conversion Factor for kX Units to Angström Units. *Journal of Applied Physics*, 18(10):929–930, 1947.

[111] G. W. Brindley. XLV. The Effect of Grain or Particle Size on X-ray Reflections from Mixed Powders and Alloys, considered in relation to the Quantitative Deterruination of Crystalline Substances by X-ray Methods. *Philosophical Magazine Series 7*, 36:347–369, 1945.

[112] G.K. Williamson and W.H.Hall. X-ray line broadening from filed aluminium and wolfram. *Acta Metall.*, 1:22–31, 1953.

[113] V.D. Mote, Y. Purushotham, and B.N. Dole. Williamson-Hall analysis in estimation of lattice strain in nanometer-sized ZnO particles. *Journal of Theoretical and Applied Physics*, 6(6), 2012.

[114] Y. T. Prabhu, K. Venkateswara Rao, V. Sesha Sai Kumar, and B. Siva Kumari. X-ray Analysis of Fe doped ZnO Nanoparticles by Williamson-Hall and Size-Strain Plot. *International Journal of Engineering and Advanced Technology (IJEAT)*, 2(4):268–274, 2013.

[115] Albert C. Thompson, Janosz Kirz, David T. Attwood, Eric M. Gullikson, Malcom R. Howells, Jeffrey B. Kortright, Yanwei Liu, Arthur L. Robinson, James H. Underwood, Kwang-Je Kim, Ingolf Lindau, Piero Pianetta, Herman Winick, Gwyn P. Williams, and James H. Scofield. *X-RAY DATA BOOKLET*. Number LBNL/PUB-490 Rev. 3. Center for X-Ray Optics and Advanced Light Source, Lawrence Berkley National Laboratory, University of California; Berkley, CA 94720, third edition, September 2009.

[116] Isabell Dreissig, Stephan Weiss, Christoph Hennig, Gert Bernhard, and Harald Zänker. Formation of uranium(IV)-silica colloids at near-neutral pH. *Geochim. Cosmochim. Acta*, 75(2):352–367, January 2011.

[117] D.T. Costin, A. Mesbah, N. Clavier, S. Szenknect, N. Dacheux, C. Poinssot, J. Ravaux, and H.P. Brau. Preparation and characterization of synthetic $Th_{0.5}U_{0.5}SiO_4$ uranothorite. *Progress in Nuclear Energy*, 57:155–160, 2012.

[118] E.D.A. Ferriss, K.B. Helean, C.R. Bryan, P.V. Brady, and R.C. Ewing. UO_2 corrosion in an iron waste package. *J. Nucl. Mater.*, 384(2):130–139, February 2009.

[119] Vadim S. Urusov. The phenomenological theory of solid solutions. In Charles E. Geiger, editor, *Solid Solutions in Silicate and Oxide Systems*, number 3 in EMU Notes in Mineralogy, chapter 6, pages 121–153. EÖTVÖS UNIVERSITY PRESS, 2001.

[120] S. Hubert, J. Purans, G. Heisbourg, P. Moisy, and N. Dacheux. Local Structure of Actinide Dioxide Solid Solutions $Th_{1-x}U_xO_2$ and $Th_{1-x}Pu_xO_2$. *Inorg. Chem.*, 45:3887–3894, 2006.

[121] A. Scheinost, H. Stanjek, D. G. Schulze, U. Gasser, and D. L. Sparks. Structural environment and Oxidation state of Mn in goethite-groutite solid-solutions. *Am. Mineral.*, 86:139–146, 2001.

[122] R.D. Shannon. Ion Radii. *Acta Crystallogr.*, A32:751–767, 1976.

[123] D. Errandonea, J. Pellicer-Porres, F.J. Manjón, A. Segura, Ch. Ferrer-Roca, R.S. Kumar, O. Tschauner, P. Rodríguez-Hernández, J. López-Solano, S. Radescu, A. Mujica, Muñoz, A., and G. Aquilanti. High-pressure structural study of the scheelite tungstates $CaWO_4$ and $SrWO_4$. *Phys. Rev. B: Condens. Matter Mater. Phys.*, 72:174106, 2005.

[124] A.F. Reid and A.E. Ringwood. Newly observed high-pressure transformations in Mn_3O_4, $CaAl_2O_4$ and $ZrSiO_4$. *Earth Planet. Sci. Lett.*, 6:205–208, 1969.

[125] Bouchaib Manoun, Robert T. Downs, and Surendra K. Saxena. A high-pressure Raman spectroscopic study of hafnon, $HfSiO_4$}. *Am. Mineral.*, 91:1888–1892, 2006.

[126] Preyoshi P. Bose, R. Mittal, and S. L. Chaplot. Lattice dynamics and high pressure phase stability of zircon structured natural silicates. *Phys. Rev. B*, 79(17):174301–, May 2009.

[127] E. Knittle and Q. Williams. High-pressure Raman spectroscopy of $ZrSiO_4$ Observation of the zircon to scheelite transition at 300 K. *Am. Mineral.*, 78:245–252, 1993.

[128] M.B Smirnov, A. P Mirgodorski, V. Yu Kazimirov, and R. Guinebretiere. Bond-switching mechanism for the zircon-scheelite phase transition. *Phys. Rev. B*, 78:094109–1–094109–10, 2008.

[129] K. Kusaba, Y. Syono, M. Kikuchi, and K. Fukoka. Shock behavior of zircon: Phase transition to scheelite structure and decomposition. *Earth Planet. Sci. Lett.*, 72:433–439, 1985.

[130] A. Meldrum, L.A. Boatner, S.J. Zinkle, S.X. Wang, L.M. Wang, and R.C. Ewing. Effects of dose rate and temperature on the crystalline-to-metamict transformation in ABO_4 orthosilicates. *Can. Mineral.*, 37:207–221, 1999.

[131] A. Meldrum, S.J. Zinkle, L.A. Boatner, and R.C. Ewing. Heavy-ion irradiation effects in the ABO_4 orthosilicates: Decomposition, amorphization, and recrystallization. *Phys. Rev. B: Condens. Matter Mater. Phys.*, 59:3981–3992, 1999.

[132] L. Nasdala, D. Wolf, and G. Irmer. The degree of metamictization in zircon: a Raman spectroscopic study. *Eur. J. Min.*, 7:471–478, 1995.

[133] L. Nasdala, R.T. Pidgeon, and D. Wolf. Heterogeneous metamictization of zircon on a microscale. *Geochim. Cosmochim. Acta*, 60(6):1091–1097, 1996.

[134] Lutz Nasdala, Andreas Kronz, Richard Wirth, Tamás Váczi, Cecilia Pérez-Soba, Arne Willner, and Allen K. Kennedy. The phenomenon of deficient electron microprobe totals in radiation-damaged and altered zircon. *Geochim. Cosmochim. Acta*, 73(6):1637–1650, March 2009.

[135] M. O'Keeffe and B.G. Hyde. An alternative approach to non-molecular crystal structures with emphasis on the arrangements of cations. In *Cation Ordering and Electron Transfer*, volume 61 of *Structure and Bonding*, pages 77–144. Springer Berlin Heidelberg, 1985.

[136] Francis Birch. Finite elastic strains of cubic crystals. *Phys. Rev.*, 71:809, 1947.

[137] F.D. Murnaghan. Finite deformations of an elastic solid. *Am. J. Math.*, 49:235–260, 1937.

[138] Björn Winkler. Personal Communication, May 2013.

[139] R. M. Hazen and L. W. Finger. Crystal structure and compressibility of zircon at high-pressure. *Am. Mineral.*, 64:196–201, 1979.

[140] Francis Birch. Composition of the Earth's Mantle. *Geophysical Journal International*, 4(Supplement 1):295–311, 1961.

[141] J.H. Nicola and H.N. Rutt. Comparative study of zircon ($ZrSiO_4$) and hafnon ($HfSiO_4$) Raman-spectra. *J. Phys. C: Solid State Phys.*, 7:1381–1386, 1974.

[142] T. Geisler, B.E. Burakov, V. Zirlin, L. Nikolaeva, and P. Pöml. A Raman spectroscopic study of high-uranium zircon from the Chernobyl "lava". *Eur. J. Min.*, 17(883–894), 2005.

[143] B.A. Kolesov, C.A. Geiger, , and T. Armbruster. The dynamic properties of zircon studied by single-crystal X-ray diffraction and Raman spectroscopy. *Eur. J. Min.*, 13:939–948, 2001.

[144] R. W. G. Syme, D. J. Lockwood, and H. J. Kerr. Raman spectrum of synthetic zircon ($ZrSiO_4$) and thorite ($ThSiO_4$). *Journal of Physics C: Solid State Physics*, 10:1335–1348, 1977.

[145] P.C. Debets. X-ray diffraction data on hydrated uranium peroxide. *Journal of Inorganic and Nuclear Chemistry*, 25(6):727–730, June 1963.

[146] W. H. Zachariasen. Ck-1367. Technical report, US Atomic Energy Comm., 1944.

[147] E.H.P. Cordfunke and A.A. Van Der Giessen. Pseudomorphic decomposition of uranium peroxide into UO_3. *Journal of Inorganic and Nuclear Chemistry*, 25(5):553–555, May 1963.

[148] G. Sattonnay, C. Ardois, C. Corbel, J.F. Lucchini, M.-F. Barthe, F. Garrido, and D. Gosset. Alpha-radiolysis effects on UO_2 alteration in water. *J. Nucl. Mater.*, 288(1):11–19, January 2001.

[149] B. Hanson, B. McNamara, E. Buck, J. Friese, E. Jenson, K. Krupka, and B. Arey. Corrosion of commercial spent nuclear fuel. 1. Formation of studtite and metastudtite. *Radiochim. Acta*, 93(3):159–168, 2005.

[150] Tori Z. Forbes, Patrick Horan, Tara Devine, Daniel McInnis, and Peter C. Burns. Alteration of dehydrated schoepite and soddyite to studtite, $[(UO_2)(O_2)(H_2O)_2](H_2O)_2$. *Am. Mineral.*, 96(1):202–206, January 2011.

[151] A. Rey, I. Casas, J. Giñez, J. Quiònes, and J. de Pablo. Effect of temperature on studtite stability: Thermogravimetry and differential scanning calorimetry investigations. *J. Nucl. Mater.*, 385(2):467–473, March 2009.

[152] K. A. H. Kubatko, K. B. Helean, A. Navrotsky, and P. C. Burns. Stability of peroxide-containing uranyl minerals. *Science*, 302(5648):1191–1193, November 2003.

[153] P. C. Burns and K. A. Hughes. Studtite, $[(UO_2)(O_2)(H_2O)(_2)](H_2O)_2$: The first structure of a peroxide mineral. *Am. Mineral.*, 88(7):1165–1168, July 2003.

[154] S. Ostanin and P. Zeller. Ab initio study of uranyl peroxides: Electronic factors behind the phase stability. *Phys. Rev. B*, 75(7):073101, February 2007.

[155] Vaes. *Bulletin société belge de Géologie, de paleontology et d'hydrologie*, 70(B):212, 1947.

[156] K. Walenta. On studtite and its composition. *Amer. Min.*, 59:166–171, 1974.

[157] T. Fairley. III.–Study of hydrogen dioxide and of certain peroxides. *J. Chem. Soc.*, 31:127, 1877.

[158] G. F. Hüttig and E. von Schröder. . *Z. Anorg. Allg. Chem.*, 121:243, 1922.

[159] J. J. Katz and E. Rabinowitch. *The Chemistry of Uranium, Part I*, pages 290 – 293. McGraw–Hill, 1951.

[160] A. Rosenheim and H. Daehr. *Z. Anorg. Allg. Chem.*, 181:177, 1929.

[161] Taichi Sato. Uranium Peroxide Hydrates. *Die Naturwissenschaften*, 48:668, 1961.

[162] Taichi Sato. Thermal Decomposition of Uranium Peroxide Hydrate. *Die Naturwissenschaften*, 48:693, 1961.

[163] Michael Deliens and Paul Piret. Metastudtite, $UO_4{\cdot}2H_2O$, a new mineral from Shinkolobwe, Shaba, Zaire. *American Mineralogist*, 68:456–458, 1983.

[164] K.-A. Kubatko. *CRYSTALLOGRAPHY, HIERARCHY OF CRYSTAL STRUCTURES AND CHEMICAL THERMODYNAMICS OF SELECT URANYL PHASES*. PhD thesis, Graduate School of the University of Notre Dame, Illinois, 2005.

[165] Jiri Čejka, J. Sejkora, and M. Deliens. New data on studtite, $UO_4{\cdot}4H_2O$, from Shinkolobwe, Shaba, Zaire. *Neues Jahrbuch fuer Mineralogie, Monatshefte*, H 3:125–137, 1996.

[166] S. Bastians, G. Crump, W. P. Griffith, and R. Withnall. Raspite and studtite: Raman spectra of two unique minerals. *J. Raman Spectrosc.*, 35(8-9):726–731, August 2004.

[167] Aurora Walshe, Tim Pru, Tonya Vitova, and Robert J. Baker. An EXAFS and HR-XANES study of the uranyl peroxides $[UO_2(\eta]^2\text{-}O_2)(H_2O)_2]{\cdot}nH_2O$ (n = 0, 2) and uranyl (oxy)hydroxide $[(UO_2)_4O(OH)_6]{\cdot}6H_2O$. *Dalton Trans.*, pages –, 2014.

[168] R. Ukazi. On the Reactivity of Uranouranic Oxide, (I) On the tthermal decomposition of uranyl nitrate (UNH), ammonium diuranate (ADU) and uranium peroxide (UPO). *Journal of the Atomic Energy Society of Japan*, 1(7):405 – 411, 1959.

[169] C. Duval. . *Anal. Chim. Acta*, 3:335, 1949.

[170] J. E. Boggs and M. El-Chehabi. . *J. Amer. Chem. Soc.*, 79:4258, 1957.

[171] Jichen Li. Inelastic neutron scattering studies of hydrogen bonding in ices. *The Journal of Chemical Physics*, 105(16):6733–6755, 1996.

[172] Nathan W. Ockwig, Randall T. Cygan, Louise J. Criscenti, and Tina M. Nenoff. Molecular dynamics studies of nanoconfined water in clinoptilolite and heulandite zeolites. *Phys. Chem. Chem. Phys.*, 10:800–807, 2008.

[173] NM. Gresley, W.P. Griffith, A.C. Laemmel, H.I.S. Nogueira, and B.C. Parkin. . *J. Mol. Catal.*, 117:185, 1997.

[174] M. J. Lipp, Zs. Jenei, J. Park Klepeis, and W. J. Evans. Raman Investigation of The Uranium Compounds U_3O_8, UF_4, UH_3 and UO_3 under Pressure at Room Temperature. Technical Report LLNL-TR-522251, Lawrence Livermore National Laboratory, 2011.

[175] D.A. Zamyatin, Yu.V. Shchapova, S.L. Votyakov, N.N. Eremin, and V.S. Urusov. Structure and thermodynamic properties of zircon-coffinite solid solutions according to the semiempirical atomistic simulation data. *Glass Physics and Chemistry*, 39(2):182–192, 2013.

[176] André Rossberg. Personal Communication, November 2012.

[177] K. Opel. *Kolloid- und Löslichkeitsuntersuchungen an Uran(IV) mittels laserinduzierter Breakdown-Detektion.* PhD thesis, TU Dresden, 2006.

List of Figures

List of Tables

Irgendwo und irgendwann
trifft man sowieso den Sensenmann
und dann denkt man bestimmt nicht: "Oh,
ich war zu selten im Büro!"

(Großstadtgeflüster)

Band / Volume 254
First-Principles Study on Pyrites and Marcasites for Photovoltaic Application
T. Schena (2015), 206 pp
ISBN: 978-3-95806-041-8

Band / Volume 255
Glass-Ceramic Sealant Reinforcement for High-Temperature Applications
B. Cela Greven (2015), xi, 119 pp
ISBN: 978-3-95806-042-5

Band / Volume 256
Entwicklung planarer $Ba_{0,5}Sr_{0,5}Co_{0,8}Fe_{0,2}O_{3-\delta}$-Membranmodule zur Sauerstoffabtrennung und Analyse ihres Transportverhaltens
P. Niehoff (2015), VIII, 134 pp
ISBN: 978-3-95806-044-9

Band / Volume 257
Extension of the Reactor Dynamics Code MGT-3D for Pebble-bed and Block-type High-Temperature-Reactors
D. Shi (2015), x, 162 pp
ISBN: 978-3-95806-045-6

Band / Volume 258
Failure Analysis of Thin Film Solar Modules using Lock-in Thermography
M. Siegloch (2015), XIII, 131 pp
ISBN: 978-3-95806-047-0

Band / Volume 259
Relation between growth rate, material quality, and device grade condition for intrinsic microcrystalline silicon:
From layer investigation to the application to thin-film tandem solar cells
S. Michard (2015), vi, 184 pp
ISBN: 978-3-95806-048-7

Band / Volume 260
Quantitative analysis of spatially resolved electroluminescence of $Cu(In,Ga)Se_2$ and a-Si:H thin-film solar cells and modules
T. Tran (2015), iii, 161 pp
ISBN: 978-3-95806-050-0

Band / Volume 261
Influence of the surface composition and morphology on the reflectivity of diagnostic mirrors in a fusion reactor
M. Matveeva (2015), 158 pp
ISBN: 978-3-95806-051-7

Band / Volume 262
Very High Cycle Fatigue Behavior of Riblet Structured High Strength Aluminum Alloy Thin Sheets
S. Stille (2015), XII, 123 pp
ISBN: 978-3-95806-054-8

Band / Volume 263
The role of soil heterogeneity on field scale evapotranspiration: 3D integrative modelling and upscaling of root water uptake
K. Huber (2015), xii, 128 pp
ISBN: 978-3-95806-057-9

Band / Volume 264
Strontium-Diffusion in Cer-Gadolinium-Oxid als Degradationsmechanismus der Festoxid-Brennstoffzelle
T. Mandt (2015), iii, 160 pp
ISBN: 978-3-95806-058-6

Band / Volume 265
Cluster analysis of European surface ozone observations for evaluation of MACC reanalysis data
O. Lyapina (2015), 187 pp
ISBN: 978-3-95806-060-9

Band / Volume 266
Real-time quantification of oxygen isotope exchange between carbon dioxide and leaf/soil water in terrestrial ecosystems with laser-based spectroscopy
L. Gangi (2015), XX, 156 pp
ISBN: 978-3-95806-061-6

Band / Volume 267
Secondary Uranium Phases of Spent Nuclear Fuel – Coffinite, $USiO_4$, and Studtite, $UO_4 \cdot 4H_2O$ – Synthesis, Characterization, and Investigations Regarding Phase Stability
S. Labs (2015), 153, xlii pp
ISBN: 978-3-95806-063-0

Weitere ***Schriften des Verlags im Forschungszentrum Jülich*** unter
http://wwwzb1.fz-juelich.de/verlagextern1/index.asp

Energie & Umwelt /
Energy & Environment
Band / Volume 267
ISBN 978-3-95806-063-0